SINGLE – PHASE FLOW AND FLOW BOILING OF WATER IN RECTANGULAR METALLIC MICROCHANNELS

A thesis submitted for the degree of Doctor of Philosophy

By

Mehmed Rafet Özdemir

College of Engineering, Design and Physical Sciences
Brunel University London
Uxbridge, UB8 3PH, UK

2016

Abstract

This experimental research aims at investigating the single-phase flow heat transfer and friction factor, flow boiling heat transfer and pressure drop, and flow visualisation in microchannels using de-ionized water. In the literature, many studies failed to explain the effect of aspect ratio on the single-phase and two-phase flow heat transfer rate and pressure drop. Because the channel aspect ratios and hydraulic diameters were varied together in those studies. Also, there is a discrepancy between past studies and the conventional theory for the flow boiling heat transfer characteristics. Accordingly, the objectives of this research can be listed as follows: (i) modifying the existing experimental facility to perform single-phase and two-phase flow heat transfer and pressure drop and two-phase flow pattern visualization experiments in microchannels, (ii) clarifying the fundamental aspects of flow boiling in micro passages, (iii) investigating the aspect ratio, heat flux, mass flux and vapour quality effects on flow patterns, heat transfer rate and pressure drop in single-phase and two-phase flow, (iv) comparing the obtained results with heat transfer and pressure drop correlations and flow pattern maps available in the literature.

Consequently, the pre-existing experimental facility was modified in the current research by changing the pre-heaters, flowmeter and piping in order to achieve the goals of this study. Four copper rectangular microchannels were designed and manufactured. Three microchannel test sections having the same hydraulic diameter and length but different aspect ratios were investigated to reveal the effect of aspect ratio on the single-phase and two-phase flow heat transfer rate and pressure drop. The surface roughness of each microchannel was also examined. It was found that the surface roughnesses of all microchannels are similar. Moreover, an additional microchannel test section was used to examine the effect of heated length on the flow boiling heat transfer coefficient and pressure drop.

The single-phase flow results demonstrated that the channel aspect ratio has no influence on the friction factor and heat transfer rate for the tested microchannels and experimental range. In the flow boiling experiments, bubbly, bubbly/slug, slug, churn and annular flow regimes were observed in the tested microchannels. The channel aspect ratio effect was found to be small on the observed flow patterns. The

experimental flow patterns were predicted well by the flow pattern map proposed by Galvis and Culham (2012) except for the slug flow regime. The flow pattern maps of Sobierska et al. (2006) and Harirchian and Garimella (2009) reasonably predicted the experimental flow pattern data. The flow boiling heat transfer results showed that the prevailing heat transfer mechanism is nucleate boiling for the low and medium heat flux inputs. On the other hand, the dominant heat transfer mechanism is unclear at the high heat flux inputs while smaller aspect ratio microchannel has better heat transfer performance for low and medium heat flux inputs. However, at high heat flux inputs the channel aspect ratio effect was found to be insignificant on the flow boiling heat transfer coefficient. The experimental flow boiling heat transfer coefficient data were reasonably predicted by the correlations of Sun and Mishima (2009), Li and Wu (2010) and Mahmoud and Karayiannis (2011) from the literature.

The flow boiling pressure drop characteristics were also examined in the tested microchannels. Outcome of the experiments consistently indicated a highly linear trend between the increasing flow boiling pressure drop and the heat and mass flux. Also, the flow boiling pressure drop increased with the increase in vapour quality. The effect of channel aspect ratio on the flow boiling pressure drop was also assessed. It was found that when the channel aspect ratio decreased, the flow boiling pressure drop increased. The experimental flow boiling pressure drop data were compared to correlations from the literature. Mishima and Hibiki (1996), Yu et al. (2002) and Zhang et al. (2010) correlations reasonably predicted the experimental flow boiling pressure drop results.

Declaration

This research is the original work of the author except where otherwise specified, or where acknowledgements are made by references. This research was conducted at the College of Engineering, Design and Physical Sciences, Brunel University London, under the supervision of Prof. T. G. Karayiannis and Prof. L. C. Wrobel.

The work has not been submitted for another degree or award to any other institution.

Acknowledgements

Firstly, I would like to express my sincere gratitude to my supervisors Professor T.G. Karayiannis and Professor L.C. Wrobel for all their guidance and patience during this work. Their comments at research meetings encouraged me to accomplish this work.

I am grateful to Dr. M.M. Mahmoud for offering me his help even during his intensive working hours. His knowledge and useful advices about the experimental facility helped me to finish my experiments.

I would also like to thank to the technicians Mr. C. Xanthos, Mr. E. Wyse and Mr. P. Yates for helping me in my experiments.

I would like to acknowledge the Turkish Ministry of Higher Education Council and Marmara University for granting me a fully funded scholarship during my study.

To my parents and my family, there are no any proper words to express my gratitude. They supported me a lot financially and morally during this period. They also constantly prayed for me. They are one in a world for me.

I am thankful to the amazing support and friendship of all my friends especially Faruk, Hakan and Haluk.

Finally I would like to thank my lovely wife deeply for her patience and encouragement all the time. Without her support, this work would not have been possible.

Contents

List of Figures

List of Tables

Nomenclature

Latin

Symbol	*Parameter*	*SI unit*
A	Cross sectional area	m^2
Bo	Boiling number, q/Gh_{fg}	-
Bd	Bond number, $D_h\left[\sigma/(g\Delta\rho)\right]^{-0.5}$	-
B_X	Systematic uncertainty in a measured parameter X	
C	Chisholm parameter	-
C_{FR}	Modified Froude number	-
Ca	Capillary number, $\mu U/\sigma$	-
Co	Confinement number, $\left[\sigma/g\Delta\rho\right]^{0.5}/D_h$	-
c_P	Specific heat capacity	$J\ kg^{-1}\ K^{-1}$
D	Tube diameter	m
D_h	Hydraulic diameter, $2WH/(W+H)$	m
$Eö$	Eötvös number, $4\pi^2\sigma/D_h^2\Delta\rho g$	-
F	Convective boiling enhancement factor	-
f	Fanning friction factor	-
F_{fl}	Fluid-Surface parameter	-
Fr	Froude number	-
G	Mass flux, $\dot{m}/A$	$kg\ m^{-2}\ s^{-1}$
g	Gravitational acceleration	$m\ s^{-2}$
h_{sp}	Single phase heat transfer coefficient	$Wm^{-2}K^{-1}$
h_{tp}	Two phase heat transfer coefficient	$Wm^{-2}K^{-1}$
h	Heat transfer coefficient	$Wm^{-2}K^{-1}$
H	Channel height	m

Symbol	*Parameter*	*SI unit*
i	Specific enthalpy	J kg^{-1}
I	Electrical current	Ampere
J_g	Gas superficial velocity	m s^{-1}
J_l	Liquid superficial velocity	m s^{-1}
k	Thermal conductivity	$Wm^{-1}K^{-1}$
K_{90}	90º turn loss coefficient	-
K_c	Contraction loss coefficient	-
K_e	Expansion loss coefficient	-
$K(\infty)$	Dimensionless incremental pressure drop number	-
L	Length	m
L_B	Bubble length	m
L_{tp}	Two-phase length	m
L_{hy}	Hydrodynamically developing length	m
L_{th}	Thermally developing length	m
La	Laplace constant, $\left[\sigma / \Delta\rho g\right]^{0.5}$	-
L^*	Dimensionless length	-
M	Maranzana number, $q_{axial\ conduction} / q_{forced\ convection}$	-
$\dot{m}$	Mass flow rate	kg s^{-1}
N_{mb}	Initiation of Nucleation number, $(h_{\lg}\alpha_g)/(c\pi\Delta\nu_{\lg}D_h)$	-
N_{Co}	Convection number	-
Nu	Nusselt number, hD/k	-
P	Pressure	Pa
P	Power	W
P_r	Reduced pressure	-
Po	Poiseulle number, f Re	-
Pr	Prandtl number, $\mu c_p / k$	-
$q^{"}$	Heat flux	W m^{-2}

Symbol	*Parameter*	*SI unit*
Q_{Loss}	Heat loss	W
Re	Reynolds number	-
Re_{LO}	Liquid only Reynolds number, GD/μ_L	-
Re_L	Liquid Reynolds number, $(1-x)GD/\mu_L$	-
Re*	Equivalent Reynolds number	-
S	Nucleate boiling suppression factor	-
S_X	Standard deviation	-
S_{BX}	Standard deviation of the systematic uncertainty	-
T	Temperature	^{0}C
t	Time	s
t_{95}	95 % confidence limit	-
U	Superficial velocity	m s^{-1}
u_{random}	Random error	-
U_r^2	Absolute uncertainty	-
V	Velocity	m s^{-1}
v	Specific volume	m^{3}kg^{-1}
W	Channel width	m
W_c	Center to center distance of microchannel widths	m
We	Weber number, $G^2 D_h / \rho\sigma$	-
We_{gs}	Weber number based on gas superficial velocity, $\rho_g J_G^2 D_h / \sigma$	-
We_{ls}	Weber number based on liquid superficial velocity, $\rho_l J_L^2 D_h / \sigma$	-
X	Martinelli parameter, $\left[(dp/dz)_L/(dp/dz)_g\right]^{0.5}$	-
$\overline{X}$	The mean value	
x	Vapour quality	-
x_e	Exit quality	-

z	Axial coordinate	-

Greek

Symbol	*Parameter*	*SI unit*
α	Thermal diffusivity	m^2 / s
α	Void fraction	-
α	Percentage of data within ± 30 %	-
β	Surface area density	$m^2 m^{-3}$
β	Aspect ratio	-
β	Percentage of data within ±30 %	-
ΔP	Pressure drop	Pa
ΔT	Temperature difference	K
ϕ	Two phase multiplier	-
k	Conductivity	$W\ m^{-1}\ K^{-1}$
μ	Viscosity	$N\ s\ m^{-2}$
v	Specific volume	$m^3\ kg^{-1}$
ρ	Density	$kg\ m^{-3}$
σ	Surface tension	$N\ m^{-1}$

Subscripts

Symbol	*Meaning*
Cu	Copper
f	Friction
g	Gas
gs	Gas superficial
g	Gravitational
h	Heated
in	Inlet

L	Liquid
ls	Liquid superficial
o	Outer
p	Plenum
v	Vapour
w	Wall

Abbreviations

Symbol	***Meaning***	***SI unit***
app	Apparent	-
acc	Acceleration	-
ch	Channel	-
CHF	Critical Heat Flux	$W\ m^{-2}$
CPU	Central Processing Unit	-
crit	Critical	-
cv	Convective	-
EDL	Electric double layer	-
Exp	Experimental value	-
FD	Fully developed	-
HALF	High amplitude low frequency	-
HFM	Homogeneous Flow Model	-
LAHF	Low amplitude high frequency	-
Lo	Liquid only	-
Lv	Liquid to vapour change	-
MAE	Mean Absolute Error	-
max	Maximum	-
min	Minimum	-
ONB	Onset of nucleate boiling	-
PID	Proportional-Integral-Derivative	-
sat	Saturation	-
SFM	Separated Flow Model	-

sp	Single phase	-
sub	Subcooled	-
tp	Two phase	-

Dimensionless Groups

Group	Definition	Expression
Bond number, *Bd* Eötvos number, *Eö*	$\frac{\textit{Buoyancy force}}{\textit{Surface tension force}}$	$D_h\left[\sigma/(g\Delta\rho)\right]^{-0.5}$
Boiling number, *Bo*	A heat flux non-dimensionalized with the latent heat and mass flux	$\frac{q}{Gh_{fg}}$
Capillary number, *Ca*	$\frac{\textit{Viscous force}}{\textit{Surface tension force}}$	$\frac{\mu V}{\sigma}$
Confinement number, *Co*		$\left[\sigma/g\Delta\rho\right]^{0.5}/D_h$
Froude number, *Fr*	$\frac{\textit{Inertia force}}{\textit{Gravitational force}}$	$\frac{V^2}{gD}$
Laplace constant, *La*		$\left[\sigma/\Delta\rho g\right]^{0.5}$
Maranzana number, *M*	$q_{\textit{axial conduction}}/q_{\textit{forced convection}}$	
Convection number, N_{CO}		$\left(\frac{1-x}{x}\right)^{0.8}\left(\frac{\rho_g}{\rho_L}\right)^{0.5}$
Nusselt number, *Nu*	$\frac{\textit{Convective heat transfer}}{\textit{Conductive heat transfer}}$	hD/k
Prandtl number, Pr	$\frac{\textit{Momentum diffusivity}}{\textit{Thermal diffusivity}}$	$\mu c_p/k$
Reynolds number, Re	$\frac{\textit{Inertial forces}}{\textit{Viscous forces}}$	$V\rho D/\mu$
Martinelli parameter, X^2	$\frac{\textit{Frictional pressure gradient of liquid}}{\textit{Frictional pressure drop of gas}}$	$\frac{\left[dp/dz\right]_{f,L}}{\left[dp/dz\right]_{f,g}}$
Weber number, *We*	$\frac{\textit{Inertia force}}{\textit{Surface tension force}}$	$\frac{\rho V^2 D}{\sigma}$

Chapter 1

Introduction

1.1 Background of Microchannel Heat Sinks

After the First and Second Industrial Revolutions, mass production commenced in the global industrial arena. This advancement in the industry initiated development of novel technological equipment and production methods. Rapid developments in miniaturization of these novel devices in all industrial sectors was combined with the drive to produce more compact, fast, reliable and cost effective products. This resulted in significant challenges for design and operation of thermal management systems. Particularly, the heat dissipation rate from compact, powerful microelectronic devices, such as microchips and transistors, reached enormous rates. In the future, these values will be expected to be higher. Phillips (1990), Pop and Goodson (2006) and Ali (2010) stated that the heat dissipation rate from densely packed integrated circuits (ICs) and laser mirrors can be as high as $1\ MW/m^2$. Lee and Mudawar (2008) reported the heat flux values in avionics and VLSI industrial systems applications may reach up to $10\ MW/m^2$. Moreover, Boyd (1985), Lee and Mudawar (2009) and Kadam and Kumar (2014) reported ultra-high heat flux values on the order of $10^2\ MW/m^2$ in applications such as cooling fusion reactors and military defence applications. Consequently, the traditional cooling methods such as air cooling cannot meet these high cooling loads. Zhou et al. (2004) reported that conventional air cooled systems cannot dissipate more than $1.5\ MW/m^2$. In a recent study, Xu et al. (2014) compared fan air-cooling and liquid-cooling systems in a numerical analysis of the cooling of a single board computer cabin system. They reported that the liquid-cooling system achieved a *56 %* lower CPU temperature than the fan air-cooling system.

At this point, microchannel heat exchanger technologies are finding novel applications in various industrial areas as game-changing shift for the design and operation of next generation, high performance thermal management systems. They offer a promising solution due to their high thermal performance, compactness and lower weight. These extremely compact heat exchanger applications provide higher plant efficiency with less coolant and low waste production. From the heat transfer point of view, smaller channel size enables higher surface area to volume ratio resulting in higher heat and mass transfer rates. Here, the term 'micro' deserves special attention which is discussed in details in Chapter 2 by presenting different definitions and criteria presented in various publications.

The first pioneering work in micro passages was conducted by Tuckerman and Pease (1981) to cool very large-scale integrated circuits (VLSI) with silicon rectangular microchannels having *98.6 μm* hydraulic diameter. They explained the microchannel heat sink concept and showed that *7.9 MW/m*^{2} heat could be removed with single-phase forced convective cooling in microchannels. This was a very high cooling rate in comparison to conventional scale channels that could only dissipate up to *0.2 MW/m*^{2} heat flux reported by Keyes (1975). However, the associated pressure drop in Tuckerman and Pease's (1981) work was high (*~ 1.3 bar*). Similarly, Missaggia et al. (1989) delivered single-phase water to a microchannel heat sink which consisted of *11* rectangular silicon microchannels (D_h*=160 μm*) to dissipate heat from two-dimensional high power density laser diode system. They demonstrated efficient cooling of laser diodes with *5 MW/m*^{2} heat removal rate and with a laser junction temperature rise of only *40 K*. However, *5.1 bar* pressure drop accompanied this high heat flux rate. In another study, Zhou et al. (2004) designed a single-phase water cooled microchannel heat exchanger with an electro-kinetic pump for computer cooling. The microchannel heat exchanger had channels in the order of *30–100 μm* hydraulic diameters. The authors stated that the system had *2.5 MW/m*^{2} average heat flux removal capability with *0.34 bar* pressure drop due to the utilization of an electro-kinetic pump rather than a mechanical pump. Nevertheless, Petty (2007) emphasised that electrically driven flows might have some drawbacks such as sensitivity to impurities which can accumulate on the channel walls, low flow rate fluid supply, ohmic formation in the fluid and high voltage need.

In conclusion, high heat removal rates such as *7.9 MW/m^2* could be achieved with single-phase liquid cooled microchannel heat exchangers with possible drawbacks. The first problem is an excessive pressure drop, which means higher pumping power. Secondly, the wall temperature of the heat exchangers changes along the stream-wise direction in single-phase flow, which is not good especially in electronic system applications.

Alternatively, research focused on flow boiling in microchannels because phase change phenomena provide higher heat flux removal rates and better thermal characteristics with less pumping power than single phase flow, see Consolini and Thome (2009), Karayiannis et al. (2010) and Özdemir et al. (2015). One of the earliest works was conducted by Moriyama et al. (1992) to investigate flow boiling characteristics of R-113 in the micro-scale. The test section consisted of rectangular microchannels having *70-219 μm* hydraulic diameters. Prior to flow boiling experiments they performed single-phase flow tests. The authors stated that the heat transfer rate during flow boiling experiments was found to be *3-20* times larger than the single-phase flow tests. In another study, Agostini et al. (2008a) carried out flow boiling experiments using a silicon multi-microchannel heat sink having *134* parallel microchannels with *122 μm* hydraulic diameter. The coolant was R-236fa. They showed that such a heat sink could remove *2.55 MW/m^2* heat flux with *0.9 bar* pressure drop. The base temperature of the chip could also be maintained below *52°C*. Lee and Mudawar (2009) compared flow boiling characteristics of HFE-7100 and R-134a in a copper microchannel heat sink with *53* channels of *341 μm* hydraulic diameters. They concluded that although R-134a tests produced large heat transfer coefficients, its cooling performance is limited by low critical heat flux (*CHF*). On the other hand, HFE-7100 tests were better suited for high-heat flux dissipation (*8.4 MW/m^2*) without encountering *CHF*. In spite of the benefits of the flow boiling heat removal systems, there are still many problems. The main challenges are providing reliable system operation with a large value of heat removal rates. Flow mal-distribution among the multi-channels and reverse flow are some of the problems that cause flow instability and lower critical heat flux (*CHF*) values and consequently dryout occurrence in the system. This might cause the burnout or serious mechanical failures of the components.

It can be concluded from the above brief review, it is a still big challenge having reliable, cost-effective and efficient method for high and ultra-high heat flux systems. Microchannel heat exchangers find heat transfer applications in various areas from electronic cooling to air-conditioning systems. However, fundamental issues are still unclear regarding usage of microchannels as presented above. Single-phase cooling systems are good for dissipating high heat fluxes but pressure drop is high. Although the flow boiling technique can achieve to dissipate ultra-high heat flux values with less pumping power, it has some limitation due to reverse flow, flow mal-distribution and reduced *CHF* that may result in the failure of the equipment.

1.2 Research Motivation and Objectives

Although many publications were presented on flow and heat transfer in microchannels since Tuckerman and Pease's first attempt (1981), inconsistent results are still being reported in the literature. Single-phase pressure drop and heat transfer mechanisms are mostly understood and it is now well accepted that the conventional models are applicable with similar published results, see Kandlikar (2012). However, there are still discrepancies in results of flow boiling phenomena in microchannels. Many researchers reported contradicting heat transfer, flow pattern and pressure drop results. Also, underlying physical phenomena are still not clear on flow boiling heat transfer in micro scale. Some of the issues the experimental data suffer from large experimental uncertainty in the measurement of channel dimensions, roughness and temperature and pressure readings. Different nucleation cavity sizes and their distribution on the channel walls in different experiments and uncertainty related to the instability conditions are other factors affecting discrepancies in results. Also, with the increasing number of studies in microchannels, different channel geometries, different working fluids, different channel material over a wide range of experimental conditions have been investigated by the research community. This diversity brought differences in wall boundary conditions. Thus, it is hard to assess and compare reported data with general models or correlations. Some researchers tried to apply conventional scale (macro-scale) correlations on their data sets. However, most of them found poor agreement between the micro scale experimental data and conventional scale correlations. Furthermore, some developed micro scale correlations and models gave poor predictions. These issues are presented and discussed in detail in Chapter 2 that includes

a literature review of single-phase and two-phase heat transfer in microchannels. Accordingly, the objectives of this study can be summarized below:

- To make modifications on the existing experimental facility for conducting single-phase and two-phase heat transfer and pressure drop and two-phase flow pattern visualisation experiments in microchannels.
- To help clarify the fundamental aspects of flow boiling in micro passages.
- To identify the effect of aspect ratio (*Width/Height*) on heat transfer rate, pressure drop and flow patterns.
- To examine the effect of heat flux, mass flux and vapour quality on the heat transfer rate, pressure drop and flow patterns.
- To make comparisons between the experimental results and existing flow pattern maps, heat transfer rate and pressure drop correlations and comment on possible improvements.

The experimental facility and test sections were re-designed and modified due to encountered problems during the preliminary tests. Firstly, the Coriolis flowmeter, which was being used in previous microchannel research, broke during the tests and it was replaced with an ultrasonic flowmeter. Three proportional-integral-derivative (PID) controlled plate heat exchanger preheaters were working in series to preheat the fluid to the desired value. Controlling these three preheaters at the same time proved challenging. Therefore two of them were removed and a rope heater was inserted along the long tubing section to provide constant and slow preheating. This prevented bubble formation in the tubes before fluid entering the test section. A glass tubing section was inserted after the preheating section to make sure that there is no upstream compressibility in the system. A new housing was designed which consisted of a large polycarbonate block. This new housing prevented leakages from the test section and minimized heat loss. The O-ring slot on the microchannels was enlarged to avoid leakages from the test section. Also, the Viton O-ring material was replaced with rubber due to its high temperature resistance and good fit to the O-ring slot. Flow visualisation was improved by adding a high-resolution microscope to the existing high speed camera. Also, the top cover of the microchannel test section was changed to provide better visualisation study.

1.3 Outline of the Thesis

The arrangement of the thesis is as follows:

Chapter 1 – Introduction: This chapter gives a brief introduction of the study. The background and possible applications of the microchannel heat exchangers are discussed. The motivation for the study and objectives of the research are presented.

Chapter 2 – Literature Review: This chapter reviews studies available in the literature on single-phase and two-phase flow in microchannels in detail. The effect of experimental parameters including mass flux, heat flux, inlet temperature, inlet pressure, working fluid and channel geometry is presented. Discrepancies between the microchannel experimental results and the conventional theory were identified. A summary of findings of the literature review is also given.

Chapter 3 – Experimental Facility and Data Reduction: The experimental equipment, flow loop, microchannel test sections, measurement instrumentation and experimental procedure are described in this Chapter in detail. The calibration procedure of the instrumentation, data reduction technique and experimental uncertainty analysis are also described in this chapter. Modifications of the pre-existing experimental facility and microchannel test sections are described to understand the effects of these changes.

Chapter 4 – Single – Phase Flow Experimental Results and Discussion: Here, single-phase flow experimental results are presented and discussed. Single-phase pressure drop, friction factor, single-phase heat transfer coefficient and Nusselt number data are compared with findings from literature. Furthermore, the experimental facility and measurement instrumentation are validated using single-phase experimental results.

Chapter 5 – Flow Boiling Heat Transfer Experimental Results and Discussion: In this chapter, experimental flow boiling heat transfer results are reported and examined. The comparisons of the experimental data with available data in the literature are assessed. Flow boiling patterns obtained from the visualisation study are also discussed in this chapter.

Chapter 6 – Flow Boiling Pressure Drop Results and Discussion: Experimental flow boiling pressure drop results are presented and discussed in this chapter. The experimental data are also compared with published correlations in this section.

Chapter 7 – Conclusions and Recommendations: This chapter presents the conclusions drawn from this research and recommendations for the direction of future research in this field.

Chapter 2

Literature Review

2.1 Introduction

Microchannel heat sinks are one of the promising methods for cooling high and ultra-high heat flux systems as discussed in Chapter 1. Kandlikar (2005) reported that heat dissipation rates as high as $10\ MW/m^2$ are possible using single phase flow in microchannel heat sinks with an enhanced surface. However, this could be accompanied by excessive pressure drop and non-uniform temperature distribution. On the contrary, flow boiling in microchannel heat sinks can achieve much higher heat transfer rate with better axial temperature uniformity, low mass flow rate and low pressure drop or less pumping power. However, there are some limitations in applying this method including the premature dryout and flow instabilities that can cause failure of the devices, see Boure et al. (1973) and Bergles and Kandlikar (2005). Also, flow boiling characteristics in microchannel heat sinks are still not completely understood with many experimental studies concluding contradicting results as stated before. Due to the aforementioned reasons, the critical review of single-phase flow and flow boiling studies in microchannels is presented in this chapter. Many studies showed that the channel cross-section has a strong influence on pressure drop and heat transfer in small passages. Therefore, microchannels having rectangular cross-section are specifically assessed in the review to have a clear understanding on the topic. Some pioneering studies that used different cross-section channels are also included.

The chapter is organized as follows: Section 2.2 presents the different definition criteria for microchannels. Section 2.3 reviews single-phase pressure drop and heat transfer

characteristics in microchannels. Section 2.4 provides a review of flow patterns, flow pattern maps, two-phase flow pressure drop, flow boiling heat transfer characteristics and flow boiling instability studies in microchannels. Finally section 2.5 summarizes the findings of this chapter.

2.2 What is a Microchannel?

Despite numerous studies on single-phase and flow boiling in microchannels, there is still no general agreement about what threshold diameter or criteria separate "micro" and "macro" passages. In the literature, some researchers used dimensionless numbers such as *Bd* number, *Eö* number and *Co* number whilst others used the hydraulic diameter range or different criteria to define the geometry as "micro". The dimensionless numbers used in this study are defined on page xxxii.

A number of researchers used dimensionless numbers to define the geometry as micro. Surface tension effect was included in those formulations. The first attempt was made by Suo and Griffith (1964) who studied the two-phase gas and liquid flow in horizontal capillary tubes. They defined the tube as a microtube when the Bond number (*Bd*) is smaller than *0.3*. On the other hand, Brauner and Maolem-Maron (1992) analysed the prediction of the complete stratified/nonstratified flow on transitional boundary over wide ranges of conduit size. They classified the tubes as a micro one when the *Eö* number is bigger than unity. In another study, Cornwell and Kew (1993) introduced the *Co* number approach to classify whether the geometry is micro or macro. The geometry was called as micro if the *Co* number is bigger than *0.5*. The Laplace constant (*La*) was also attained as a criterion by Triplett et al. (1999). They defined the geometry as micro when the *La* constant is greater than the hydraulic diameter of the channel. Another group of researchers such as Peng and Wang (1998) and Thome (2004) postulated that the bubble departure diameter or, in other wordsi initiation of nucleation needed to be considered as a criterion. Peng and Wang (1998) defined the N_{mb} number, that should be less than or equal to unity, for micro-scale.

Contrary to the above researchers, some investigators used the hydraulic diameter for the classification of microchannels and macrochannels. Mehendale et al. (2000) categorized the heat exchangers as:

- Micro heat exchanger: $1 \leq D_h \leq 100\ \mu m$,
- Meso heat exchanger: $100\ \mu m < D_h \leq 1\ mm$,
- Compact heat exchanger: $1\ mm < D_h \leq 6\ mm$,
- Conventional heat exchanger: $6\ mm < D_h$.

Similarly, Kandlikar and Grande (2003) also used the hydraulic diameter as a criterion where;

- Microchannel: $10 \leq D_h \leq 200\ \mu m$,
- Minichannel: $200\ \mu m \leq D_h \leq 3mm$,
- Conventional channel: $6\ mm < D_h$.

The above published hydraulic diameter ranges and non-dimensional numbers criteria were applied to saturated flow boiling of water at *115 kPa* and *89 ºC* inlet conditions to calculate the threshold diameter from macro to micro passages in Table 2.1. The inlet pressure and temperature were *115 kPa* and *89 ºC* respectively in the current study. The inlet temperature was determined by gradually decreasing it from *98 ºC* until there was no vapour formation (upstream compressibility) before the inlet of the microchannels. The inlet pressure was chosen a value above the saturation pressure which was advised in the previous study of the group, see Mirmanto (2012). It is also worth mentioning that the term water refers to the de-ionized water in this study, similar to many works in the literature.

As seen in Table 2.1 below, there is a discrepancy in the literature on defining the channels as a micro or macro for all criteria, including hydraulic diameter ranges and non-dimensional numbers based criteria.

Table 2.1 Hydraulic diameter threshold of macro to micro passages transition based on various published criteria.

Reference	*Dh [mm]*
Suo and Griffith (1964)	$D_h \leq 0.76$
Brauner and Maolem – Maron (1992)	$D_h \leq 15.9$
Cornwell and Kew (1997)	$D_h \leq 5.01$
Peng and Wang (1998)	$D_h \leq 0.19$
Triplett et al. (1999)	$D_h \leq 2.48$
Mehendale et al. (2000)	$0.001 \leq D_h \leq 0.1$
Kandlikar and Grande (2003)	$0.01 \leq D_h \leq 0.2$

2.3 Single-phase Pressure Drop and Heat Transfer in Microchannels

According to Lee et al. (2005) and Kandlikar (2012), single-phase flow in microchannels is well established and obeys conventional theory. Therefore, single-phase flow results can be used to validate the measuring instruments and data prediction processes before flow boiling tests. Also, many single-phase parameters are used in flow boiling models. However, some studies reported that dimension can influence the single-phase flow thus some effects need to be considered while evaluating the effect of single-phase parameters, see Guo and Li (2003) and Rosa et al. (2009). Single-phase pressure drop and heat transfer in microchannel studies are reviewed in this section.

2.3.1 Single-Phase Pressure Drop Studies

In the literature, a large number of researchers reported that single-phase pressure drop in microchannels could be predicted well by conventional theory and macroscale correlations. In conventional theory, the Poiseulle's number ($Po = f \times Re$) is constant (16 for tubes). Pfund et al. (2000) conducted experiments with water over a broad range of Reynolds number range ($60 < Re < 3450$) in smooth and rough $100\ mm$ long

rectangular microchannels having different hydraulic diameter and aspect ratio (D_h = *253-990 μm, W/H = 19.2-78.1*). Entrance and exit losses and careful uncertainty analysis of all measurements were considered by the authors. They reported that the results for smooth microchannels are in a good agreement with conventional scale theory. Xu et al. (2000) investigated the substrate material effect on single phase water flow in microchannels. They tested six single aluminium microchannel and six single silicon microchannel of different hydraulic diameter, aspect ratio and channel length (D_h *= 29.4-391.3 μm, W/H = 0.04-1.72, L = 10-50 mm*) over a *Re* ranging from *20* to *4000* accounting for entrance and exit losses. The results were predicted well by conventional fully developed flow theory as shown in Fig. 2.1. However, the authors stated that microchannels that were made of silicon were in better agreement with theory than those made of aluminium. The authors attributed this to the precise measurements of the channel dimensions of silicon channels that were anodically bonded to the wafer. On the other hand, aluminium microchannels that were machined to the surface included high measurement errors due to machining.

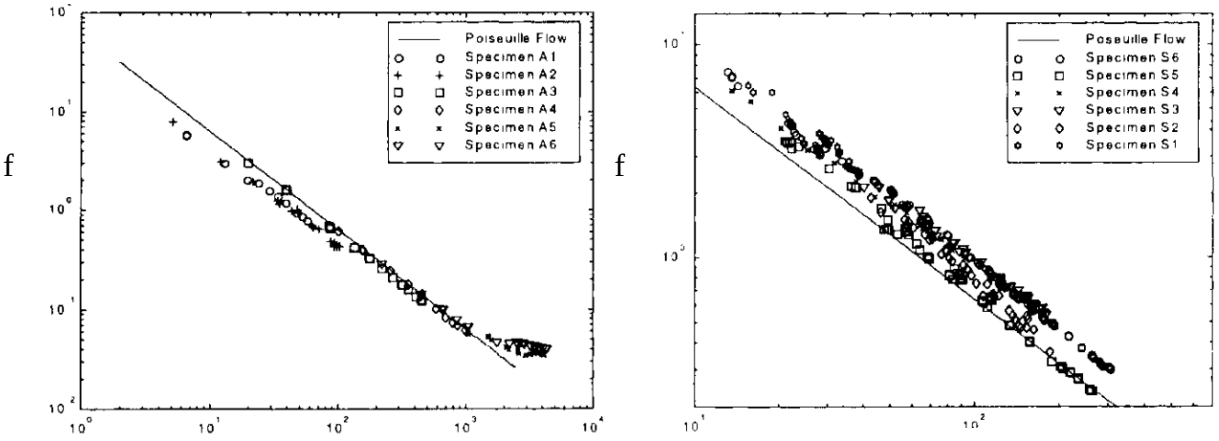

Figure 2.1 Friction factor versus Reynolds number for: (a) Aluminium microchannels, (b) Silicon microchannels, Xu et al. (2000).

Single-phase flow laminar to turbulent transition in microchannels was also investigated. De-ionized water flow in twenty one identical parallel rectangular copper microchannels were analysed by Qu and Mudawar (2002a) over a *Re* number range

from *137* to *1670*. The microchannels had *349 μm* hydraulic diameters, *0.32* aspect ratios and *44.6 mm* length. Expansion and contraction losses were considered by the authors. The measured and calculated pressure drop data were found to be in good agreement with each other as can be seen in Fig. 2.2. The calculated pressure drop data were evaluated using the conventional scale theory. The authors also reported that they did not observe early transition from laminar to turbulent region in their study.

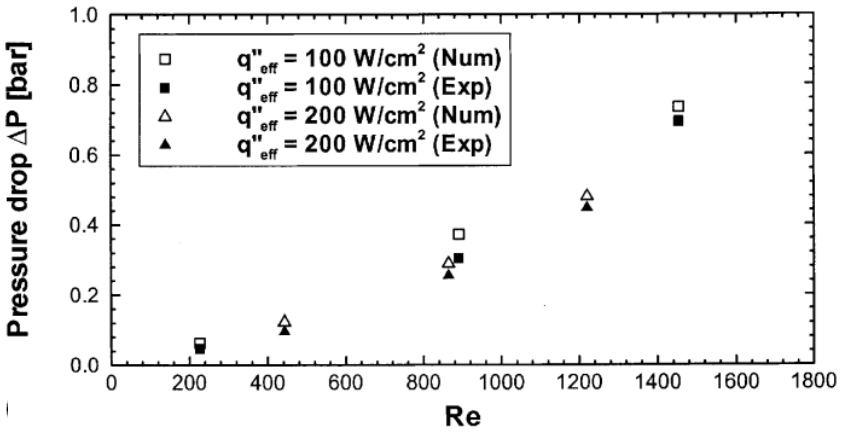

Figure 2.2 Comparison of measured and calculated pressure drop data, Qu and Mudawar (2002a).

On the contrary, Hsieh et al. (2004) conducted single-phase liquid flow in a single rectangular polymethylmethacrylate (PMMA) microchannel. The hydraulic diameter and aspect ratio of the channel was *146 μm* and *1.74* respectively. De-ionised water was pumped to the system over a range of *Re* number from *45* to *969*. Their measured friction factor data was found to be in agreement with the conventional theory *(5.6 %* larger than the conventional theory) in the laminar region when the hydrodynamic entrance effects were accounted along the channel length (*L = 23.9 mm*). On the other hand, in transitional and turbulent regions the friction factor was not independent from *Re* number, see Fig. 2.3. Moreover, they reported very early transition from laminar to the turbulent region (*Re~240*). In another study, Steinke and Kandlikar (2006) performed experiments in 26 silicon rectangular parallel microchannels having *10 mm* length, *227 μm* hydraulic diameter and *1.25* aspect ratio. Their *Re* number range was between *14* and *789*. They reported that if the measured friction factor data were corrected for inlet and exit losses and developing flow, the experimental data shows

better agreement with the conventional theory as shown in Fig. 2.4. They also added that accurate channel dimension and surface roughness measurements and uncertainty analysis play vital role in evaluating accurate experimental friction factor data.

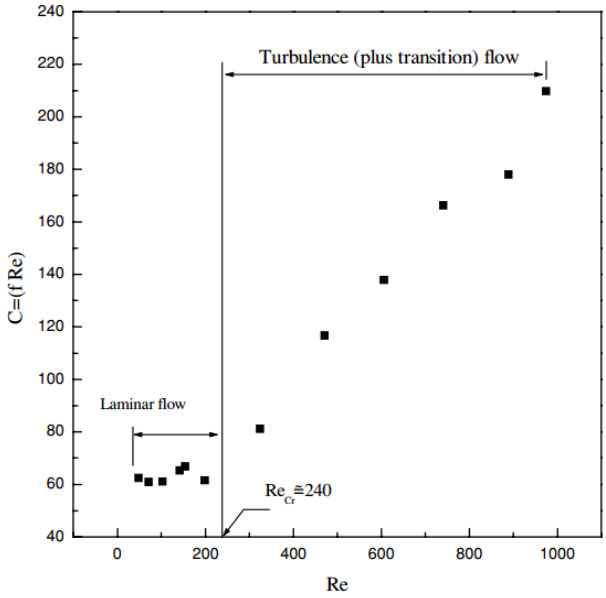

Figure 2.3 The relationship between friction constant (Po) and Re number, Hsieh et al. (2004).

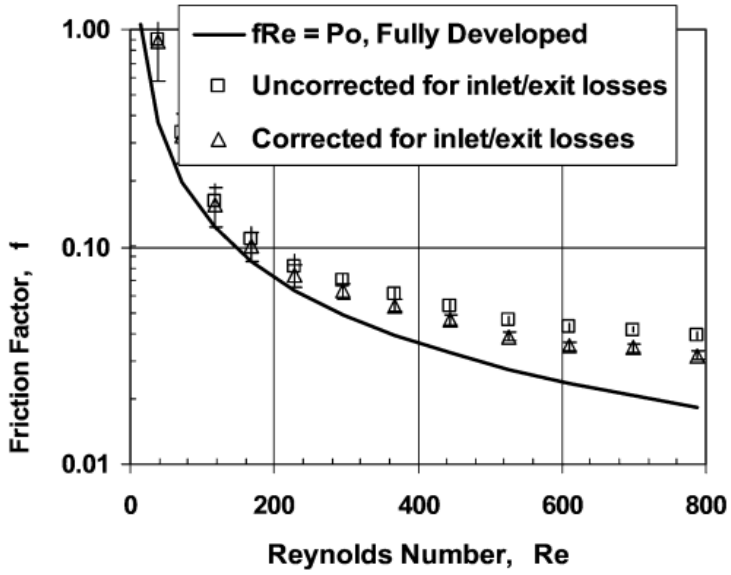

Figure 2.4. Friction factor versus Reynolds number considering entrance and exit losses, Steinke and Kandlikar (2006).

Surface roughness effect was also studied by Shen et al. (2006) in a brass microchannel heat sink which consisted of twenty six parallel rectangular channels having *436 μm* hydraulic diameter, *0.37* aspect ratio and *50 mm* length. De-ionised water was used as the working fluid in a *Re* number range from *162* to *1257*. The microchannels had a relative surface roughness *4-6 %* of the channel hydraulic diameter. They concluded that surface roughness has a considerable influence on liquid laminar flow in microchannels due to increasing of *Po* that was higher than conventional theory, see Fig. 2.5. They also reported that at high *Re* numbers, the discrepancy between the measured friction factor values and the predicted friction factor values was higher than at low *Re* numbers. It is worth mentioning that Shen et al. (2006) used the *Po* number *67* instead of *64*. The authors calculated this value based on the aspect ratio of the channel instead of using conventional value (64) for the smooth tube.

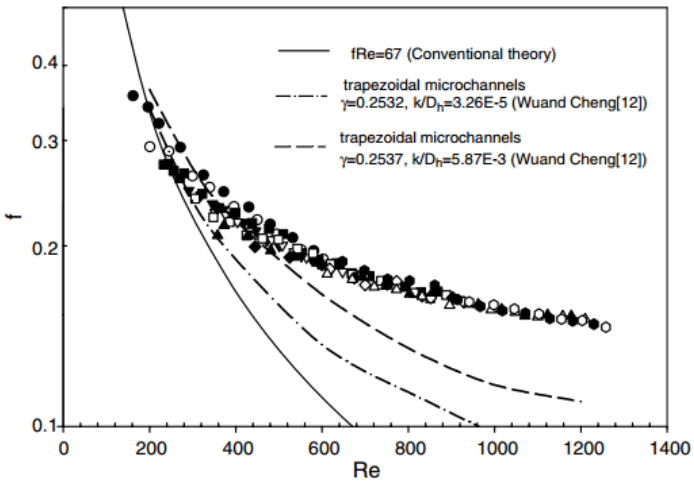

Figure 2.5 Friction factor versus Reynolds number, Shen et al. (2006).

Gamrat et al. (2008) investigated the effect of surface roughness on laminar flow in a silicon single microchannel having different hydraulic diameter (D_h = *190-550 μm*) and aspect ratio (*11.7-35*) but the same length (*L = 50 mm*) with de-ionised water. They created two types of wall roughness; i) controlled wall roughness that was periodically distributed to the channel with a relative roughness *~ 0.075* with respect to the channel height , ii) randomly distributed roughness to the channel with a relative roughness changing from *~0.02 to ~0.064* with respect to the channel height. Experimental friction factor data for the rough microchannels was higher than the fully-developed flow theory

as shown in Fig. 2.6. They also reported that, friction factor values increased with increasing relative roughness and are independent of *Re* number in the laminar flow regime (*1000 < Re < 2000*). However, this might be because of the transition of the flow from laminar to turbulent. The authors did not make a comment on this point.

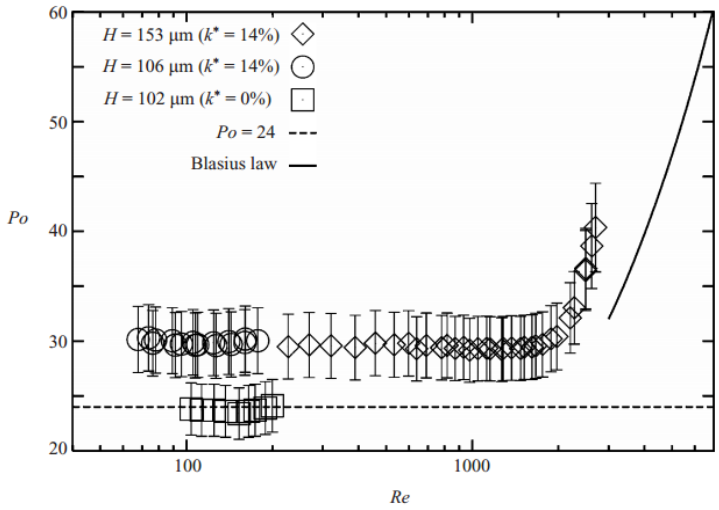

Figure 2.6 Poiseuille number versus Reynolds number for the semi-rough and smooth microchannels, Gamrat et al. (2008).

Mirmanto (2012) conducted sets of experiments in a single copper microchannel having *438 μm*, *560 μm* and *635μm* hydraulic diameters, *1.28*, *2.56* and *4.38* aspect ratios and *62 mm* length. De-ionized water was tested over a *Re* range from *160* to *3300*. The experimental results were compared to fully-developed laminar flow theory of Shah and London (1978), fully-developed turbulent flow theory of Blasius (1913), developing laminar flow theory of Shah (1978) and developing turbulent flow theory of Phillips (1987) proposed for conventional scale channels. They reported that the measured friction factors were found to be higher than the conventional scale fully-developed theory both in laminar and turbulent regions. On the other hand, the results were reasonably predicted by the developing flow theory. They concluded that when entrance effects, experimental uncertainties, inlet and exit pressure losses, departure from laminar flow were carefully evaluated, the results indicate that equations developed for conventional scale flow are applicable for water flows in microchannels of that sizes. In a recent study, Sahar et al. (2015) examined the effect of aspect ratio and hydraulic

diameter on single-phase friction factor numerically using a single microchannel. The aspect ratio of the channels was varied from *0.1* to *2.56* while the hydraulic diameter and channel length were constant at *0.56 mm* and *62 mm* respectively. They reported that the aspect ratio has no significant influence on the friction factor for aspect ratio values from *0.5* to *2.56*. However, they stated that the friction factor increased with decreasing aspect ratio in the aspect ratio range of *0.5-0.1*, see Fig. 2.7.

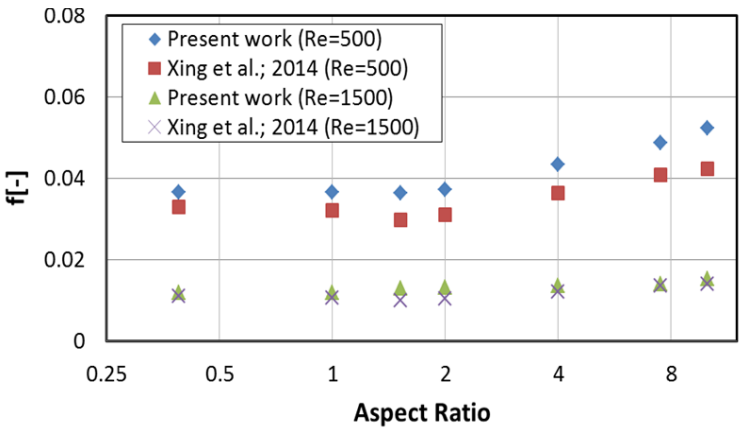

Figure 2.7 Effect of aspect ratio on the friction factor at Re = 500 and comparison with the data of Xing et al. (2014), Sahar et al. (2015).

It is worth mentioning that, Sahar et al. (2015) defined the aspect ratio as the ratio of the height over the width different to this study. Therefore, this point should be noted while evaluating Fig. 2.7. The design of the numerical model of Sahar et al. (2015) is identical with the current study such that the de-ionized water enters and leaves the channel in a similar way to the test section. Moreover, the numerical model results were compared to the experimental results of test section 1 in the current study and found to predict the experimental friction factor data very well, see Sahar et al. (2015). Similar to Sahar et al. (2015), Zhang et al. (2014) found that the channel aspect ratio has insignificant effect on the friction factor in a range of aspect ratio *1.58-2.22* at constant channel hydraulic diameter (D_h = *0.61 mm*) over a *Re* range from *200-2800*.

From the above review, we can infer that the single-phase friction factor in microchannels can be predicted using conventional scale theory and correlations. However, measurement uncertainties, inlet and exit pressure losses, developing effects

in entrance region, channel surface roughness and laminar to turbulent transition should be carefully considered. In addition to this, it was found that the channel aspect ratio has no effect on the single-phase friction factor, see Zhang et al. (2014) and Sahar et al. (2015).

2.3.2 Single-Phase Heat Transfer Studies

Similarly to the single-phase friction factor, heat transfer in microchannels was investigated by many researchers in the literature. Peng and Peterson (1996) examined the single-phase heat transfer in stainless steel parallel rectangular microchannels using water. They examined twelve microchannels having different hydraulic diameter (*133-367 μm*), aspect ratio (*0.33-2*) but the same channel length (*45 mm*) over a *Re* range from *136* to *794*. The authors concluded that the geometric configuration of the microchannel has a critical effect on the single-phase convective heat transfer. They did not compare their results with any data sets available for conventional scale channels. However, they proposed two single-phase convective heat transfer correlations to consider the effect of the channel geometry of the microchannels in laminar and in turbulent regimes, see Eq. (1.1) and Eq. (1.2).

Laminar flow, Peng and Peterson (1996):

$$Nu = 0.1165\left(\frac{D_h}{W_c}\right)^{0.81}\left(\frac{H}{W}\right)^{-0.79}\mathrm{Re}^{0.62}\,\mathrm{Pr}^{1/3} \tag{1.1}$$

Turbulent flow, Peng and Peterson (1996):

$$Nu = 0.072\left(\frac{D_h}{W_c}\right)^{1.15}\left[1-2.421((H/W)-0.5)^2\right]\mathrm{Re}^{0.8}\,\mathrm{Pr}^{1/3} \tag{1.2}$$

In laminar and in turbulent regimes, the Nusselt number (*Nu*) was found to depend on the Reynolds number, the Prandlt number, the microchannel aspect ratio and the ratio between the hydraulic diameter and the center to center distance of microchannel widths (W_c). Harms et al. (1999) conducted experiments in two silicon rectangular microchannel heat exchangers having single and multiple channels of *404 μm* hydraulic diameter, *4* and *25* aspect ratio and *25 mm* channel length. The working fluid was de-ionized water and the *Re* number range was from *173* to *12900*. They reported that the experimental local *Nu* number agreed well with developing channel flow correlations for conventional scale channels proposed by Shah and London (1978) in laminar regime. In turbulent regime Gnielinski (1976) correlation which was developed for fully developed turbulent regime predicted well their data. In another study, Gao et al. (2002) studied entrance effects in rectangular brass microchannels in the range of Reynolds number *200–3000*. The hydraulic diameters were between *0.2* and *2 mm* and the aspect ratios were between *0.004* and *0.04*. De-ionised water was the test fluid. They observed good agreement of the measured *Nu* and the developing flow correlations proposed by Shah and London (1978) for hydraulic diameters down to *1 mm*, while the *Nu* number was found to be *60 %* smaller than the correlations for smaller channels (D_h < *1 mm*). Lee et al. (2005) investigated single-phase heat transfer in ten copper parallel rectangular microchannels of different hydraulic diameters (*318–903 μm*), for *Re = 300–3500* using de-ionized water. The experimental uncertainty in the Nusselt number was estimated to be in the range *6–17%* and was found to be in disagreement with the data sets available for conventional scale channels in the literature, see Fig. 2.8. However they found good agreement between their experimental results and their numerical predictions, where they were able to consider entrance effects.

Surface roughness effect on single-phase heat transfer was studied by Shen et al. (2006). Details of the microchannel test section and experimental method were mentioned in the single-phase pressure drop section. They concluded that surface roughness effect, which was *4-6 %* of the hydraulic diameter, is responsible for the increasing trend of the *Nu* number with *Re* number. However, predicted *Nu* number was lower than the conventional prediction of Shah and London (1978) as can be seen in Fig 2.9. The authors attributed this to a combination of cross-sectional aspect ratio and surface roughness effects.

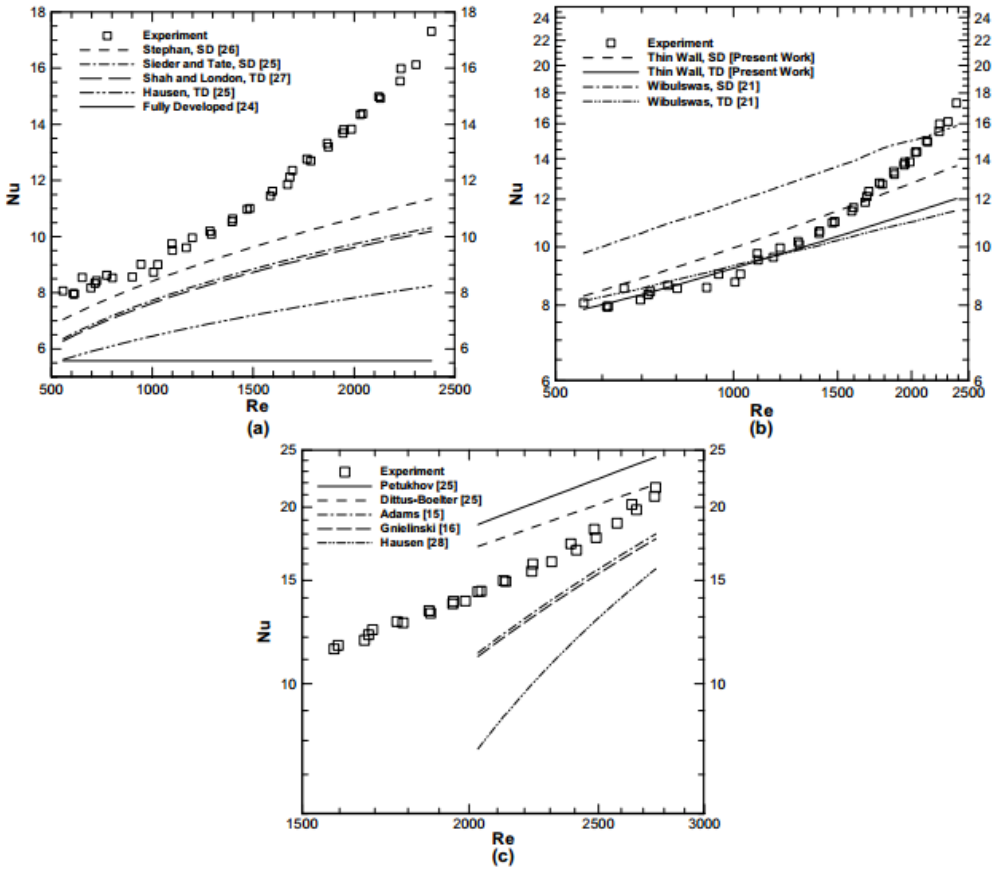

Figure 2.8 Nusselt number versus Reynolds number comparison of experimental data against: (a) conventional scale correlations for laminar flow, (b) numerical predictions for laminar flow and (c) conventional scale correlations for turbulent flow, Lee et al. (2005).

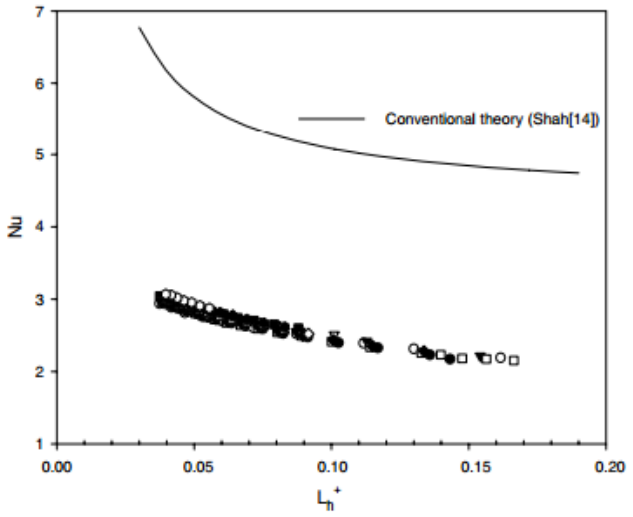

Figure 2.9 Nusselt number versus non-dimensional thermal length, Shen et al. (2006).

Axial heat conduction is also an important parameter in microchannels that needs to be accounted. Gamrat et al. (2005) investigated conduction effects in rectangular microchannels numerically, with a 2D and 3D conjugate heat transfer models, Reynolds numbers in the range *200–3000* using water as the test fluid. They analysed the microchannel heat sink of Gao et al. (2002) which was mentioned earlier, on page 19. Gao et al. (2002) observed a significant reduction in the measured *Nu* when the hydraulic diameter was below *1 mm*. This reduction could not be predicted by the numerical model of the Gamrat et al. (2005). Thus, they concluded that, the strong reduction in the Nusselt number observed in experiments cannot be explained by conduction effects due to the complex geometry, like axial conduction in the walls or lack of two-dimensionality of the heat flux distribution. Maranzana et al. (2004) introduced a dimensionless number *M*, the Maranzana number, which is the ratio between the axial heat conduction in the walls of the channel and the heat transfer by convection in the fluid. They proposed that when the $M < 0.01$ the axial heat conduction in the channel walls can be neglected.

Rosa et al. (2009) presented a comprehensive review on scaling effect on the heat transfer characteristics in microchannels. They analysed the entrance effects, conjugate heat transfer, viscous heating and electric double layer (EDL) effects, thermophysical properties, surface roughness effects and rarefaction and compressibility effects (for gases only) on the heat transfer characteristics in micro passages which can be negligible in conventional sized channels. Moreover, the authors investigated the effect of measurement uncertainties on the heat transfer characteristics in small scale channels. They concluded that the entrance effects, thermophysical properties of the working fluid, conjugate heat transfer effects, EDL effects, surface roughness and measurement uncertainties have an influence on the heat transfer characteristics in microchannels. Therefore, these parameters are needed to be considered in micro-scale.

Recently, Mirmanto (2012) conducted sets of experiments to investigate single-phase heat transfer in microchannels. Details of the test section and experimental range were mentioned in the previous section. They reported that the measured *Nu* numbers are higher than conventional theory predictions for fully-developed laminar flow. On the

other hand, their results agreed well with the developing laminar flow theory proposed by Shah and London (1978). In the turbulent regime, Nusselt numbers are predicted by the Dittus-Boelter (1930) fully-developed flow correlation but are higher than those predicted using the Gnielinski equation (1976), see Fig. 2.10. They concluded that when entrance effects, experimental uncertainties, inlet and exit pressure losses, departure from laminar flow were considered, the results indicate that equations developed for conventional scale flow are applicable for water flows in microchannels of that sizes.

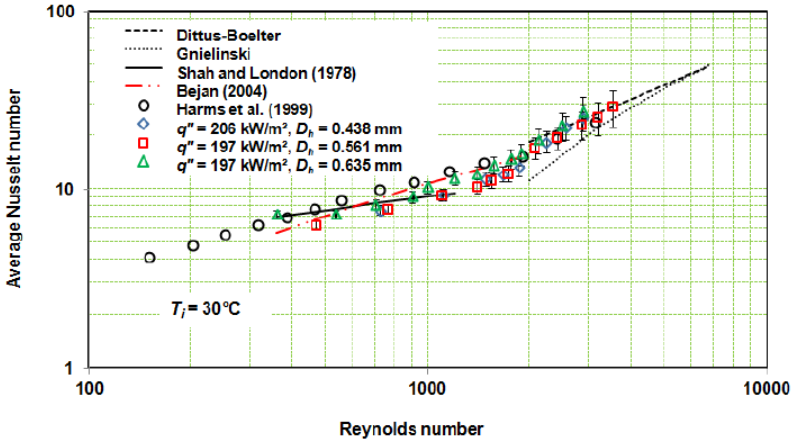

Figure 2.10 Variation of Nusselt number with Reynolds number and comparisons with conventional correlations and experimental results of Harms et al. (1999), Mirmanto (2012).

Sahar et al. (2015) examined the channel aspect ratio effect on the single-phase heat transfer coefficient. Details of the test sections were described in the friction factor section, on page 16. They reported that the channel aspect ratio has no significant effect on the single-phase heat transfer coefficient as shown in Fig. 2.11. Similarly, Zhang et al. (2014) reported that, the aspect ratio ranging from *1.58* to *2.22* with constant hydraulic diameter (D_h = *0.61 mm*) does not significantly affect the heat transfer coefficient in rectangular microchannels.

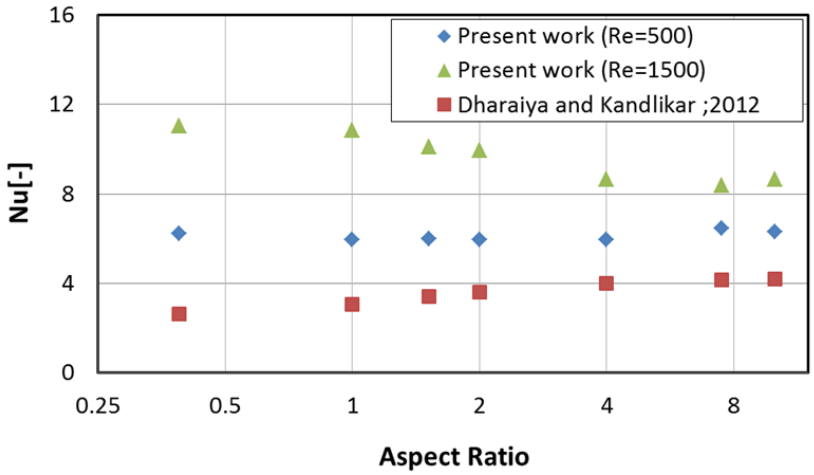

Figure 2.11 Effect of aspect ratio on the Nusselt number at Re = 500 and Re = 1500 and comparison with Dharaiya and Kandlikar (2012), Sahar et al. (2015).

In conclusion, single-phase heat transfer studies in microchannels are reviewed in this section. Sources of the discrepancies between the conventional theory and the measured parameters were assessed. Conventional theories and correlations are suitable to describe single-phase heat transfer characteristics in microchannels once cross-section geometry, scaling effects and measurement uncertainties are carefully employed. Moreover, it was found that the channel aspect ratio has insignificant effect on the single-phase heat transfer coefficient. The following effects should be considered when the single-phase heat transfer characteristics are investigated in microchannels.

- Inlet and exit pressure losses.
- Developing effects in entrance region.
- Channel surface roughness.
- Laminar to turbulent transition.
- Temperature dependence of the fluid properties.
- Measurement uncertainties.
- Axial conduction effect especially in low *Re* number flows.
- Accurate measurement of channel geometrical dimensions.

2.4 Flow Boiling in Microchannels

Boiling can be defined as the sudden evaporation of the liquid when the liquid is heated above its boiling point. Flow boiling refers to the boiling of the liquid while flowing over the heated surface which is the focus of this study and thereby issues related to flow boiling in microchannels are reviewed in this section.

2.4.1 Flow patterns in microchannels

In microchannels flow visualization is important due to its direct link with heat transfer characteristics and pressure drop. Therefore, characterizing flow patterns is required for a better understanding of underlying physical mechanism(s) of the heat transfer process in microchannels. Flow patterns in microchannels are different than the conventional scale ones as the surface tension force becomes dominant over the gravity force in small scales, see Watel (2003). The commonly observed flow patterns in large diameter horizontal channels are bubbly, slug, plug, annular, stratified, annular-mist and wavy flow as reported by Thome (2004). Kandlikar (2002) reported that the dominant flow patterns in microchannels are isolated bubble, confined bubble/slug and annular flow. It is worth to mention that there are no proper general definitions for flow patterns in the literature. Also, some researchers claimed that the adiabatic flow patterns are similar to the flow boiling patterns in microchannels considering some justifications, see Kandlikar (2002) and Balasubramanian et al. (2013). The above reasons might be the source of discrepancies among the published flow boiling results. Therefore, adiabatic and flow boiling patterns in microchannels are reviewed critically in this section.

2.4.1.1 Adiabatic flow patterns

In this research era it is still not clear whether adiabatic two-phase flow patterns can be used to describe two-phase flow patterns. Therefore adiabatic flow pattern studies were reviewed in the literature. Triplett et al. (1999) carried out a visualisation study for air-water in two circular ($D = 1.1$ and 1.45 mm) tubes and in microchannels with semi-triangular cross sections ($D_h = 1.09$ and 1.49 mm) at horizontal orientation. Tube materials were Pyrex and semi-triangular channel materials were polycarbonate. The visualisation study was conducted at the middle of the test section. The authors stated

that the entrance effects were not taken into consideration. However, the visualisation study location was a hundred channel diameter distances from the entrance of the test section. They observed bubbly, slug, churn, slug-annular and annular flow patterns for all test sections as seen in Fig. 2.12 and Fig. 2.13. The authors stated that the flow patterns and the transition boundaries for all test sections were similar.

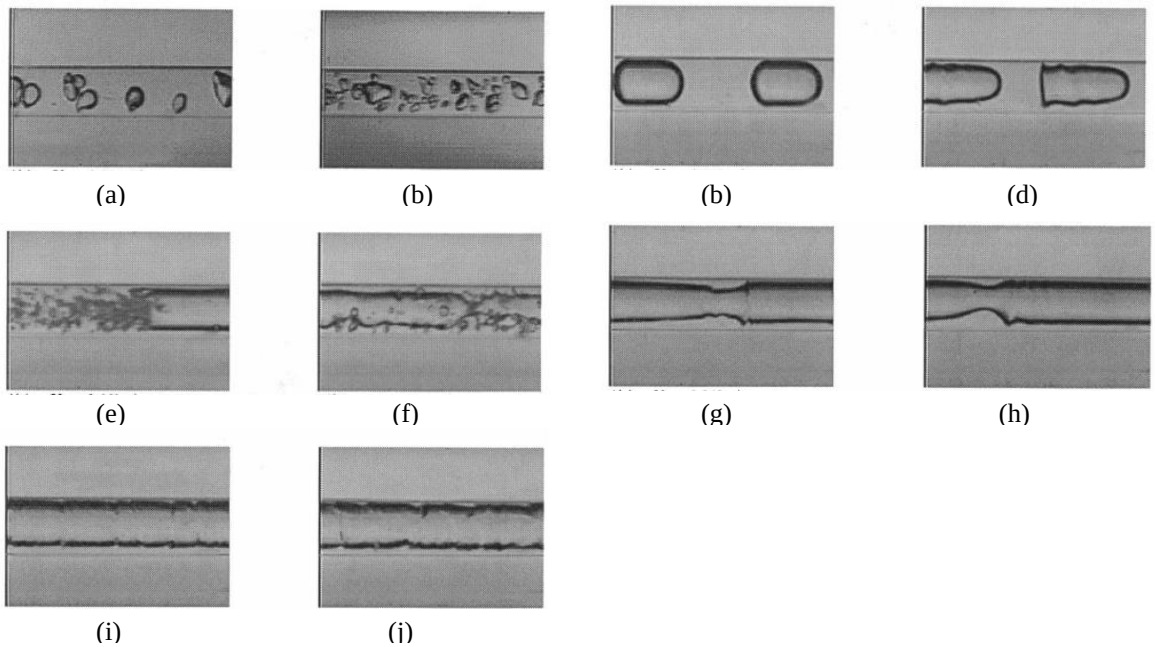

Figure 2.12 The adiabatic flow patterns in the 1.1 mm diameter horizontal circular channel: (a), (b) bubbly; (c), (d) slug; (e), (f) churn; (g), (h) slug-annular; (i), (j) annular, Triplett et al. (1999).

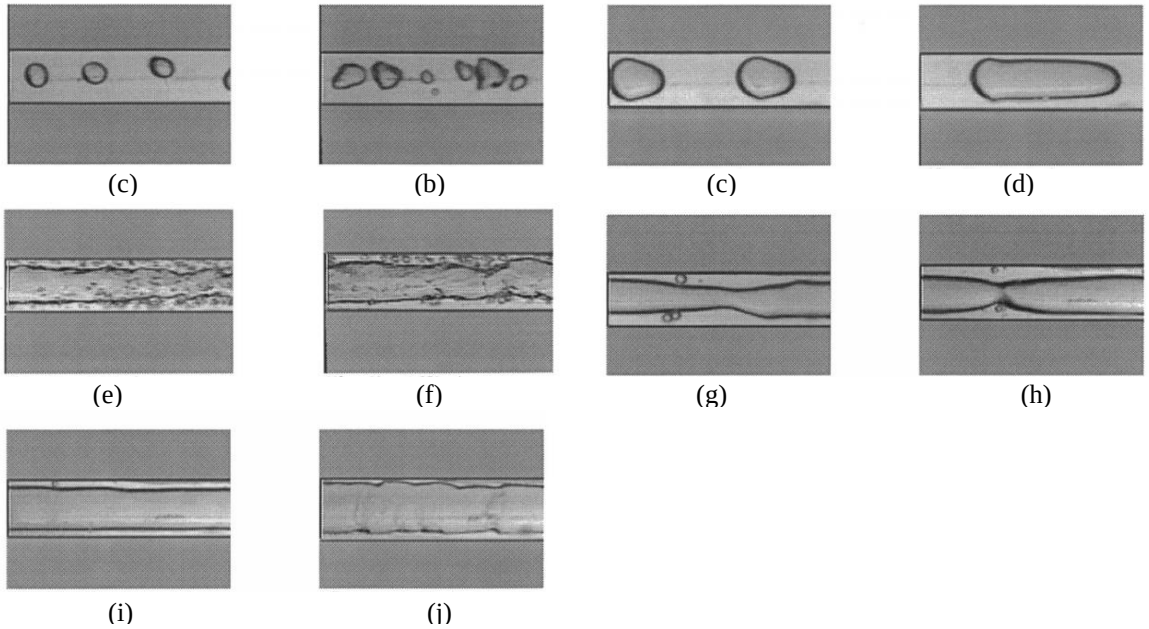

Figure 2.13 The adiabatic flow patterns in the 1.09 mm hydraulic-diameter horizontal semi-triangular channel: (a), (b) bubbly; (c), (d) slug; (e), (f) churn; (g), (h) slug-annular; (i), (j) annular, Triplett et al. (1999).

The effect of channel diameter and shape on flow patterns for air-water flow in horizontal Pyrex glass tubes ($D = 1.3\text{-}5.5\ mm$) and in a plastic microchannel ($D_h = 5.36\ mm$) was investigated by Coleman and Garimella (1999). Gas superficial velocity (J_g) range was from 0.1 to $100\ ms^{-1}$ whereas the liquid superficial velocity (J_l) range was from 0.01 to $10\ ms^{-1}$. They observed dispersed bubbly flow, bubbly flow, elongated bubbly flow, slug flow, annular flow, wavy-annular flow and stratified flow in the circular microchannels and rectangular microchannel. The authors defined an intermittent flow regime where the elongated bubbly flow and slug flow occurred together that caused discontinuities in the liquid and gas flow. They reported that the channel diameter has an important role on the flow patterns and transition boundaries due to the surface tension effect, see Fig. 2.14. For example, the transition from intermittent to dispersed bubbly or bubbly flow existed at higher liquid superficial velocities for channels having smaller diameter. Also, stratified flow diminished in channels having diameter less than $5.5\ mm$. Moreover, channel shape found to have an effect on flow transition boundaries but did not influence the observed flow patterns. In the rectangular microchannel, transition to the dispersed flow appeared at higher liquid superficial velocity values than the circular microchannel. On the other hand, in the

circular channel transition to annular flow occurred at higher gas superficial velocity values than the rectangular microchannel, see Fig 2.15.

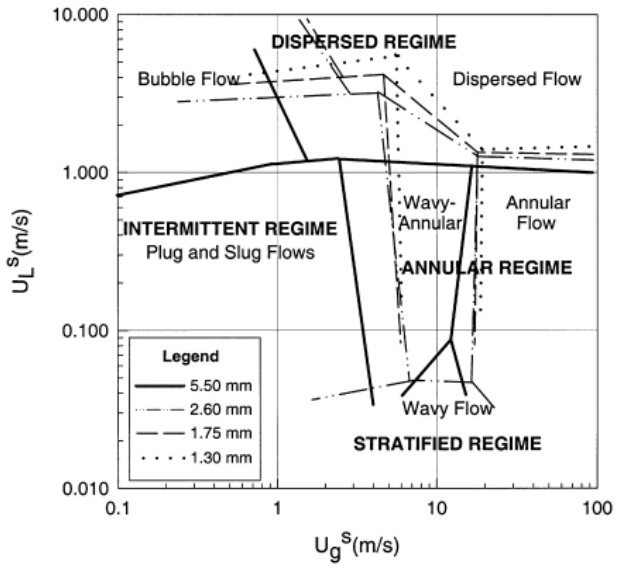

Fig. 2.14 Flow regime transitions in horizontal circular microchannels having different diameters, Coleman and Garimella (1999).

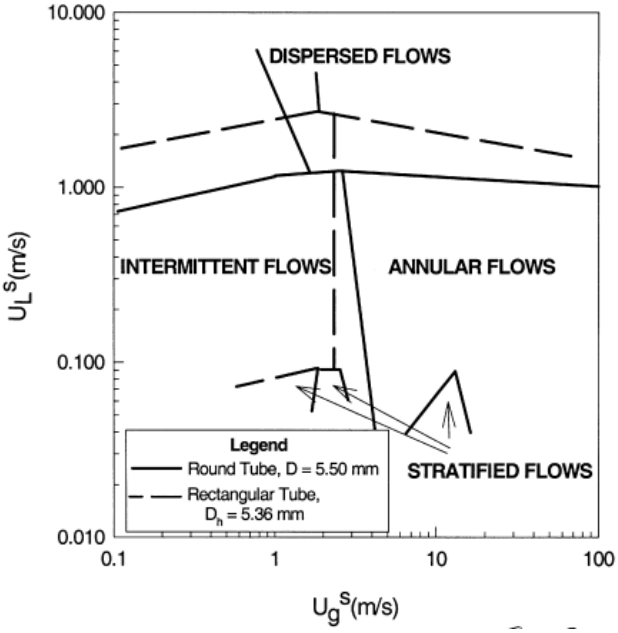

Fig. 2.15 Comparison of flow regime transitions of horizontal circular microchannel and horizontal rectangular microchannel, Coleman and Garimella (1999).

In another study, Xu et al. (1999) investigated an adiabatic vertical air-water two-phase flow in Pyrex-glass rectangular microchannels of *12 mm* width, *260 mm* length with different heights (*0.3, 0.6* and *1 mm*) resulting in *0.59, 1.14* and *1.85 mm* hydraulic diameters respectively. The flow regimes for the *1.14* and *1.85 mm* hydraulic diameter channels were found to be similar with the conventional scale flow patterns. However, flow regimes for the smallest hydraulic diameter test section were quite different as seen in Figure 2.16. For instance, bubbly flow was never observed in this test section. They reported that, at high liquid flow rates and low gas flow rates cap-bubbly flow occurred in the channel (see Fig. 2.16 (a)) where coalescence of isolated bubbles was observed due to the confined space in the small channels. On the other hand, at low gas and low liquid flow rates slug-droplet flow was observed in the channel as can be seen in Fig. 2.16 (b). In this pattern, some liquid droplets were stuck on the channel wall and were pushed by the elongated slugs.

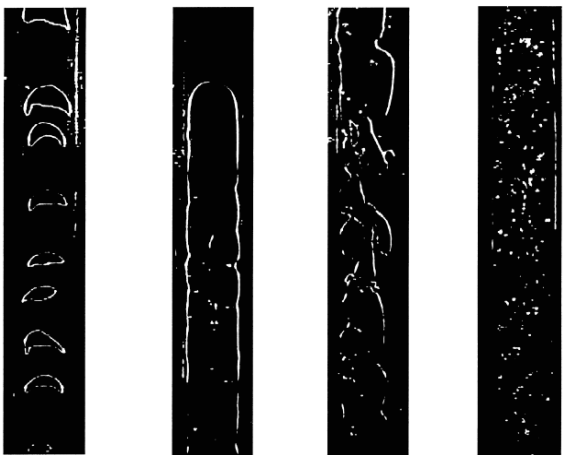

(a) (b) (c) (d)

Figure 2.16 The flow patterns in vertical rectangular channel with 0.59 mm hydraulic diameter: (a) cap-bubbly; (b) slug-droplet; (c) churn; (d) annular-droplet, Xu et al. (1999).

The authors attributed this to the fact that surface tension force becomes dominant as the channel diameter decreases. Churn flow was observed for a large range of liquid flow rates and medium gas flow rates and had similar characteristics in the larger channels. Another unique flow pattern was named as annular-droplet flow which was observed with the further increase in the gas flow rate at churn flow condition, see Fig. 2.16 (d).

In the annular-droplet flow, isolated liquid droplets existed on the channel wall with the continuous gas core flow which is different from the classical annular flow existing in conventional scales. It is worth to mention that the authors did not present any flow pattern images for the *1.14* and *1.85 mm* hydraulic diameter channels.

Similarly, Qu et al. (2004) reported that flow patterns in microchannels are significantly different from those in the conventional scale channels. They conducted experiments of nitrogen-water flow in an acrylic horizontal rectangular microchannel having *0.68 mm* hydraulic diameter and *120 mm* length. Flow patterns were visualized at the middle of the channel to avoid entrance and outlet effects. Slug and annular with occasional occurrence of bubbly flow were the prevailing flow patterns. However, churn and stratified flow were never encountered. Also, transition to annular flow occurred at lower superficial gas velocity than larger channels. Choi et al. (2011) performed an experimental study in horizontal rectangular photosensitive glass microchannels. The microchannels had *0.49, 0.49, 0.32 and 0.14 mm* hydraulic diameters and *1.09, 1.49, 2.13* and *6.25* aspect ratios, respectively. Experiments were conducted with liquid water and nitrogen gas two-phase flow. Bubbly, slug bubble, elongated bubble, transition and liquid ring flow patterns were sequentially observed as the superficial gas velocity was increased as seen in Fig. 2.17. The authors stated that liquid ring flow was developed from slug flow when the superficial gas velocity was increased to the extent at which liquid slugs become quite short enabling to form a stable liquid bridge between the consecutive gas slugs. The elongated bubbly flow regime was found to be dominant as the hydraulic diameter decreased due to the confinement effect and the liquid portion in the corner was decreased. Moreover, they examined the effect of aspect ratio on flow pattern transition boundaries using two microchannels having same hydraulic diameter (*0.49 mm*) but different channel aspect ratios (*1.09* and *1.49*). It was found that the transition from the elongated bubbly flow to liquid ring flow occurred at higher superficial gas velocity value for the channel having higher aspect ratio. On the other hand, as the channel aspect ratio increased, the transition boundary between the bubbly flow to slug bubble flow was slightly shifted to the lower superficial gas velocity value. However, the authors did not present any comparison figure for the effect of channel aspect ratio and hydraulic diameter on the flow pattern transition boundaries.

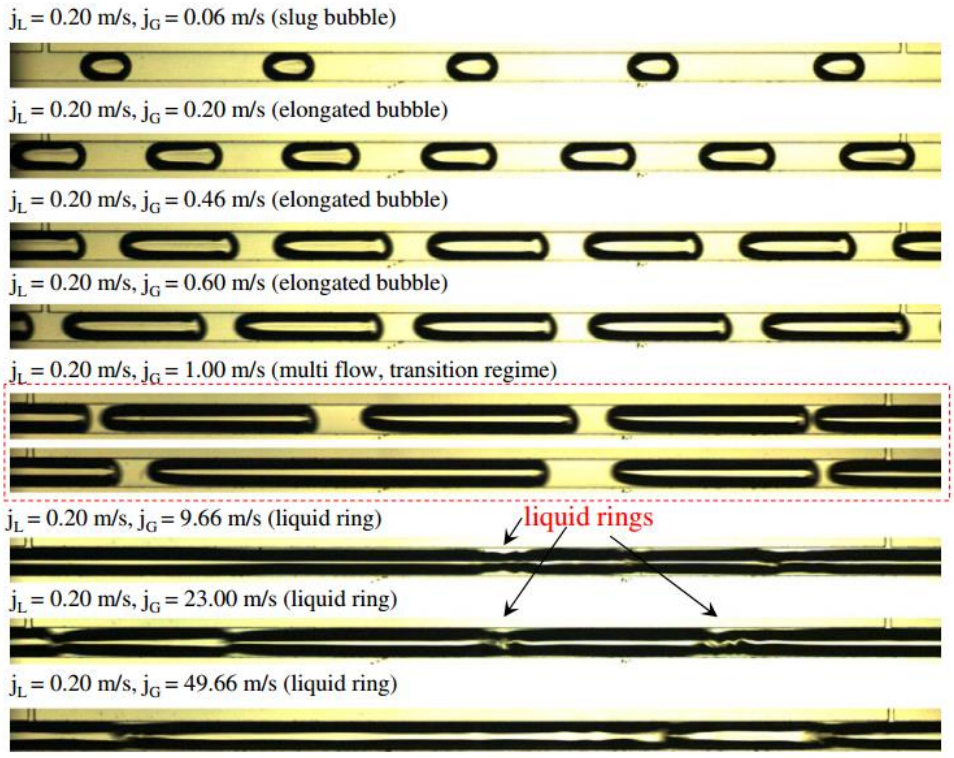

Figure 2.17 The flow patterns in the horizontal microchannel with 0.49 mm hydraulic diameter and 1.09 aspect ratio as the gas superficial velocity increases (j_l = *0.2 m/s, 0.06 m/s*< j_g <*49.66 m/s*), Choi et al. (2011).

In this section, observed flow patterns and effect of some parameters such as channel hydraulic diameter and aspect ratio on adiabatic flow patterns and flow pattern transition boundaries are presented and discussed using the experimental studies available in the literature. From the above review, it can be seen that the channel diameter has a significant influence on the flow patterns and transition boundaries. As the channel diameter decreased some conventional scale flow patterns (stratified flow and churn flow) were not observed by some researchers. Moreover, some researchers found new flow patterns in microchannels (cap-bubbly flow and liquid ring flow). This is probably because the effect of surface tension increases when the channel diameter decreases. On the other hand, transition boundaries between the flow patterns were shifted in smaller channels. However, there is a discrepancy in reporting on this. Coleman and Garimella (1999) stated that the transition boundaries of the bubbly/slug, slug/churn and churn/annular flow patterns were shifted to higher superficial gas velocity when the diameter decreases. Contrarily, Xu et al. (1999) reported the opposite effect of the diameter.

2.4.1.2 Flow boiling patterns

In microchannels, flow boiling patterns might be different than the adiabatic flow patterns. For instance, Shuai et al. (2003), Huh and Kim (2006) and Revellin and Thome (2007) stated that churn flow diminished in flow boiling in microchannels. Similiarly, Sobierska et al. (2006) reported only bubbly, slug and annular flow. They performed experiments using water in a single copper vertical rectangular microchannel with hydraulic diameter *1.2 mm* and aspect ratio *0.43*. The total length of the channel was *330 mm* and flow visualisation was conducted at five locations along the channel. The inlet subcooling was varied from *2* to *20 K*. However, they did not mention where exactly these flow patterns were observed along the channel. It is worth mentioning that bubbly flow was observed under subcooled conditions in their study, i.e. fluid bulk temperature was below saturation. Megahed and Hassan (2009) carried out experiments with FC-72 in silicone rectangular multi-microchannels having hydraulic diameter *0.247 mm*, aspect ratio *0.82*, and *16 mm* length. Flow visualisation was conducted at three locations along the transverse direction at the middle of the heat sink and also near the channel exit. The flow patterns reported at one heat flux value of *130.6 kW/m^2* and mass flux of *341 kg/m^{2}s* demonstrated that the flow patterns observed along the transverse direction are different. Slug flow was observed in the central channels while wispy-annular flow was observed in the outer channels. This indicates that the flow was not uniformly distributed among the channels. Near the channel exit, three main flow patterns were observed in the central channels, namely bubbly, slug and annular flow

The effect of heat flux and mass flux on flow boiling patterns was reported by many researchers in the literature. Chen and Garimella (2006) conducted a visualisation study on flow boiling of FC-77 in horizontal silicone multi-microchannels with *0.389 mm* hydraulic diameter, aspect ratio *1* and *12.7 mm* length over a range of heat flux (*40–730 kW/m^2*) and at three different mass flux (*332*, *446* and *570 kg/m^{2}s*). Visualisation was conducted near the channel exit at the centreline of the heat sink. They reported that bubbly flow is dominant at low heat flux while bubbles grow and merge faster as heat flux increases resulting in slug flow at intermediate heat flux. As the heat flux increased further, alternating wispy-annular flow and churn flow were observed. At these conditions, when the camera was moved to the channel inlet region, flow reversal was observed. Thus, the formation of alternating wispy-annular and churn flow was

attributed to the occurrence of flow reversal. The authors did not discuss the mass flux effect on the flow patterns in their study. Galvis and Culham (2012) investigated flow boiling characteristics of water in horizontal copper single microchannels having different hydraulic diameters (*0.22* and *0.42 mm*) but the same length (*21.9 mm*) and channel aspect ratio (*1.2*). They reported that the bubbly, slug, churn, annular, wavy-annular and inverted annular flow patterns were observed in the microchannels as the heat flux was increased gradually, see Fig. 2.18. Moreover, flow reversal and the intermittent flow pattern was observed in the tested microchannels. Following the annular flow pattern, local dryout condition and re-wetting of the channel was observed in their study. The authors also examined the effect of mass flux on the flow patterns. They stated that the flow pattern transitions were shifted to higher heat flux inputs as the mass flux was increased.

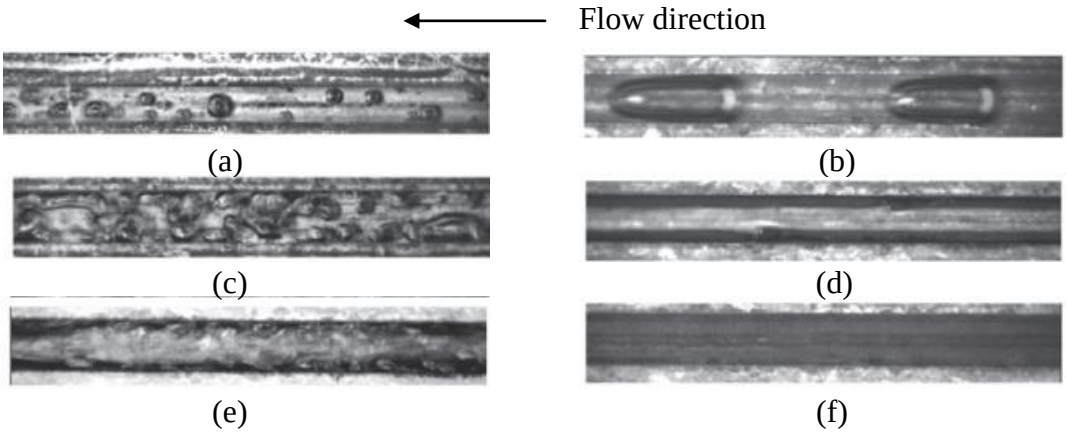

Figure 2.18 Flow patterns in the 0.42 mm hydraulic diameter copper horizontal microchannel at G = 365 kg/m^{2}s and q" = 61.2-1414 kW/m^2: (a) bubbly flow, (b) slug flow, (c) churn flow, (d) annular flow, (e) wavy-annular flow and (f) inverted annular flow, Galvis and Culham (2012).

In another study, Balasubramanian et al. (2013) investigated de-ionized water flow boiling in copper rectangular multi-microchannels with hydraulic diameter *0.34 mm*, aspect ratio *0.17* and two channel lengths *25* and *20 mm*. As the heat flux was increased, dispersed bubbly flow, intermittent flow and annular flow patterns were observed as shown in Fig. 2.19. The intermittent flow regime was defined as a combination of the

elongated bubbly flow and slug flow regimes where they occurred alternately over different time periods. Similar to Galvis and Culham (2012), they reported that the flow patterns occurred at higher heat flux values with the increase in mass flux. Moreover, the authors found a reasonable prediction between their data and the Taitel-Dukler (1976) adiabatic flow pattern map at low heat flux values. At high heat flux values the prediction of the Taitel-Dukler (1976) flow map became inferior.

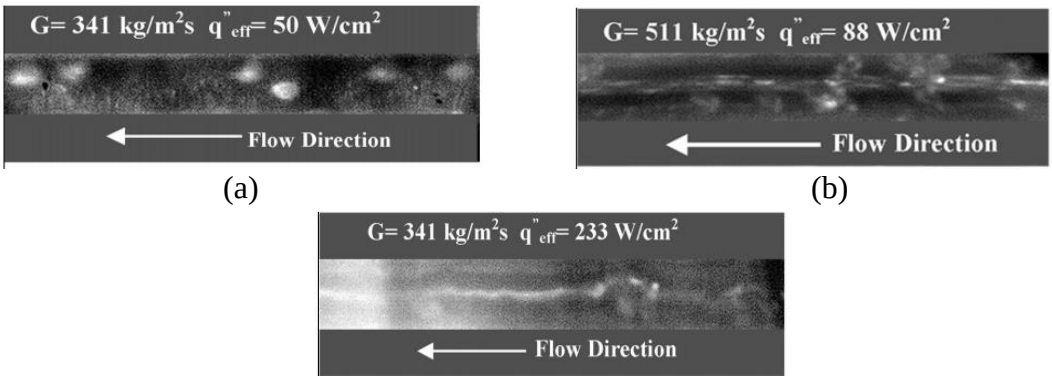

Figure 2.19 The flow patterns in the horizontal silicon microchannel with 0.34 mm hydraulic diameter, 0.17 aspect ratio and 20 mm length: (a) Dispersed bubbly flow at G =341 kg/m^{2}s and q" = 50 W/cm^2, (b) Intermittent flow at G =511 kg/m^{2}s and q" = 88 W/cm^2; (c) Annular flow at G =341 kg/m^{2}s and q" = 233 W/cm^2, Balasubramanian et al. (2013).

The hydraulic diameter effect on flow boiling patterns was studied by Mirmanto (2012) using three copper microchannels having different hydraulic diameter (D_h = *438*, *566* and *635*μm) and aspect ratio (β = *1.28, 2.56* and *4.38*) but the same channel length (L = *62 mm*). Details of the test sections and experimental range were described in the single-phase section. The author concluded that the hydraulic diameter effect on the flow boiling patterns in the tested experimental conditions and microchannel dimensions were insignificant. On the contrary, Wang and Sefiane (2012) found a hydraulic diameter effect on the flow boiling patterns in borosilicate glass horizontal microchannels with a hydraulic diameter of *571* μm, *762* μm and *1454* μm using FC-72 as a working fluid. The aspect ratio of the channels was *20, 20* and *10* and the heated length was *80 mm*. They reported that the flow regimes were found to be different in

three channels at the similar mass flux and heat flux values, see Fig. 2.20. In the *571 μm* microchannel, regular vapour collisions and thin liquid film were observed during annular flow. However, entrained droplet and thicker liquid film compared to *571 μm* microchannel was reported in the *762 μm* microchannel. On the other hand, they stated that more intense nucleation occurred in the *1454 μm* microchannel compared to other channels during the evaporating of the liquid film.

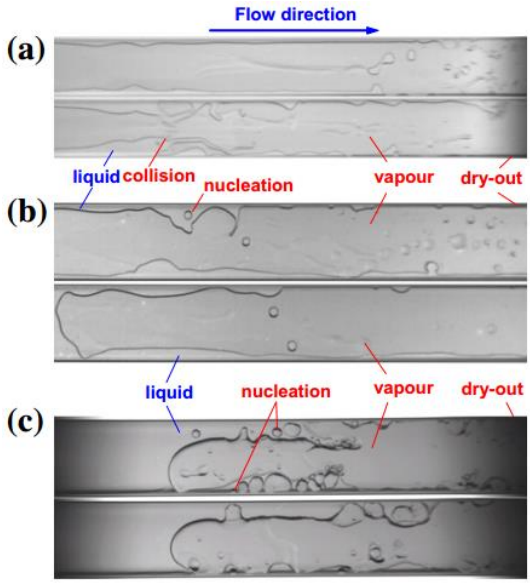

Figure 2.20 Flow regimes of FC-72 in three horizontal borosilicate glass microchannels at G = 44.8 kg/m^{2}s^1: (a) D_h = 571 μm at q" = 6 kW/m^2, (b) D_h = 762 μm at q" = 5.95 kW/m^2 and (c) D_h = 1454 μm at q" = 7.56 kW/m^2, Wang and Sefiane (2012).

Channel aspect ratio effect on the flow boiling patterns was also examined by some researchers in the literature. Soupremanien et al. (2011) investigated flow boiling characteristics of Forane-365HX in two horizontal rectangular stainless steel microchannels with same hydraulic diameter (D_h *= 1.4 mm*) and length (*L = 83 mm*) and different aspect ratios (β *= 2.3* and *7*). They observed bubbly flow, slug flow, churn flow and annular flow patterns in the two tested microchannels at similar heat flux and mass flux values. In the bubbly flow regime, the bubbles were smaller and isolated (isolated bubbly flow regime) in the higher aspect ratio channel whilst typical bubbly flow was encountered in the lower aspect ratio channel. In a recent study, Markal et al. (2016) performed sets of experiments to examine the flow boiling characteristics of de-

ionized water in six parallel rectangular silicon microchannels. The hydraulic diameters and the lengths of the channels were identical ($D_h = 100\ \mu m$ and $L = 48\ mm$) whilst the channel aspect ratios were varied from *0.37* to *5*. They observed periodical flow patterns in the all tested microchannels. This periodical flow patterns consisted of three stages namely i) re-wetting stage, ii) evaporation and slug-annular/annular flow stage and iii) partial dryout/dryout stage. They reported that the period of the flow patterns were longer for the higher aspect ratio channels than the lower aspect ratio channels.

In this section, flow boiling pattern studies in microchannels are reviewed from the literature. It was found that some adiabatic flow patterns (churn flow) may not exist during flow boiling tests (Shuai et al. (2003), Huh and Kim (2006) and Revellin and Thome (2007)). In multi-microchannels, flow boiling patterns can be different in parallel channels (Megahed and Hassan (2009)). The effect of heat flux and mass flux was found to have an effect on flow boiling patterns. The flow boiling patterns transformed from bubbly flow to slug flow, slug flow to churn flow, churn flow to annular flow in general (Chen and Garimella (2006), Galvis and Culham (2012) and Mirmanto (2012)) with the increase in heat flux. Flow reversal was also found by some researchers during flow boiling in microchannels (Galvis and Culham (2012), Balasubramanian et al. (2013) and Markal et al. (2016). The flow boiling patterns occurred at higher heat flux values at higher mass fluxes. The effect of hydraulic diameter and aspect ratio on flow boiling patterns in microchannels is unclear. Some studies show that hydraulic diameter and aspect ratio has an effect on flow boiling patterns, some others reported no hydraulic diameter and aspect ratio effect.

2.4.2 Flow pattern maps

Flow pattern maps are the most common type of method used to determine flow patterns and transition boundaries that exist under different circumstances. Since flow regimes are strongly related to the prediction of pressure drop and heat transfer rate, flow pattern maps become quite important tools. The flow pattern maps are available in the literature for horizontal and vertical two-phase flow in conventional size channels, see Baker (1954), Hewitt and Roberts (1969), Mandhane et al. (1974) and Taitel et al. (1980). Superficial gas and liquid velocities were used to plot these flow pattern maps

as coordinates. Accordingly, many researchers compared their results for microchannels with the flow pattern maps that were proposed for the macroscale. Some of them found a good agreement (Triplett et al. (1999), Balasubramanian et al. (2013)) whilst most reported that flow pattern maps developed for macroscale are not suitable for predicting flow patterns in microchannels, see Zhao and Bi (2001), Chen et al. (2006), Revellin and Thome (2007) and Ong and Thome (2009). Therefore, many researchers developed flow pattern maps and transition models for micro passages for diabatic and adiabatic conditions.

Akbar et al. (2003) developed a map based on air-water flow experimental data from the literature. They defined four regions in their map: annular region (inertia dominated), bubbly, plug/slug regions (surface tension dominated), dispersed flow region and transition region. These regions were created based on the three transition criteria that are given by Eq. (1.3) - Eq. (1.5).

Surface tension dominated region:
$$\begin{cases} We_{gs} \le 0.11 We_{ls}^{0.315} & for \quad We_{ls} \le 3 \\ We_{gs} \le 1 & for \quad We_{ls} > 3 \end{cases} \tag{1.3}$$

Inertia dominated region:
$$11 We_{ls}^{0.14} \le We_{gs} \quad for \quad We_{ls} \le 3 \tag{1.4}$$

Dispersed flow region:
$$We_{gs} > 1 \quad for \quad We_{ls} > 3 \tag{1.5}$$

The flow pattern map of Akbar et al. (2003) is depicted in Fig. 2.21. It is worth mentioning that the transition region occupies a large area on the flow map which is generally much smaller in microchannels. Hassan et al. (2005) proposed two maps for vertical and horizontal microchannels using *1475* air-water data points from the literature and their experimental data in borosilicate glass circular tubes with diameter *3 mm, 1 mm* and *0.8 mm*. The selected microchannels from the literature had a hydraulic diameter less than *1 mm*. They created flow maps based on their experimental flow patterns for each channel. Consequently, they made average transition lines between flow patterns in order to propose universal flow maps, see Fig. 2.22.

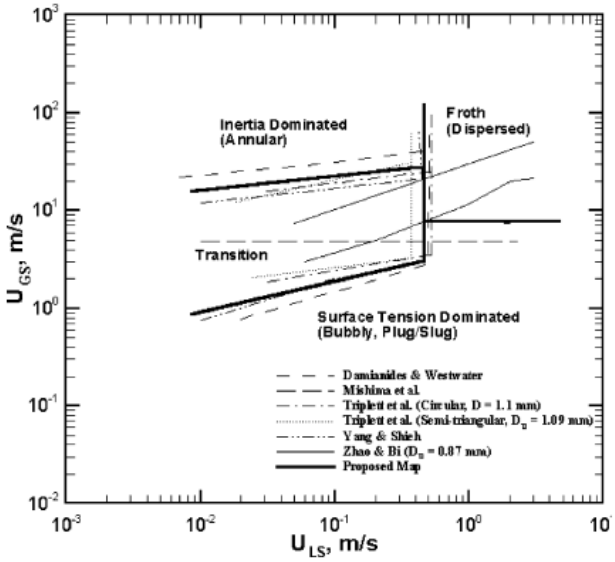

Figure 2.21 Proposed flow regime map for the microchannels ($D_h \leq 1$mm) using air-water experimental data from the literature, Akbar et al. (2003).

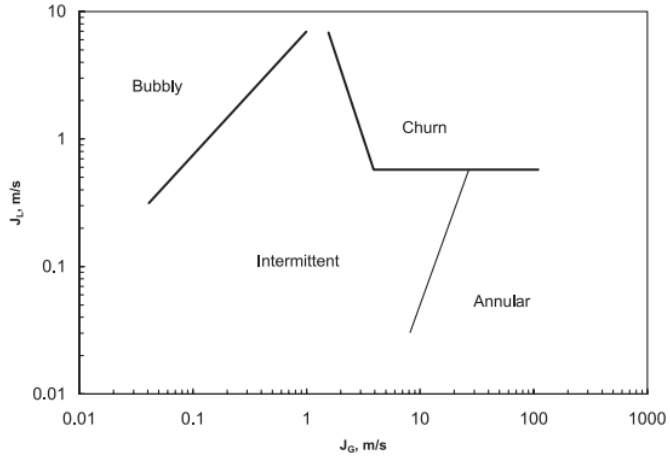

Figure 2.22 Flow map for horizontal channels having hydraulic diameter less than 1 mm based on air-water flow, Hassan et al. (2005).

Chen (2006) developed flow maps and transition criteria for using dimensional and non-dimensional numbers based on experimental results of R-134a in four stainless steel vertical tubes of inner diameters *1.1, 2.01, 2.88* and *4.26 mm* and different inlet pressures (*6, 10* and *14 bar*). Bubbly, slug, dispersed bubbly, churn and annular flow regimes were identified in Chen's flow map. The details of these criteria can be found in

Chen (2006). The flow pattern map of Chen for the *2.01 mm* diameter tube at *10 bar* pressure is presented in Fig. 2.23 as an example. The author reported that the system pressure, fluid properties and channel diameter found to have an effect on flow pattern transition boundaries. At higher system pressure operations, the churn/annular and slug/churn flow transition boundaries occurred at lower vapour velocities. On the other hand dispersed bubbly/bubbly flow transition boundaries were shifted to lower liquid velocities as the system pressure was increased. The system pressure effect on the other flow pattern transition lines found to be insignificant by the author. The effect of channel diameter on flow pattern transition boundaries were also evaluated by Chen (2006). He reported that the transition boundaries from slug to churn flow and from churn to annular flow was shifted to higher superficial gas velocities with the decrease in hydraulic diameter. However, the transition boundaries from dispersed bubbly to churn flow and from churn flow to annular flow were not affected by tube diameter.

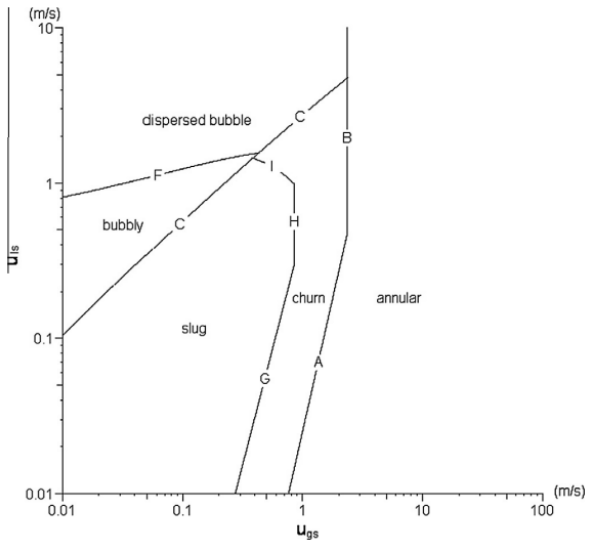

Figure 2.23 The flow boiling pattern map and transition boundaries developed by Chen (2006) for D = 2.01 mm and P = 10 bar.

Another flow map was created by Sobierska et al. (2006) where the horizontal axis is the quality and vertical axis is the mass flux. They presented flow boiling characteristics of water in a rectangular vertical microchannel of *1.2 mm* hydraulic diameter. Bubbly flow occupies the area at very low qualities and slug flow pattern area was in the middle. On the other hand the annular flow existed at higher vapour qualities (right

hand side of the map). It is worth to mention that the authors created the flow pattern map based on their visualisation results. They did not propose any criteria for the flow pattern transition boundaries.

Harirchian and Garimella (2010) proposed a flow map based on their experimental study to investigate flow boiling characteristics of FC-77 in silicon horizontal parallel rectangular microchannels. Twelve microchannels having a hydraulic diameter range of *0.096 mm* and *0.707 mm* were tested over a *225-1420 kg/m^{2}s* mass flux and *0-400 kW/*m^2 heat flux ranges. They found five flow regimes as bubbly, slug, churn, wispy-annular and annular flow. However, they grouped the bubbly flow and slug flow as confined flow whilst churn flow, wispy-annular flow and annular flow regimes were grouped as unconfined flow. They proposed a confinement criterion using a new non-dimensional number named convective-confinement number ($Bd^{0.5}$ *x* Re_{LO}) which is given in Eq. (1.6) below. Accordingly, a new flow map was created by the authors using the convective-confinement number and non-dimensional heat flux (Bo *x* Re_{LO}) as can be seen in Fig. 2.24.

$$Bd^{0.5} \times \mathrm{Re}_{LO} = 160 \tag{1.6}$$

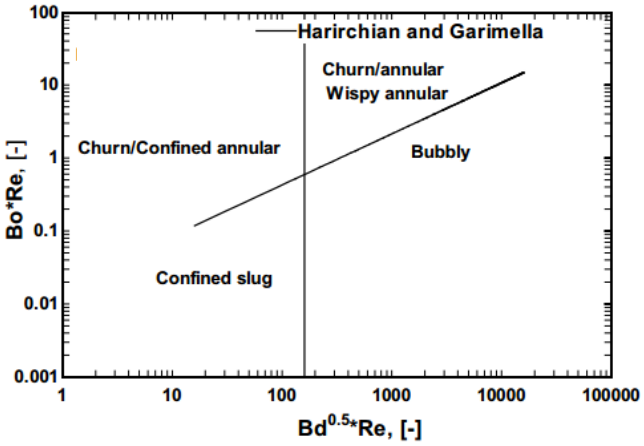

Fig. 2.24 Flow regime map based on FC-77 experimental data in parallel silicon horizontal microchannels, Harirchian and Garimella (2010).

The vertical transition line in Fig. 2.24 is given in Eq. (1.6) whilst the other transition line is given in Eq. (1.7) below.

$$Bo \times \mathrm{Re}_{LO} = 0.017(Bd^{0.5} \times \mathrm{Re}_{LO})^{0.7} \quad (1.7)$$

They stated that the transition boundaries from bubbly or slug flow to churn/wispy-annular or churn/annular flow were shifted to higher superficial gas velocity values as the channel hydraulic diameter decreased.

The above literature review showed that there is disagreement and inconsistency between flow patterns transition boundaries in microchannels. The flow patterns transition boundaries could not be predicted well by the conventional scale flow pattern models, Coleman and Garimella (1999), Zhao and Bi (2001), Chen (2006), Revellin and Thome (2007) and Ong and Thome (2009). As the channel hydraulic diameter becomes smaller, the transition boundaries of the dispersed bubbly/bubbly, intermittent/dispersed bubbly and intermittent/bubbly flow patterns shifts to higher liquid superficial velocities, Coleman and Garimella (1999) and Chen (2006). Also, when the hydraulic diameter decreased, the bubbly/slug, slug/churn and churn/annular flow patterns transition boundaries occurred as higher superficial gas velocities, Coleman and Garimella (2006), Chen (2006) and Harirchian and Garimella (2010). At higher system pressure operations, the churn/annular and slug/churn flow transition boundaries occurred at lower vapour velocities. On the other hand dispersed bubbly/bubbly flow transition boundaries were shifted to lower liquid velocities as the system pressure was increased. The effect of system pressure on the other flow pattern transition boundaries was not noted, Chen (2006).

2.4.3 Flow boiling heat transfer characteristics

2.4.3.1 Boiling incipience in Microchannels

In forced flow boiling, the start of bubble nucleation is called the onset of bubble nucleation as boiling incipience. Good understanding of the boiling incipience process is necessary in order to investigate flow boiling phenomena in detail. The studies that

investigated flow boiling incipience in microchannels are reviewed critically in this section.

When the temperature of the heated surface exceeds the saturation temperature of the liquid at the corresponding pressure the boiling process initiates. This considerable wall temperature increase is called temperature overshoot. Boiling incipience can be seen on plots such as, $\Delta P - q''$ curve, $q'' - \Delta T_{sub}$ curve or $h - q''$ at fixed mass flux. On the other hand, initiation of boiling can be also detected by high speed flow visualisation. Studies in the literature show that boiling incipience in microchannels is different than the conventional channels. Kennedy et al. (2000) tested two copper microtubes ($D = 1.17$ *mm* and *1.45 mm*, $L = 160$ *mm*) under uniform heating and subcooled water flow conditions over a wide range of mass flux from *800 kg/m^{2}s* to *4500 kg/m^{2}s*. The Bergles and Rohsenow (1964) correlation which is widely used to predict onset of nucleate boiling heat flux for conventional channels underpredicted their experimental data for the smaller microtube. However, the correlation reasonably predicted experimental data for a larger microtube. The Bergles and Rohsenow (1964) correlation is given in Eqns. (1.8) and (1.9).

$$q''_{ONB} = 5.30P^{1.156}[1.8(T_w - T_{sat})_{ONB}]^n \tag{1.8}$$

$$n = 2.41 / P^{0.0234} \tag{1.9}$$

The boiling incipience heat flux is higher for the microchannels compared to conventional channels, which was reported by many researchers in the literature, Inasaka et al. (1989), Qu and Mudawar (2002b), Ghiaasiaan and Chedester (2002) and Wang et al. (2014). The reason of this might be that the temperature gradient near the walls of microchannels is higher than the conventional scale channels resulting in large thermocapillary force, see Ghiaasiaan and Chedester (2002). Ghiaasiaan and Chedester (2002) analysed available data in the literature about boiling incipience of water in microtubes having small diameters ($D = 0.1–1$ *mm*). They found that the conventional scale correlations of Sato and Matsumura (1963) and Bergles and Rohsenow (1964) under predicted the related boiling incipience heat flux values for microtube data.

Accordingly, they proposed a semi-empirical model that is based on the hypothesis that in microchannels the thermo-capillary forces tends to suppress the inertia force on wall cavities. According to their model, boiling incipience heat flux increases with increasing inlet subcooling. The model also stated that the channel diameter has a strong effect on the boiling incipience heat flux. Qu and Mudawar (2002b) experimentally investigated boiling incipience heat flux in a copper rectangular parallel multi-microchannel heat sink ($D_h = 349\ \mu m$, $\beta = 0.32$) by using de-ionised water as a coolant. The inlet subcooling was varied from *15K* to *75K*. Boiling incipience was detected using a microscope where the initial bubbles grew and detached from the microchannel wall near the outlet. They reported that boiling incipience in microchannels is different than in conventional scale channels. First bubbles grew and departed into the liquid flow in the tested microchannel contrary to the process in the conventional scale channels where the bubbles grow, nucleate and collapse locally. Although the majority of the first bubbles appeared on the channel bottom wall, some bubbles also occurred on the sidewalls. Subsequently, they proposed a mechanistic model to predict the boiling incipience heat flux in rectangular microchannels. The model was developed based on a bubble departure criterion which combines the force balance on a bubble and superheating bubble interface. Moreover, their model could predict the size of bubbles occurred on the surface and the sidewalls of the microchannel, the location of the first departed bubble and the temperature field around the bubble interface.

Contrary to above findings, some researchers reported that the boiling incipience heat flux in microchannels can be predicted using correlations proposed for conventional scale channels, Liu et al. (2005) and Mosyak et al. (2012). Liu et al. (2005) conducted experiments in rectangular parallel copper microchannels ($D_h = 0.38\ mm$, $\beta = 0.43$) using de-ionised water to investigate the onset of nucleate boiling (ONB) in microchannels. High-speed camera visualisation enabled the researchers to detect initiation of boiling. The authors developed an analytical model to predict boiling incipience heat flux in microchannels including the effect of inlet fluid velocity, inlet subcooling, contact angle, microchannel dimensions and exit fluid pressure. Their model predicted well their experimental results. Moreover, they reported that the developed model agreed very well with the conventional scale correlations of Bergles and Rohsenow (1964) and Davis and Anderson (1966).

The effect of inlet fluid velocity, system pressure, inlet subcooling, heat flux and mass flux on the boiling incipience in microchannels was investigated in the literature. Piasecka et al. (2004) and Piasecka and Poniewski (2004) investigated boiling incipience of R-123 in a vertical microchannel having *1.95 mm* hydraulic diameter, *360 mm* length and aspect ratio *40*. The boiling location was determined from the temperature distribution of the one side heated wall obtained using the liquid crystal thermography technique. The authors called this location "boiling front" where the temperature of the heating surface drops suddenly. They reported that increasing system pressure did not affect the boiling front. However, distance of this location increased from the channel inlet as the inlet liquid velocity and inlet subcooling increased. In other words, as the inlet liquid velocity and inlet subcooling increased the boiling front was shifted to the channel outlet. These findings are not surprising since the higher wall superheat (T_w-T_{sat}) values are needed in order to initiate the boiling process at the entry region compared to other regions, see Martin-Callizo et al. (2007a) and Qi et al. (2007). Martin-Callizo et al. (2007a) examined the flow boiling curve in a microtube having diameter *0.64 mm* and *213 mm* length. They presented the flow boiling curve for three axial locations and different mass flux values. It was found that the required wall superheat value to initiate the boiling was much higher at the entry region compared to other regions especially at the highest mass flux operation. Liu et al. (2005) also investigated the effect of inlet fluid velocity and inlet subcooling on boiling incipience. Details of the test sections and experimental conditions were described previously, on page 42. They reported that although boiling incipience heat flux increased with the inlet fluid velocity, it decreased with decreasing inlet subcooling, see Fig. 2.25. Moreover, they observed a single bubble or a few bubbles near the channel exit at the boiling incipience condition. The bubbles occurred generally at the channel bottom wall surface and near the edges but not exactly at the edges.

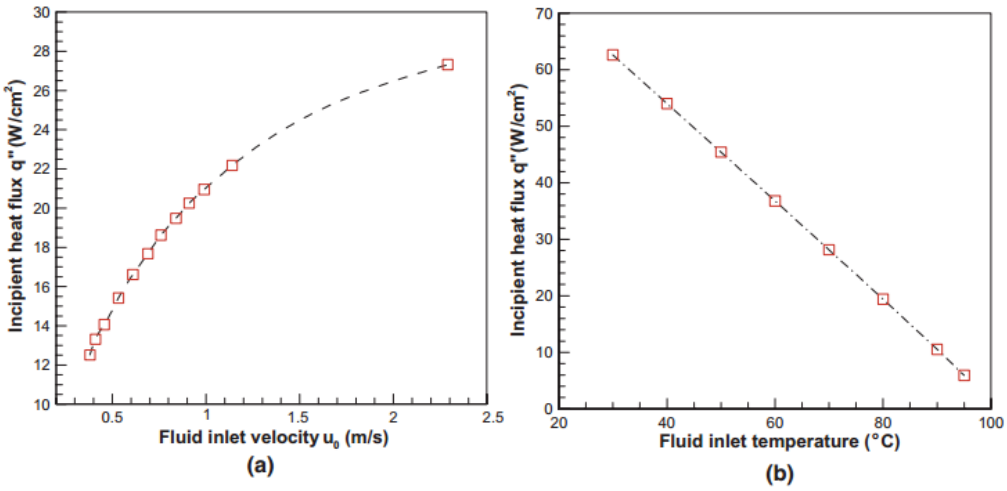

Figure 2.25 Effect of various parameters on boiling incipient heat flux in rectangular parallel copper microchannels: (a) effect of fluid inlet velocity, (b) effect of inlet subcooling, Liu et al. (2005).

In a recent study, Wang et al. (2014) tested a single stainless steel vertical rectangular microchannel having *2 mm* hydraulic diameter and aspect ratio of *1* using de-ionised water. Tests were performed over a mass flux range *100-1500 kg/m^{2}s* corresponding to *20-200 kW/m^2* heat flux. Inlet subcooling was varied between *20* and *74 K* and pressure was changed from *0.2* to *2 MPa*. They investigated the effect of system pressure, inlet subcooling, heat flux and mass flux on boiling incipience. Also different boiling incipience criteria were analysed (*ΔP-q"*, *ΔP-G*, *h-q"* and *h-G* curves). They reported that, boiling incipience heat flux increased with increasing inlet subcooling and mass flux, but it is independent of system pressure as can be seen in Fig. 2.26. It was also found that no significant discrepancies occurred between the four boiling incipience criteria.

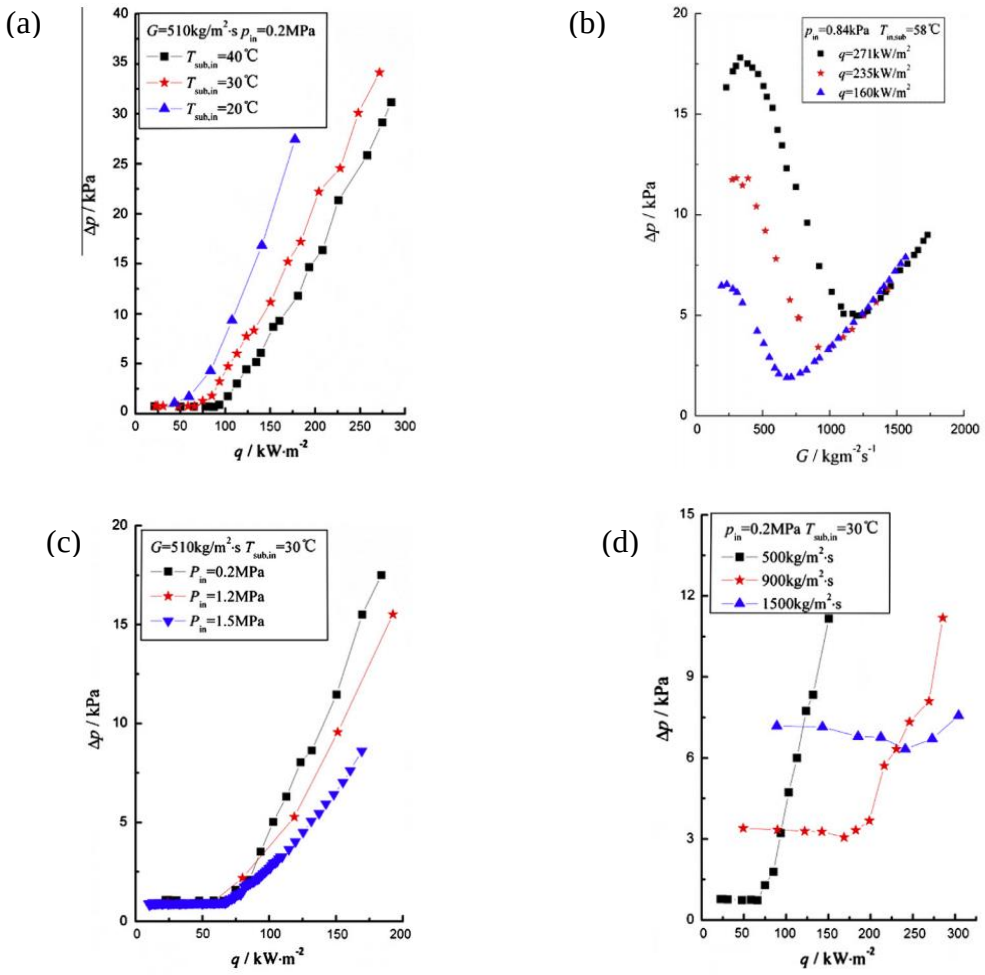

Figure 2.26 Effect of various parameters on the boiling incipience in a single stainless steel vertical microchannel: (a) effect of inlet subcooling, (b) effect of heat flux, (c) effect of system pressure and (d) effect of mass flux, Wang et al. (2014).

The above literature review reveals the boiling incipience characteristics in the microchannels. These characteristics can be summarised as follows:

- First bubbles grow and depart into the liquid flow in microchannels contrary to the process in larger channels where the bubbles grow, nucleate and collapse locally, Qu and Mudawar (2002b).
- The first nucleating bubbles appear on the microchannel sidewalls as well as the channel bottom wall, Qu and Mudawar (2002b) and Liu et al. (2005).

- Some researchers reported that the boiling incipience heat flux for the microchannels is higher compared to conventional scale channels, Inasaka et al. (1989), Kennedy et al. (2000), Ghiaasiaan and Chedester (2002), Qu and Mudawar (2002b) and Wang et al. (2014). Ghiaasiaan and Chedester (2002) attributed this to the large effect of thermo-capillary force compared to the inertia force.
- The boiling incipience heat flux increases with increasing inlet fluid velocity, inlet subcooling and mass flux. On the other hand, system pressure had no influence on the boiling incipience heat flux, Liu et al. (2005) and Wang et al. (2014).

2.4.3.2 Heat transfer mechanism(s)

Collier and Thome (1994) stated that flow boiling heat transfer mechanisms in conventional scale are nucleate boiling and convective boiling. However, some researchers reported nucleate boiling as a dominant mechanism in microchannels, some others reported convective boiling or convective-nucleate boiling as dominant mechanism(s). In the nucleate boiling region, the heat transfer coefficient is mainly dependent on the heat flux whereas the effect of mass flux and vapour quality is insignificant. On the other hand, in convective boiling the heat transfer coefficient depends on mass flux and vapour quality and does not depend on heat flux.

Lazarek and Black (1982) examined the two-phase heat transfer coefficient of R-113 in a vertical stainless steel tube having *3.15 mm* diameter and heated lengths of *123 mm* and *246 mm* over a broad range of liquid Reynolds number (*Re = 791-4745*). Inlet subcooling and inlet pressure was *33 K* and *170 kPa* respectively. They reported that the higher boiling heat transfer coefficients were observed with the increase in heat flux (*64-178 kW/m*^{2}) whilst the effect of local vapor quality (*x = 0-0.7*) was insignificant. Therefore, the dominant heat transfer mechanism was reported as nucleate boiling by the authors. Galvis and Culham (2012) examined the water flow boiling characteristics in two different single copper microchannels having the same length (*21.9 mm*) and aspect ratio (*1.2*) but different hydraulic diameters (*0.2 mm* and *0.14 mm*). The inlet subcooling was *50–54 K* during the experiments with *350–1300 kg/m*^{2}*s* mass flux range,

112–3720 kW/m^2 heat flux range and *0–0.47* vapour quality. They reported that the heat transfer coefficient decreased with heat flux up to a certain heat flux value for both microchannels. After that the heat transfer coefficient remained constant with increasing heat flux. On the other hand the mass flux effect on the heat transfer coefficient was insignificant. However, they reported that the nucleate boiling was the prevailing heat transfer mechanism.

In contrast to the above researchers, Kew and Cornwell (1997) measured the flow boiling heat transfer coefficient of R-141b in *500 mm* long vertical stainless steel tubes with diameters of *1.39 mm, 2.87 mm* and *3.69 mm*. The experimental ranges were from *188 kg/m^{2}s* to *1480 kg/m^{2}s* for mass flux, from *9.7 kW/m^2* to *90 kW/m^2* for heat flux and from *-0.05* to *0.8* for vapour quality. In the *2.87 mm* and *3.69 mm* diameter tubes the heat transfer coefficient increased with heat flux at low quality, whilst at higher qualities the heat transfer coefficient was a function of quality and independent of heat flux similar to conventional tubes. However results for the *1.39 mm* tube showed that the heat transfer coefficient fell rapidly with increasing quality. This decrease was attributed to local dryout by rapidly growing bubble that filled the tube. In a recent study, Markal et al. (2016) performed sets of experiments to examine the flow boiling characteristics. Details of the microchannel test section and experimental conditions were mentioned previously in the flow boiling patterns section, on page 35. They reported that the heat transfer coefficient increased with increasing mass flux. Moreover, it was reported that the heat transfer coefficient decreased as the heat flux increased. They reported that the dominance of convective boiling existed during the tests.

The above review indicates that there is no common conclusion about the dominant heat transfer mechanism(s) and the effect of heat and mass flux on the boiling heat transfer coefficient in microchannels. Table 2.2 includes some past studies that mention the heat transfer mechanism(s). As can be seen from the table 2.2, there is a disagreement on the dominant heat transfer mechanism(s) in microchannels. Ten authors stated that nucleate boiling was the prevailing heat transfer mechanism. However, in eight papers convective boiling was given as the dominant heat transfer mechanism whilst seven authors mentioned both nucleate and convective boiling mechanism(s) occurred together.

Table 2.2 Heat Transfer mechanism(s) published in the literature

Author	Fluid	Material, Geometry	Diameter	Heat transfer mechanism(s)
Lazarek and Black (1982)	R-113	Stainless steel, circular	D = 3.15 mm	Nucleate Boiling
Kew and Cornwell (1997)	R-141b	Stainless steel, circular	D = 1.39, 2.87, 3.69 mm	Nucleate and Convective Boiling
Bao et al. (2000)	R-11, HCFC-123	Copper, circular	D = 1.95 mm	Nucleate Boiling
Lin et al. (2001)	R-141b	Copper, circular-rectangular	D = 1.1, 1.8, 2.8 and 3.6 mm D_h = 2 mm	Nucleate and Convective Boiling
Qu and Mudawar (2003a)	Water	Copper, rectangular	D_h = 0.349 mm	Convective Boiling
Wen et al. (2004)	Water	Stainless steel, rectangular	D_h = 1.2 mm	Nucleate Boiling
Steinke and Kandlikar (2004a)	Water	Copper, rectangular	D_h = 0.207 mm	Nucleate Boiling
Lee and Mudawar (2005a)	R-134a	Copper, rectangular	D_h = 0.35 mm	Nucleate and Convective Boiling
Kosar et al. (2005)	Water	Silicon, rectangular	D_h = 0.227 mm	Nucleate and Convective Boiling
Sobierska et al. (2006)	Water	Copper, rectangular	D_h = 1.2 mm	Nucleate Boiling
Huh and Kim (2007)	Water	PDMS, rectangular	D_h = 0.1 mm	Nucleate Boiling

Table 2.2 Continued.

Lee and Garimella (2008)	Water	Silicon, rectangular	D_h = 0.16, 0.29, 0.4, 0.54 mm	Nucleate and Convective Boiling
Ong and Thome (2009)	R-134a, R-236fa, R-245fa	Stainless steel, circular	D = 1.03 mm	Convective Boiling
Mahmoud (2011)	R-134a	Stainless steel, circular	D = 0.52 and 1.1 mm	Nucleate and Convective Boiling
Mirmanto (2012)	Water	Copper, rectangular	D_h = 044, 0.56 and 0.64 mm	Nucleate Boiling
Galvis and Culham (2012)	Water	Copper, rectangular	D_h = 0.14 and 0.2 mm	Nucleate Boiling
Wang and Sefiane (2012)	FC-72	Borosilicate glass, rectangular	D_h = 0.57, 0.76 and 1.45 mm	Convective Boiling
Mortada et al. (2012)	R-134a, R-1234yf	Aluminium, rectangular	D_h = 1.1 mm	Convective Boiling
McNeil et al. (2013)	R-113	Copper, rectangular	D_h = 1 mm	Nucleate and Convective Boiling
Lim et al. (2015)	Water	Copper, rectangular	D_h = 0.5 mm	Nucleate Boiling
Anwar et al. (2015)	R-600a	Stainless steel, circular	D = 1.60 mm	Nucleate Boiling
Markal et al. (2016)	Water	Silicon, rectangular	D_h = 0.1 mm	Convective Boiling

2.4.3.3 Effect of geometrical parameters

It is important to discuss the effect of size and geometry of the channel on the flow boiling heat transfer coefficient in the micro-scale. In the literature, different heat transfer characteristics were reported due to various experimental conditions. But, generally speaking the flow boiling heat transfer coefficient increases with decreasing hydraulic diameter in microchannels. The effect of channel hydraulic diameter, channel geometry and channel aspect ratio on the flow boiling heat transfer coefficient in microchannels are presented in this section.

The effect of channel geometry on the flow boiling heat transfer coefficient was investigated by Tran et al. (1996) with R-12 in brass circular channel (*D = 2.46 mm, L = 900 mm*) and a rectangular channel (D_h *= 2.40 mm, L = 900 mm*). They reported that the effect of geometry on the heat transfer coefficient was not significant. Lin et al. (2001) also investigated flow boiling in four stainless steel microtubes with diameters *1.1, 1.8, 2.8* and *3.6 mm* and one square channel with *2 mm* hydraulic diameter using R-141b as the working fluid. Although the authors did not present any comparison figure for the circular and rectangular channels, they stated that the channel geometry has an effect on the dryout conditions rather than the heat transfer performance. On the other hand, Yen et al. (2006) tested smooth pyrex glass circular and square microchannels with same diameters (D_h *~ 0.21 mm*) to investigate the effect of cross-section on the local flow boiling heat transfer coefficient. They concluded that the heat transfer coefficient was higher for square microchannel as can be seen from Fig. 2.27. The authors attributed this to sharp edges in the square microchannel which behaved as effective nucleation sites that enhanced the boiling process. From the above review, it can be concluded that the channels having sharp cross-sections have superior heat transfer characteristics in micro-scale. Although Tran et al. (1996) and Lin et al. (2001) did not report any significant differences between circular and rectangular channels, their channel sizes were greater than *2 mm*. Microchannels are generally referred to channels having hydraulic diameter less than *1 mm*, see section 2.2. Moreover, the surface roughness has a considerable influence on the boiling incipience. The nucleation process is strongly related with the cavities on the channel surface as discussed earlier. Tran et al. (1996) and Lin et al. (2001) did not report any parameter about the surface roughness of the compared circular and rectangular channels. On the other hand, Yen et

al. (2006) investigated the surface roughness of each channel used for comparison. They stated that the two microchannels have similar surface roughness characteristics.

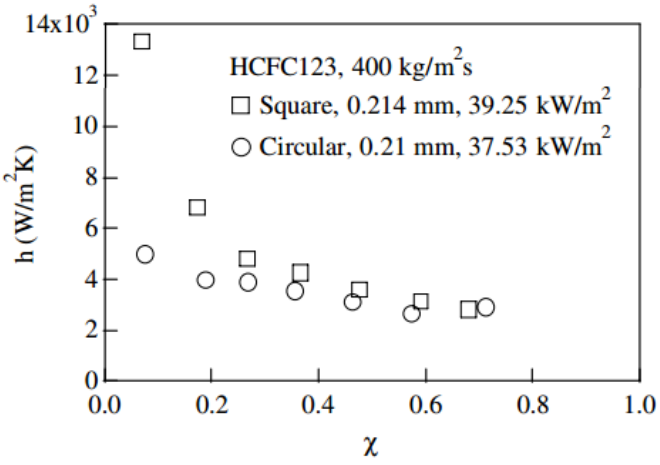

Figure 2.27 Local heat transfer coefficient versus vapour quality for circular and square microchannels using HCFC123 at G = 400 kg/m^{2}s and similar heat flux values, Yen et al. (2006).

The effect of channel diameter on the flow boiling heat transfer coefficient was examined by many researchers in the literature. Saitoh et al. (2005) carried out an experimental study to investigate the effect of tube diameter on the local flow boiling heat transfer coefficient of R-134a. Tubes with inner diameters of *0.51, 1.12* and *3.1 mm* and heated lengths *550, 935* and *3235 mm* were used. They presented the effect of heat flux and mass flux for each tube as shown in Fig. 2.28. It can be seen from the Fig. 2.28, the local heat transfer coefficient increased with the decrease in tube diameter up to around *0.5* quality value. After that the heat transfer coefficient declined sharply with increasing quality for the smallest tube. The authors attributed this to the occurrence of dryout in the smallest tube at a value of vapour quality around *0.5*. They concluded that the heat transfer coefficient increases with the decrease in tube diameter. The improvement was found to be about *27 %* when the diameter of the tube decreased from *3.1* to *0.51 mm*.

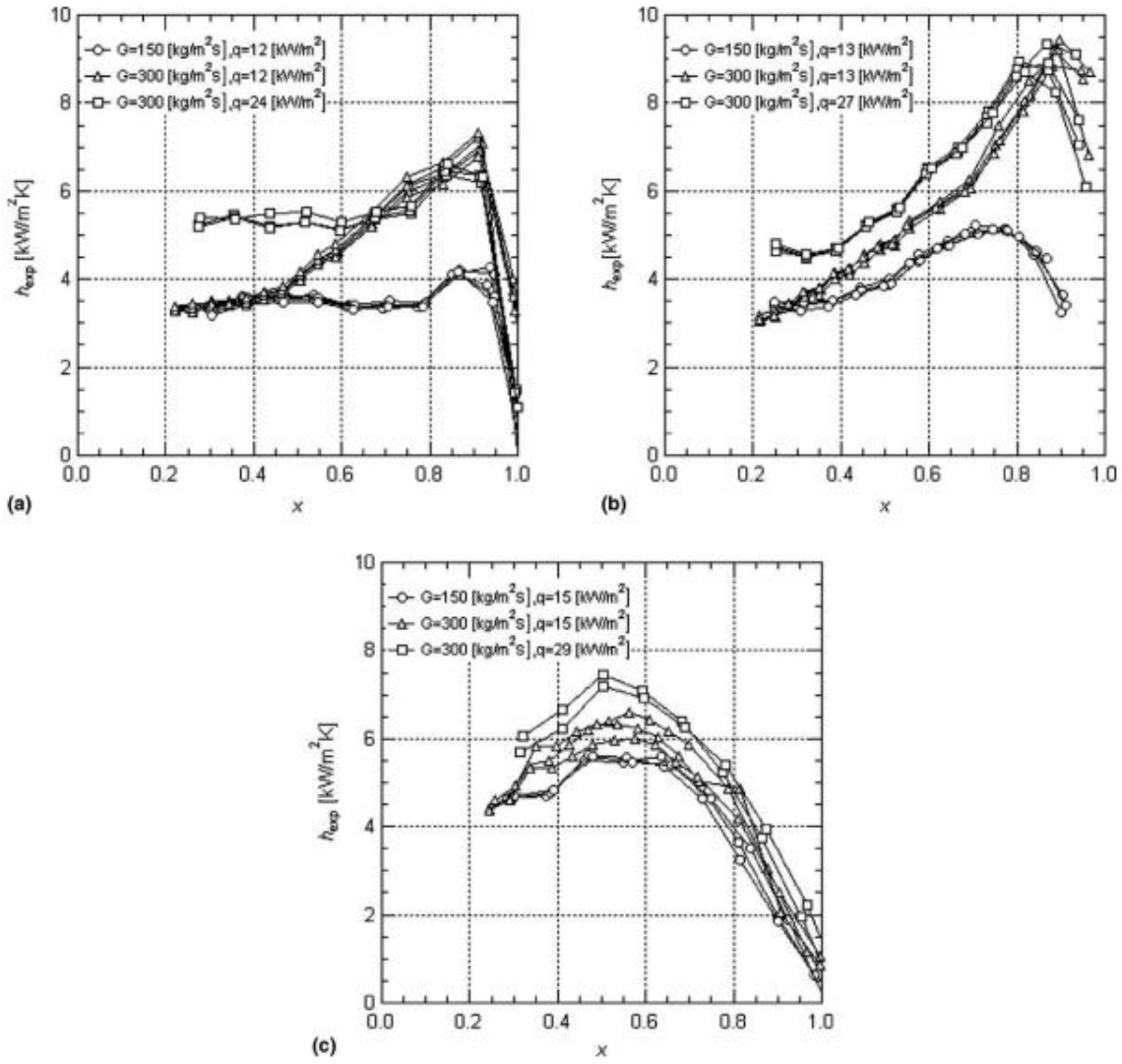

Figure 2.28 Effect of mass flux and heat flux for three tubes using R-134a: (a) 3.1 mm ID, (b) 1.12 mm ID, (c) 0.51 mm ID, Saitoh et al. (2005).

Martin-Callizo et al. (2007b) explored the effect of tube diameter on the local flow boiling heat transfer coefficient with three stainless steel tubes having diameters *0.83, 1.22* and *1.70 mm* and *220 mm* heated length. The working fluid was R-134a. They reported that the smaller tubes had higher local flow boiling coefficients as seen in Fig. 2.29. It is worth mentioning that the experiments were conducted at subcooled condition, so that maximum local quality values were around *0.025*. Karayiannis et al. (2008) presented average flow boiling heat transfer coefficient trends of R-134a in five vertical stainless steel tubes of internal diameter *4.26, 2.88, 2.01, 1.1* and *0.52 mm* and heated lengths of *500, 300, 211, 150* and *100 mm* respectively. They reported that the average flow boiling heat transfer coefficient increased significantly as the tube

diameter decreased from *2.88 mm* to other smaller tubes as shown in Fig. 2.30. When the channel diameter varied from *2.88* to *2.01 mm*, *2.01* to *1.1 mm* and *1.1* to *0.52 mm*, the heat transfer coefficient increased *14 %*, *17 %* and *73 %* respectively. It is worth mentioning that the authors excluded the data in the comparison after dryout condition.

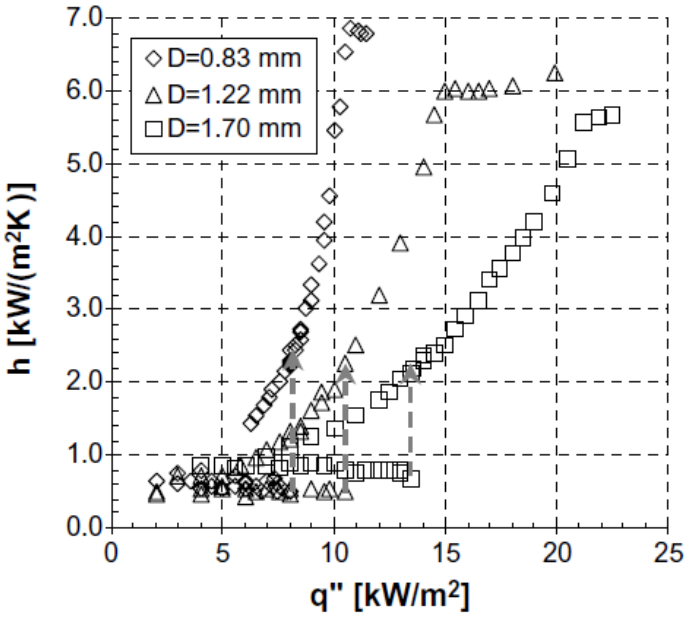

Fig 2.29 Effect of tube diameter on the local heat transfer coefficient at 10 K inlet subcooling and 700 kg/m^{2}s mass flux, Martin-Callizo et al. (2007b).

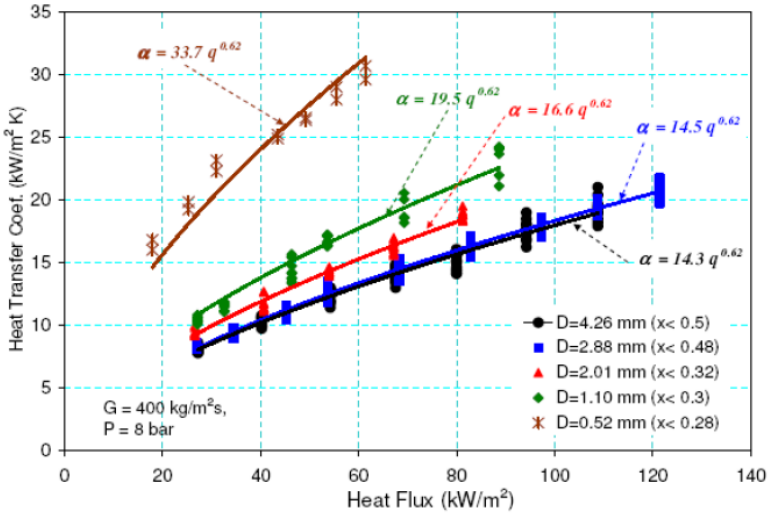

Fig 2.30 Effect of tube diameter on the average flow boiling heat transfer coefficient at 400 kg/m^{2}s mass flux and 8 bar system pressure, Karayiannis et al. (2008).

Consolini and Thome (2009) measured local flow boiling heat transfer coefficients for stainless steel tube diameters with *0.51* and *0.79 mm* with the same heated length of *75 mm* with working fluids R-134a, R-236fa and R-245fa. They stated that the heat transfer coefficient increased with decreasing tube diameter, see Fig. 2.31.

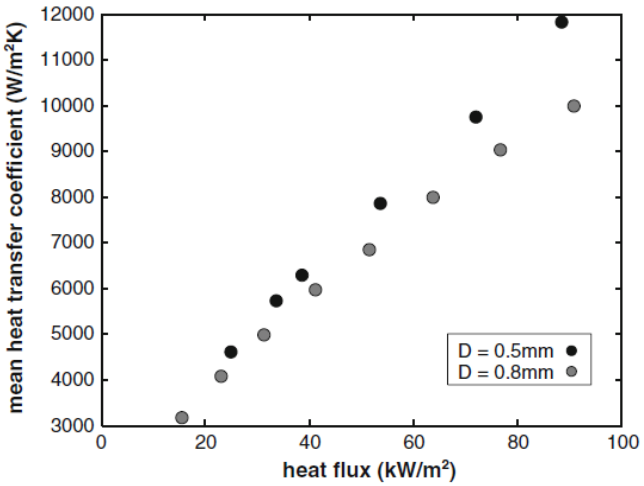

Fig 2.31 Effect of tube diameter on the average heat transfer coefficient for R236fa at 8 bar and 1000 kg/m^{2}s mass flux, Consolini and Thome et al. (2009).

In another study, Liu et al. (2011) examined the boiling heat transfer coeffient in brass parallel rectangular microchannels using water in two test sections with *0.29 mm* and *1.2 mm* hydraulic diameters. They concluded that the microchannel having smaller hydraulic diameter had higher heat transfer coefficient than the larger one, see Fig. 2.32.

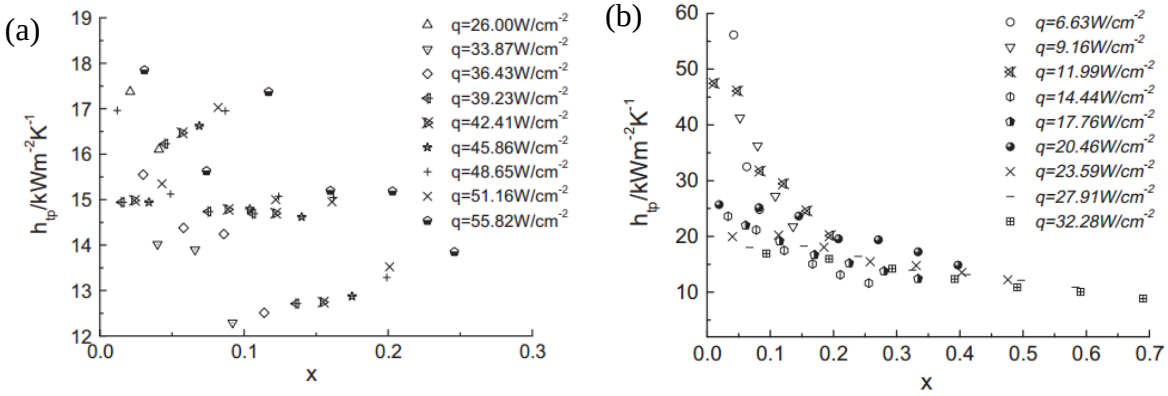

Figure 2.32 Heat transfer coefficient with increasing heat flux; (a) D_h = 1.12 mm, G = 44.36 kg/m^{2}s, (b) D_h = 0.29 mm, G = 49.59 kg/m^{2}s, Liu et al. (2011).

Mirmanto (2012) also examined the hydraulic diameter effect on the flow boiling heat transfer coefficient in a single rectangular copper microchannel. The channels had identical height (*H = 0.39 mm*) and different widths of *0.5, 1* and *1.71 mm* resulting in *0.438, 0.561* and *0.635 mm* hydraulic diameters, respectively. He reported that higher heat transfer coefficient up to low qualities (*x ~ 0.05*) existed for the smaller hydraulic diameter channel. However, the hydraulic diameter effect was unclear at higher qualities, see Fig. 2.33. As can be seen from Fig. 2.33, it is difficult to draw any conclusions from his study since the vapour quality was very small (*x ~ 0.2*).

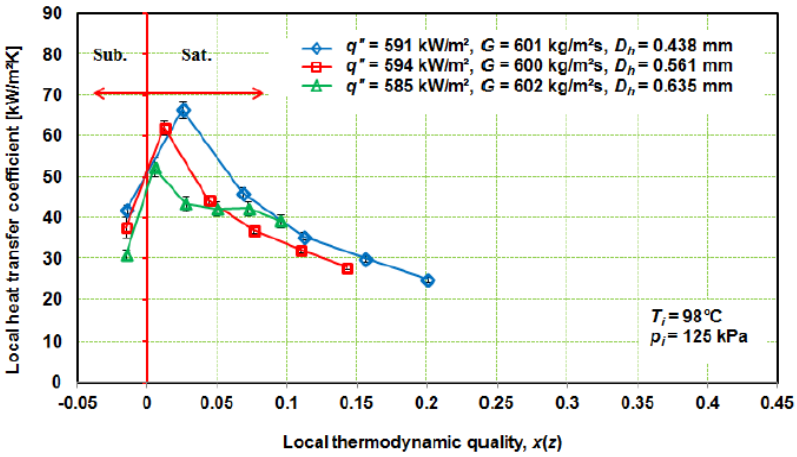

Figure 2.33 Effect of hydraulic diameter on the local heat transfer coefficient with increasin quality at G = 600 kg/m²s and similar heat flux values, Mirmanto (2012).

In another study, Wang and Sefiane (2012) carried out experiments on flow boiling heat transfer in microchannels using FC-72 as the working fluid. Three borosilicate glass test sections having rectangular parallel channels were used. Channel hydraulic diameters and aspect ratios were *0.57, 0.76* and *1.45 mm* and *20, 20* and *10* respectively. They compared the local heat transfer coefficient of two microchannels over same heat flux range for two different mass fluxes, see Fig. 2.34. They reported that the local heat transfer coefficient increased with decreasing hydraulic diameter, especially when the mass flux was higher. It can be seen from the Fig. 2.34 that the local heat transfer coefficient is much higher for the smaller microchannel up to vapour quality around *0.25*. For higher vapour qualities (*x > 0.25*) the hydraulic diameter effect on the boiling heat transfer coefficient seems small. However, the authors did not comment on this

point. The possible reason of this might be that the heat transfer coefficient decreases in microchannels beyond a vapour quality around ~ *0.1* as can also be seen from the studies above. The slope of this decrease was found to be higher as the channel diameter decreases, see also Saitoh et al. (2005), Liu et al. (2011) and Mirmanto (2012).

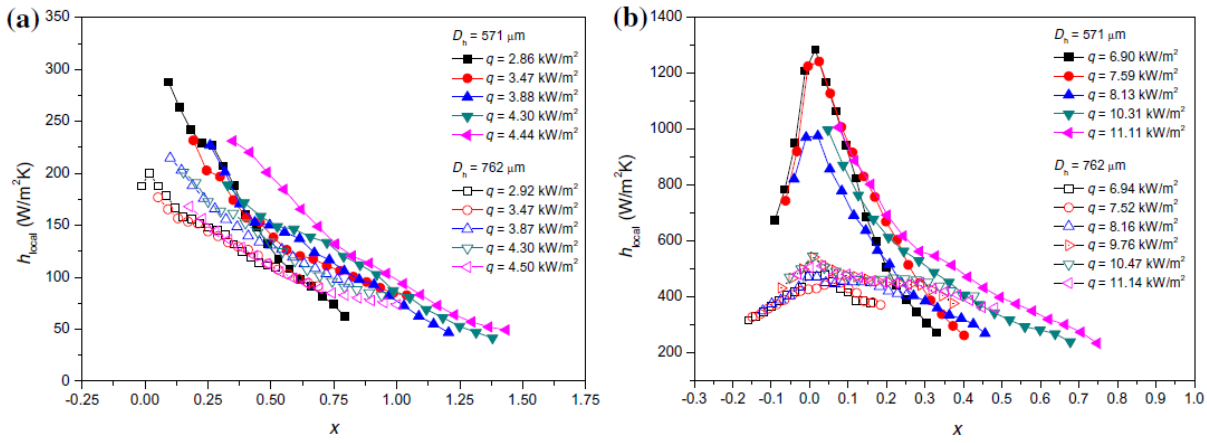

Figure 2.34 Effect of channel diameter on the heat transfer coefficient at the same heat flux range for two different mass fluxes: (a) G = 11.2 kg/m^{2}s, (b) G = 44.8 kg/m^{2}s, Wang and Sefiane (2012).

Contrary to above researchers, a few researchers reported that decreasing channel diameter does not increase the flow boiling heat transfer coefficient. Kew and Cornwell (1997) evaluated the flow boiling heat transfer coefficient of R-141b in three stainless steel tubes *500 mm* long with diameters *1.39, 2.87* and *3.69 mm*. The effect of tube diameter on the heat transfer coefficient was found to be insignificant. However, it is hard to draw any conclusions since they did not present any comparison figure for the heat transfer performances of the three tubes. Harirchian and Garimella (2009b) conducted experiments to examine the channel size effect on the flow boiling heat transfer in silicon parallel rectangular microchannels using FC-77. Twelve different test sections with hydraulic diameters ranging from *0.096* to *0.707 mm* were tested. They plotted the average heat transfer coefficient versus the channel cross-sectional area as presented in Fig 2.35. From this figure it can be seen that for the lower heat fluxes (*80* and *100 kw/m^2*), the heat transfer coefficient is relatively insensitive to the channel cross-sectional area for areas of *0.089 mm^2* and larger where nucleate boiling is dominant. Moreover the authors reported that the heat transfer coefficient increases

when the channel cross-sectional area decreases below the critical value (*0.089 mm*^{2}). They attributed this to a confinement effect and the evaoparation of the thin liquid film evoparation. They concluded that the cross-sectional area is the determining geometric parameter that affects flow boiling heat transfer coefficient in microchannels.

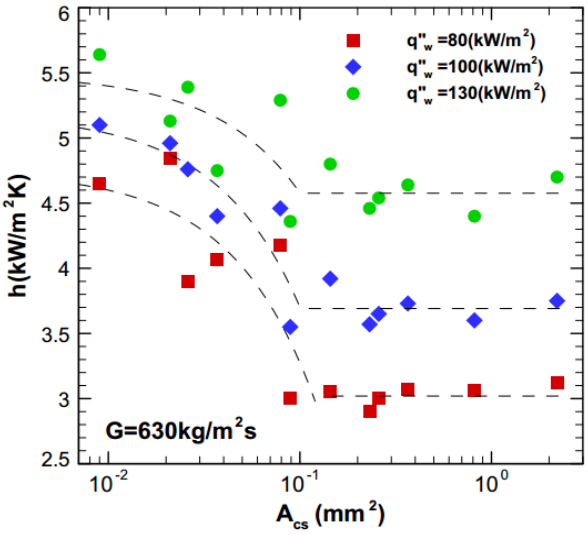

Figure 2.35 Effect of microchannel cross-sectional area on the average heat transfer coefficient at 630 kg/m^{2}s mass flux, Harirchian and Garimella (2009b).

In conclusion, most of the authors reported that the heat transfer coefficient increases as the channel hydraulic diameter decreases in micro-scale. A few researchers concluded that the effect of diameter on the heat transfer coefficient is insignificant. Some past studies on the effect of channel diameter on the flow boiling heat transfer coefficient in microchannels are listed in Table 2.3.

Table 2.3 Effect of hydraulic diameter on the heat transfer coefficient in the literature

Author	Fluid	Material, Geometry	Diameter	Remark(s)
Tran et al. (1996)	R-12	Brass, circular-rectangular	D_h = 2.4 mm	Effect of channel cross section on h_{tp} was not significant.
Kew and Cornwell (1997)	R-141b	Stainless steel, circular	D = 1.39, 2.87 and 3.69 mm	D effect on h_{tp} was not clearly stated.
Lin et al. (2001a)	R-141b	Copper, circular-rectangular	D = 1.1, 1.8, 2.8 and 3.6 mm D_h = 2 mm	As D decreased h_{tp} did not change significantly.
Saitoh et al. (2005)	R-134a	Stainless steel,circular	D = 0.51, 1.12 and 3.1 mm	As D decreased h_{tp} increased.
Hetsroni et al. (2005)	Water, Ethanol	Silicon, triangular	D_h = 0.1 - 0.22 mm	h_{tp} increased as D_h increased.
Martin-Callizo et al. (2007b)	R-134a	Stainless steel, circular	D = 0.83, 1.22 and 1.70 mm	As D decreased h_{tp} increased.
Karayiannis et al. (2008)	R-134a	Stainless steel, circular	D = 0.52, 1.1, 2.01, 2.88 and 4.26 mm	As D decreased from 2.88 mm to smaller, h_{tp} increased.

Table 2.3 Continued.

Consolini and Thome (2009)	R-134a, R-236fa, R-245fa	Stainless steel, circular	D = 0.51 and 0.79 mm	As D decreased h_{tp} increased.
Harirchian and Garimella (2009b)	FC-77	Silicon, rectangular	D_h = 0.096 - 0.75 mm	Cross-sectional area of the microchannel has substantial role on h_{tp}. h_{tp} was not depend on size in microchannels having 0.089 mm^2 and higher.
Basu et al. (2011)	R-134a	Stainless steel, circular	D = 0.5, 0.96 and 1.60 mm	As D decreased h_{tp} did not change significantly.
Liu et al. (2011)	Water	Brass, rectangular	D_h = 0.29 and 1.2 mm	As D_h decreased h_{tp} increased.
Mirmanto (2012)	Water	Copper, rectangular	D_h = 0.44, 0.56 and 0.64 mm	h_{tp} increased as D_h decreased at low vapour qualities. At high vapour qualities effect of D_h on h_{tp} was unclear.
Wang and Sefiane (2012)	FC-72	Borosilicate glass, rectangular	D_h = 0.57, 076 and 1.45 mm	As D_h decreased h_{tp} increased.

The effect of aspect ratio on the flow boiling heat transfer coefficient in microchannels was also investigated by some researchers. However, only two studies in the literature examined the channel aspect ratio effect on the heat transfer coefficient. Soupremanien et al. (2011) tested two aluminium test sections with single channel of same hydraulic diameters and lengths (D_h = *1.4 mm* and L = *83 mm*) but different aspect ratios (*6.99* and *2.32*) using Forane-365HX fluid. They reported that, the channel having *6.99* aspect ratio exhibited higher heat transfer coefficient than the other channel at low heat flux values. On the other hand, the heat transfer coefficient was higher for the *2.32* aspect ratio channel at high heat flux values. The authors attributed this to earlier dryout occurence in the channel having higher aspect ratio. However, they did not present any comparison figure. Moreover, they only tested two microchannels. Therefore it is hard to draw any conclusions based on their results. In a recent study, Markal et al. (2016) investigated the flow boiling characteristics of de-ionised water in six parallel rectangular silicon microchannels. The hydraulic diameters and the lengths of the channels were same (D_h = *100 μm* and L = *48 mm*) whilst the aspect ratio of the channels were varied from *0.37* to *5*. They reported that the heat transfer coefficient increased as the aspect ratio increased up to a value of *3.54*. On the other hand when the aspect ratio increased from *3.54* to *5*, the heat transfer coefficient decreased, see Figure 2.36. However, it is confusing that the authors presented the heat transfer coefficient variation for different local vapour quality intervals for different aspect ratio channels.

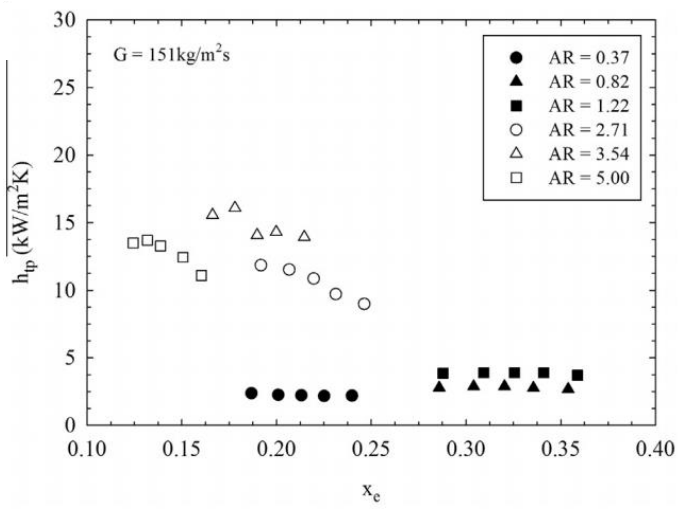

Figure 2.36 Heat transfer coefficient against local vapour quality at 151 kg/m^{2}s mass flux for the channels having different aspect ratio, Markal et al. (2016).

2.4.4 Heat transfer correlations

This section gives a review on the correlations that were developed to predict flow boiling heat transfer coefficients in micro-scale. Some conventional-scale correlations are also included since they were used to predict the heat transfer coefficient in the micro-scale studies. The applicability range and the equations of these correlations are given in appendix A. In this section, principles of each correlation are presented briefly.

2.4.4.1 Macroscale correlations

Generally speaking, flow boiling heat transfer mechanisms consist of convective and nucleate boiling components. Therefore, heat transfer correlations were developed considering these two components. Shah (1982) compared the nucleate boiling and convective boiling components of the flow boiling heat transfer coefficient in his correlation based on 780 data points. He reported that the larger one can be considered as a flow boiling heat transfer coefficient. The convective boiling term was defined the function of the Convection number (N_{CO}). The nucleate boiling term was described using the boiling number (*Bo*). Alternatively, Gungor and Winterton (1987) developed a heat transfer correlation for horizontal and vertical tubes for both subcooled and saturated flow boiling regions based on *4300* data points from water and different refrigerants. They added convective and nucleate boiling component separately different than the correlation of Shah (1982). Each component was also modified with enhancement factors *S* and *F*. The nucleate boiling term was estimated using the Cooper pool boiling correlation. The convective boiling term was described using the Boiling number (*Bo*) and the liquid Froude number (Fr_L). The correlation was tested and predicted the experimental data with a *21.4 %* deviation for saturated boiling region and *25 %* deviation for the subcooled boiling region. Kandlikar (1990) used the same method as Shah (1982) to develop a flow boiling heat transfer correlation for horizontal and vertical tubes. Kandlikar separated the regions as convective boiling dominant region and nucleate boiling dominant region. Afterwards, he considered the larger one as a total heat transfer coefficient similar to Shah (1982). The convective boiling term was defined as a function of the Convection number (N_{CO}). Nucleate boiling term was identified using the boiling number (*Bo*). Additionally, he introduced a fluid-surface parameter (F_{fl}) in the nucleate boiling term in order to account for the effect of fluid

type. However, this parameter equals to unity for water. Liu and Winterton (1991) developed a flow boiling heat transfer correlation based on *4202* data points for saturated boiling region and *991* data points for subcooled boiling region. Similar to Gungor and Winterton (1987) they added the nucleate boiling and convective boiling components. Each component was also modified with respective enhancement factors *S* and *F*. They used the power law model $n = 2$ to combine the convective and nucleate boiling components.

2.4.4.2 Microscale correlations

Accordingly, several correlations were developed to predict the flow boiling heat transfer coefficient at the microscale. The first attempt was made by Lazarek and Black (1982) for saturated flow boiling of R-113 in a *3.1 mm* diameter stainless steel tube. Nucleate boiling was taken into consideration as a dominant mechanism. The boiling heat transfer coefficient was assumed as a function of liquid Re number (Re_L) and Boiling number (*Bo*). The correlation predicted the experimental data with *15 %* error. Yu et al. (2002) analysed flow boiling heat transfer in a horizontal tube of *2.98 mm* diameter. They proposed that the heat transfer coefficient is dependent on the heat flux rather than mass flux. Therefore, they developed a correlation based on the assumption that nucleate boiling is the prevailing heat transfer mechanism similar to Lazarek and Black (1982). However, they correlated the flow boiling heat transfer coefficient as a function of liquid Weber number (We_L) and Boiling number (*Bo*). Their correlation predicted well their experimental data (within *2%* error). Kandlikar and Balasubramanian (2004) modified the original Kandlikar (1990) correlation in order to use in the micro-scale. They did not account the liquid Froude number (Fr_L) in the new correlation since the channel orientation is insignificant in microchannels. The new correlation also included very low Reynolds number range ($Re < 100$). Lee and Mudawar (2005a) conducted experiments to explore the heat transfer characteristics of R-134a in a microchannel heat sink with a *0.213 mm* width and *0.713 mm* height. They proposed a flow boiling heat transfer coefficient correlation based on *207* water data points and *111* R-134a data points. Their correlation was a function of the Martinelli parameter (*X*), Boiling number (*Bo*) and liquid Weber number (We_L) to consider different fluids effect. Moreover, their correlation is divided into three different quality regions; i) $x_e < 0.05$, ii) $0.05 < x_e < 0.55$ and iii) $x_e > 0.55$. The first region ($x_e < 0.05$)

was assumed to be nucleate boiling dominant region whilst the other two regions ($0.05 < x_e$) were believed to be dominated by the convective boiling by the authors. However, the authors did not include the heat flux effect in the first region ($x_e < 0.05$) although they stated that the prevailing heat transfer mechanism is nucleate boiling for this region.

In another study, Sun and Mishima (2009) made modifications to the correlation of Lazarek and Black (1982) based on the *2505* data points gathered from eleven different fluids including water. They introduced the liquid Weber number (We_L) into the Lazarek and Black (1982) correlation using the regression approach. Li and Wu (2010a) gathered the flow boiling heat transfer data available in the literature. Their data included 3744 data points, different working fluids including water for hydraulic diameter range from *0.16 mm* to *3.1 mm*. They introduced the Bond number (*Bd*) into their correlation in order to consider the surface tension effect. Consequently they correlated the data as a function of Boiling number (*Bo*), Bond number (*Bd*) and liquid Reynolds number (Re_L). The correlation reasonably predicted the experimental data (*26.13 %* error). Mahmoud and Karayiannis (2011) produced two correlations for two quality regions ($x \leq 0.3$ and $0.3 < x$) based on *5152* data points of R-134a. They correlated the flow boiling heat transfer coefficient using the boiling number (*Bo*), the liquid Weber number (We_L), the liquid Reynolds number (Re_L) and the confinement number (*Co*). They stated that the boiling number (*Bo*) considered the effect of heat flux and mass flux, the liquid Weber number (We_L) considered the inertia and surface tension effects, the liquid Reynolds number (Re_L) considered the inertia and viscous forces and the confinement number (*Co*) took into accounts of effect of the tube diameter in their correlation. Moreover, they reported that the correlation was able to predict their experimental data with an error of *14.3 %* whilst the *92 %* of the data could be predicted within the $\pm$ *30 %* error bands. In a recent study Lim et al. (2015) proposed a flow boiling heat transfer correlation for water data based on their experimental study. They modified the liquid Froude number (Fr_L) to produce a new non-dimensional number called as modified Froude number (C_{FR}). This new number was developed based on the flow pattern whether it is annular flow or non-annular flow. Consequently, they correlated the flow boiling heat transfer coefficient as a function of the Boiling number (*Bo*), Reynolds number (*Re*) and modified Froude number (C_{FR}) using least square method.

2.4.5 Flow boiling pressure drop

Previous studies on flow boiling pressure drop characteristics in microchannels are presented in this section. The effect of heat flux, mass flux, system pressure and geometrical parameters such as diameter and aspect ratio on the flow boiling pressure drop are assessed. Generally speaking, flow boiling pressure drop was found to increase with decreasing channel diameter and increasing heat flux and mass flux in the literature. Warrier et al. (2002) conducted flow boiling experiments in parallel rectangular alumunium microchannels with *0.75 mm* hydraulic diameter using FC-84 as the working fluid. They found that, the pressure drop decreased slightly from single-phase region to onset of nucleate boiling point. When the boiling commenced, the pressure drop started to increase linearly with applied heat flux. Lee and Mudawar (2005b) measured pressure drop in a copper rectangular parallel microchannel heat sink with R-134a as the working fluid. The hydraulic diameter of the channels were *0.35 mm*. It was found that, the pressure drop increased with heat flux and mass flux, see Fig. 2.37. However, increasing heat flux at constant mass flux resulted in an increase in the pressure drop up to a certain value. Beyond this heat flux inputs, pressure drop became constant or slightly decreased. Lee and Mudawar (2005b) attributed this trend to the fact that increasing heat flux beyond a certain value causes the occurence of complete vapour downstream of the channel that decreases the two-phase frictional pressure drop component.

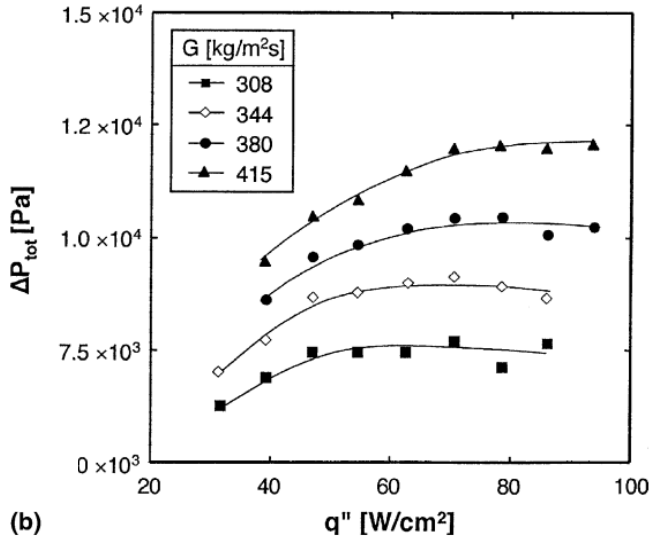

Figure 2.37 Variation of the measure pressure drop of R-134a with heat flux for different mass fluxes in copper rectangular microchannels, Lee and Mudwar (2005b).

In another study, Lee and Garimella (2008) examined flow boiling pressure drop characteristics of de-ionised water in a silicon parallel microchannel arrays. They tested four different microchannels having *0.16, 0.29, 0.4* and *0.54 mm* hydraulic diameters. Similar to other researchers, they reported that the pressure drop increases with increasing heat flux and mass flux. Similar to above studies, other past experimental studies in the literature agreed that the flow boiling pressure drop increased with increasing heat flux and mass flux in microchannels, see Tong et al. (1997), Tran et al. (2000), Sobierska et al. (2006), Yun et al. (2006), Karayiannis et al. (2008), Singh et al. (2008), Mahmoud (2011), Mirmanto (2012) and Markal et al. (2016).

The effect of system pressure on the flow boiling pressure drop was also investigated in the literature. Tran et al. (2000) investigated the flow boiling pressure drop in two circular channels of *2.46* and *2.92 mm* diameters and one rectangular microchannel having *2.4 mm* hydraulic diameter using R-134a, R-113 and R-12. They reported that the flow boiling pressure drop increased with decreasing sytem pressure for all tests. Huo et al. (2007) and Karayiannis et al. (2008) examined the flow boiling pressure drop using five circular channels using R-134a as the working fluid. The diameter range of the tubes were from *0.52 mm* to *4.26 mm*. They stated that decreasing system pressure resulted in an increase in the flow boiling pressure drop in the tested channels. The authors attributed this to the reduction in liquid to vapour density ratio as the pressure increases. Similarly, Mahmoud (2011) tested two microtubes having diameters *0.52 mm* and *1.1 mm* at the mass flux of *400 kg/m^{2}s* and *6,8* and *10 bar* system pressure using R-134a. The author reported that the flow boiling pressure drop increases with decreasing system pressure. The above literature review showed that the flow boiling pressure drop increases with decreasing system pressure in microchannels.

The effect of geometrical parameters on the flow boiling pressure drop was examined by many researchers in the literature. Tong et al. (1997) carried out experiments with stainless steel tubes having diameters ranging from *1.05* to *2.44 mm*. They found that the flow boiling pressure drop increases as the tube diameter decreases. Tong et al. (1997) attributed this to the fact that the thinning of a boundary layer with the decrease in the diameter at a given mass flux results in higher shear stress leading to higher

pressure drop. In another study, Shuai et al. (2003) investigated the flow boiling pressure drop of water in two rectangular microchannels having hydraulic diameters of *0.8 mm* and *2.67 mm*. They reported that the flow boiling pressure drop in the smaller channel was much higher than the larger channel. Mahmoud (2011) compared the flow boiling pressure drop of two stainless steel tubes (*D = 0.52* and *1.1 mm*) at *6 bar* system pressure and *400 kg/m^{2}s* mass flux using R-134a as shown in Fig. 2.38. It was found that when the diameter decreased from *1.1 mm* to *0.52 mm* the pressure drop per unit length increased around *300 %*. The author attributed this to the high velocity gradient in the boundary layer next to the wall arising from the thinning of the liquid film when the diameter decreased. Consequently, the frictional pressure drop increased due to the large velocity gradient.

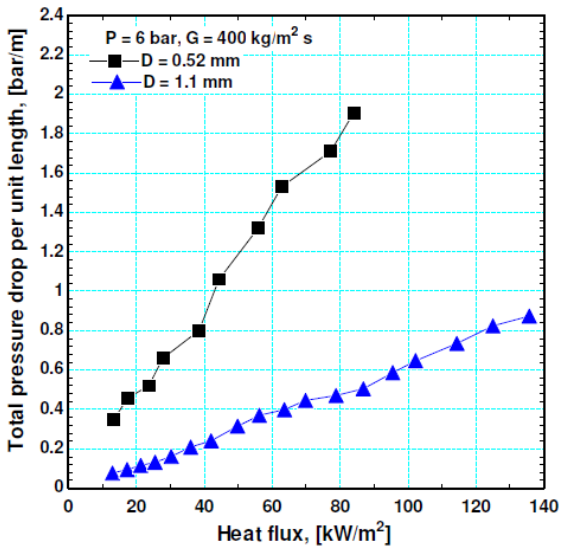

Figure 2.38 The effect of tube diameter on the flow boiling pressure drop at G = 400 kg/m^{2}s and P = 6 bar, Mahmoud (2011).

Mirmanto (2012) also presented the hydraulic diameter effect on the flow boiling pressure drop in copper rectangular single microchannel with *0.44, 0.56* and *0.64 mm* hydraulic diameter. Similar to above researchers he reported that, flow boiling pressure drop increases with decreasing channel diameter. In another study, Harirchian and Garimella (2009b) conducted experiments to examine the channel size effect on the flow boiling pressure drop of FC-77 in parallel rectangular microchannels, see Fig. 2.39. They reported that the flow boiling pressure drop increases with decreasing

channel cross-sectional area at a given wall heat flux input. Moreover they reported that the channels with similar cross-sectional areas and different aspect ratios exhibited similar flow boiling pressure drops in value.

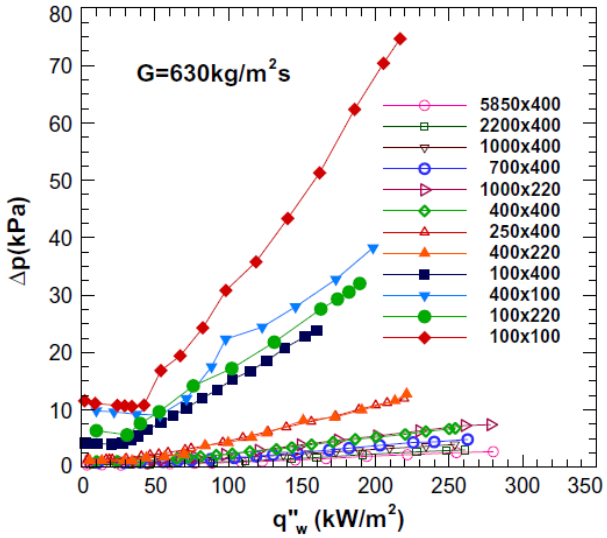

Figure 2.39 Effect of microchannel cross-sectional area on the pressure drop for FC-77 at G = 630 kg/m^{2}s, Harirchian and Garimella (2009b).

The channel aspect ratio effect on the flow boiling pressure drop was examined by Singh et al. (2008). Singh et al. (2008) tested silicon rectangular microchannels with varying aspect ratios (*1.23-3.75*) but constant hydraulic diameters (*142 μm*) and lengths (*20 mm*). They reported that, the flow boiling pressure drop first decreases with an increase in aspect ratio from *1.23* to *1.56*, and then increases with a further increase in aspect ratio at particular heat flux and mass flux input. Contrary to Singh et al. (2008), Soupremanien et al. (2011) stated that the flow boiling pressure drop is higher for the lower aspect ratio channel with increasing heat flux. They investigated the effect of the channel aspect ratio on the flow boiling pressure drop of Foreane-365HX using two aluminium microchannels having same hydraulic diameters and lengths (D_h = *1.4 mm* and *L = 83 mm*) but different aspect ratios (*6.99* and *2.32*). The authors attributed this to the fact that the confinement of the bubbles is higher for the channel having lower aspect ratio leading to a higher pressure drop. This is due to the fact that the lower aspect ratio channel had smaller channel width than the other one so that the confinement is higher for the lower aspect ratio channel. In a recent study, Markal et al.

(2016) also performed sets of experiments to examine the effect of channel aspect ratio on the flow boiling pressure drop of de-ionised water in six rectangular multi-microchannels. The hydraulic diameters and the lengths of the channels were same (D_h *= 100 μm* and *L = 48 mm*) but the channel aspect ratios were different (*0.37-5*). Markal et al. (2016) reported that there is no regular relationship between the pressure drop and the channel aspect ratio as presented in Fig. 2.40. They attributed this behaviour to the complex nature of flow physics. However, they did not present any explanation based on these results.

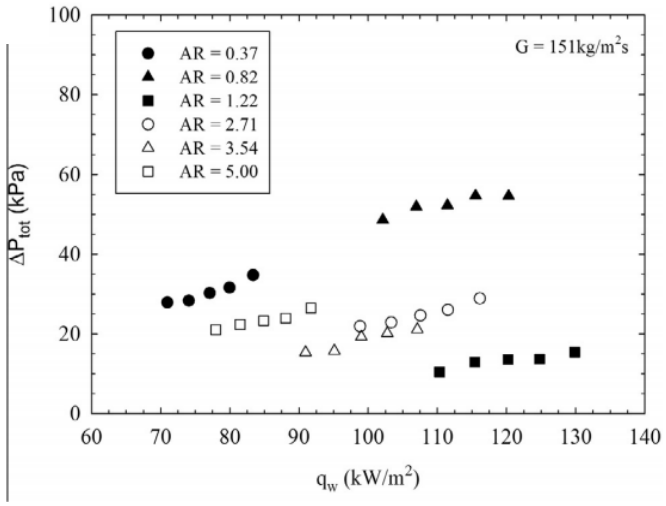

Figure 2.40 Effect of the channel aspect ratio on the pressure drop with increasing wall heat flux at G = 151 kg/m^{2}s, Markal et al. (2016).

The presented literature review shows that the flow boiling pressure drop in microchannels increases with increasing heat flux, increasing mass flux, decreasing system pressure and decreasing channel diameter. On the other hand, effect of the channel aspect ratio on the flow boiling pressure drop is inconclusive. It was found that effect of the channel aspect ratio on the flow boiling pressure drop was investigated in only three studies. In one study, it was reported that the flow boiling pressure drop increases as the channel aspect ratio increases, see Singh et al. (2008). In another study, the researchers found that the flow boiling pressure drop was higher in the lower aspect ratio channel, Soupremanien et al. (2011). Moreover, in a recent study, it was found that there is no any regular relationship between the effect of the channel aspect ratio and the flow boiling pressure drop, Markal et al. (2016).

2.4.6 Flow boiling pressure drop correlations

Two-phase pressure drop correlations are important in order to design reliable and high performance microchannel heat sinks. In horizontal channels, total two-phase pressure drop is the sum of frictional and accelerational pressure drop components. On the other hand, the gravitational pressure drop compoonent needs to be added in vertical channels. In literature, several correlations were proposed to predict the total two-phase pressure drop. In this section, principles of each correlation that were used to compare the experimental data are presented. The applicability range and the details of these correlations are given in appendix B.

The homogenous flow model (HFM) and seperated flow model (SFM) are the two fundamental approaches that were proposed to model the two-phase pressure drop. The details of these approaches can be found in Collier and Thome (1994). The homogenous flow model was proposed for horizontal flow in channels based on steam-water mixture for various system pressures. The two-phase fluid was assumed to be a single-phase fluid with its mixture properties weighted by vapour quality. On the other hand, the fluid was seperated into liquid and vapour phases in the seperated flow model. The equations of frictional and accelerational two-phase pressure drop components are presented in Eq. (1.8 – 1.11) for both models.

Frictional Pressure Drop

$$\Delta P_f = \frac{2 f_L L G^2 \nu_L}{D_h}\left[1+\frac{x_e}{2}\left(\frac{\nu_{Lg}}{\nu_L}\right)\right] \qquad \text{(HFM)} \qquad (1.8)$$

$$\Delta P_f = \frac{L_{tp}}{x_e}\int_0^{x_e}\frac{2 f_L G^2 (1-x_e)^2 \nu_l}{D_h}\phi_L^2 dx \qquad \text{(SFM)} \qquad (1.9)$$

Accelerational Pressure Drop

$$\Delta P_a = G^2 \nu_{Lg} x_e \qquad \text{(HFM)} \qquad (1.10)$$

$$\Delta P_a = G^2 \nu_L\left[\frac{x_e^2}{\alpha_e}\left(\frac{\nu_g}{\nu_L}\right)+\frac{(1-x_e)^2}{1-\alpha_e}-1\right] \qquad \text{(SFM)} \qquad (1.11)$$

From Eqs. (1.8) and (1.10), it can be deduced that the total two-phase pressure drop can be calculated straightforwardly using the HFM. On the other hand, void fraction (α) and two-phase multiplier (ϕ^2_L) are needed to calculated in the SFM. Consequently, several correlations were proposed to predict the void fraction and the two-phase multiplier in the literature. The principle of the two-phase multiplier was first proposed by Lockhart and Martinelli (1949). Lockhart and Martinelli (1949) defined the two-phase multiplier as a function of the Martinelli parameter (X) for different flow phases (laminar/turbulent) as given in Eq. (1.12).

$$\phi_L^2 = 1 + \frac{C}{X} + \frac{1}{X^2} \tag{1.12}$$

The constant (C) is called as Chisholm constant and takes a value ranging from *5* to *20* dependent on the phase of the flow, see Chisholm (1967).

In this way, many researchers attempted to use the HFM and SFM approaches to predict the total two-phase pressure drop in microchannels. Some researchers found that these models predicted their data poorly, see Tran et al. (2000), Zhang and Webb (2001), Kawahara et al. (2002), Qu and Mudawar (2003b), Wen et al. (2004) and Karayiannis et al. (2008). Ribatski (2013) stated that, the reason for the poor prediction of the conventional models might be: i) the liquid part of the flow is laminar in two-phase microchannel flows, which is different than for conventional scale channels and ii) the surface tension effect is more significant in microchannels than conventional scale channels. Also, Ribatski et al. (2006) also reported that, bubbly flow was rarely encountered in microchannels due to the confinement of the channel where the bubbles coalesce or grow and occupy the entire channel size. Contrary to the above, some other researchers reported that, the HFM predicted their experimental data well, see Lee and Mudawar (2005b), Qi et al. (2007) and Agostini et al. (2008b). Mahmoud (2011) stated that, the HFM showed success in some studies and failure some others might be attributed to different fluid tested in these studies. Mahmoud (2011) added that fluid properties have an influence on the boundaries of the isolated bubbly and slug flow regimes where the HFM works better. Consequently, many researchers such as Mishima

and Hibiki (1996), Yu et al. (2002), Warrier et al. (2002) Qu and Mudawar (2003b) and Zhang et al. (2010) developed new two-phase pressure drop correlations for micro-scale. In these correlations, the two-phase multiplier (ϕ^2_L) in Eq. (1.12) were modified in order to take account the microscale effects. For example Mishima and Hibiki (1996) defined the Chilshom's constant (C) is a function of hydraulic diameter as given in Eq. (1.13). On the other hand, Yu et al. (2002) used a two-phase multiplier (ϕ^2_L) as only function of the Martinelli parameter, see Eq. (1.14).

$$C = 21(1 - e^{0.319 D_h}) \tag{1.13}$$

$$\phi_L^2 = \frac{1}{X^{1.9}} \tag{1.14}$$

The details of the each correlation are presented and discussed in Chapter 6 and the equations and the applicability range of the correlations are given in appendix B.

2.4.7 Flow boiling instabilities

Flow boiling instability is one of the important issues in microchannel heat exchangers. Flow instabilities affect the system performance and may cause system failures. For example, it reduces the critical heat flux (CHF) value in microchannels and may cause premature dry-out. Therefore identifying the operating conditions of stable flow boiling is very important for the reliable design of micro heat exchangers. In general, two-phase flow instabilities are divided into two sub-categories. Static instabilities consist of flow pattern transition instability and Ledinegg instability. Pressure and thermal oscillations as well as parallel channel instability are defined as dynamic instabilities in the literature, see Boure et al. (1973), Bergles (1977) and Ruspini et al. (2014). The Ledinegg instability (flow excursion) was defined as; when the system changes from unstable flow to stable flow in the pressure drop versus mass flux curve, the flow excursion to the system occurs.

Flow boiling instabilities in microchannels are much more common and have greater effect on the overall system performance than conventional scale ones owing to their

low flow velocity operation and occurrence in confined space. The most encountered instabilities in microchannels are Ledinegg instability, flow pattern transition instability (considered as abrupt transition from bubbly flow to slug or annular flow, Ruspini et al. (2014)), non-uniform flow distribution among the channels (mal-distribution of the flow) and pressure, mass flux and thermal oscillations. Moreover, the rapid bubble growth instability is unique in micro-scale where the bubbles grow explosively in the channel and travel both to upstream and downstream of the test section. Consequently, many researchers examined the flow boiling instabilities in microchannels.

Brutin et al. (2003) analysed the heat and mass transfer and two-phase flow instabilities in vertical aluminium rectangular microchannels of *0.889 mm* hydraulic diameter, aspect ratio of *8* and two different lengths i.e. *50 mm* and *200 mm*. N-pentane was used as the working fluid. Brutin et al. (2003) defined the stability criterion with flow pattern analysis and pressure drop oscillations at the upstream and downstream of the channel. For example at the mass flux *240 kg/m^{2}s* stable flow was reported from boiling incipience up to heat flux *200 kW/m^2* with insignificant inlet and outlet pressure drop oscillations (*0.5 kPa/m-5 kPa/m*). Unstable flow was observed between heat flux *380 kW/m^2-500 kW/m^2* with appreciable inlet and outlet pressure drop oscillations (*20 kPa/m-100 kPa/m*) and reverse vapour slug flow. However, they did not present inlet, outlet and wall temperature oscillations for both steady and unsteady flow modes. Wu and Cheng (2003) performed sets of experiments in parallel silicon microchannels with trapezoidal cross section. Water was used as the coolant and two different sized microchannel were tested (D_h *= 0.083* and *0.159 mm*) having *15* and *8* channels, respectively. They reported that at constant mass flux when the heat flux was increased gradually large fluid inlet and outlet pressure, temperature, wall temperature oscillations with large amplitudes was observed. Also, the mass flux decreased rapidly at the boiling incipience. Their visualisation study showed that at the middle of the channel single phase, bubbly, slug, elongated slug, churn flows appeared periodically at the boiling incipience. However, they reported neither measurement nor visualisation results after boiling incipience. The authors concluded that fluctuation periods at boiling incipience depend on channel dimensions, heat flux and mass flux.

In another study, Wu and Cheng (2004) tested a microchannel heat sink with same characteristics of their previous study above but having different hydraulic diameter

(*0.186 mm*). They increased the heat flux after boiling incipience and three flow boiling modes was identified; i) Liquid/two- phase alternating flow at low heat flux and high mass flux, ii) Stable two-phase flow at moderate heat flux and mass flux, iii) Liquid/two-phase/vapour alternating flow at high heat flux and mass flux. Large amplitude pressure and temperature oscillations and periodic reverse flow were reported at unstable boiling modes. The authors stated that unstable flow boiling strictly depends on the heat flux and mass flux. Steinke and Kandlikar (2004b) performed an experimental study on the flow boiling of water in copper multi-microchannels of *0.207 mm* hydraulic diameter, *1.08* aspect ratio and *57.15 mm* long. The mass flux ranged from *157* to *1782 kg/m^{2}s*, heat flux from *5* to *930 kW/m^2* and the inlet sub-cooling was *78 K*. Under some conditions, they observed parallel channel instability where bubbles moved towards to inlet of the channel due to rapid bubble growth in some channels whilst the flow was stable in other channels at the same time. Xu et al. (2005) tested *26* copper rectangular parallel microchannels (*W = 0.3 mm, H = 0.8 mm*) to analyse the onset of flow boiling instability in microchannels of methanol and water. The experimental conditions were in a range of *20 kg/m^{2}s-1200 kg/m^{2}s* mass flux, *100 W-450 W* heating power and *30°C, 50°C* and *70°C* inlet temperatures. They described two types of instabilities accompanied with thermal oscillations; i) large amplitude/long period oscillation occurred at low inlet fluid temperatures with expanded vapour slug flow towards to inlet and outlet plenum of the heat sink, ii) small amplitude/short period oscillation was present in the system with stable fluid temperatures but out of phase pressure drop. However, Xu et al. (2005) stated that the onset of flow boiling instability occurred when the outlet fluid temperature was *4-7 K* below the saturation temperature. Hetsroni et al. (2005) investigated the heat transfer coefficient and visualised flow patterns during explosive boiling of water in *21* silicon microchannel with triangular cross section (*Dh = 0.129 mm*) over a *95-340 kg/m^{2}s* mass flux and *80-330 kW/m^2* heat flux ranges. It is worth mentioning that they did not perform any degassing process during the experiments so that gas vapour mixture occurred below the saturation temperature. Their results showed that long vapour slugs occurred in a microchannel at low mass flux values with periodic wetting dryout. They described this behaviour as an explosive boiling phenomenon.

Upstream compressibility and the Ledinegg instability were shown to be the reasons of the vapour slug back flow phenomenon in microchannels by Bergles and Kandlikar

(2005). Also, Gedupudi et al. (2009a, 2009b, 2009c) performed a numerical study and concluded that upstream compressibility in the system is responsible for the back flow due to improper degassing or boiling in preheaters that causes non-dissolved air in the system. Kandlikar (2006) discussed nucleation and flow instability in microchannels. He reported that the location of boiling incipience affects flow reversal. When nucleation occurs near the channel exit, the flow resistance in the back flow direction is higher and consequently no flow reversal occurs. On the contrary, when nucleation occurs near the channel inlet, the flow resistance in the backflow direction is lower and thus flow reversal occurs.

Wang et al. (2007) investigated experimentally flow boiling instabilities of water in silicon multi-microchannels and in a single channel at *35 °C* inlet temperature. Both test sections had an identical trapezoidal cross section with *186 μm* hydraulic diameter and *30 mm* length. They defined two modes of unstable boiling. The first mode is a long period oscillation (more than *1 s*) while the second is a short period oscillation (less than *0.1 s*). The unstable mode with long period oscillation occurred for $0.96\ kJ/kg < q''/G < 2.14\ kJ/kg$ in the multi-microchannels and for $0.09\ kJ/kg < q''/G < 0.32\ kJ/kg$ in the single microchannel. However, unstable flow boiling mode with short period oscillation occurred for $q''/G > 0.32\ kJ/kg$ and $q''/G > 2.14\ kJ/kg$ in the single and multi-microchannels, respectively. In the long period oscillation instability mode they indicated that the oscillation period of temperature in the single microchannel (*10 - 80 ms*) was much longer than that in the multi-microchannels (*2.5 - 9.8 ms*) at the same heat flux. Additionally, in the short period oscillation mode they observed that the vapour bubble expands periodically to the upstream side the test section with periodic oscillation in the inlet pressure. Chang and Pan (2007) investigated experimentally flow boiling instability of water in a silicon-based multi-microhannel heat sink having *0.0863 mm* hydraulic diameter, *1.3* aspect ratio and *42 mm* channel length. They presented flow patterns captured along the centerline of the heat sink near the inlet, near the middle and near the outlet at mass flux $22\ kg/m^2s$ at different heat flux. Instability due to boiling incipience was not observed. At the lowest heat flux and near the channel inlet, small nucleating bubbles were observed in some of the channels while near the channel exit the flow pattern varied between slug and annular flow. However, when the heat flux was increased to $15.8\ kW/m^2$, unstable flow was observed. In this case the flow was alternating between slug and annular flow with back and forth motion and large

amplitude pressure drop oscillation. The pressure drop oscillation corresponding to the stable case was less than *6 kPa* while it was greater than *6 kPa* for the unstable case. Bogojevic et al. (2009) carried out an experimental study with water to investigate flow boiling instabilities in silicone based multi-microchannels with *0.194 mm* hydraulic diameter, aspect ratio of *0.55* and *15 mm* length. Two inlet sub-cooling degrees were tested (*29 K and 75 K*) over mass flux range *41.7-433.3 kg/m^{2}s* and the heat flux range *178-445 kW/m^2*. The stability/instability criterion was chosen as the oscillation in the measured pressure and temperature. They reported two kinds of instability namely high amplitude low frequency (HALF) with a frequency range *0.9-2.88 Hz* and low amplitude high frequency (LAHF) with a frequency range *23-25 Hz*. Their results demonstrated that flow instability depends on the ratio of heat to mass flux ($q^{"}/G$) and the inlet subcooling degree. For the high inlet sub-cooling test (*75 K*), stable flow occurred for $q^{"}/G < 2.62$ *kJ/kg* while for the lowest inlet sub-cooling test (*29 K*) stable flow occurred for $q^{"}/G < 0.99$ *kJ/kg*. In another study Bogojevic et al. (2011) examined the non-uniform heating effect on flow boiling instabilities in a same microchannel heat sink as in their previous study using de-ionised water. They divided the microchannel heat sink into three regions axially to create local hotspots with non-uniform heat input. At low heat fluxes, HALF pressure and temperature signals were recorded whilst LAHF temperature and pressure signals were detected at high heat fluxes. In another study, Balasubramanian et al. (2013) conducted flow boiling experiments in parallel copper microchannels having two different planform areas of *25 mm x 25 mm* and *20 mm x 10 mm*. The channels had *0.3 mm* width and *0.12 mm* height and the working fluid was de-ionised water. They observed pressure drop fluctuations and wall temperature oscillations when instabilities occurred. They also reported the reversal vapour slug flow instability when the heat flux was increased at low mass flux values. However, instabilities decreased at higher mass flux values.

Following the above literature review on flow boiling instabilities in microchannels it is worth mentioning the studies that tried to suppress instabilities in micro-scale. Qu and Mudawar (2004) investigated flow boiling of de-ionised water in *21* parallel rectangular copper microchannels having *0.231 mm* width and *0.712 mm* depth. After boiling was initiated, the flow pattern in the microchannels became rapidly intermittent flow with increasing heat flux. Flow reversal between the inlet and outlet of the channel with significant pressure and temperature fluctuations were observed by the authors.

However, they managed to mitigate the pressure drop oscillation instability by installing a control valve at the upstream of the test section. Kandlikar et al. (2006) proposed that the wall superheat at the nucleation location should be as low as possible in order to stabilize the two-phase flow instabilities. This is probably because that the wall superheats at the boiling incipience is higher in microchannels compared to conventional scale channels as presented in boiling incipience section on page 40. Therefore, Kandlikar et al. (2006) introduced artificial nucleation cavities and inlet control valves at the upstream of the parallel microchannel test section. They reported that the two-phase flow instabilities and flow reversal was prevented in their experiments. Kosar et al. (2006) performed an experiment with *5* parallel rectangular silicon microchannels of *0.2 mm* width and *0.264 mm* depth with inlet restrictors. They stated that small orifices at the channels inlet can prevent pressure and parallel channel instabilities in microchannels. Kuan and Kandlilar (2007) installed flow restrictors at the inlet of the each channel that were *1.054 mm* wide and *0.197 mm* depth consist of *6* parallel copper rectangular microchannels. They compared the results with and without the flow restrictor and reported that microchannels having flow restrictors at the inlet yielded *6.1 %* better heat transfer performance than the normal ones due avoiding reverse flow. Similarly, Kuo and Peles (2008) reported that the presence of re-entrant cavities into the microchannel heat sink helped in reducing the pressure drop oscillations, parallel channel instability and flow reversal problem by creating nucleation sites and also extended CHF. Wang et al. (2008) performed experiments with three different inlet and outlet configurations. The first configuration had both inlet and outlet restrictors at the test section, the second configuration did not have any restrictions and the third configurations had only restrictions at the inlet of each microchannel as shown in Fig. 2.41. They observed that flow became stable and flow reversal was reduced in the third configuration whilst temperature and pressure fluctuations with reverse flow existed in the first and second configurations. The possible explanation of this might be that the inlet and outlet restrictors at the first test section are due to the inlet and outlet flow manifold. These restrictors are quite different than the restrictors at the third test section. Therefore, the stable flow conditions were not encountered in the first test section.

Another approach in order to suppress the flow boiling instabilities was proposed by Thome and Dupont (2007), Xu et al. (2009) and Liu et al. (2010). They introduced seed bubble generation on microheaters which were located at the microchannel upstream and driven by a pulse voltage signal. They reported that seed bubbles grew further by soaking up energy from superheated liquids and prevented thermal and pressure oscillations and in turn improved flow and heat transfer performance in microchannels.

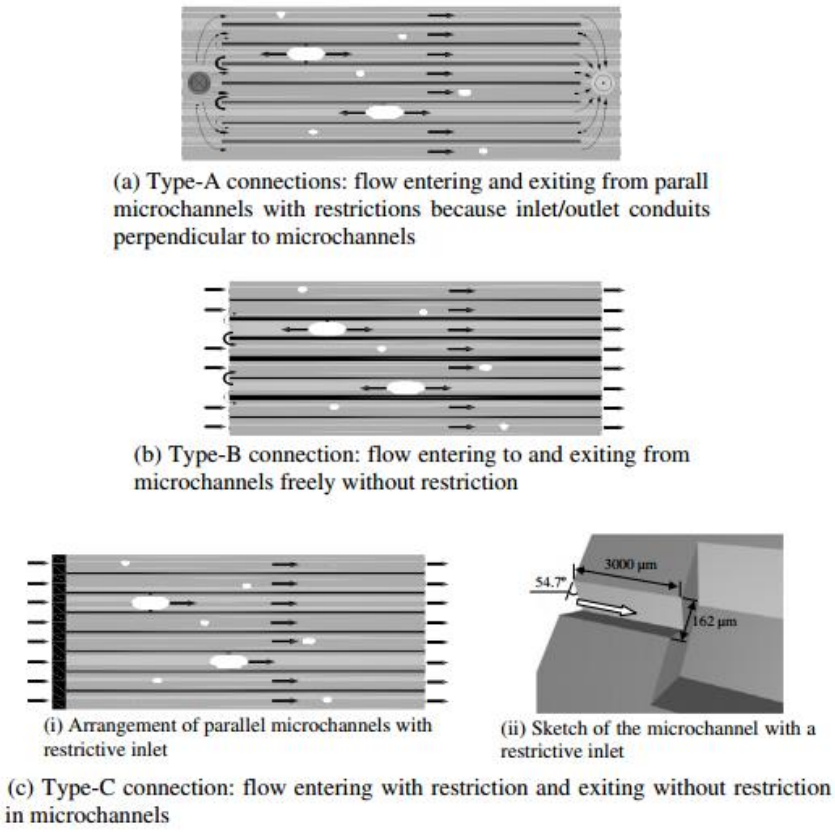

(a) Type-A connections: flow entering and exiting from parall microchannels with restrictions because inlet/outlet conduits perpendicular to microchannels

(b) Type-B connection: flow entering to and exiting from microchannels freely without restriction

(i) Arrangement of parallel microchannels with restrictive inlet

(ii) Sketch of the microchannel with a restrictive inlet

(c) Type-C connection: flow entering with restriction and exiting without restriction in microchannels

Figure 2.41 Parallel microchannels with three different inlet/outlet connections, Wang et al. (2008).

In another study Kuo and Peles (2009) experimentally studied effects of pressure on flow boiling instabilities using water in silicon microchannels of *0.2 mm* width and *0.25 mm* depth. The mass flux range was *86-520 kg/m^{2}s* and the pressure range was *50-205 kPa*. They found that high system pressure reduced pressure fluctuations. In addition, it reduced the bubble departure diameter and also extended CHF. Zhang et al. (2009) studied the Ledinegg instability in microchannels. They proposed that less channels, high system pressure, low heat flux, low subcooling and short channels should be

preferred in order to avoid instability problems to obtain better heat transfer performance in microchannels. In a recent study, Tuo and Hrnjak (2013) recommended a new vapour venting method to suppress flow reversal problem. They installed two venting valves at the inlet plenum to vent the back vapour slug flow. They reported that the cooling capacity was increased *5 %* with this new method.

2.5 Summary and Conclusions

A detailed literature review on single-phase flow and flow boiling in microchannels is presented above. Single-phase pressure drop and heat transfer characteristics, two-phase flow patterns and flow maps, flow boiling heat transfer characteristics, two-phase flow pressure drop, prediction of boiling heat transfer and pressure drop and flow boiling instabilities are included in this review. Conclusions are given below.

Single-phase flow

In the literature, many studies were conducted to investigate single-phase friction factor and heat transfer characteristics in micro-scale. A lot of work was carried out to reveal the sources of the discrepancies between the conventional theory and the single-phase parameters. Although recent studies showed that conventional theory is valid in single-phase friction factor and heat transfer in microchannels, some points are needed to be considered while evaluating single-phase flow in micro-scale.

1. Inlet and exit pressure losses need to be considered, Pfund et al. (2000), Mahmoud (2011) and Mirmanto (2012).
2. Developing effects need to be evaluated in the entrance region, Harms et al. (1999), Gao et al. (2002), Steinke and Kandlikar (2006) and Mirmanto (2012).
3. The friction factor and *Nu* number strongly depend on channel surface characteristics, Kandlikar (2006), Shen et al. (2006) and Rosa et al. (2009).
4. Laminar to turbulent transition in microchannels may occur earlier than conventional channels due to size effect, Guo and Li (2003), Hsieh et al. (2004) and Liu et al. (2007).

5. Thermo-physical properties of the working fluids need to be considered due to viscous heating effects which can be very high at the microscales, Rosa et al. (2009).
6. Measurement uncertainties need to be evaluated properly in order to have accurate results, Pfund et al. (2000), Lee et al. (2005), Steinke and Kandlikar (2006), Rosa et al. (2009) and Mirmanto (2012).
7. Axial conduction has an effect on *Nu* number in low *Re* operations (*Re* < *500*), Maranzana et al. (2004) and Gamrat et al. (2005).

Flow patterns and maps

Literature studies on the flow patterns and flow maps in microchannels are presented above. The findings of the above review are summarized below.

1. Flow patterns in micro-scale are different than conventional channels. While some new flow patterns can arise in microchannels, some conventional flow patterns, such as stratified flow, may disappear in micro-scale due to size effect, Triplett et al. (1999), Coleman and Garimella (1999) and Qu et al. (2004). The reason of this is attributed to the dominant surface tension force in small scale.
2. There is no general definition for micro-scale flow patterns in literature due to different experimental conditions and observational area.
3. There is a discrepancy about whether adiabatic two-phase flow patterns are similar to the flow boiling flow patterns or not. Some adiabatic flow patterns, such as churn flow, may not exist during flow boiling, Shuai et al. (2003), Huh and Kim (2006) and Revellin and Thome (2007).
4. The observed flow patterns in multi-microchannels might be different in parallel channels during flow boiling, Megahed and Hassan (2009).
5. The flow boiling patterns changed from bubbly flow to slug flow, slug flow to churn flow, churn flow to annular flow in general when the heat flux was increased. On the other hand, the flow boiling patterns occurred at higher heat flux values as the increase in mass flux, Chen and Garimella (2006), Galvis and Culham (2012) and Mirmanto (2012).

6. Reverse flow was also observed by some researchers during flow boiling in microchannels, Galvis and Culham (2012), Balasubramanian et al. (2013) and Markal et al. (2016).
7. The effect of aspect ratio and hydraulic diameter on the flow patterns in microchannels is not clear. Some studies reported that the aspect ratio and hydraulic diameter has an effect on the flow patterns, Coleman and Garimella (1999), Xu et al. (1999), Choi et al. (2011), Soupremanien et al. (2011), Wang and Sefiane (2012) and Markal et al. (2016). However, some others researchers stated that there is no hydraulic diameter and aspect ratio effect on the flow patterns, Triplett et al. (1999) and Mirmanto (2012).
8. The conventional scale flow pattern models could not predict the flow patterns transition boundaries, Coleman and Garimella (1999), Zhao and Bi (2001), Chen (2006), Revellin and Thome (2007) and Ong and Thome (2009).
9. The transition boundaries of the dispersed bubbly/bubbly, intermittent/dispersed bubbly and intermittent/bubbly flow patterns shifts to higher liquid superficial velocities when the channel hydraulic diameter was decreased, Coleman and Garimella (1999) and Chen (2006).
10. The bubbly/slug, slug/churn and churn/annular flow patterns transition boundaries occurred in higher superficial gas velocities when the hydraulic diameter was decreased, Coleman and Garimella (1999), Chen (2006) and Harirchian and Garimella (2010). Contrarily, Xu et al. (1999) stated the opposite effect of diameter.
11. The churn/annular and slug/churn flow transition boundaries occurs at lower vapour velocities at higher system pressure operations. However, dispersed bubbly/bubbly flow transition boundaries were shifted to lower liquid velocities as the system pressure was increased. The effect of system pressure on the other flow pattern transition boundaries is insignificant, Chen (2006).

Flow boiling heat transfer characteristics

Flow boiling heat transfer characteristics in micro-scale based on the above detailed review are given below.

Boiling incipience

1. Boiling incipience can be detected by using $\Delta P - q''$, $q'' - \Delta T_{sub}$, $h - q''$ curves and flow visualisation. All methods were found to be consistent with each other, Wang et al. (2014).
2. The characteristics of boiling incipience in microchannels were found to be different than conventional scale channels. First bubbles nucleated and grew to the channel size before leaving the cavity in micro-scale contrary to macro-scale where the bubbles nucleate, grow and collapse locally before leaving the cavity, Qu and Mudawar (2002b).
3. The first nucleating bubbles nucleated on the microchannel sidewalls as well as the channel bottom wall, Qu and Mudawar (2002b) and Liu et al. (2005).
4. Some researchers reported that the boiling incipience heat flux for the microchannels higher compared to conventional scale channels, Inasaka et al. (1989), Kennedy et al. (2000), Ghiaasiaan and Chedester (2002), Qu and Mudawar (2002b) and Wang et al. (2014). Ghiaasiaan and Chedester (2002) attributed this to the large effect of thermo-capillary force compared to the inertia force.
5. The boiling incipience heat flux increased with increasing inlet fluid velocity, inlet subcooling and mass flux. On the other hand, system pressure had no influence on the boiling incipience heat flux, Liu et al. (2005) and Wang et al. (2014).

Effect of heat flux and mass flux

The literature review indicates that the dominant heat transfer mechanism(s) and the effect of heat and mass flux on the flow boiling heat transfer coefficient in microchannels is not clear. There is a disagreement on the dominant heat transfer mechanism(s) in microchannels as shown in table 2.2, on pages 51 and 52. A group of researchers reported that nucleate boiling is the dominant heat transfer mechanism. On the other hand, some researchers concluded that convective boiling or convective/nucleate boiling mechanism(s) are the dominant heat transfer mechanism(s) in microchannels.

Effect of geometry

1. Most of the studies concluded that the flow boiling heat transfer coefficient increases as the hydraulic diameter decreases in micro-scale. Only a few researchers concluded that the effect of the diameter on the flow boiling heat transfer coefficient is not significant.
2. It was found that the channel cross-section has an influence on the heat transfer coefficient. Channels having sharp cross-section, such as rectangular, triangular cross-sections, were found to enhance the nucleation process. This is due to the sharp edges in the square microchannel that behave as effective nucleation sites.
3. The studies on the effect of the channel aspect ratio on the flow boiling heat transfer coefficient are inconclusive. Some researchers reported that, the channel aspect ratio has an influence on the flow boiling heat transfer coefficient; some others stated the opposite effect of channel aspect ratio. However, only two studies were performed in the literature to analyse the effect of the channel aspect ratio on the flow boiling heat transfer coefficient.

Flow boiling pressure drop

In microchannels, it was found that the flow boiling pressure drop has similar characteristics in conventional scale channels. The following conclusions are summarised from the above literature review.

1. All experimental studies concluded that the flow boiling pressure drop increases with increasing mass flux, increasing heat flux, decreasing system pressure and decreasing channel diameter.
2. The effect of the channel aspect ratio on the flow boiling pressure drop was examined in only three studies and is not conclusive. In one study, it was found that the flow boiling pressure drop increases as the channel aspect ratio increases, see Singh et al. (2008). In another study, the researchers state that the flow boiling pressure drop is higher in the lower aspect ratio channel, Soupremanien et al. (2011). In a recent study, it was found that there is not any regular relationship between the effect of the channel aspect ratio and the flow boiling pressure drop, Markal et al. (2016).

Flow boiling instabilities

1. Inlet and outlet temperature and pressure signal fluctuations, wall temperature signal fluctuations and mass flux oscillatins having high amplitudes were recorded during flow boiling in microchannels, Brutin et al. (2003), Wu and Cheng (2003), Wu and Cheng (2004), Xu et al. (2005), Wang et al. (2007), Bogojevic et al. (2009), Bogojevic et al. (2011) and Balasubramanian et al. (2013).
2. It was found that the temperature, pressure and mass flux signal fluctuations and period of these fluctuations increase as the heat flux to mass flux ratio increases (q''/G), Wu and Cheng (2003), Wang et al. (2007), Bogojevic et al. (2009), Bogojevic et al. (2011) and Balasubramanian et al. (2013).
3. Most of the researchers attributed the flow boiling instability to the rapid bubble growth phenomenon which is unique in microchannels due to their confined space. Bubbles nucleate, grow and travel to the upstream and downstream of the microchannels leading to flow reversal in rapid bubble growth phenomenon, Wu and Cheng (2004), Kandlikar (2004), Hetsroni et al. (2005) and Chang and Pan (2005).
4. Upstream compressibility was found to be responsible for the flow reversal in microchannels, Bergles and Kandlikar (2005) and Kandlikar (2006). It was reported that the occurrence of the upstream compressibility is due to the improper degassing of the system that causes non-dissolved air in the system, Gedupudi et al. (2009a), Gedupudi et al. (2009b) and Gedupudi et al. (2009c).
5. Flow boiling instabilities have an effect on the local flow boiling heat transfer behaviour. The local heat transfer coefficient was found to be higher by some investigators in the stable flow boiling compared to unstable flow boiling conditions, Kuan and Kandlikar (2007), Kuo and Peles (2008), Kuo and Peles (2009), Consolini and Thome (2009) and Tuo and Hrnjak (2013). Moreover, the CHF value was found to be extended under stable flow boiling conditions, Kuo and Peles (2008) and Kuo and Peles (2009).
6. Flow boiling instabilities can be supressed with several methods. Qu and Mudawar (2004), Kandlikar et al. (2006), Kosar et al. (2006), Kuan and Kandlikar (2007), Kuo and Peles (2008) and Wang et al. (2008) mitigated the flow boiling instabilities by designing microchannels with inlet restrictions or

using microchannels having artificial cavities. On the other hand, a group of researchers such as Thome and Dupont (2007), Xu et al. (2009) and Liu et al. (2010) proposed seed bubble generation on microheaters at the upstream of the microchannel. They reported that these seed bubbles prevent flow boiling instabilities by soaking up energy from superheated liquids.

Chapter 3

Experimental Facility and Methodology

3.1 Introduction

In this chapter, a detailed description of the experimental facility, the test sections, experimental procedures, measurement equipment and calibration process, and uncertainty analysis and data reduction techniques for single-phase and two-phase flow tests are presented. The chapter is organised as follows: The experimental facility is described in section 3.2. Section 3.3 gives description of the test sections. Section 3.4 provides a description for the calibration procedures of the measurement sensors. The uncertainty analysis and data reduction equations are included in section 3.5 whereas the experimental procedure is given in section 3.6. Finally, section 3.7 gives a summary of the chapter.

3.2 Experimental Facility

The experimental facility used in this study was originally designed by Gedupudi et al. (2008). Mirmanto (2009) modified the existing facility to conduct single-phase and flow boiling experiments in microchannels. However, the current experimental facility was modified and developed during this work in order to achieve the goals of this study.

The closed loop experimental facility is made of stainless steel tubing and fittings which are designed to deliver the working fluid to the microchannel test sections at desired inlet conditions. The system consists of several components that are presented in the following subsections in detail. A high-speed, high-resolution Phantom V6 camera is

also located on top of the microchannel test section to observe flow patterns. The camera is integrated with a stereo microscope (Huvitz HSZ-600) for better flow visualisation. Temperature and pressure readings are obtained from the test rig via National Instrument data acquisition hardware system. A computer program was developed using the Labview V8 software program to process temperature and pressure signals collected during experiments. The chiller unit is also connected to the flow loop to provide chilled glycol to the system as; i) to condense the vapour that leaves from the microchannel test section, ii) to provide the desired vapour-liquid balance in the liquid tank and iii) to cool flowing boiled water from the liquid tank to the micro gear pump. A photograph of the experimental facility is shown in Figure 3.1. Figure 3.2 depicts a schematic drawing of the experimental facility.

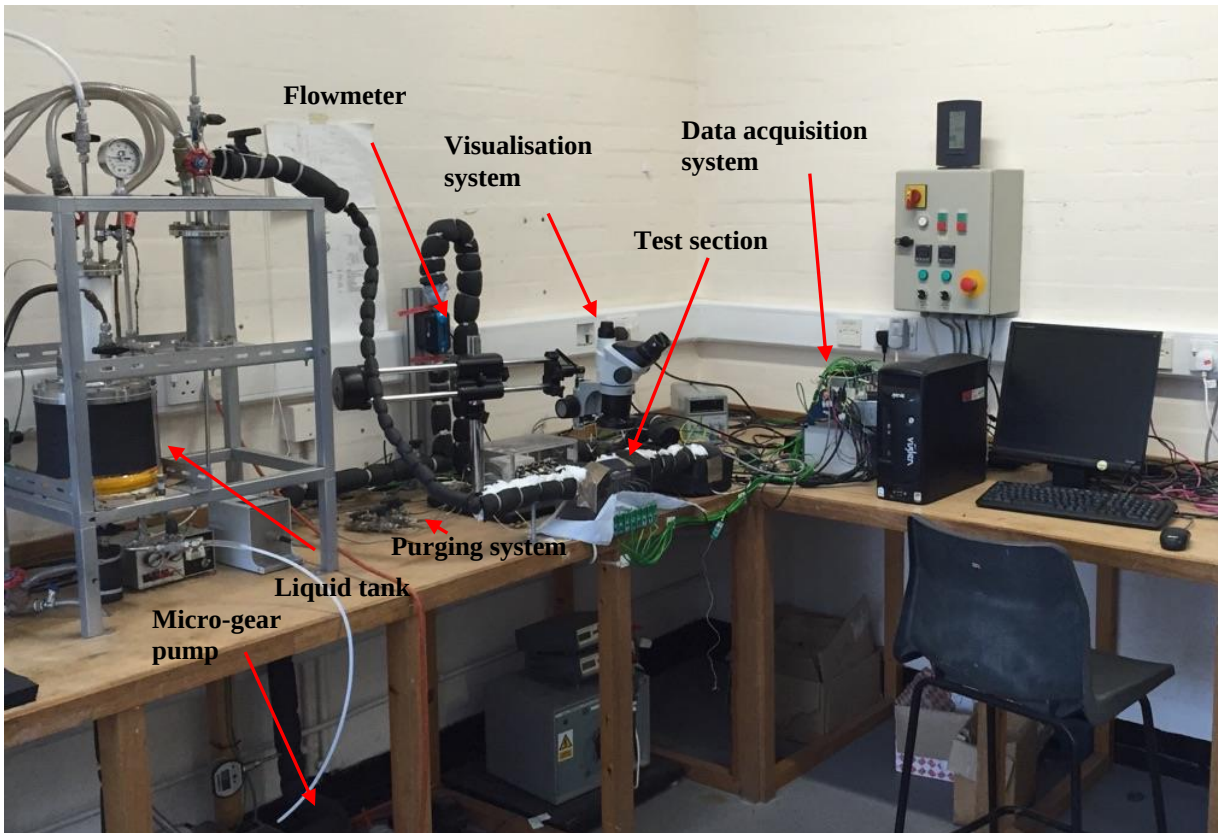

Figure 3.1 Photograph of the experimental facility.

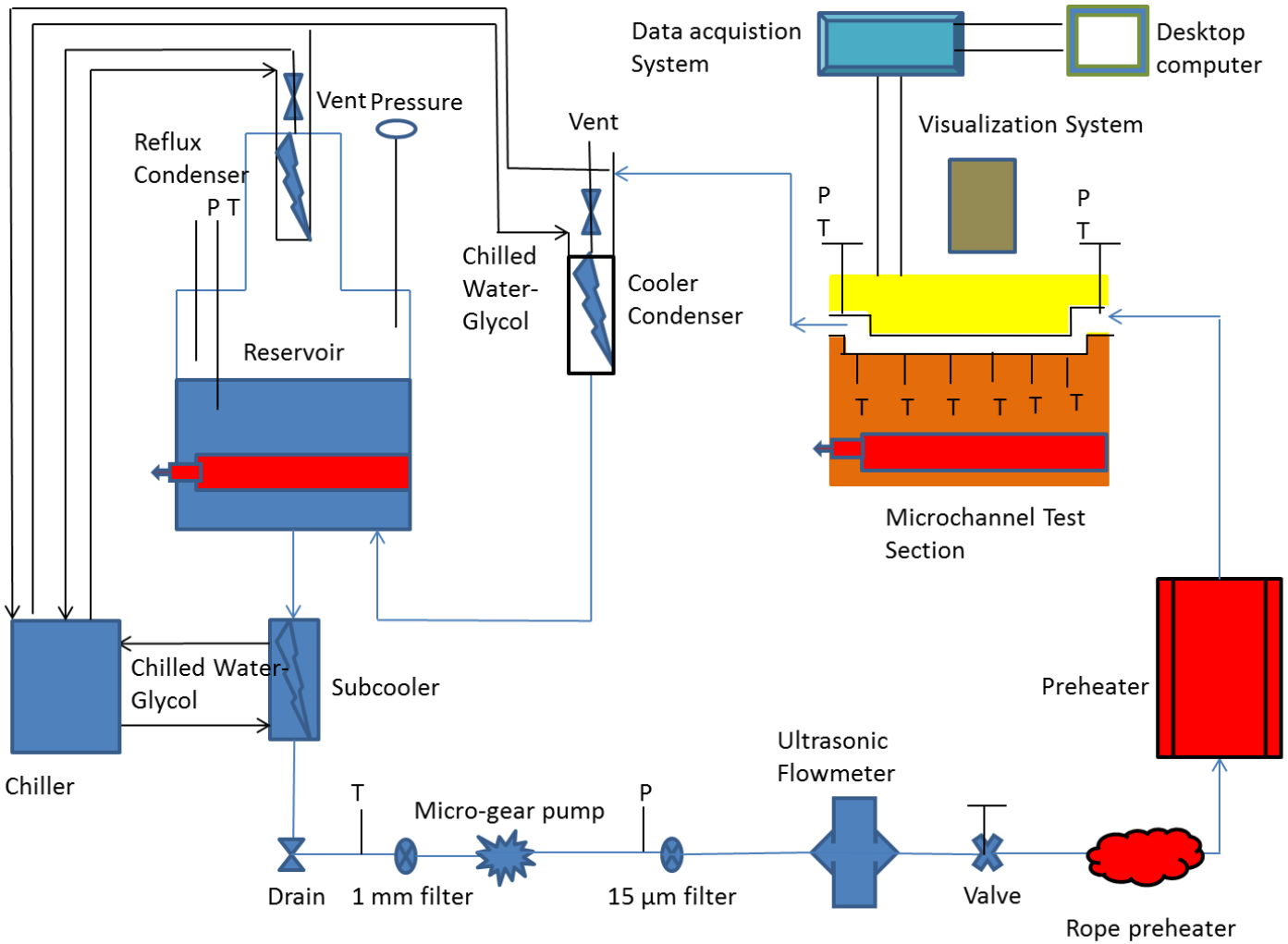

Figure 3.2 Schematic diagram of the experimental facility.

3.2.1 Liquid tank

The three litres volume stainless steel (SS316L) cylindrical liquid tank stores the working fluid (de-ionised water) of the system. A *1500 Watt* cartridge heater having *19 mm* inner diameter and *152 mm* length is welded horizontally into the liquid tank to supply heat. The tank is equipped with a sight glass, a pressure sensor, a pressure gauge and a thermocouple. The sight glass allows monitoring the liquid level inside the tank and a pressure sensor provides a measure of the vapour pressure inside the tank, see Fig. 3.3. The vapour temperature inside the tank is measured with the thermocouple that is connected to the programmable PID controller (West 6100©) to adjust the liquid vapour temperature at desired value. Above the liquid tank, a reflux condenser is connected to condense formed vapour and maintain boiling equilibrium. A degassing line with a vent valve is also connected to the reflux condenser to release trapped gas from the system to the atmosphere. Another feeding line is placed at the bottom of the liquid tank to fill de-ionized water to the tank. A vacuum pump can be used to evacuate air from the liquid tank and is connected with a line at the top of the liquid tank.

3.2.2 Reflux condenser and cooler-condenser

The reflux condenser is placed on top of the liquid tank to condense the formed vapour in the liquid tank to adjust boiling equilibrium. On the other hand, the flowing de-ionized water is condensed by a cooler-condenser, see Fig. 3.3. Condensers are made of stainless steel (SS316) helical coils. The chiller unit supplies glycol-water at a desired temperature in order to feed the condensers.

3.2.3 Subcooler

The stainless steel (SS316) subcooler is a pipe heat exchanger used to cool the boiled working fluid that is flowing from the liquid tank to the pump below *50 °C*. The subcooler consists of a double pipe heat exchanger. The length of the heat exchanger is *600 mm* and the inner diameter is *6 mm* with *1 mm* wall thickness. The pipe outer diameter is *13 mm* with *1.5 mm* wall thickness. This is shown in Fig. 3.4 (a). The subcooler is supplied with water-glycol solution to the pipes at a desired temperature value with *100 g/min* maximum flow rate.

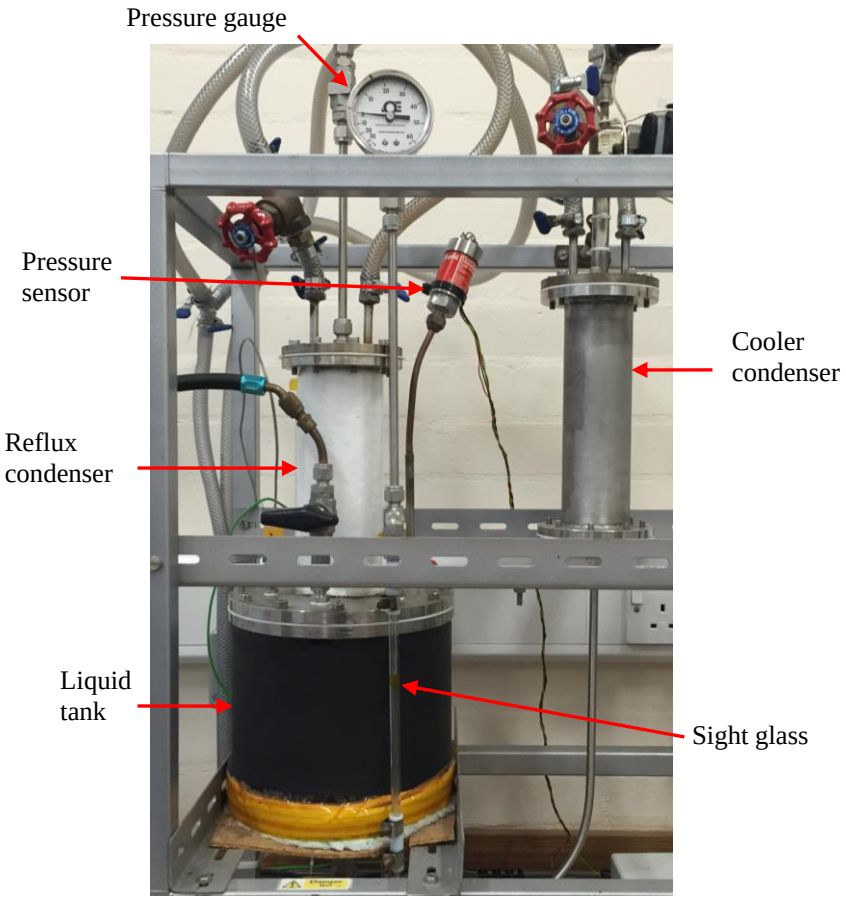

Figure 3.3 Photograph of the liquid tank, cooler condenser and reflux condenser.

3.2.4 Gear pump

De-ionized water is delivered to the flow loop by a magnetically coupled gear pump (GA-T23PFSB©) that is programmable with Ismatec Reglo ZS© digital regulator unit, see Fig. 3.4 (a-b). The micro-gear pump has stainless steel (SS316L) base material, PPS (carbon fibre/PTFE) gears and PTFE static seals and can supply *5-460 ml/min* flow rate range. The maximum differential pressure and system pressure are *5.2 bar* and *21 bar*, respectively. The performance of the micro-gear pump was obtained from the manufacturer (Micropump©) and is shown in Fig. 3.5.

(a) (b)

Figure 3.4 Photograph of; (a) subcooler and micro-gear pump (Micropump©), (b) Regulator unit (Ismatec©).

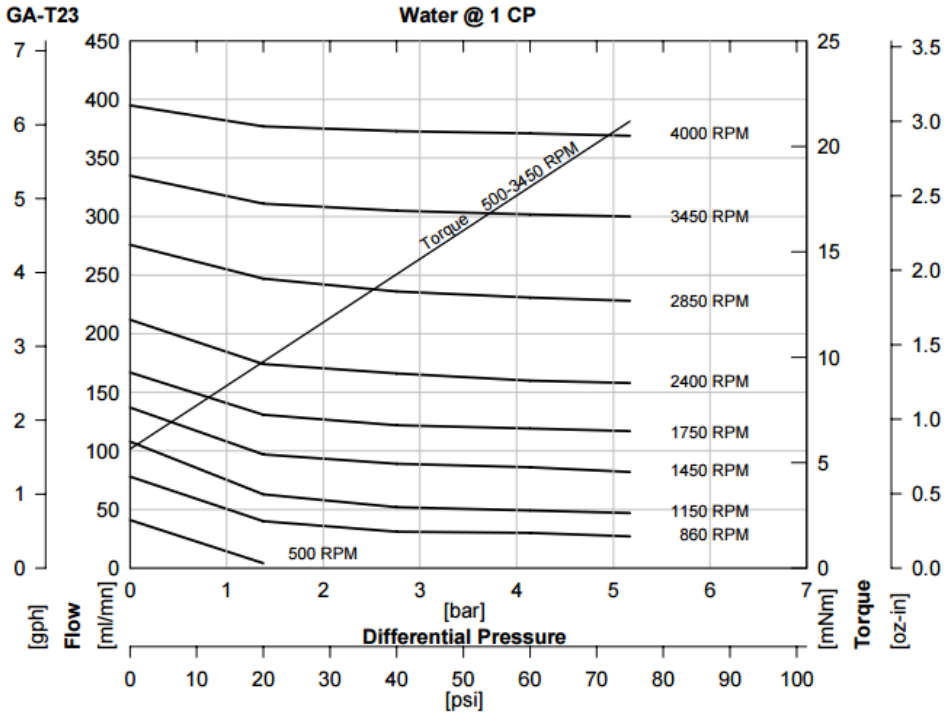

Figure 3.5 Performance of the micro-gear pump with water at 1 cP (0.001 Pa.s).

3.2.5 Chiller unit

A chiller unit with R22 refrigerant is used to provide water-glycol solution to the reflux condenser, cooler-condenser and subcooler units in the flow loop, see Fig. 3.6. The chiller unit works based on the vapour compression refrigeration cycle principle.

Figure 3.6 Photograph of the chiller unit.

3.2.6 Ultrasonic flowmeter

The ultrasonic flowmeter (Atrato 710-V20-D©) measures the flow rate of working fluid, see Fig. 3.7. The flowmeter can measure the flow rate from *2 ml/min* to *500 ml/min* and is supplied by *9-20 Vdc* power input and gives analogue output signal in *mA* (*4-20 mA*) and voltage (*0-10 V*). This is a flowmeter with Viton seals, half inch NPT fittings and stainless steel (SS316L) flow tube with PEEK end fittings comprising a local digital display and analogue output. The linearity of the readings is ± *1.0 %* with a repeatability of ± *0.1 %* based on manufacturer's data.

Fig 3.7 Photograph of the flowmeter (Atrato©).

3.2.7 Rope pre-heater

An Omegalux© rope heater (HTC-120) with *260 Watts* capacity having Fibrox heating cord is inserted to the system after the flowmeter in order to promote gradual heating for the de-ionised water as shown in Fig. 3.8. This is designed to prevent boiling inside the tube before the test section. A thermocouple was pasted to the surface of the tube, where the rope heater has effect, to control necessary power input from AC power supply.

Fig 3.8 Photograph of the rope pre-heater (Omega©).

3.2.8 Electric pre-heater

An additional electric pre-heater was installed to elevate the water temperature to the desired inlet conditions. The pre-heater is made of an aluminium block fitted with two cartridge heaters having *250 Watts* capacity. The PID controller controls the power

input for the cartridge heaters in order to provide a desired inlet temperature for the microchannel test sections.

3.2.9 Visualisation System

Flow patterns were observed with a high-speed, high-resolution camera (Phantom V6©) which is located on top of the test section. The camera recorded the flow patterns with *512x512 pixels* image resolution and 1000 pictures per second sample rate. The camera is integrated with a stereo microscope (Huvitz HSZ-600©) for better flow visualisation. The lighting was provided with a LED ring illuminator (MA341305©) that consists of *144* LED bulbs and is divided into four separate areas for quad lighting. The LED ring illuminator is attached to the head of the stereo microscope with three screws. Once steady state condition is achieved during experiments, flow patterns are recorded to a computer during *1 second* (*1000* pictures) at the inlet, middle and outlet of the test section.

3.2.10 Data acquisition system

All data are recorded at a frequency of *1 kHz* for *3 minutes* using National Instruments© compact modular data acquisition (DAQ) system with LabView© (V8) programmable software. The compact modular DAQ system has an 8-slot chassis with different modules connected to a computer with USB, see Fig. 3.9. NI 9205 module measures the voltage signal from the ultrasonic flowmeter and the pressure transducers. Three NI 9211 modules are thermocouple input modules are used to measure the fluid and wall temperatures in the test section. Finally, the NI 9219 module measures the temperature readings from other thermocouples in the experimental facility such as temperature of the pump and ambient temperature etc.

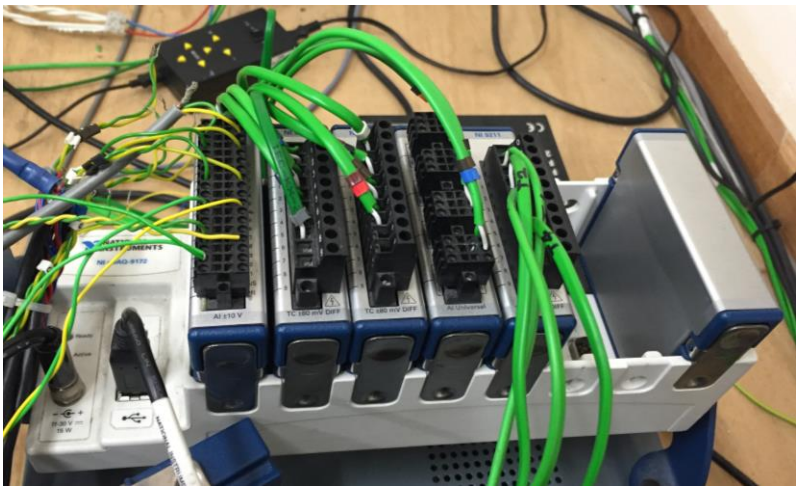

Fig 3.9 Photograph of the data acquisition system (National Instruments©).

3.2.11 Purging system

Two mini tubes (capillary) for the inlet and differential pressure transducers are used the flush any trapped gas/air out from the test section to obtain accurate pressure measurements during the experiments as shown in Fig. 3.1. These mini tubes are controlled using ball valves.

3.2.12 Modifications to experimental facility

The pre-existed experimental facility was modified and some components were changed in the current study. Firstly, the Coriolis flowmeter was replaced with the ultrasonic flowmeter due to the failure of the Coriolis flowmeter during the tests. Secondly, the pre-heating of the fluid was performed by three serial connected PID controlled plate heat exchanger pre-heaters in the previous microchannel research. However, controlling those three pre-heaters well at the same time proved difficult and caused abrupt bubble formation in the tubes. Therefore, the two pre-heaters were removed and a rope heater was inserted along the long tubing section to provide constant and low wattage preheating that prevented bubble formation in the tubes before the fluid entered the test section. A glass tube section was also inserted after the preheating section to make sure that there is no bubble formation (upstream compressibility) in the pre-heaters. Flow visualisations were improved by inserting high-resolution stereo microscope to the existing high speed camera. Modifications in the microchannel test sections were also performed that are stated in the following sections.

3.3 Microchannel Test Sections

Four microchannel test sections were manufactured and investigated in the present study. All microchannel blocks were machined from oxygen-free copper blocks having *12 mm* width and *25 mm* height. Three test section blocks have same length (*72 mm*) and the other one is *96.8 mm* in length. The top surfaces of the oxygen-free copper blocks were cut with a micro-milling machine (Kern HSPC 2216). The O-ring slots, inlet and outlet plenums and the microchannel test sections were all manufactured using the micro-milling machine. All microchannel test sections have single rectangular channel and circle inlet/outlet plenums. The diameters of the inlet and outlet plenums are determined by the constant ratio (8.055) of the plenum area divided by the channel cross-sectional area that is presented in Eq. (3.1), Eq. (3.2) and Eq. (3.3). The dimensions of the microchannels are presented in Table 3.1.

$$\frac{A_p}{A_{ch}} = 8.055 \tag{3.1}$$

$$A_p = \frac{\pi D_p^2}{4} \tag{3.2}$$

$$A_{ch} = WH \tag{3.3}$$

Table 3.1 Dimensions of the microchannels in the current study.

Test section	Height, mm	Width, mm	Length, mm	Hydraulic Diameter, mm	Aspect ratio	Inlet/Outlet Plenums Diameter, mm
TS 1	0.39	1	62.0	0.56	2.56	2.0
TS 2	0.34	1.68	62.0	0.56	4.94	2.4
TS 3	0.84	0.42	62.0	0.56	0.5	1.9
TS 4	0.39	1	86.8	0.56	2.56	2.0

The microchannel test sections were heated using one cartridge heater (Elmatic© *600 W*) inserted below the channel in a direction parallel to the flow that is located in a drilled *7 mm* hole through the copper block. The local axial wall temperatures were measured in the *0.6 mm* inner diameter and *6 mm* length holes at the side of each microchannel test section. The holes were located *1.1 mm* distance below the channel bottom to accommodate K-type thermocouples. Additionally, an O-ring slot was machined on the top surface of the microchannels to seal leakage between the top cover and microchannels. The photograph of the copper microchannel test section (TS4) is included in Fig. 3.10 as a demonstration. The engineering drawing of TS4 is presented in Fig. 3.11 as an example.

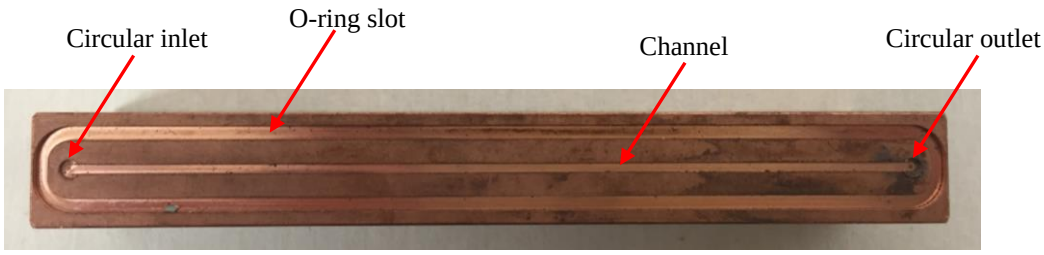

Figure 3.10 Photograph of the test section 4.

Consequently, the microchannel test sections were assembled into the housing components. A large polycarbonate block was designed and manufactured to accommodate the microchannel test sections in the flow loop. The engineering drawing of the polycarbonate housing is shown in Fig. 3.12. The top cover is also made of a transparent polycarbonate material to enable flow visualization. The top cover was manufactured in order to provide inlet and outlet flow connections, thermocouple holes and pressure taps. The engineering drawing of the polycarbonate top cover is provided in Fig. 3.13. Housing, microchannel test section and top cover were assembled together as shown in Fig. 3.14.

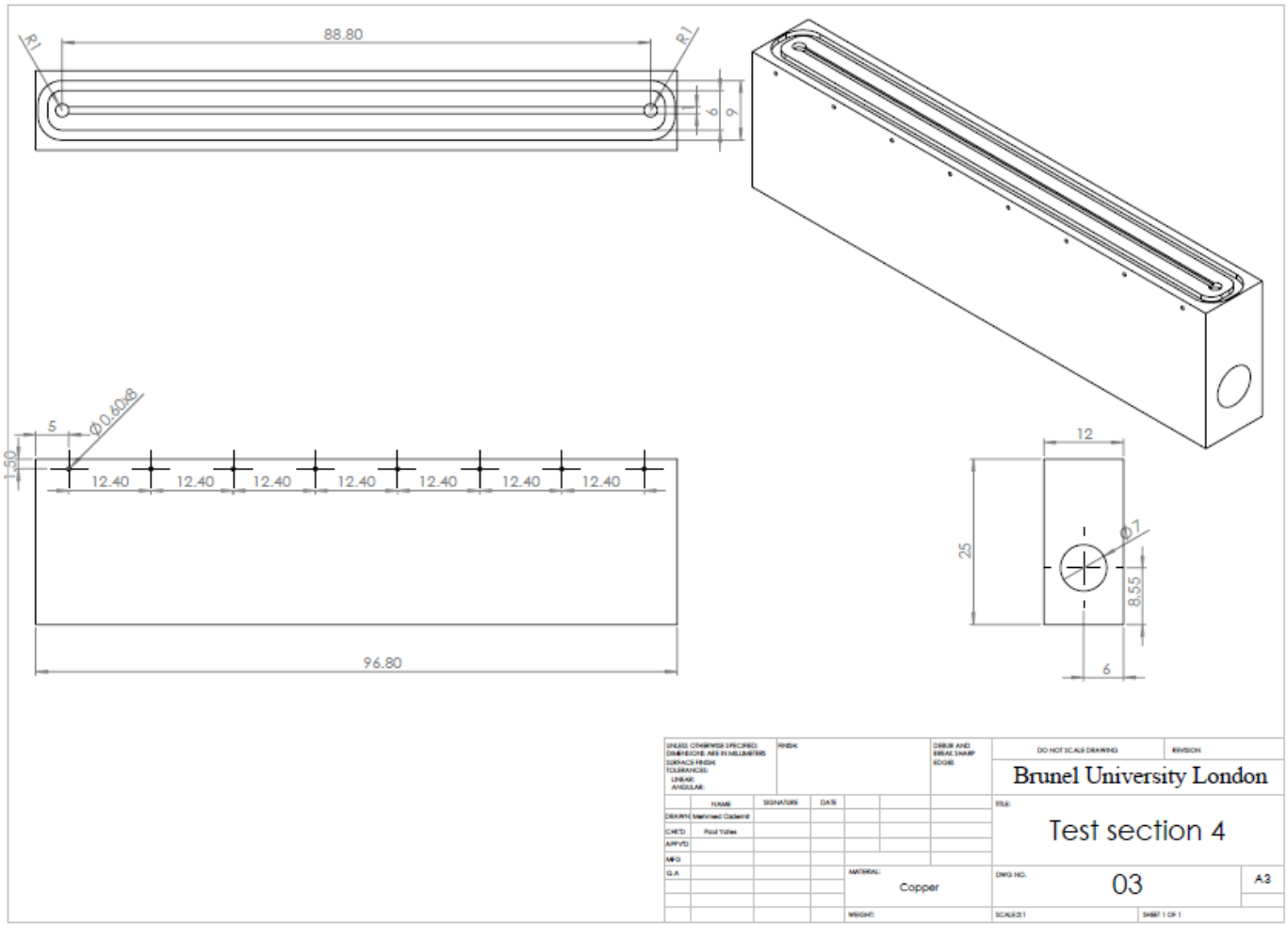

Figure 3.11 Engineering drawing of the microchannel test section 4 (TS4), dimensions in mm.

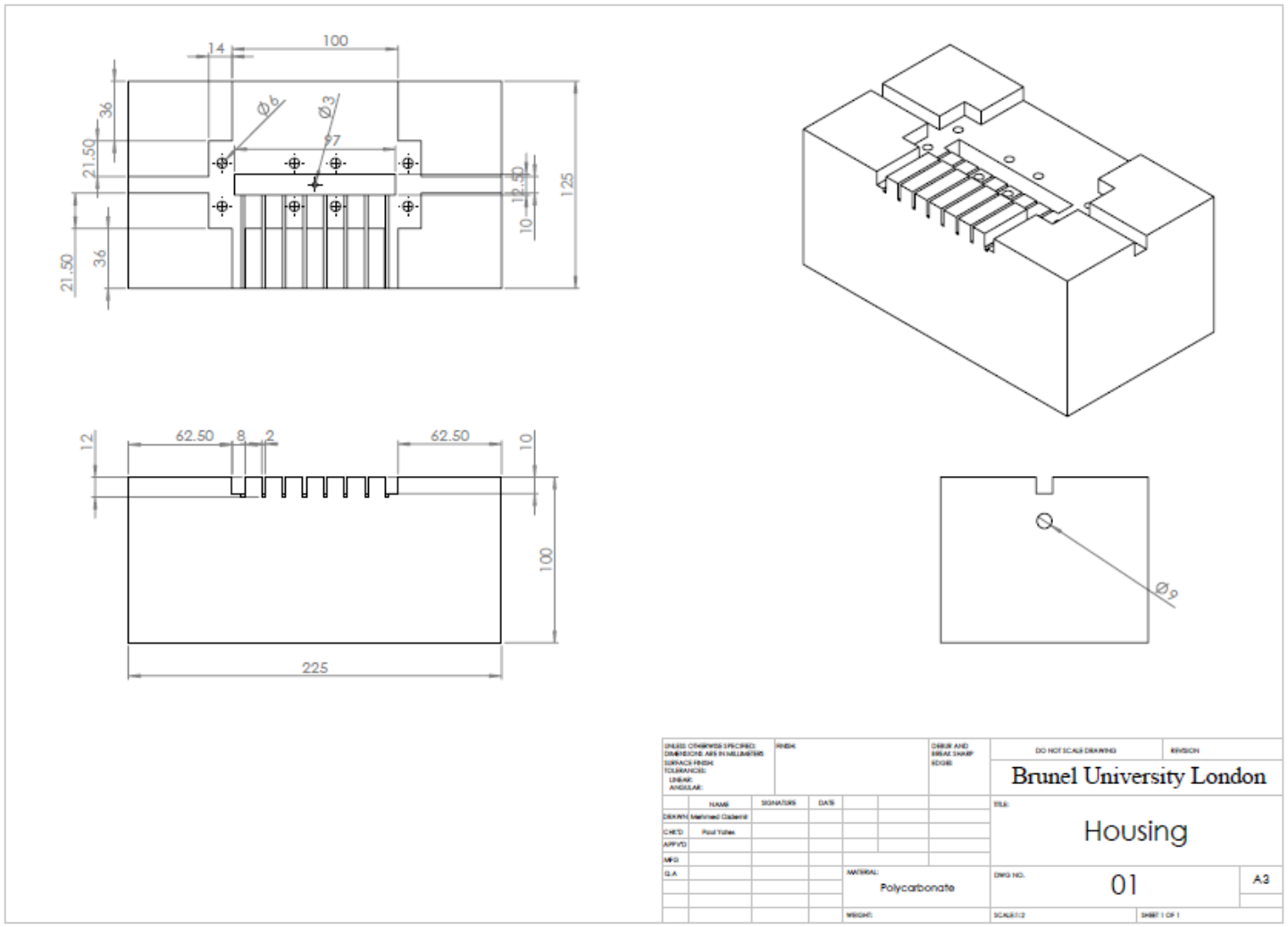

Fig 3.12 Engineering drawing of the polycarbonate housing, dimensions in mm.

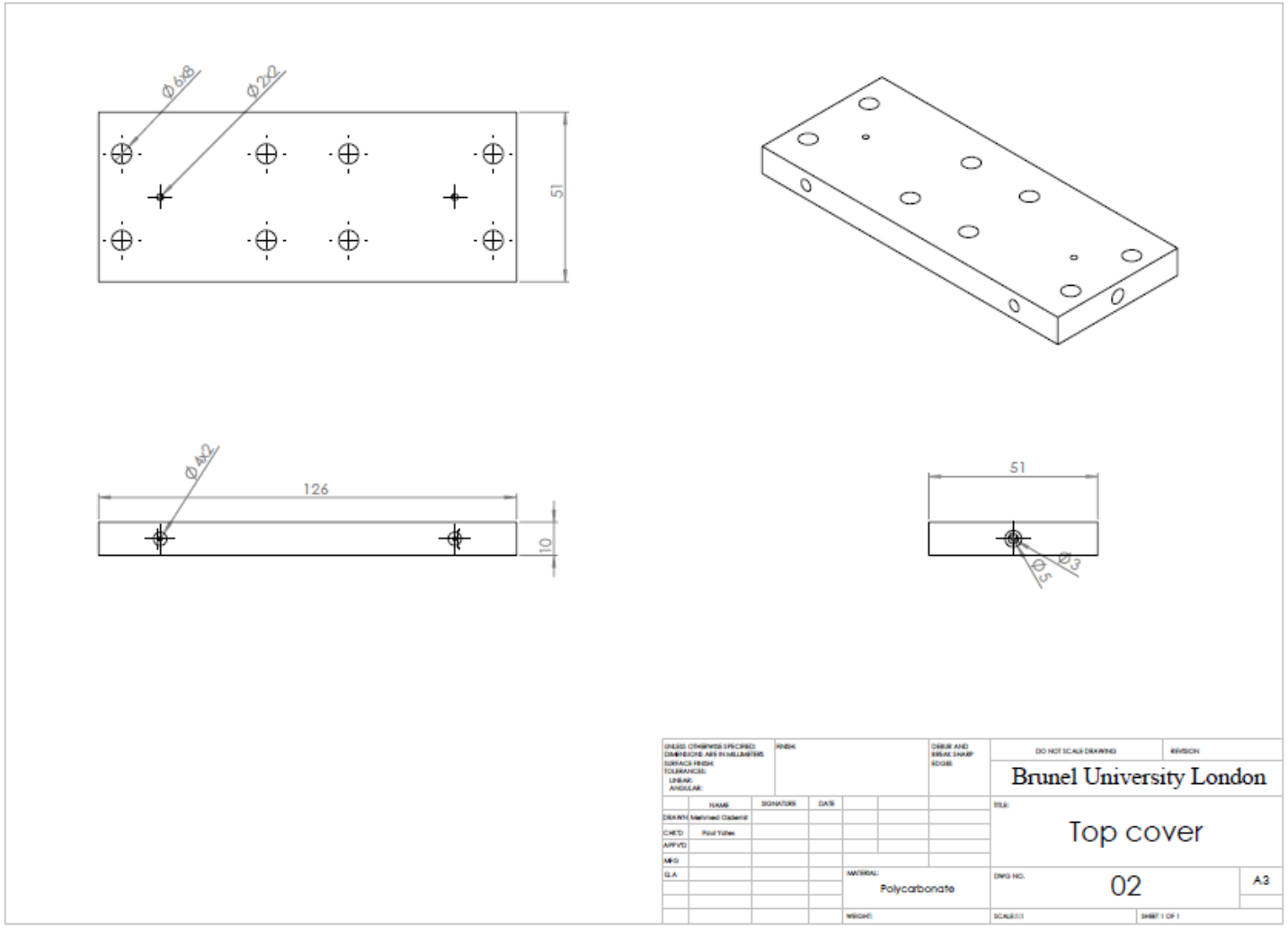

Fig 3.13 Engineering drawing of the polycarbonate top cover, dimensions in mm.

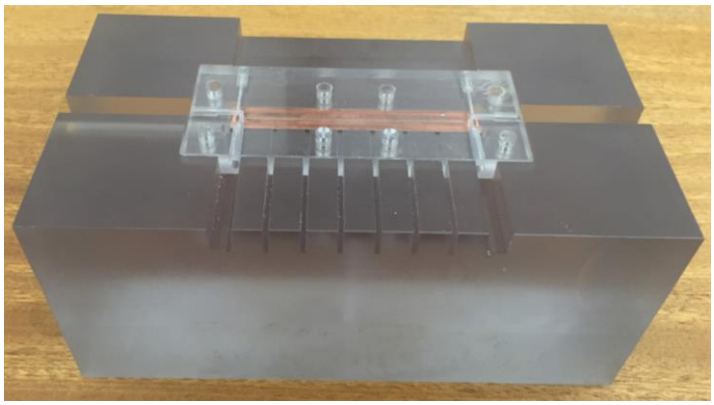

(a)

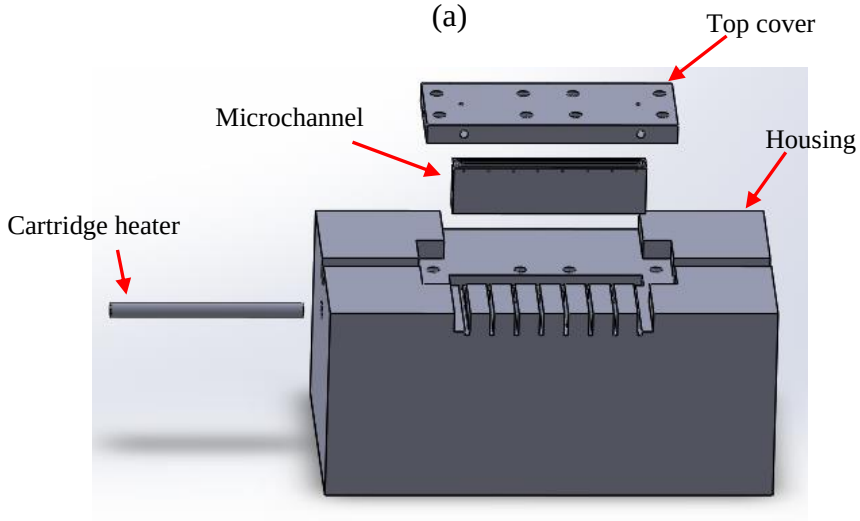

(b)

Fig 3.14 Assembly of the housing, top cover and microchannel test section; (a) Photograph, (b) Exploded view.

The modifications that were performed in the microchannel test sections for this research to overcome previous problems are listed as a summary:

1. Firstly, copper microchannels were manufactured.
2. O-ring slot of the microchannels were re-designed and enlarged to prevent leakages.
3. Viton O-ring material was used instead of rubber due to Viton's high temperature resistance and firmness compared to rubber.

4. Nitrile foam housing was replaced with large polycarbonate housing block to increase solidity of the system and minimise heat loss from copper microchannels.
5. The top cover of the microcohannel test section assembly was also re-designed and changed to improve the flow visualisation quality.
6. Inlet and outlet flow connections were provided by mechanical screws instead of epoxy glued tubes.

3.3.1 Surface roughness and geometrical measurements

The depths, widths and lengths of the channels were measured with a microscope (TSER Technology V-200©), scanning electron microscope (SEM) and digital vernier calliper, respectively. The microscope has an accuracy of ± *1 μm*. The high resolution (*1 nm*) SEM has an accuracy of ± *1 μm*. The resolution of vernier calliper is *0.1 mm*. Moreover, surface roughness measurements of the channels were also performed due to the influence of the surface roughness on flow behaviour and flow boiling heat transfer process. The base surfaces of the microchannels for each test sections are measured with a Zygo NewView 5000© surface profiler. The measurements were performed at three different locations. The average surface roughness values of each microchannel are presented in Table 3.2. Fig. 3.15 presents the surface roughness measurements for the TS3 as an example at three different locations. Fig. 3.15 shows the roughness values that were evaluated over sample areas of *0.176 mm x 0.132 mm* on the surface of microchannel near the inlet, near the middle and near the outlet. Moreover, the surface of microchannel was shown in each picture in order to see surface characteristics. Table 3.2 shows that the surfaces of all test sections except test section 1 are similar to each other. On the other hand, the surface of the tes section 1 seem rougher than other test sections. However, the difference is not too much.

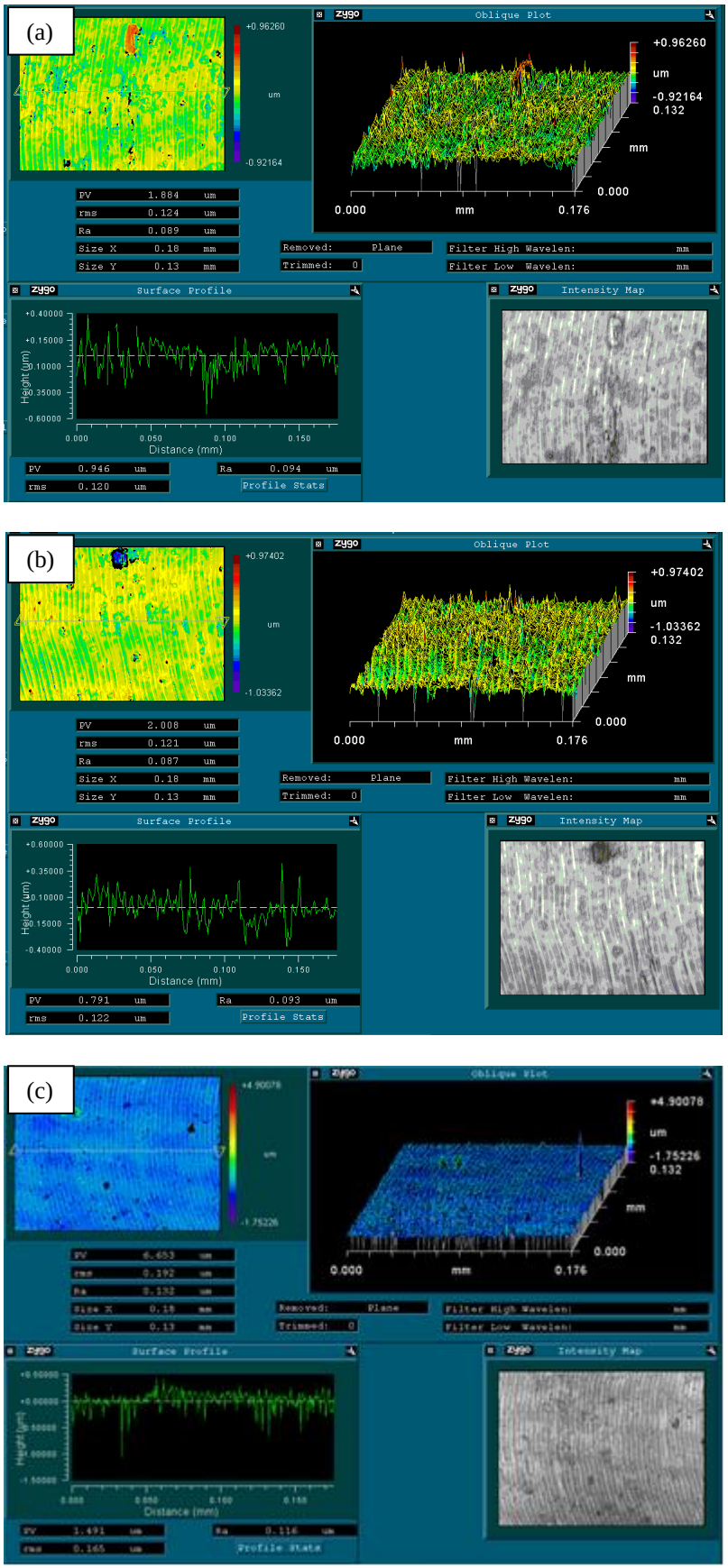

Figure 3.15 Surface roughness measurements of test section 3 at; (a) near inlet, (b) near middle and (c) near outlet of the channel.

Table 3.2 Local surface roughness (Ra) measurements and averaged values for all microchannels.

Test Section	Near Inlet, μm	Near Middle, μm	Near Outlet, μm	Average, μm
TS1	0.693	0.428	0.368	0.496
TS2	0.132	0.135	0.150	0.139
TS3	0.088	0.087	0.131	0.102
TS4	0.084	0.086	0.089	0.086

3.4 Calibration of the experimental apparatus

Calibration defines the accuracy and reliability of measurements and is important to provide reliable experimental results. It is relating one measurement to another measurement that has known or an assigned accuracy and is called the "standard". Standards may vary in each country depending on the type of industry. However, manufacturers state their measurement criterion and provide their calibration curves for different applications in general. In this section, the calibration technique of the experimental devices and sensors is presented. The calibration curve of some devices is provided by the manufacturers that are also mentioned briefly below.

3.4.1 Ultrasonic flowmeter calibration

The Atrato (710-V20-D) is used to measure the flow rate during experiments in this study. Calibration equation of the flowmeter is supplied by the manufacturer (Atrato©) namely $A= 62.5B-124.5$. Here, mass flow rate (g/min) is represented by A and output voltage is represented by B.

3.4.2 Thermocouple calibration

Miniature *0.5 mm* probe diameter and *150 mm* probe length mineral insulated K type thermocouples are used in the current study in order to measure the ambient temperature, surface temperature of the pre-heaters, inlet and outlet fluid temperatures and wall temperatures of the test sections. This type of thermocouples have stainless

steel sheath material, insulated junction, rapid response and broad operating range *(-100 °C – 800 °C)*.

The thermocouples were calibrated against a precision thermometer (ASL F250 MKII©) having platinum resistance thermometer with *±0.005 K* accuracy, broad range of operating conditions *(-200 °C-962 °C)* and selectable resolution of *0.001 °C* or *0.01 °C*, see Fig. 3.19. The ASL F250 MKII precision thermometer is equipped with front panel data entry enabling to enter probe calibration data. The thermocouples were tied to the precision thermometer and submerged in an Omega constant temperature circulating liquid bath filled with antifreeze liquid having *130 °C* boiling point. The bath is equipped with a heating thermoregulatory component (HCTB-3030) having circulating pump, temperature controller and immersion heater, see Fig. 3.19. The thermocouples were connected to the Data acquisition system to record temperature values simultaneously with precision thermometer in LabView software. Temperature readings of the thermocouples and precision thermometer were recorded from just above the ambient temperature until *~ 110 °C* in *5°C* increment steps. After that, a linear calibration curve was obtained for each thermocouple against precision thermometer to be used as calibration equation, see appendix C.

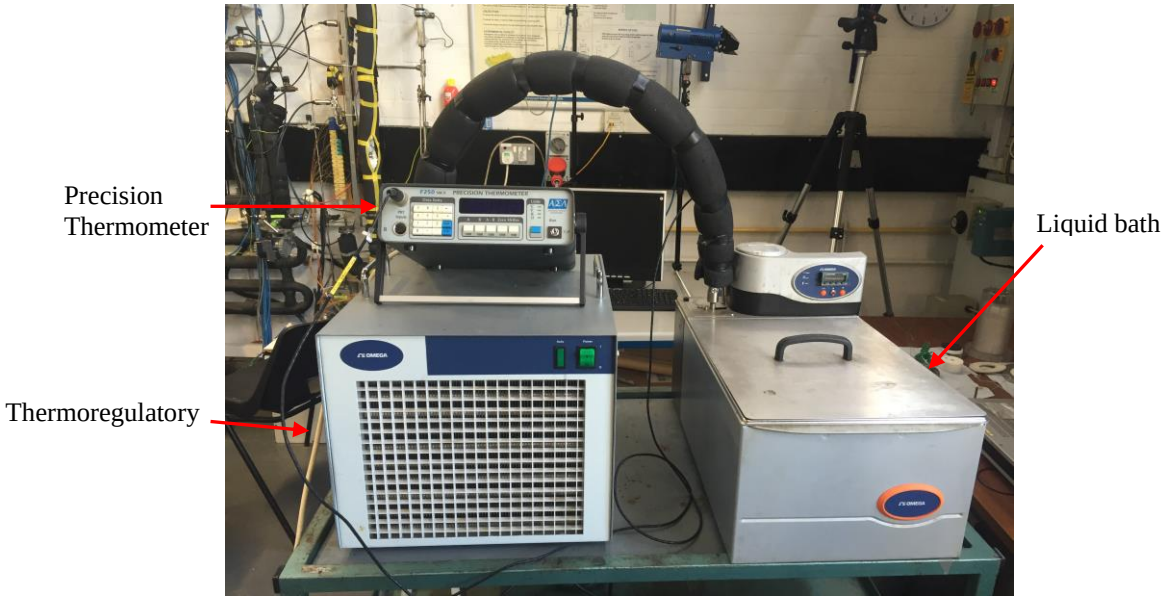

Figure 3.16 Photograph of the thermocouple calibration equipment.

3.4.3 Pressure sensor calibration

An Omega differential pressure transducer (PX409-015DWU) was used to measure the differential pressure between the inlet and outlet of the microchannel test section. The transducer has 316L stainless steel wetted parts and precision micro-machined silicon core having *0-15 psi* measurement range and *0.08 %* full scale accuracy. The transducer supplied by *9-30 Vdc* and produces *4* to *20 mA* output current.

A calibration certificate for the transducer was supplied by the manufacturer (Omega©) as a *5* point calibration. However, calibration of the transducer was also performed in the laboratory. A deadweight tester that has a resolution of *6.895 kPa* was used to calibrate the transducer over the range both increasing and decreasing pressure, see Fig. 3.20. The transducer was connected to data acquisition system and output voltage readings were recorded in LabView software. A linear calibration curve was obtained with a ± *0.4 kPa* standard deviation, see appendix C. It is worth mentioning that the calibration certificate of the manufacturer and the obtained calibration curve were similar to each other (*MAE = 3.2 %*).

Figure 3.17 Photograph of the deadweight tester.

3.5 Data Reduction and Uncertainty Analysis

The parameters investigated in this study, such as local flow boiling heat transfer coefficient, single-phase heat transfer coefficient and two-phase frictional pressure drop are calculated based on the formulas that are described below. Afterwards, propagated uncertainty analysis for the experimental parameters is presented.

3.5.1 Single-Phase data reduction

The experimental Fanning friction factor (f_{ch}), local single-phase heat transfer coefficient ($h_{sp}(z)$) and average Nusselt number (Nu) are the calculated parameters for single-phase flow. The single-phase Fanning friction factor (f_{ch}) is calculated as:

$$f_{ch} = \frac{\rho_l D_h \Delta P_{ch}}{2LG^2} \tag{3.4}$$

In Eq. (3.4), the channel pressure drop (ΔP_{ch}) is calculated using Eq. (3.5). ρ_l is the liquid density and L is the channel length. The mass flux (G) and the channel hydraulic diameter (D_h) are calculated using Eq. (3.6) and Eq. (3.7).

$$\Delta P_{ch} = \Delta P_{meas} - \Delta P_{loss} \tag{3.5}$$

$$G = \frac{\dot{m}}{A_c} \tag{3.6}$$

$$D_h = \frac{2HW}{W+H} \tag{3.7}$$

ΔP_{meas} is the overall pressure drop between the channel inlet and outlet plenums. It is measured directly using the differential pressure sensor. ΔP_{loss} defined by Eq. (3.8) below, is the pressure loss due to the inlet and outlet manifolds and the sudden contraction and enlargement.

H, *W* and $\dot{m}$ represent the channel height, channel width and flow rate, respectively.

$$\Delta P_{loss} = 2(\frac{1}{2}\rho_l V_p^2 K_{90}) + \frac{1}{2}\rho_l V_{ch}^2 (K_c + K_e) \tag{3.8}$$

In Eq. (3.8), V_p and V_{ch} are the liquid velocities in the plenum and in the channel, respectively. The flow enters and leaves the channel in a direction normal to the flow direction. Here, K_{90} is the loss coefficient due to $90°$ turns of the flow in inlet and outlet plenums which is determined as *1.2* by Philips (1987). K_c is the sudden contraction loss coefficient and K_e is the sudden enlargement loss coefficient for the channel inlet and outlet, respectively. Their values were interpolated from tabular information provided by Shah and London (1978).

The local single-phase heat transfer coefficient ($h_{sp}(z)$) and average Nusselt number (*Nu*) are calculated as:

$$h_{sp}(z) = \frac{q''}{T_w(z) - T_f(z)} \tag{3.9}$$

$$Nu = \frac{1}{L}\int_0^L \frac{h_{sp}(z) D_h}{k_l} dz \tag{3.10}$$

where the channel wall temperature at axial location *z* ($T_w(z)$) was corrected using the 1D heat conduction equation as given by Eq. (3.11) below. k_l is the liquid thermal conductivity and $T_f(z)$ is calculated by Eq. (3.12) below based on an energy balance assuming uniform heat flux boundary conditions. The heat flux (*q''*) was defined in Eq. (3.13).

$$T_w(z) = T_{tc}(z) - \frac{q''t}{k_{Cu}} \tag{3.11}$$

$$T_f(z) = T_i + \frac{q''Wz}{\dot{m}c_p} \tag{3.12}$$

$$q'' = \frac{P - Q_{loss}}{A_{ht}} \tag{3.13}$$

In Eq. (3.11), $T_{tc}(z)$ is the local thermocouple reading, k_{Cu} is the copper thermal conductivity and the distance from the channel bottom to the thermocouple location (t) is 1.1 mm. In Eq. (3.12), T_i is the fluid inlet temperature and c_p is the liquid specific heat. In Eq. (3.13), P is the applied electrical power, A_{ht} is the heat transfer area which is defined in Eq. (3.14). The heat loss from the test section (Q_{loss}) was estimated by applying an electrical power (P) to the test section when there is no fluid inside. The temperature difference between the bottom wall and ambient was recorded for each heating power after attaining steady state. The applied power was then plotted versus this temperature difference and the data were fitted to obtain an equation to calculate the heat loss (Q_{loss}) during single-phase and boiling experiments. In other words, the temperature difference between the test section bottom wall and the ambient during an actual experiment was used to assess the Q_{loss}. The percentage of the heat loss varied from *5.2* to *9.2 %* over the experimental range. The top cover was assumed to be adiabatic. Uniform heat flux assumption in the axial and transverse direction of the channel on all three walls was applied.

$$A_{ht} = (2H + W)L \tag{3.14}$$

3.5.2 Two-Phase flow data reduction

The fluid enters the channel as a sub-cooled liquid. Therefore, the channel is divided into a single-phase region and two-phase region. The single-phase region starts from the channel inlet to the location of zero thermodynamic quality with length L_{sub}. Thus, the length of the two-phase region (L_{sat}) becomes:

$$L_{sat} = L - L_{sub} \tag{3.15}$$

The length of the single-phase region (L_{sub}) is calculated iteratively using the following equations.

$$L_{sub} = \frac{\dot{m} c_p (T_{sat} - T_i)}{q''(2H + W)} \tag{3.16}$$

$$P_{sat}(L_{sub}) = P_i - \frac{2 f_{app} G^2}{\rho_l D_h} L_{sub} \tag{3.17}$$

$$f_{app} = \frac{3.44}{\mathrm{Re}\sqrt{L^*_{sub}}} + \frac{(f_{FD}\,\mathrm{Re}) + \frac{K(\infty)}{4L^*_{sub}} - \frac{3.44}{\sqrt{L^*_{sub}}}}{\mathrm{Re}(1 + C(L^*_{sub})^{-2})} \tag{3.18}$$

f_{app} is the apparent friction factor that was taken from Shah (1978) and T_{sat} is the liquid saturation temperature. The values of the constant C, $f_{FD}Re$ and $K(\infty)$ in Eq. (3.18) are given in Shah (1978) for rectangular channels. The dimensionless length (L^*_{sub}) in Eq. (3.18) can be determined by Eq. (3.19). The fully-developed Poiseuille number ($f_{FD}Re$) is given by Shah and London (1978) in Eq. (3.20) in the form of a function of the channel aspect ratio (β).

$$L^*_{sub} = \frac{L_{sub}}{\mathrm{Re}\, D_h} \tag{3.19}$$

$$(f_{FD}\,\mathrm{Re}) = 24(1 - 1.3553\beta + 1.9467\beta^2 - 1.7012\beta^3 + 0.9564\beta^4 - 0.2537\beta^5) \tag{3.20}$$

The local pressure in the two-phase part was assumed to decrease linearly with the axial length z and it can be calculated as:

$$P_{sat}(z) = P_{sat}(L_{sub}) - \frac{z - L_{sub}}{L - L_{sub}} \Delta P_{tp} \tag{3.21}$$

where the net two-phase pressure drop across the channel is defined as:

$$\Delta P_{tp} = \Delta P_{ch} - \Delta P_{sp} \tag{3.22}$$

The single-phase pressure drop (ΔP_{sp}) can be determined based on the length of the single-phase region (L_{sub}) calculated using Eq. (3.16)-Eq. (3.18) and the apparent friction factor defined by Eq. (3.18). The local two-phase heat transfer coefficient was defined as:

$$h_{tp}(z) = \frac{q''}{T_w(z) - T_{sat}(z)} \tag{3.23}$$

The local saturation temperature ($T_{sat}(z)$) in Eq. (3.23) is calculated based on the local pressure given by Eq. (3.21). The vapour quality ($x(z)$) was determined by Eq. (3.24) and Eq. (3.25).

$$i(z) = i_i + \frac{q''(2H+W)z}{\dot{m}} \tag{3.24}$$

$$x(z) = \frac{i(z) - i_l(z)}{i_{lg}(z)} \tag{3.25}$$

The local inlet specific enthalpy ($i_i(z)$) is calculated based on the measured inlet pressure (P_i) and the inlet temperature (T_i). In Eq. (3.25), $i_l(z)$ is local liquid specific enthalpy and $i_{lg}(z)$ is local enthalpy of vaporisation.

3.5.3 Flow pattern map data reduction

Flow pattern maps are established by using the liquid superficial velocity (J_l) and the gas superficial velocity (J_g) which are calculated as:

$$J_l(z) = \frac{G(1-x(z))}{\rho_l(z)} \tag{3.26}$$

$$J_g(z) = \frac{Gx(z)}{\rho_g(z)} \tag{3.27}$$

where *x(z)* is the local thermodynamic mass quality and *G* is the mass flux. ρ_l and ρ_g are the liquid and vapour densities of the working fluid.

3.5.4 Propagated uncertainty analysis

Measurements of any physical quantity are always subject to some uncertainty. The main sources of experimental uncertainties can be due to the low accuracy of the measuring instruments, assumptions in the experimental procedure and environmental factors. The propagation of uncertainty is the method to calculate combined uncertainty due to separate effects of each experimental parameter. In this study, the propagated uncertainty analysis was conducted according to the method explained in Coleman and Steele (2009).

The total error in a measurement is the sum of random errors and bias errors. The bias errors are the permanent errors due to the measuring instrument. Bias errors can be reduced by frequent and precise calibrations of the measuring instruments. However, the random errors are specific for each measurement and result from the *N* experimental readings. Random errors are predicted using statistical analysis assuming that a sample of *N* measurements obeys Gaussian or normal distribution with a certain confidence level and can be reduced by increasing the sample size of the readings. In this study, a *95%* confidence level is used as recommended by Coleman and Steele (2009). Consequently, the random error (u_{random}) of *X* can be calculated as:

$$u_{random} = t_{95\%} S_x \tag{3.28}$$

$$S_x = \sqrt{\frac{1}{N-1}\sum_{i=1}^{N}(X_i - \overline{X})^2} \tag{3.29}$$

$$\overline{X} = \frac{1}{N}\sum_{i=1}^{N} X_i \tag{3.30}$$

where $t_{95\%}$ is the t distribution value having 95% confidence level, S_x is the standard deviation of the measured sample and $\overline{X}$ is the mean value of the readings. Bias uncertainty of the measured quantity (X) and the standard deviation of the bias uncertainty (S_{Bx}) are calculated as follows:

$$B_x = \sqrt{\sum_{k=1}^{M} (B_x)_k^2} \tag{3.31}$$

$$S_{Bx} = \frac{B_x}{2} \tag{3.32}$$

where B_x is the bias uncertainty from the measuring instrument and can be provided by the manufacturer or calibration curve. The combined uncertainty of the bias and random uncertainties (u_c) are determined using Eq. (3.33). The overall uncertainty (U) of any measured quantity is calculated by Eq. (3.34).

$$u_c = \sqrt{S_{Bx}^2 + S_x^2} \tag{3.33}$$

$$U = t_{95\%} u_c \tag{3.34}$$

Consequently, the uncertainty propagation of a number of j measured quantities is calculated as follows:

$$r = r(X_1, X_2, ..., X_j) \tag{3.35}$$

$$U_r^2 = \left(\frac{\partial r}{\partial X_1}\right)^2 U_{x1}^2 + \left(\frac{\partial r}{\partial X_2}\right)^2 U_{x2}^2 + ... + \left(\frac{\partial r}{\partial X_j}\right)^2 U_{xj}^2 \tag{3.36}$$

$$\frac{U_r^2}{r^2} = \left(\frac{X_1}{r}\frac{\partial r}{\partial X_1}\right)^2 \left(\frac{U_{x1}}{X_1}\right)^2 + \left(\frac{X_2}{r}\frac{\partial r}{\partial X_2}\right)^2 \left(\frac{U_{x2}}{X_2}\right)^2 + ... + \left(\frac{X_j}{r}\frac{\partial r}{\partial X_j}\right)^2 \left(\frac{U_{xj}}{X_j}\right)^2 \tag{3.37}$$

where U_r^2 is the absolute uncertainty and Eq. (3.37) is the dimensionless form of the absolute uncertainty that is called relative uncertainty. In that way, propagated uncertainty analysis was performed according to the above presented approach in the current study. Table 3.3 presents the bias uncertainty value for the each measured quantity.

Table 3.3 Uncertainty values for the measured parameters

Measured parameter	Measured instrument	Uncertainty
Mass flow rate	Ultrasonic flowmeter	± 0.00001 kg/s (manufacturer calibration certificate)
Channel depth	SEM	± 0.002 mm
Channel width	TSER microscope	± 0.002 mm
Channel length	Vernier calliper	± 0.1 mm
Pressures	Differential pressure transducers	± 0.43 kPa (calibration)
AC voltage	Multimeter	± 0.03 V (manufacturer calibration certificate)
AC current	Multimeter	± 0.01 A (manufacturer calibration certificate)
Temperatures	K type thermocouple	± 0.24 K (calibration)

The propagated uncertainty analysis of the calculated parameters is performed using Eq. (3.36). Hydraulic diameter (D_h) is expressed in Eq. (3.7). In that way, the absolute uncertainty in the hydraulic diameter is expressed as follows:

$$U_{D_h} = \sqrt{\left[2\frac{W^2}{(H+W)^2}\right]^2 U_H^2 + \left[2\frac{H^2}{(H+W)^2}\right]^2 U_W^2} \tag{3.38}$$

where U_H and U_W are the absolute uncertainty in the channel depth and width, respectively. Similarly, absolute uncertainties of channel cross-sectional area (U_{Ach}) and channel pressure drop ($U_{\Delta Pch}$) are defined in Eq. (3.39) and Eq. (3.40).

$$U_{Ach} = \sqrt{H^2 U_W^2 + W^2 U_H^2} \tag{3.39}$$

$$U_{\Delta Pch} = \sqrt{U_{\Delta Pmeas}^2 + U_{\Delta Ploss}^2} \tag{3.40}$$

where $U_{\Delta Pmeas}$ and $U_{\Delta Ploss}$ are the absolute uncertainty in the measured and loss pressure drop, respectively. Consequently, the uncertainty in the fanning friction factor is result of the uncertainty in the hydraulic diameter, mass flow rate, channel pressure drop, channel length and channel cross-sectional area and is expressed in Eq. (3.41).

$$U_{fch} = f_{ch}\left[\sqrt{\left(\frac{U_{\Delta Pch}}{\Delta P_{ch}}\right)^2 + \left(\frac{U_{Dh}}{D_h}\right)^2 + \left(\frac{2U_{Ach}}{A_{ch}}\right)^2 + \left(\frac{U_L}{L}\right)^2 + \left(\frac{2U_{\dot{m}}}{\dot{m}}\right)^2}\right] \tag{3.41}$$

In order to calculate the uncertainty in the single-phase heat transfer coefficient, the uncertainty in the heat flux is calculated using the following equations.

$$U_{q''} = \sqrt{\left[\frac{U_{Qnet}}{A_{ht}}\right]^2 + \left[Q_{net}\frac{U_{Aht}}{A_{ht}^2}\right]^2} \tag{3.42}$$

where U_{Qnet} and U_{Aht} are the uncertainties in the net applied heat flux and heat transfer area, respectively, and is calculated as follows:

$$Q_{net} = P - Q_{loss} \tag{3.43}$$

$$U_{Qnet} = \sqrt{U_P^2 + U_{Qloss}^2} \tag{3.44}$$

$$U_{Aht} = \sqrt{\left[\left(2H+W\right)U_L\right]^2 + \left(2LU_H\right)^2 + \left(LU_W\right)^2} \tag{3.45}$$

where U_P is the uncertainty in the applied power and U_{Qloss} is the uncertainty in the heat loss and are expressed as:

$$U_P = \sqrt{\left(IU_V\right)^2 + \left(VU_I\right)^2} \tag{3.46}$$

where U_V and U_I are the uncertainty in applied voltage and applied current, respectively. Consequently, the uncertainty in average single-phase heat transfer coefficient and average Nusselt number are calculated using the following equations.

$$U_{\overline{h_{sp}}} = \sqrt{\left[\frac{U_{q''}}{\overline{T_w} - \overline{T_f}}\right]^2 + \left[q''\left(\frac{U_{\overline{T_w}}}{\overline{T_w}^2 - \overline{T_f}}\right)\right]^2 + \left[q''\left(\frac{U_{\overline{T_f}}}{\overline{T_w} - \overline{T_f}^2}\right)\right]^2} \tag{3.47}$$

$$U_{\overline{Nu}} = \sqrt{\left[D_h \frac{U_{\overline{h_{sp}}}}{k_l}\right]^2 + \left[\overline{h_{sp}} \frac{U_{D_h}}{k_l}\right]^2} \tag{3.48}$$

The two-phase pressure drop is determined using Eq. (3.22) as stated before. Accordingly, the two-phase pressure drop uncertainty (Δ_{Ptp}) can be determined as follows:

$$U_{\Delta P_{tp}} = \Delta P_{tp} \sqrt{\left(\frac{U_{\Delta P_{ch}}}{\Delta P_{ch} - \Delta P_{sp}}\right)^2 + \left(\frac{U_{\Delta P_{sp}}}{\Delta P_{ch} - \Delta P_{sp}}\right)^2} \tag{3.49}$$

where the uncertainty in channel pressure drop (Δ_{Pch}) is defined in Eq. (3.40). The single-phase pressure drop (Δ_{Psp}) and the single-phase pressure drop uncertainty are expressed as:

$$\Delta P_{sp} = \frac{2 f_{app} G^2}{\rho_l D_h} L_{sub} \tag{3.50}$$

$$U_{\Delta P_{sp}} = \Delta P_{sp} \sqrt{\left(\frac{2U_G}{G}\right)^2 + \left(\frac{U_{L_{sub}}}{L_{sub}}\right)^2 + \left(\frac{U_{D_h}}{D_h}\right)^2} \tag{3.51}$$

where U_G and U_{Lsub} are the uncertainties in the mass flux and subcooled length, respectively. They can be obtained using Eq. (3.52) and Eq. (3.53).

$$U_G = G \sqrt{\left(\frac{U_{\dot{m}}}{\dot{m}}\right)^2 + \left(\frac{U_{A_{ch}}}{A_{ch}}\right)^2} \tag{3.52}$$

$$U_{L_{sub}} = L_{sub} \sqrt{\left(\frac{U_{\dot{m}}}{\dot{m}}\right)^2 + \left(\frac{-U_{T_i}}{T_{sat}(z) - T_i}\right)^2 + \left(\frac{-U_{q''}}{q''}\right)^2 + \left(\frac{-2U_H}{2H+W}\right)^2 + \left(\frac{-U_W}{2H+W}\right)^2} \tag{3.53}$$

Similarly, the uncertainty in the two-phase length (U_{Ltp}) is calculated as follows:

$$U_{L_{tp}} = \sqrt{(U_L)^2 + (U_{L_{sub}})^2} \tag{3.54}$$

As mentioned above, the uniform heat flux boundary condition was assumed in the current study. Consequently, the two-phase heat transfer coefficient uncertainty is obtained using Eq. (3.55).

$$U_{h_{tp}(z)} = h_{tp}(z) \sqrt{\left(\frac{U_{q''}}{q''}\right)^2 + \left(\frac{U_{T_w}}{T_w - T_{sat}(z)}\right)^2} \tag{3.55}$$

Similarly, the uncertainty in the local thermodynamic mass quality is calculated. It's worth mentioning that the liquid local saturation enthalpy uncertainty and the

evaporation ($i_{lg}(z)$) uncertainty are negligibly small. So that the uncertainty in the local thermodynamic mass quality is:

$$U_{x(z)} = \frac{U_{i(z)}}{i_{\lg}(z)} \tag{3.56}$$

where, $U_{i(z)}$ is the uncertainty in the local enthalpy. The local enthalpy consists of inlet liquid enthalpy component and local heat rate with a length of z component. The uncertainty in the inlet liquid enthalpy can be negligible. Accordingly, the local enthalpy uncertainty is:

$$U_{i(z)} = \sqrt{\left(\frac{(2H+W)z}{\dot{m}}U_{q"}\right)^2 + \left(\frac{2q"z}{\dot{m}}U_H\right)^2 + \left(\frac{q"z}{\dot{m}}U_W\right)^2 + \left(\frac{q"(2H+W)}{\dot{m}}U_z\right)^2 + \left(\frac{q"(2H+W)}{\dot{m}}U_{\dot{m}}\right)^2} \tag{3.57}$$

Finally, the uncertainties in vapour and liquid superficial velocities (U_{Jg} and U_{Jl}) are calculated using Eq. (3.58) and Eq. (3.59), respectively.

$$U_{J_g} = J_g\sqrt{\left(\frac{U_G}{G}\right)^2 + \left(\frac{U_{x(z)}}{x(z)}\right)^2} \tag{3.58}$$

$$U_{J_l} = J_l\sqrt{\left(\frac{U_G}{G}\right)^2 + \left(\frac{U_{x(z)}}{(1-x(z))}\right)^2} \tag{3.59}$$

The uncertainties for the single-phase experiments and flow boiling experiments are presented in Table 3.4 and Table 3.5, respectively.

Table 3.4 Uncertainties for single-phase experiments

Parameter	Uncertainty
Hydraulic diameter, D_h [mm]	± 0.32-0.49 %
Heat transfer area, A_{ht} [mm^2]	± 0.19-0.25 %
Mass flux, G [kg/m^{2}s]	± 0.91-11.4 %
Heat flux, q'' [kW/m^2]	± 8.1-9.8 %
Pressure drop, ΔP_{ch} [kPa]	± 0.77-34.5 %
Channel friction factor, f_{ch}	± 2.01-41.3 %
Average heat transfer coefficient, $\overline{h_{sp}}$ [kW/m^{2}K]	± 7.1-11.8 %
Average Nusselt number, $\overline{Nu}$	± 7.1-11.8 %

Table 3.5 Uncertainties for boiling heat transfer experiments

Parameter	Uncertainty
Mass flux, G [kg/m^{2}s]	± 0.91-12.6 %
Heat flux, q'' [kW/m^2]	± 2.18-6.51 %
Local heat transfer coefficient, $h_{tp}(z)$ [kW/m^{2}K]	± 5.2-7.9 %
Local thermodynamic mass quality, $x(z)$	± 0-9.4 %

3.6 Experimental Procedures

This section presents the sets of procedures that are needed to perform single-phase and flow boiling experiments in this study. Prior to each experiment, the preparation stage, including the de-gassing procedure is also explained in detail.

3.6.1 Preparation for experiments

Before beginning any data collection for both single-phase and flow boiling experiments, a preparation stage needs to be completed to ensure that the steady-state condition and the overall stability of the system are achieved. This preparation stage also includes a de-gassing procedure that is very important especially in micro-scale. Any trapped gases need to be evacuated from the test rig to get accurate measurements during the experiments. The preparation stage for the experiments can be presented step by step as follows:

1. Switch the main power supply on in order to operate all instruments in the test rig.
2. Turn the computer on and run the LabView software program.
3. Open all valves on the rig including the valves for the inlet and outlet pressure taps to provide liquid flow.
4. Operate the micro-gear pump at high flow rate (e.g. 200 *ml/min*) approximately half hour to ensure that there is no deadlock in the flow loop and to have clear liquid flow in the test rig.
5. Turn the micro-gear pump off. Close all valves on the test rig including purging lines to isolate the liquid tank from the flow loop.
6. Operate the vacuum pump to reduce the gauge pressure inside the liquid tank between *-20* and *-30 in Hg* (*-67.7* and *-101.6 kPa*). After that, turn the vacuum pump off and close the vacuum pump valve.
7. Check the liquid in the tank to ensure the level is enough to start experiment. If there is not enough liquid in the tank, open the liquid feed valve to fill the liquid tank with de-ionized water until the mark on the sight glass reached.
8. If the gauge pressure inside the liquid tank rises above the *-20 in Hg*, repeat step 6.
9. Adjust the liquid temperature inside the liquid tank to a corresponding saturation temperature *(≈ 101 °C*) from the PIV controller unit on the main power supply box and turn the cartridge heater on to boil the de-ionized

water inside the liquid tank, approximately *1.5* hours. After the gauge pressure inside the liquid tank reached above *0 in Hg*, the vent valve should be opened in every *15* minutes to discharge any gas to the ambient. Note that the vent valve is placed on the top of the reflux condenser.

10. Supply the chilled water-glycol solution to the subcooler to ensure that the de-ionised water temperature before the micro gear pump is lower than *50 °C* by turning the chiller unit on.
11. Open the valves between the liquid tank and flow loop and turn the gear pump on to provide the de-ionized water go around through the flow loop.

The experimental rig is now ready for performing experiments for both single-phase and two-phase flow tests after the above preparation stage completed.

3.6.2 Single-phase experiments procedures

Single-phase experiments were conducted in the current study to obtain the friction factor and heat transfer data. Adiabatic experiments were conducted to obtain friction factor data. Afterwards, diabatic experiments were also performed to obtain heat transfer data. The procedures for both types of experiments are presented in this section. Consequently, the procedures for adiabatic experiments are stated step by step as follows:

1. Complete the preparation stage, as presented in section 3.6.1.
2. Regulate the micro-gear pump speed to the desired mass flux. Check the mass flux value on the LabView software program.
3. Turn on the rope pre-heater to adjust the inlet liquid temperature at the desired value. Note that, the inlet temperature for the single-phase experiments were *35 °C*. So that, the rope pre-heater was sufficient to provide adequate pre-heating in the single-phase experiments.
4. After the inlet liquid temperature reached to the desired value, wait approximately *20* minutes so that the steady-state condition is achieved in the

rig. In steady-state condition, the temperatures, pressures and mass flux data does not change significantly with time which is shown in Chapter 5.

5. Record and save temperature, pressure, mass flux and other necessary data with LabView software program during *3* minutes.
6. Increase the micro-gear pump speed to the other mass flux values and repeat step 3-5.
7. After saving the data at the maximum required mass flux, decrease the micro-gear pump speed to the recorded mass flux values and repeat step 3-5.
8. After finishing experiment, turn the rope pre-heater micro-gear pump and chiller unit off, respectively. After turning the computer off, switch off the main power supply.

Similarly, the procedures for diabatic experiments can be described as follows:

1. Perform the step 1-3 for the adiabatic experiments.
2. Switch the power supply on and adjust the power to the desired value. Note that, the adjusted power value should not be as high as to cause boiling in the test section.
3. After setting the power to the desired value, wait approximately *20* minutes to reach steady-state condition.
4. Record and save all data including temperatures and mass flux using LabView software program during 3 minutes.
5. Increase the micro-gear pump speed to the other mass flux values and repeat step 3 and 4.
6. After saving the data at the maximum required mass flux, decrease the micro-gear pump speed to the recorded mass flux values and repeat step 3-5.
7. After finishing the experiment, turn the rope pre-heater and power supply off, decrease the mass flow rate and turn the micro-gear pump and chiller unit off. After turning the computer off, switch off the main power supply.

3.6.3 Flow boiling experiments procedures

In this study, flow boiling experiments were conducted to obtain the flow boiling heat transfer coefficient, flow patterns and flow boiling pressure drop data for the operational mass flux and heat flux input. The procedures for flow boiling experiments are described step by step as follows:

1. Perform the preparation stage including de-gassing procedure carefully.
2. Regulate the micro-gear pump speed to the desired mass flux. Check the mass flux value on the LabView software program.
3. Turn on the rope pre-heater and electric pre-heater to adjust the inlet liquid temperature at the desired value. Note that, the electric pre-heater is controlled by the PIV controller. Since the PIV gives sinusoidal power input, the electric pre-heater temperature should be adjusted gradually so as not to initiate boiling inside the electric pre-heater.
4. After the inlet liquid temperature has reached the desired value, wait approximately *20* minutes so that the steady-state condition is achieved in the rig. In steady-state condition, the temperatures, pressures and mass flux data do not change significantly with time.
5. Switch the power supply on and increase the power gradually until the boiling process initiates inside the test section. After the steady-state condition is achieved, save the data. Increase the power input gradually and record all data in each step. Do not increase the power when either the microchannel wall temperature reaches approximately *130 °C* or the dryout condition is reached. Note that, when the heat flux is increased the inlet pressure increased and mass flux decreased under flow boiling conditions. Therefore, the inlet pressure and mass flux should be adjusted to retain constant at each power input step. This can be done by decreasing the temperature in the liquid tank. Also, at each power step at flow boiling conditions record flow visualization at near inlet, near middle and near outlet of the microchannels with high-speed camera and stereo microscope.

6. Increase the micro-gear pump speed to the other mass flux values and repeat step 5.
7. After finishing the experiment, turn the power supply, rope pre-heater, electric pre-heater micro-gear pump and chiller unit off. After turning the computer off, switch off the main power supply, high-speed camera and stereo microscope.

3.7 Summary

The experimental facility was first constructed by Gedupudi (2008) to investigate flow boiling characteristics including heat transfer, pressure drop and flow patterns in silicon based microchannels. Mirmanto (2009) upgraded the pre-existed experimental facility to achieve the goals of his study. The Coriolis flowmeter was used to record the flow rate of the working fluid in the experimental facility. In the current study, the Coriolis flowmeter was replaced with the ultrasonic flowmeter. Four test sections were designed and manufactured to be used in this study. These test sections are three microchannels having the same channel length and hydraulic diameter but different aspect ratio and one microchannel having same hydraulic diameter and aspect ratio but longer in length.

A flow visualisation study was performed with the Phantom V6 high speed camera in the previous experimental facility. In the current study, a stereo microscope was integrated with the high-speed camera to improve the quality of visualisation studies. The three electric pre-heaters were replaced with one rope-preheater and one electric pre-heater in the current study to provide safe, reliable and a gradual pre-heating process. The microchannel housing, O-ring slot, top cover plate and O-ring material were modified in the current study to overcome the leaking and heat loss problems. All measuring instruments were carefully calibrated and propagated uncertainty analysis was performed. Dimensions of the microchannel heat sinks were measured carefully with microscope and scanning electron microscope with surface roughness measurements in surface profiler. After the modifications, the experimental facility became ready to perform the necessary experiments.

Chapter 4

Single-Phase Flow Results and Discussions

4.1 Introduction

The single-phase friction factor and heat transfer characteristics of the microchannel test sections are examined in this Chapter. It has commonly been assumed that the single-phase flow theory is well established compared to flow boiling theory in microchannels. Hence, the experimental facility and measurement instruments were commissioned conducting single-phase experiments prior to flow boiling experiments. The experimental friction factor and average *Nusselt* number data were evaluated for the test sections and were compared to conventional scale correlations and as well as some micro-scale correlations in laminar, transitional and turbulent regions. Moreover, the channel aspect ratio effect on single-phase friction factor and heat transfer was investigated using three microchannel test sections having the same hydraulic diameter ($D_h = 0.56\ mm$) and different channel aspect ratios ($\beta = 2.56$, 4.94 and 0.5). It is worth mentioning that the inlet pressure and temperature were $101.325\ kPa$ and $35°C$, respectively, during the single-phase experiments.

The chapter has been organised in the following way: section 4.2 deals with single-phase friction factor results. Single-phase heat transfer results are presented and discussed in section 4.3. Finally, a summary of the chapter is provided in section 4.4.

4.2 Single-phase Friction Factor

As a preliminary test, single-phase pressure drop experiments were performed with a stainless steel smooth tube to ensure the experimental equipment (pressure transducers and flowmeter) are reliable and accurate in order to measure pressure drop data. The tube was selected to be long enough having long upstream and downstream calming sections to provide a fully developed flow, see Fig. 4.1 (a). The pressure transducers having same diameter piping with the tube were inserted to a tube carefully to ensure there is no entrance and exit disturbances during the flow as shown in Fig. 4.1 (b). The inner diameter of the tube was measured with a TSER V-200 microscope and was *1.45 mm*. The length of the tube is *172 mm* and was measured between the inlet and outlet pressure transducer locations. The upstream and downstream calming sections of the tube are *140 mm*. It is worth mentioning that, the manufacturer stated the inner diameter of the tube is *1.175 mm*. However, the measurements were conducted several times with a microscope and the inner diameter of the tube was found to be different than the manufacturer's catalogue value as mentioned above.

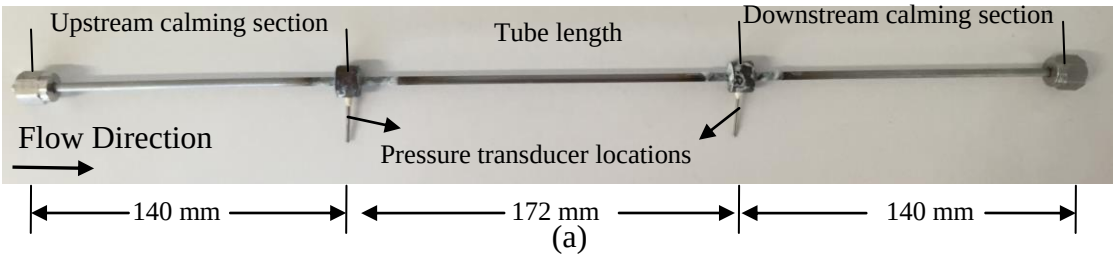

(a)

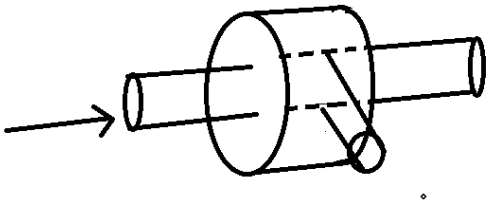

(b)

Figure 4.1 (a) Photograph of the tube test section, dimensions in mm, (b) Sketch of the pressure transducers allocation.

Previous studies have reported that measuring the channel dimensions accurately are highly important especially in micro-scale. Xu et al. (2000) and Steinke and Kandlikar (2006) stated that inaccurate measurements of the channel dimensions is one of the main sources of the differences between the theory and experimental results. Consequently, the single-phase pressure drop tests were initially evaluated using manufacturer's catalogue inner tube diameter value. The experimental results were approximately *20 %* lower than the theoretical results. Then, the experimental results were re-evaluated using the inner diameter value measured with the microscope. The experimental results agreed with the conventional scale theory proposed for tubes both in the laminar region and turbulent region as seen in Fig. 4.2. The corresponding conventional scale fanning friction factor correlations for laminar and turbulent regions are stated in Eq. (4.1) and Eq. (4.2) below.

Conventional scale laminar flow theory, Shah and London (1978):

$$f = \frac{16}{\mathrm{Re}} \tag{4.1}$$

Conventional scale turbulent flow theory, Blasius (1913):

$$f = 0.079\,\mathrm{Re}^{-0.25} \tag{4.2}$$

Figure 4.2 provides the experimental fanning friction factor results obtained from the experiments performed at two different days in order to ensure the repeatability of the measurements. The corresponding absolute errors between the experimental data and theory are in a range *5.2-5.8 %* for laminar regime and *7.9-11.1 %* for the turbulent regime.

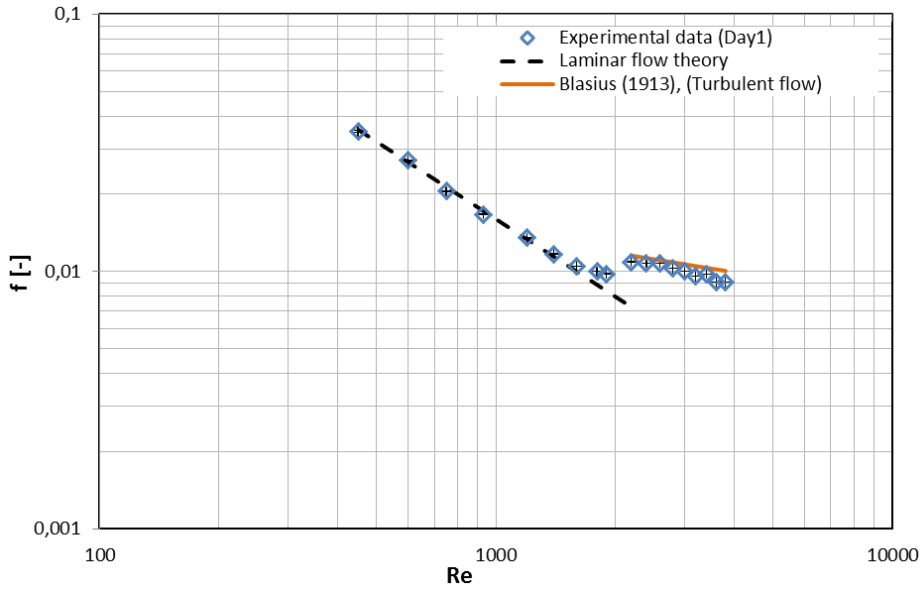

(a)

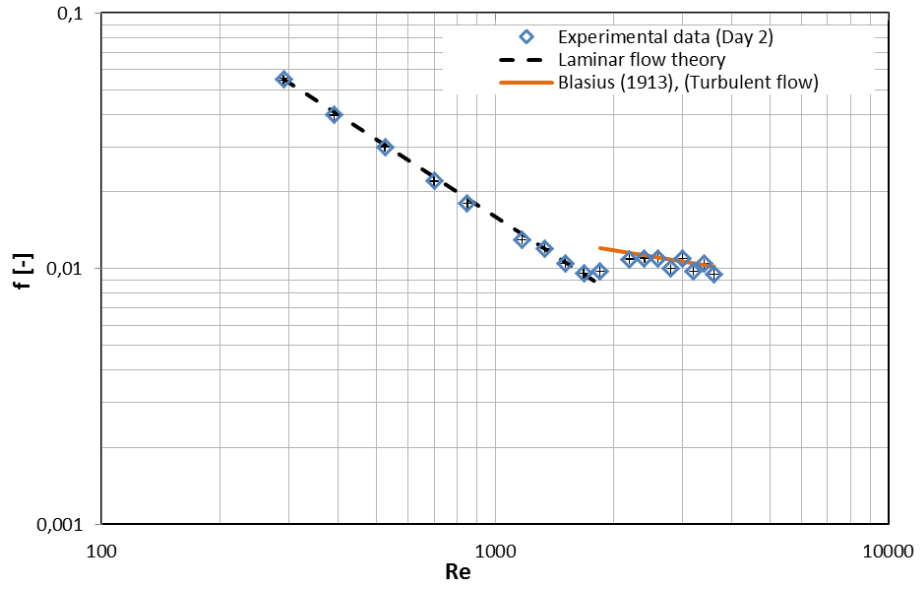

(b)

Figure 4.2 Experimental fanning friction factor results comparison laminar and turbulent flow theory for a stainless steel tube; (a) Day 1, (b) Day 2.

Accordingly, the single-phase pressure drop experiments were carried out for each microchannel test sections. However, the pressure drop values for the microchannels were not obtained directly since the pressure losses exist due to; i) *90°* turns at the inlet

and outlet, ii) sudden contraction at the inlet and sudden enlargement at the outlet. Figure 4.3 illustrates the above pressure losses clearly.

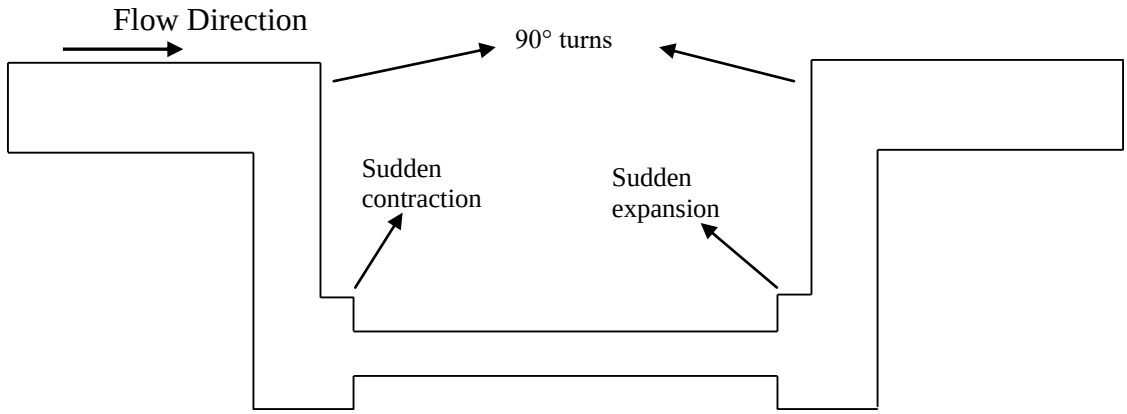

Figure 4.3 Sketch of the pressure losses in a microchannel test section in the current study.

Thus, the net pressure drop of the channel can be calculated by subtracting the pressure losses from the total pressure drop as stated in Eq. (3.5) and Eq. (3.8) of Chapter 3. The loss coefficient due to *90°* turns (K_{90}) was taken as *1.2* from Philips (1987). On the other hand, the loss coefficients due to sudden enlargement (K_e) and sudden contraction (K_c) depend on the ratio of the cross sectional area of the channel over the cross sectional area of the plenum, which is kept constant (*0.124*) for all microchannel test sections in the current study as stated in Eq. (3.1). The K_e and K_c loss coefficients were obtained from graphical information of Kays and London (1998) and found to be;

Laminar region: $K_c = 0.95$ and $K_e = 0.79$ (4.3)

Turbulent region: $K_c = 0.61$ and $K_e = 0.83$ (4.4)

As a result, the experimental friction factor (f_{ch}) is determined using Eq. 3.4 in chapter 3 for each microchannel test section. The friction factor data were compared with the conventional scale correlations for fully developed flow and developing flow both in laminar and turbulent regions; see Eq. (4.5), Eq. (4.6), Eq. (4.8) and Eq. (4.9).

Fully developed laminar flow, Shah and London(1987):

$$f_{FD} = \frac{24}{\mathrm{Re}}(1 - 1.3553\beta + 1.9467\beta^2 - 1.7012\beta^3 + 0.9654\beta^4 - 0.2537\beta^5) \tag{4.5}$$

Developing laminar flow, Shah and London (1978):

$$f_{app} = \frac{3.44}{\mathrm{Re}\sqrt{L^*}} + \frac{f_{FD}\,\mathrm{Re} + \frac{K(\infty)}{4L^*} - \frac{3.44}{\sqrt{L^*}}}{\mathrm{Re}\left[1 + \frac{C}{L^{*2}}\right]} \tag{4.6}$$

$$L^* = \frac{L}{D_h\,\mathrm{Re}} \tag{4.7}$$

Fully developed turbulent flow, Blasius (1913):

$$f = 0.079\,\mathrm{Re}^{-0.25} \tag{4.8}$$

Developing turbulent flow, Phillips (1987):

$$f_{appturb} = \left(0.0929 + \frac{1.01612 D_h}{L}\right)\mathrm{Re}^{*\left(-0.268\frac{0.3293 D_h}{L}\right)} \tag{4.9}$$

$$\mathrm{Re}^* = \mathrm{Re}(2/3 + \frac{11}{24}\beta(2-\beta)) \tag{4.10}$$

where β is the channel aspect ratio, $K(\infty)$ is the dimensionless incremental pressure drop number for fully developed flow, C is the dimensionless correction factor, L^* is the

dimensionless channel length and *Re** is an equivalent *Reynold`s* number. Phillips (1987) found that the calculated turbulent friction factor is higher than the measured friction factor for rectangular ducts. He attributed this to the fact that the turbulent friction factor is a strong function of the channel aspect ratio. Therefore, the equivalent *Reynold's* number proposed by Phillips (1987) was used in this study. The values of *K(∞)* and *C* are interpolated from the table that was provided by Shah and London (1978) and are given in Table 4.1.

Table 4.1 K(∞) and C values for all test sections.

	TS1	TS2	TS3	TS4
K(∞)	1.152	0.934	1.28	1.152
C	1.6087×10^{-4}	7.71×10^{-5}	2.1×10^{-4}	1.6087×10^{-4}

4.2.1 Friction factor results

The experimental friction factor data comparison with conventional scale fully developed and developing flow correlations for each test section are presented in Fig. 4.4.

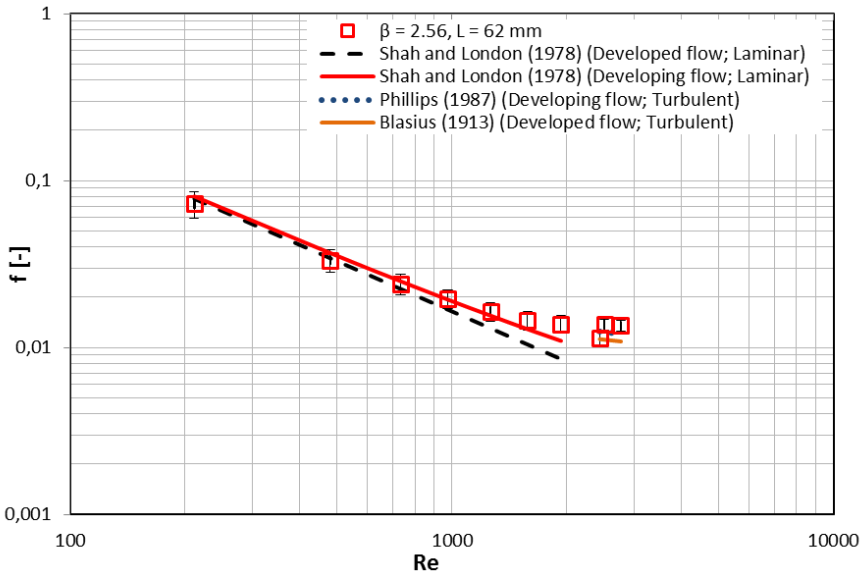

(a)

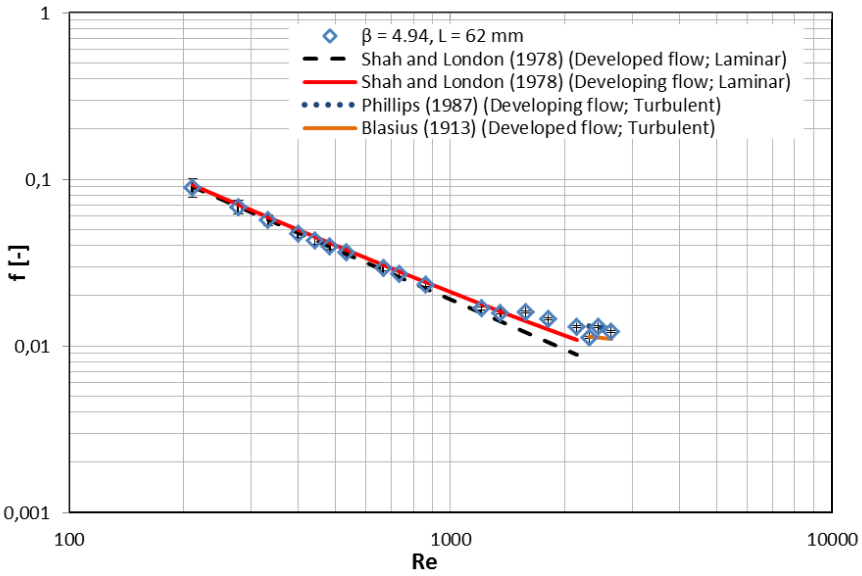
β = 4.94, L = 62 mm
Shah and London (1978) (Developed flow; Laminar)
Shah and London (1978) (Developing flow; Laminar)
Phillips (1987) (Developing flow; Turbulent)
Blasius (1913) (Developed flow; Turbulent)
1
0,1
0,01
0,001
f [-]
100
1000
10000
Re

(b)

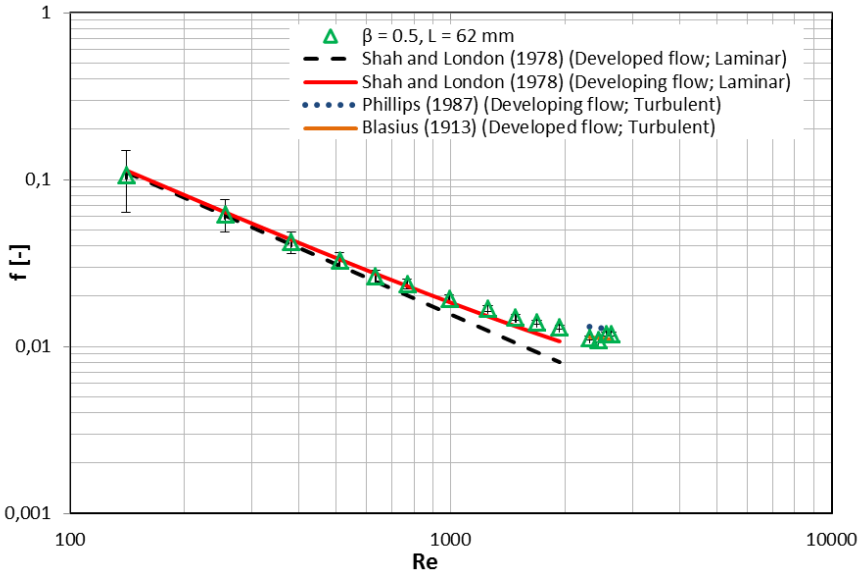
β = 0.5, L = 62 mm
Shah and London (1978) (Developed flow; Laminar)
Shah and London (1978) (Developing flow; Laminar)
Phillips (1987) (Developing flow; Turbulent)
Blasius (1913) (Developed flow; Turbulent)
1
0,1
0,01
0,001
f [-]
100
1000
10000
Re

(c)

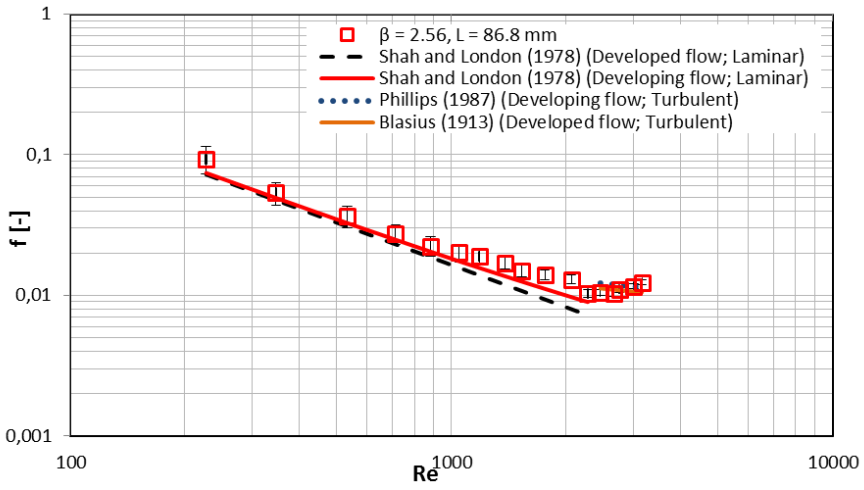

(d)

Figure 4.4 Single-phase friction factor comparison with laminar and turbulent flow correlations: (a) test section 1, (b) test section 2, (c) test section 3, (d) test section 4.

The figure shows that there has been a slight shift from fully developed flow theory to developing flow theory in the friction factor data as *Reynolds* number increase in laminar region for each test section. The developing laminar flow theory reasonably predicted the experimental data for all test sections with a Mean Absolute Error (*MAE*) of *3.5-12.4 %*. A possible explanation for this might be that the flow could not be fully developed due to the sharp *90°* turn and the contraction at the entrance disturbing the flow and causes the entrance effect. Accordingly, the hydrodynamically developing lengths were calculated using equation (4.11) that was proposed for a circular tube in the laminar region as Shah and Bhatti (1987):

$$L_{hy} = 0.056\,\mathrm{Re}\,D_h \tag{4.11}$$

Equation 4.11 is given for laminar flows ($Re \leq 2100$). Also, it can be seen from equation (4.11) that the hydrodynamically developing length is a function of *Reynold's* number and the hydraulic diameter of the channel. As the hydraulic diameters of the test sections are similar, the hydrodynamically developing lengths would be the same for all test sections at the same *Reynold's* number. Table 4.2 illustrates the hydrodynamically developing lengths for the test sections at different *Re* numbers. Also the percentage

values of the hydrodynamically developing lengths of the total channel length are included in Table 4.2 columns 3 and 4 to see the effect more clearly. According to these findings, we can infer that the flow is obviously under the effect of hydrodynamically developing flow even at low *Re* numbers. On the other hand, the experimental data are reasonably well predicted with a range of *MAE 4.2-13.2 %* and *9.1-12.4 %* by fully developed turbulent flow theory and developing turbulent flow theory, respectively, for the tested microchannel test sections. Overall, these results indicate that conventional theory is suitable to predict single-phase flow friction factor in these tested microchannels and at these experimental conditions.

Table 4.2 Hydrodynamically developing lengths for each test section.

Test sections 1,2,3 and 4			
Re	L_{hy} (mm)	L_{hy} */L (%)*, Test section 1, 2 and 3	L_{hy} */L (%)*, Test section 4
210.7	6.7	10.8	7.7
441.3	14	22.6	16.1
862.3	27.3	44	31.5
1207	38.2	61.6	44
1485	47	75.8	54.1
1808	57.3	92.4	66
2147	68	109.7	78.3

Furthermore, it can be deduced from Fig. 4.4 that the laminar to turbulent transition occurred at *Reynolds* numbers between *1500* and *2000* for the tested microchannels. These findings are in line with those of previous studies such as Harms et al. (1999), Lee et al. (2005), Mirmanto (2012) and Zhang et al. (2014). Harms et al. (1999) carried out an experimental study with de-ionized water in a rectangular microchannel (D_h =

404 μm) over a range of *Reynolds* number from *173* to *12900*. They found that the flow became turbulent at *Re~1500*. The authors attributed this to the existence of entrance effects since the flow was developing in their study. Similarly, Zhang et al. (2014) reported that the laminar to turbulent transition occurred at *Re = 1200-1600*. They investigated the flow and heat transfer characteristics of six microchannels with hydraulic diameters ranging from *480* to *840 μm* and aspect ratio varying from *1.14* to *2.22* using water. Moreover, the authors reported that channel aspect ratio has no relationship with early transition. On the other hand, some other studies in the literature reported that the laminar to turbulent transition in microchannels appeared at similar *Re* numbers *(~1800-2300*) as in conventional scale channels if the entrance and roughness effects are negligibly small, see Sharp and Adrian (2004), Celata et al. (2006) and Wibel and Ehrhard (2009). Wibel and Ehrhard (2009) tested rectangular stainless steel microchannels having the average roughness of the channel walls are about *1-2 μm* in general and specific channels are of roughness about *25 μm*. They reported that the transition from laminar to turbulent flow for smooth channels are in the *Re* number range of *1900-2200*. On the other hand this transition value was around *Re 1000* for the rough channels. They concluded that channel roughness has a strong influence on laminar to turbulent transition. Similarly, Natrajan and Christensen (2010) performed an experiment with three rectangular microchannels having smooth and rough surfaces (with RMS roughness heights of *7.51 μm* and *15.1 μm*). The results indicated that transition from laminar flow to turbulent flow occurred at *Re~1800* for the smooth channel. However, transition took place at lower *Re* numbers for rough channels (*Re~1500* and *Re~1300*).

Taken together, the above findings imply that there is an association between laminar to turbulent transition *Re* number and entrance effect (developing flow). The 90° sharp entrance and sudden contraction causes a flow disturbance and leads to achieve the turbulent flow earlier. It can be also seen from Fig. 4.2 (the stainless steel tube data) that the transition takes place around *Re* number ~ 1800-2000 when there is no disturbance in the flow. In summary, the slight early laminar to turbulent flow transition than the conventional channels in this study can be attributed to developing flow conditions.

4.2.2 Effect of aspect ratio on the friction factor

The effect of channel aspect ratio on the single-phase friction factor was also investigated in the current study. Hence, the experimental friction factor data for three microchannel test section are compared in Fig. 4.5. The figure shows that the friction factor is not affected significantly by the channel aspect ratio for the three test sections at similar *Re* numbers. The friction factor in the wider channel ($\beta = 4.94$) was slightly higher than the other channels in the laminar region. But, the difference is not notable. Some studies in the literature proposed that channel aspect ratio has an influence on single-phase friction factor. However, in those studies the channel aspect ratio and the hydraulic diameters of the channels were varied together, see Chapter 2 page 10-17, therefore failing to explain the effect of aspect ratio on single phase-friction factor due to the aforementioned reason. In the current study, the hydraulic diameter and length of the each test section were kept constant ($D_h = 0.56$ *mm* and $L = 62$ *mm*) while the channel aspect ratio was varied (*0.5, 2.56* and *4.94*). Sahar et al. (2015) investigated numerically the effect of aspect ratio and hydraulic diameter on single-phase flow and heat transfer in a single microchannel. They varied the channel aspect ratio from *0.1* to *2.56* while the hydraulic diameter and channel length were kept constant at *0.56 mm* and *62 mm*, respectively. They reported that the aspect ratio has an insignificant effect on the friction factor for aspect ratio values from *0.5* to *2.56*. These findings are consistent with data obtained in the current experimental study. However, the friction factor increased with decreasing aspect ratio in the aspect ratio range *0.5-0.1* in their study. It is worth to mention that, the design of the numerical model of Sahar et al. (2015) is identical with the current study such that the de-ionised water enters and leaves the channel in a similar way to the test section. The numerical model results also were compared to the experimental results of test section 1 and found to predict the experimental friction factor data very well, see Sahar et al. (2015). Similarly, Zhang et al. (2014) reported that the channel aspect ratio has no influence on the friction factor in a range of aspect ratio *1.58-2.22* at constant channel hydraulic diameter ($D_h = 0.61$ *mm*) over a *Re* range from *200-2800*.

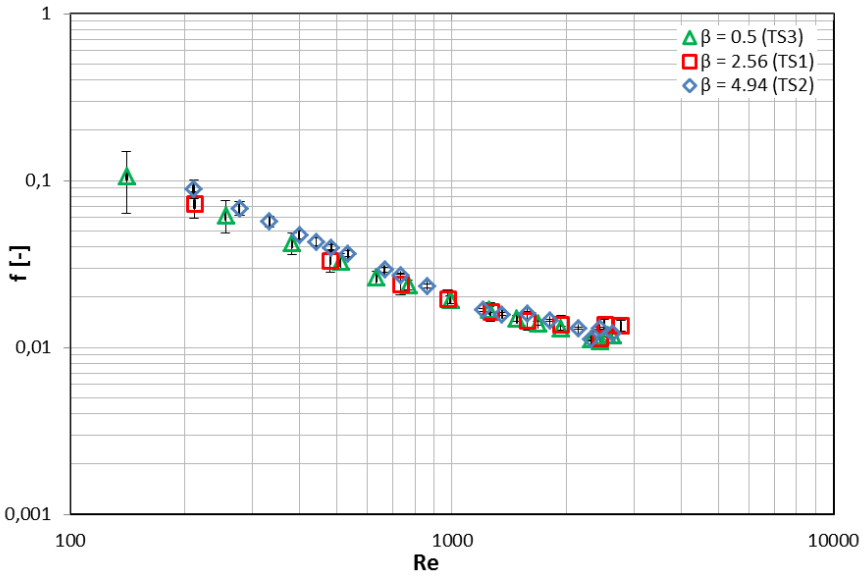

Figure 4.5 Effect of aspect ratio on friction factor for test section 1, 2 and 3.

4.3 Single-phase Heat Transfer

Single-phase heat transfer characteristics of the microchannel test sections are presented and discussed in this section. Average *Nusselt* number data are plotted versus *Reynolds* number to explain the heat transfer values. Experimental average *Nusselt* number data are also compared to conventional scale and some micro-scale correlations in laminar, transitional and turbulent regions. Additionally, the aspect ratio effect on single-phase heat transfer coefficient is assessed.

In these tests, inlet and outlet fluid temperatures were measured at the plenums and wall temperatures were obtained at six different places for the test sections 1, 2 and 3 and eight different locations for test section 4 along the channel. Heat losses from the test sections to the ambient were evaluated. Heat loss can be estimated using two different methods; i) the difference between the total power input and the sensible heat gain by the fluid under single-phase heat transfer conditions are measured and is correlated as a function of the average wall temperature for each inlet condition, ii) the test section is completely drained fluid and is then heated by applying a constant power until steady state condition is reached. The wall temperature readings from the thermocouples are then recorded over a certain time period (three minutes in this study) and averaged. The tests are repeated for different levels of input power. The average wall temperature is

then correlated to the input power and a linear relationship is obtained. In the current study, both techniques were performed and no significant difference was observed (~ *1.1 %*). Therefore the heat losses from the test sections were obtained using second technique as stated in Chapter 3.

The polycarbonate top cover was assumed to be adiabatic. That is why, the uniform heat flux assumption were applied in the axial and transverse direction of the channel on three walls. However, the average *Nusselt* number was also calculated using a uniform wall temperature boundary condition for test section 1 by using equations 4.12, 4.13 and 4.14. Figure 4.6 illustrates the average Nusselt number predictions using both methods for test section 1. It is apparent from this figure that the difference between the two methods is negligibly small (*MAE = 4.6 %*).

$$\overline{Nu}_{LMTD} = \bar{h}_{LMTD} \frac{D_h}{k_l} \tag{4.12}$$

$$\bar{h}_{LMTD} = \frac{q''}{\Delta T_{LM}} \tag{4.13}$$

$$\Delta T_{LM} = \frac{T_o - T_i}{\ln\left[\frac{\overline{T_{wall}} - \overline{T_i}}{T_{wall} - T_o}\right]} \tag{4.14}$$

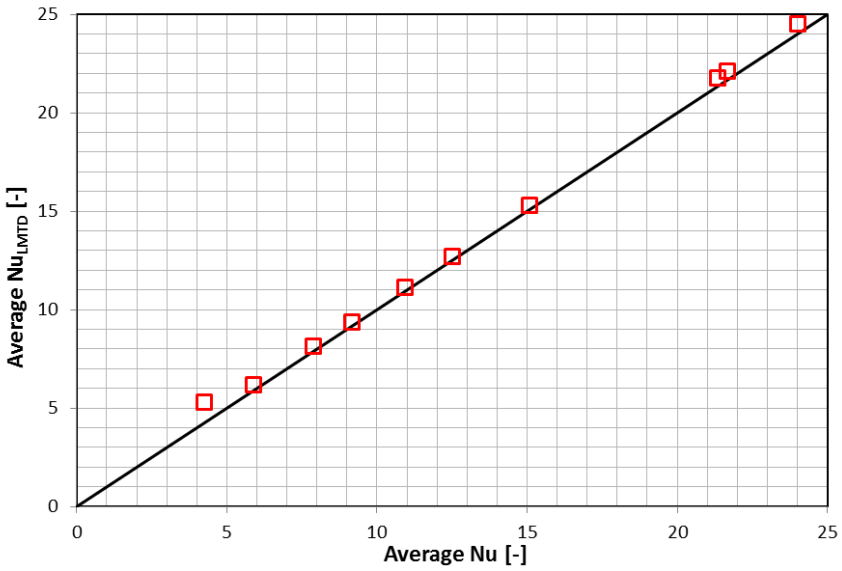

Figure 4.6 Average Nu number comparison using two methods for test section 1.

Thus, the average *Nusselt* number data for each test section was obtained using constant heat flux boundary condition in the current study. Results were compared to selected conventional scale fully developed and developing flow correlations and some micro-scale correlations. The correlations are given below:

Fully developed laminar flow, Shah and London (1978):

$$\overline{Nu} = 8.235(1 - 10.6044\beta + 61.1755\beta^2 - 155.1803\beta^3 + 176.9203\beta^4 - 72.9236\beta^5) \quad (4.15)$$

Developing laminar flow, Shah and London (1978):

$$\overline{Nu} = 0.775 L^{*-1/3} 15^{1/3} \quad (4.16)$$

$$L^* = \frac{L}{\mathrm{Re}\,\mathrm{Pr}\,D_h} \quad (4.17)$$

Fully developed turbulent flow, Dittus Boelter (1930):

$$\overline{Nu} = 0.026\,\mathrm{Re}^{0.8}\,\mathrm{Pr}^{0.3} \tag{4.18}$$

Developing turbulent flow, Petukhov-Popov (1963):

$$\overline{Nu} = \frac{\frac{fp}{2}\,\mathrm{Re}\,\mathrm{Pr}}{C + 12.7\left[\frac{fp}{2}\right]^{0.5}(\mathrm{Pr}^{2/3} - 1)} \tag{4.19}$$

$$fp = 0.00128 + 0.1143\,\mathrm{Re}^{-0.311} \tag{4.20}$$

$$C = 1.07 + \frac{900}{\mathrm{Re}} - \left[\frac{0.63}{1 + 10\,\mathrm{Pr}}\right] \tag{4.21}$$

Developing laminar flow, Mirmanto (2012):

$$\overline{Nu} = \mathrm{Re}^{0.283}\,\mathrm{Pr}^{-0.513}\,L*^{-0.309} \tag{4.22}$$

Developing turbulent flow, Mirmanto (2012):

$$\overline{Nu} = 0.032\,\mathrm{Re}^{0.841}\,\mathrm{Pr}^{-0.51}\,L*^{-0.153} \tag{4.23}$$

4.3.1 Heat transfer results

The average *Nusselt* number results for each test section are set out in Figure 4.7. The figures reveal that the average *Nusselt* number increases with *Reynolds* number in the laminar regime for all test sections conversely to the fully developed heat transfer theory. The most likely reason of this trend, calming section was not introduced to the

test sections in the current study. Therefore, the flow seems to be thermally developing flow. A strong relationship between heat transfer enhancement and thermal entrance region has been reported in the literature. The thin thermal boundary layer in the thermally developing region could increase the heat transfer compared to the thermally fully developed region in the laminar regime. The thermally developing entrance length can be determined with the Shah and London (1978) equation which is given below.

$$L_{th} = 0.056 \,\mathrm{Re}\, D_h \,\mathrm{Pr} \tag{4.24}$$

Table 4.3 illustrates the thermal entrance length for all test sections at different *Reynolds* numbers. From the table, it is clear that the thermal entrance lengths are occupying nearly half of the total channels length even at the smallest *Reynolds* number of *211.4*. These findings further support the idea of thermally developing flow presence in the laminar regime for all test sections. In addition, figure 4.7 shows that the transition *Reynolds* number from laminar to turbulent regime is around *1500-2000* which is consistent with the results obtained from the friction factor data.

The experimental data is compared to selected published *Nusselt* number correlations. Although the Mirmanto (2012) correlation, proposed for thermally developing flows, predicted the experimental data for test section 1 and 3 (*MAE = 5.5 %* and *9.2 %*), the correlation overpredicted the experimental data for test section 2 and 4 (*MAE = 21.3 %* and *20.5 %*) in the laminar regime. In turbulent region, the correlations of Petukhov - Popov (1963), Dittus - Boelter (1930) and Mirmanto (2012) predicted the experimental data well (*MAE = 0.8-2.5 %* and *4.6-5.8 %*) for test section 1 and 3. However, the correlations predicted reasonably the experimental data for test section 2 and 4 (*MAE = 18.9-23 %* and *12.6-18.1 %*).

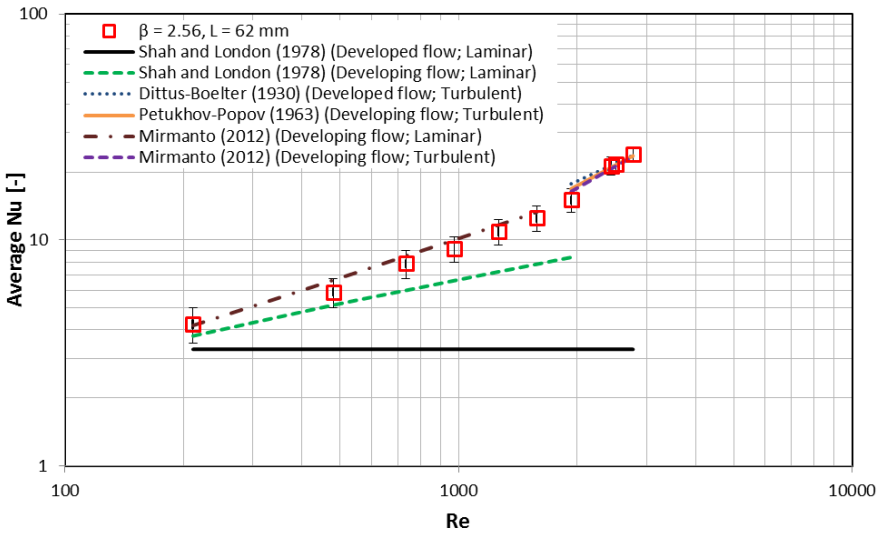
β = 2.56, L = 62 mm
Shah and London (1978) (Developed flow; Laminar)
Shah and London (1978) (Developing flow; Laminar)
Dittus-Boelter (1930) (Developed flow; Turbulent)
Petukhov-Popov (1963) (Developing flow; Turbulent)
Mirmanto (2012) (Developing flow; Laminar)
Mirmanto (2012) (Developing flow; Turbulent)
Average Nu [-]
100
10
1
100
1000
10000
Re

(a)

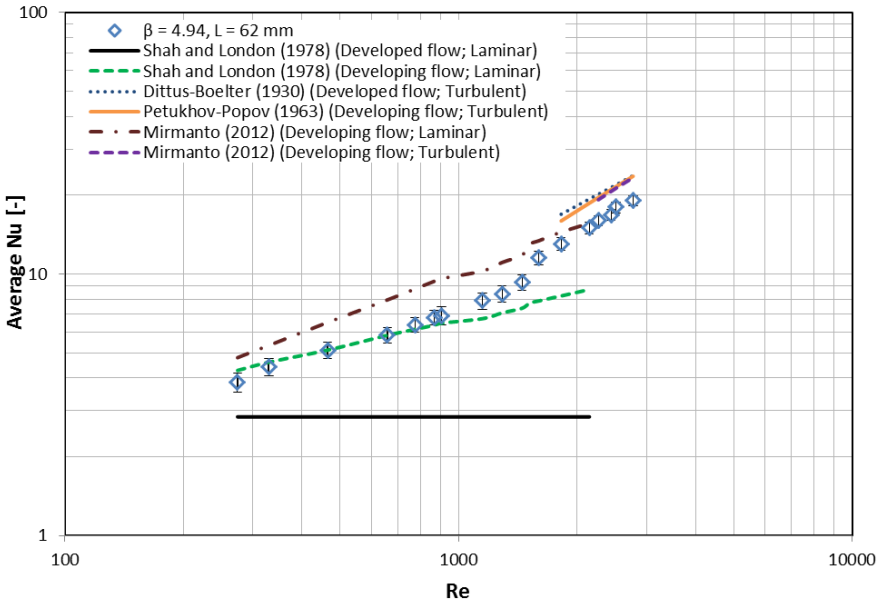
β = 4.94, L = 62 mm
Shah and London (1978) (Developed flow; Laminar)
Shah and London (1978) (Developing flow; Laminar)
Dittus-Boelter (1930) (Developed flow; Turbulent)
Petukhov-Popov (1963) (Developing flow; Turbulent)
Mirmanto (2012) (Developing flow; Laminar)
Mirmanto (2012) (Developing flow; Turbulent)
Average Nu [-]
100
10
1
100
1000
10000
Re

(b)

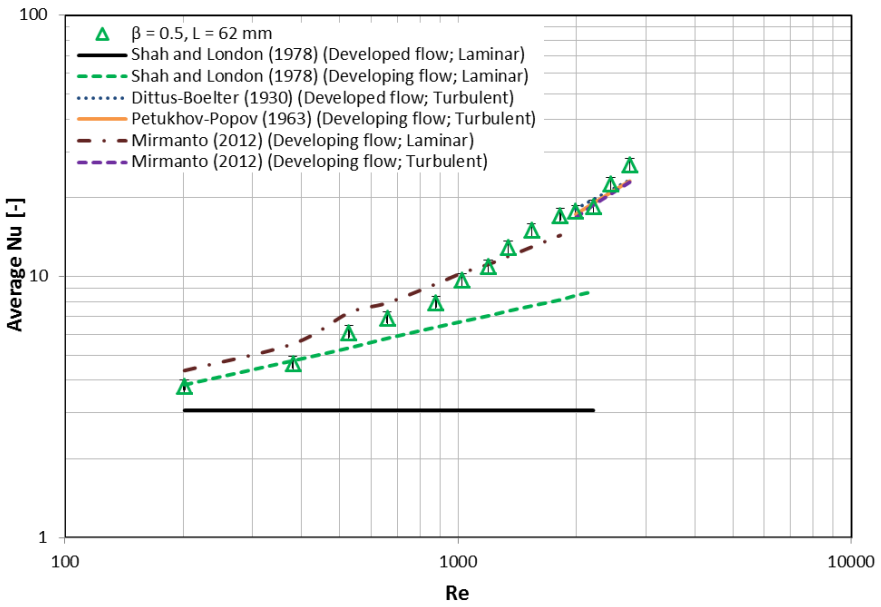

(c)

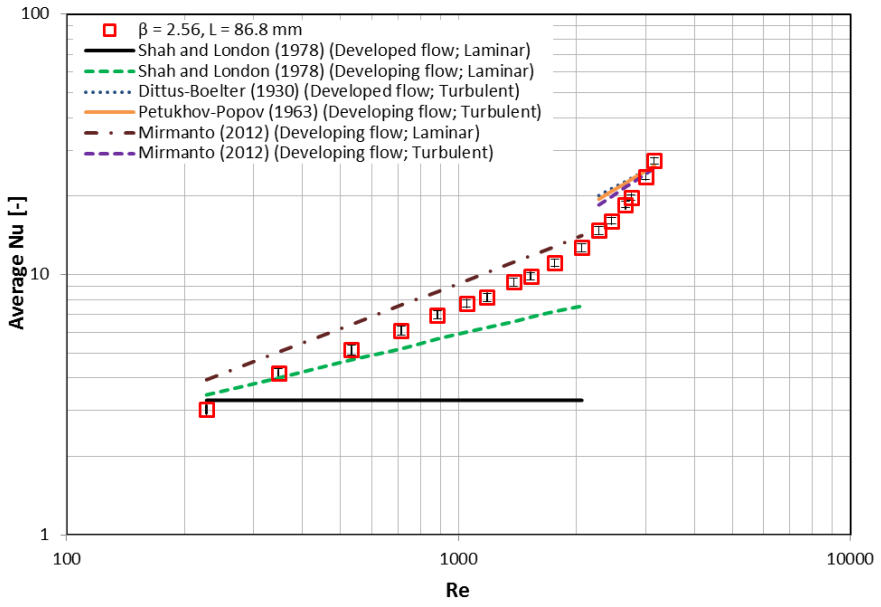

(d)

Figure 4.7 Average Nusselt number comparison with conventional and micro-scale laminar and turbulent flow correlations: (a) test section 1, (b) test section 2, (c) test section 3, (d) test section 4.

Table 4.3 Thermally developing lengths for each test section.

Test sections 1,2,3 and 4			
Re	L_{th} (mm)	L_{th}/L *(%)*, Test section 1, 2 and 3.	L_{th}/L *(%)*, Test section4.
211.4	26.6	42.9	30.5
480.1	68.08	109.8	71.2
734.4	106.8	172.2	114.7
975	144.1	232.4	152.5
1262	188.7	304.4	207.2
1578	237.7	383.4	261.3
1931	292.9	472.4	320.2

4.3.2 Effect of aspect ratio on the heat transfer

The channel aspect ratio effect on single-phase heat transfer coefficient was also investigated. Figure 4.8 depicts the average *Nusselt* number data comparisons for test section 1, 2 and 3 for a broad *Reynolds* number range. The figure shows that the heat transfer performance of test section 1 ($\beta = 2.56$) is higher than the other test sections up to around *Reynolds* number *700*. However, the average *Nusselt* number of test section 3 ($\beta = 0.5$) started to be superior after *Reynolds* number *700*. On the other hand, the heat transfer performance of test section 2 ($\beta = 4.94$) seems to be slightly lower compared to test section 1 and 3. However, no significant channel aspect ratio effect on the single-phase heat transfer coefficient can be identified based on these results. All these results are within the experimental error range as can be seen in figure 4.8. In the same way, Sahar et al. (2015) reported that the channel aspect ratio dependence on the single-phase heat transfer coefficient is insignificant. Similarly, Zhang et al. (2014) found that, the aspect ratio ranging from *1.58* to *2.22* with constant hydraulic diameter ($D_h = 0.61\ mm$) does not have a significantly effect on the heat transfer process in rectangular microchannels.

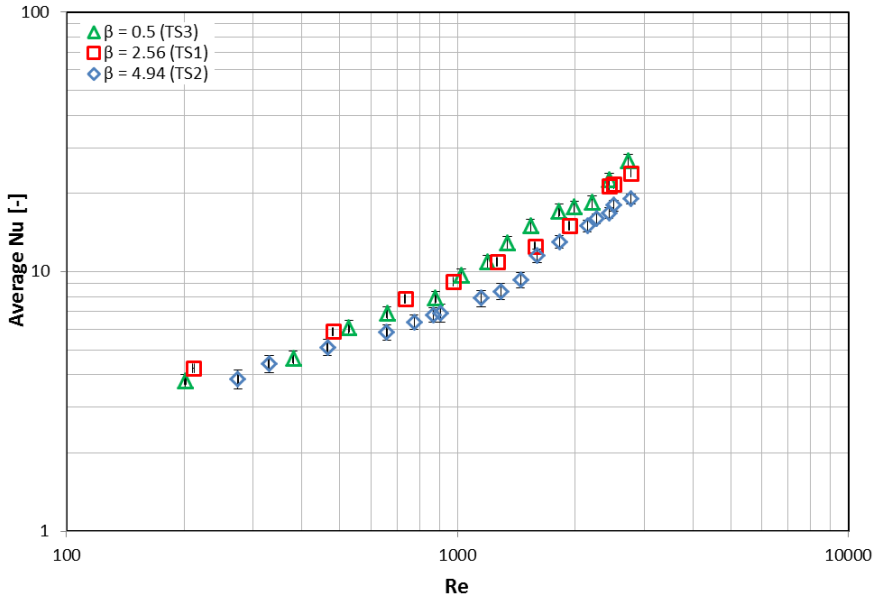

Figure 4.8 Effect of aspect ratio on average Nusselt number for test section 1, 2 and 3.

4.4 Summary

In this section, the results of single-phase friction factor and heat transfer experiments for all microchannel test sections were presented. In this investigation, the experimental apparatus were validated using a stainless steel tube. The experimental friction factor data for a stainless steel tube agreed with the conventional scale fully developed flow correlations over the experimental range (*Re = 150-3800*) .

Accordingly, the experimental friction factor data of the microchannel test sections were compared to conventional scale correlations. The Shah and London (1978) developing flow correlation reasonably predicted the experimental friction factor data in the laminar regime. These results are likely to be related to the presence of hydrodynamically developing flow conditions for all test sections. Another important finding was that the laminar to turbulent transition region was found to be consistent with previously published results. Furthermore, the experimental friction factor was predicted fairly well by the conventional scale developing flow and fully developed flow correlations in the turbulent regime. The effect of the channel aspect ratio on the single-phase friction factor was also investigated using three microchannel test sections having the same

hydraulic diameter and length but different channel aspect ratio. It is concluded that the channel aspect ratio has no significant effect on the friction factor.

The experimental *Nusselt* numbers are in reasonable agreement with the correlation of Mirmanto (2012) and the Shah and London (1978) thermally developing flow theory in the laminar region. Accordingly, thermal entrance lengths were calculated and it was found that the thermally developing flow conditions are strongly dominant during the tests. In turbulent flow, the experimental *Nusselt* numbers were predicted well with correlations proposed by Dittus-Boelter (1930), Petukhov-Popov (1963) and Mirmanto (2012) for test sections 1 and 3. On the other hand, these correlations predicted reasonably the experimental *Nusselt* numbers of test section 2 and 4. Finally, the channel aspect ratio effect on experimental *Nusselt* number was assessed. The analysis showed that, the channel aspect ratio has no significant effect on experimental *Nusselt* number for the tested microchannels.

Chapter 5

Flow Boiling Heat Transfer and Flow Patterns Results and Discussions

5.1 Introduction

The fifth chapter introduces the findings of the research, focusing on the two key themes, namely flow boiling patterns and flow boiling heat transfer characteristics in the four investigated microchannel test sections. Three test sections have different channel aspect ratio and the same hydraulic diameter and channel length to present channel aspect ratio effect. The other test section has *0.56 mm* hydraulic diameter, *2.56* aspect ratio and *86.8* mm channel length which is provided to understand the local heat transfer coefficient trend in regard to vapour quality one. The inlet temperature and pressure were kept constant at *89°C* and *115 kPa*, respectively during the experiments. The heat transfer results are explained with the help of the local heat transfer coefficient versus local vapour quality and axial distance versus local heat transfer coefficient graphs. The boiling curves for each test section are also plotted and discussed. Moreover, the experimental flow boiling heat transfer coefficients are compared with selected macro and micro scale correlations.

This study mainly intends to examine the heat transfer process. However, the flow boiling patterns were also captured during the experiments at three locations (inlet region, middle region and outlet region) to enable a better understanding of the heat transfer and pressure drop results. The comparisons of the observed flow patterns with some flow pattern maps available in the literature are presented and discussed. This chapter has been divided into five sections. Section 5.1 gives an introduction for the

chapter. The flow patterns and their comparisons with existing flow pattern maps are presented in section 5.2. Section 5.3 deals with flow boiling heat transfer results and discussions whereas the comparisons of the experimental heat transfer data with flow boiling correlations are presented in section 5.4. A summary of the chapter is included in section 5.5

5.2 Flow Boiling Patterns

In this section, the visualised flow regimes are analysed and discussed. A high-speed, high-resolution camera (Phantom V6) at a speed of 814 frames per second, 512 x 256 pixel resolution and 10000 post trigger were used to record the flow patterns along the microchannels. The camera was located on top of the test section and integrated with a stereo microscope (Huvitz HSZ-600) for better flow visualization. The mass flux, heat flux and channel aspect ratio effects on the flow patterns are presented for all microchannel test sections. Additionally, the flow patterns are compared to some flow pattern maps available in the literature. As mentioned in Chapter 2 (literature review section), the universal definitions for the flow patterns in microchannels are not available. Therefore, flow patterns classification in this study is characterized and sketched in the form of line diagrams below, see figure 5.1, in order to avoid the confusion.

Bubbly flow is the two-phase flow where the vapour flows along the streamwise direction within a liquid in the form of discrete or elongated round bubbles. When the temperature of the heated surface increases above the liquid saturation temperature, bubbles nucleate and detach from the nucleation sites (cavities in the channel). The size of the bubbles is smaller than the cross-section of the microchannels in the bubbly flow. However, the size and shape of the bubbles may be different at different heat flux and mass flux operations. For example, the bubble size is smaller at higher mass fluxes compared to lower mass fluxes. The schematic drawing of the bubbly flow is depicted in Fig. 5.1 (a).

When the heat flux is increased in bubbly flow regime, the bubble generation rate becomes higher and dense resulting in *slug flow* regime where the bubbles coalesce and occupy the entire cross-section of the microchannels. The length of these elongated bubbles change at different channel dimensions and operating conditions. The elongated bubbles or slugs are separated by liquid slugs as seen in Fig. 5.1 (b).

If the applied heat flux to the system increased further, the shape and size of the formed elongated bubbles in *slug flow* become non-uniform in the shape of vapour chunks and vapour pockets. Moreover, this non-uniform shaped vapour chunks move randomly resulting in the disappearance of the interface between vapour chunks. This flow regime is named as *churn flow*. The line diagram of the churn flow is presented in Fig. 5.1 (c).

In the *annular flow* regime, continuous vapour flow is observed in the centre of the microchannel while the thin and stable liquid film is seen between the vapour core and microchannel walls as depicted in Fig. 5.1 (d). At higher heat flux values, the liquid film becomes thinner. Also in some circumstances, small spherical droplets are entrained into the vapour core.

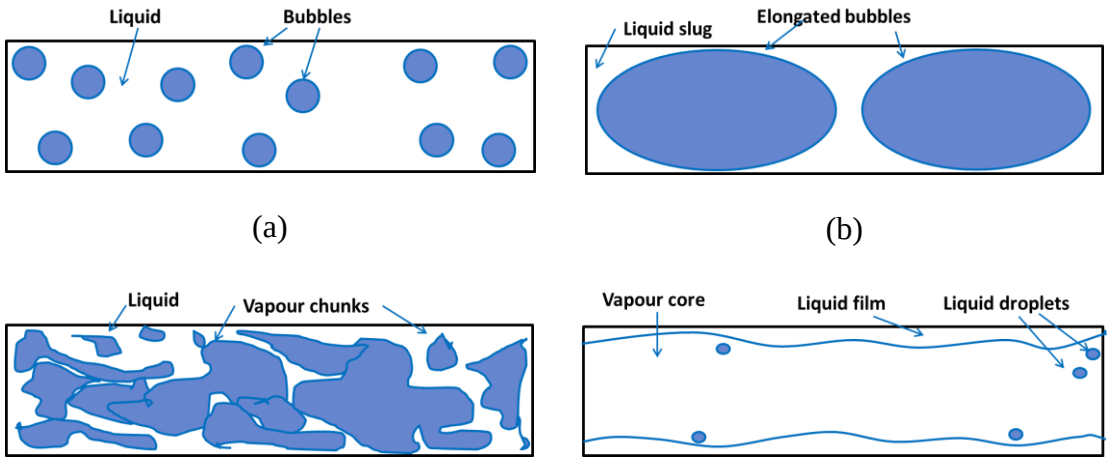

Figure 5.1 Line diagrams of the flow regimes: (a) bubbly flow, (b) slug flow, (c) churn flow and (d) annular flow.

In addition to the above flow regimes, a periodic flow regime appeared in the current study where bubbly flow, slug flow, reverse flow, local-dryout and re-wetting stages occurred periodically with pressure drop oscillations. This unstable flow regime was reported by many researchers in the literature such as Galvis and Culham (2012), Balasubramanian et al. (2013) and Markal et al. (2016). The periodic flow regime was encountered in all microchannels at the two lowest mass flux operations ($G = 200\ kg/m^2s$ and $G = 400\ kg/m^2s$) except the TS2. The formation of periodic flow regime depends on the channel geometry and test conditions which is discussed in the following sections. Figure 5.2 displays the periodic evolution of the flow pattern observed in this study for TS1 at $G = 400\ kg/m^2s$ near the middle of the channel. The figure demonstrates that small bubbles nucleate at the channel corners at time designated as $t = 0\ ms$. At this condition, the central region of the microchannel was in single-phase flow. After *5 ms*, one bubble grew and spanned the channel width with smaller bubbles still observed at the channel edges. Continuing the analysis of Fig. 5.2 it can be seen that after *6 ms*, the big bubble merged with the small bubbles and an elongated bubble was formed. The tail of this elongated bubble seems deformed (no spherical shape) while the nose of this bubble is not shown in the picture, see Fig. 5.2 ($t = 7\ ms$). This picture shows also another bubble with a spherical head coming from the inlet region. These pictures demonstrate that bubbles nucleate, grow and merge rapidly before departure from the nucleation sites. This results in the formation of an elongated bubble which expands rapidly in the upstream and downstream sides of the channel. The nose of the bubbles moves faster than the tail. This could be attributed to the partial blockage of the channel resulting from the rapid growth of the bubble, without actually departing from the nucleation site. Thus, the quantity of the liquid in the downstream side of the channel becomes smaller compared to the upstream side. Given that the heat flux is constant, this can result in higher evaporation rate downstream of the bubble (thin liquid film have less thermal resistance). The pictures indicate also that the tail of the bubble moves slowly towards the channel inlet (back flow) until another bubble comes from the entry region of the channel. After *9 ms*, the picture shows "annular-like" flow patterns but it is not annular flow. This pattern resulted from the coalescence of elongated bubbles. Additionally, this "annular-like" flow pattern was prevailing when the camera was moved to a location near the channel inlet and outlet regions. Moreover, this pattern remained in the channel for a time period resulted in local-dryout as can demonstrated at time *20 ms*. It is interesting to note that, after *22 ms*, fresh liquid

entered the channel and re-wetted the channel. After the re-wetting stage small bubbles were observed to nucleate near the channel corners again at time designated as *t = 32 ms*. This means that there is a periodic evolution of these flow patterns and the period is *32 ms* for this mass flux and this microchannel.

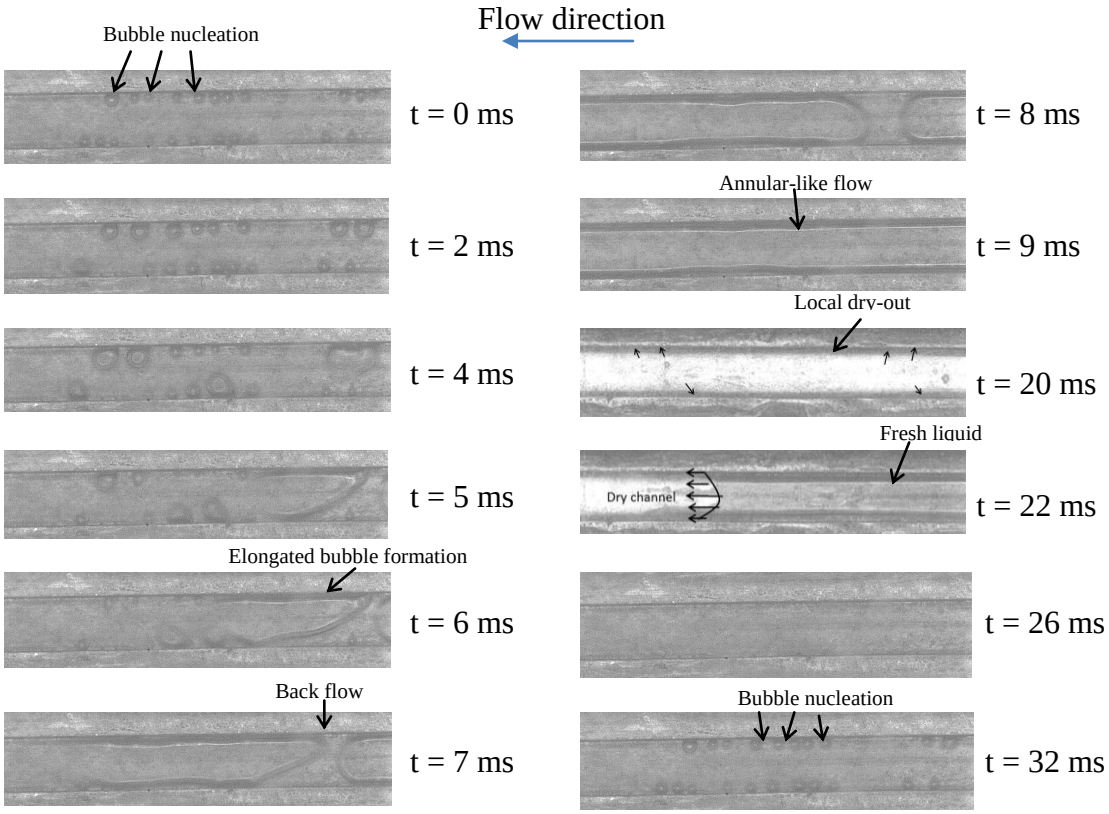

Figure 5.2 Sequence of flow images at the middle of the channel at periodic flow regime for the $\beta = 2.56$ and microchannel (TS1) at $q'' = 99.15\ kW/m^2$ and $G = 400\ kg/m^2s$.

5.2.1 Effect of Heat Flux and Mass Flux on Flow Patterns

The flow patterns exhibited different features with increasing heat flux in the microchannel test sections. Also, the flow patterns may vary at different mass fluxes and same heat fluxes. The observed flow patterns in all microchannel test sections are summarised in Figs. 5.3 (a-d) over the range of heat flux and mass flux tested. As can be seen from Figs. 5.3 (a-d) the flow patterns changed from single-phase flow to bubbly flow, bubbly flow to slug flow, slug flow to churn flow and churn flow to annular flow with the increase in heat flux for all test sections especially when the observation is

being conducted at the outlet region. A transitional flow regime (bubbly/slug flow) was also visualized frequently between the bubbly flow and slug flow regimes.

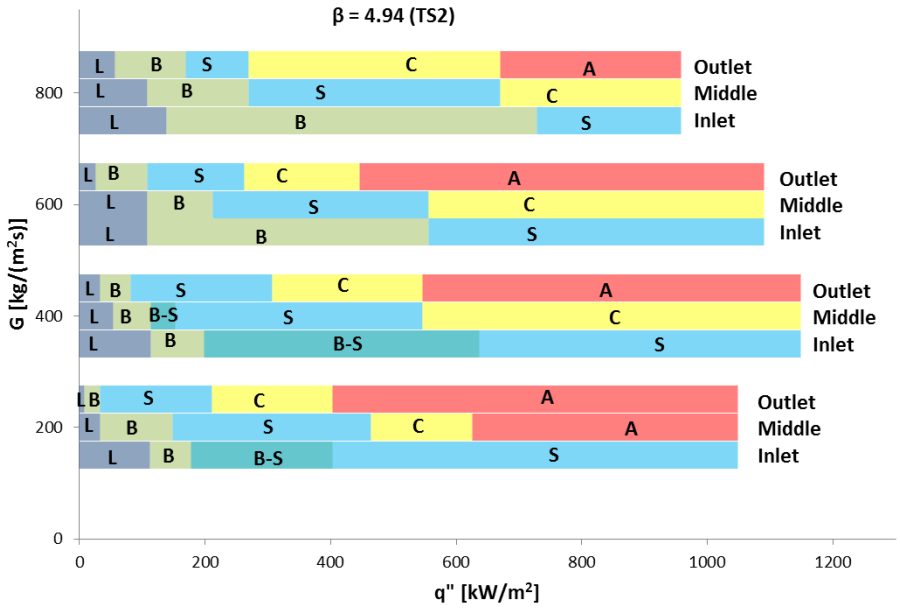

(a)

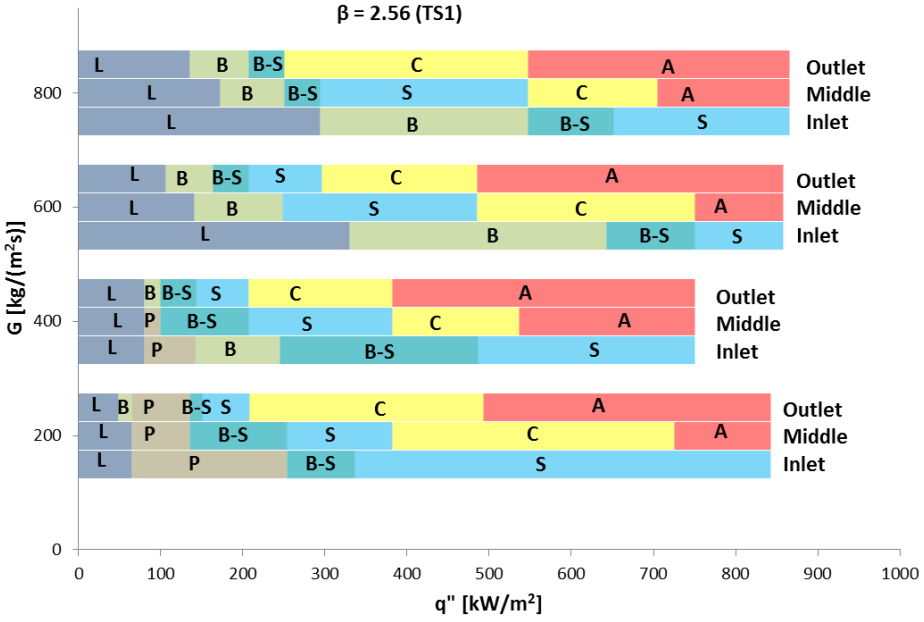

(b)

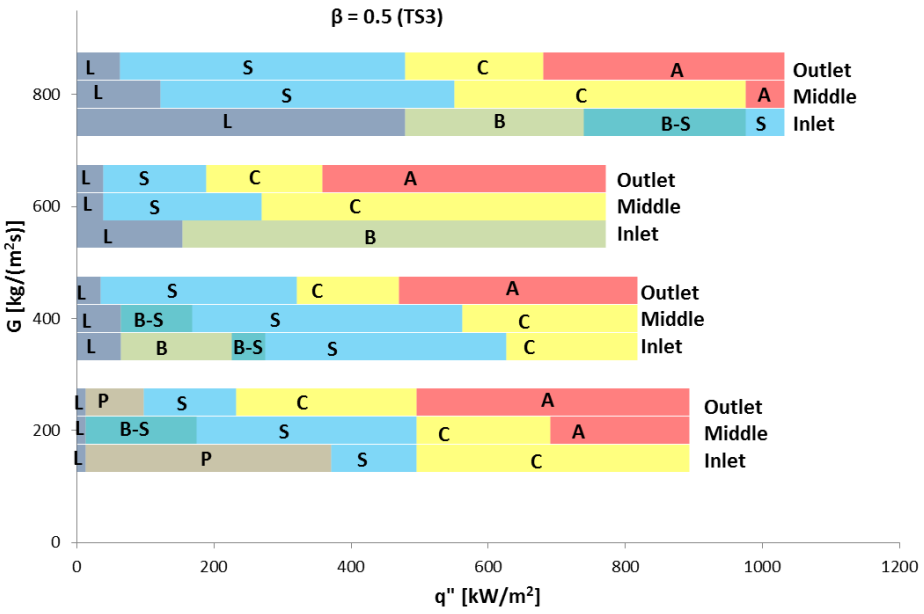

(c)

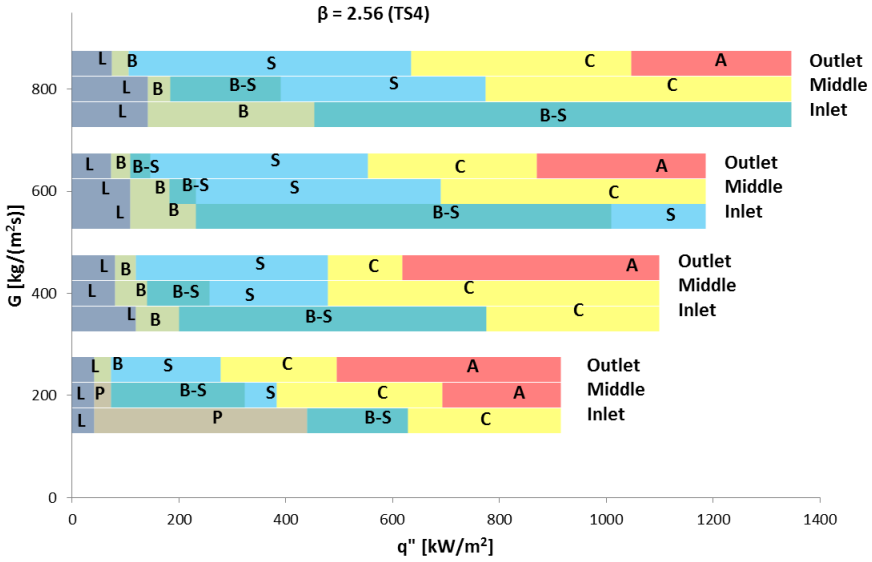

(d)

Figure 5.3 Histogram of flow boiling patterns at three locations: (a) TS2, (b) TS1, (c) TS3 and (d) TS4, L: single-phase liquid, P: Periodic flow, B: bubbly flow, B-S: Bubbly/Slug flow, S: slug flow, C: churn flow and A: annular flow.

On the other hand, bubbly flow and slug flow were the dominant flow patterns in the inlet region of the microchannels. This is because the subcooled state liquid went into the channels and heated along the channel length. Hence at a fixed heat flux the flow

pattern changed along the microchannels. For example analysing fig. 5.3 (b), at the mass flux of *600 kg/m^{2}s* and heat flux near *500 kW/m^2* the observed flow pattern was bubbly flow at the inlet region, it changed from bubbly to churn flow at the middle region and at the outlet region it transformed from churn to annular flow. Figure 5.4 shows the observed flow patterns along the microchannel length for the TS1 at the heat flux *535.6 kW/m^2* and mass flux *600 kg/m^{2}s*.

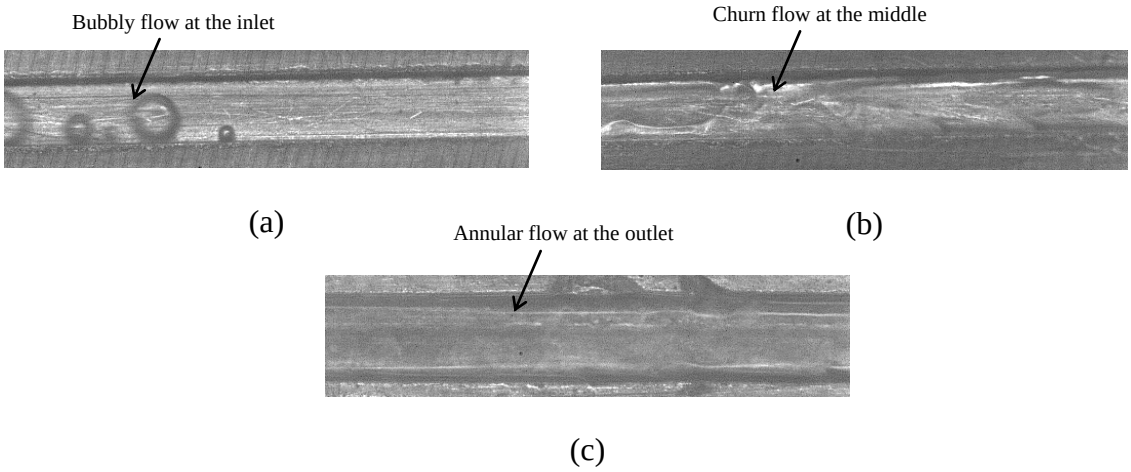

Figure 5.4 Flow patterns for the TS1 at 535.6 kW/m^2 heat flux and 600 kg/m^{2}s mass flux: (a) inlet region, bubbly flow, (b) middle region, churn flow and (c) outlet region, annular flow.

The flow patterns also change as the mass flux increase or decrease similar to heat flux. It can be seen from Figs. 5.3 (a-d) that, as the mass flux increases boiling initiates at higher heat flux values. Therefore inverse transition (annular flow to single-phase flow) between flow patterns takes place with increasing mass flux. For example, for the TS3 at *400 kW/m^2* (Fig. 5.3 (c)), the observed flow pattern was slug flow at the inlet region of the microchannel at the mass flux of *200 kg/m^{2}s*. However, it changed to bubbly flow and single-phase flow for the mass flux of *600 kg/m^{2}s* and *800 kg/m^{2}s* respectively. Similarly, for the TS2 at *600 kW/m^2* (Fig. 5.3 (a)), the observed flow pattern was annular flow rather than churn flow at the outlet region of the microchannel when the mass flux was raised from 400 kg/m^{2}s to 800 kg/m^{2}s. In addition to that, the bubbly flow diversified as the mass flux increases. For the low mass fluxes (*G = 200 kg/m^{2}s* and *G = 400 kg/m^{2}s*), bubbles occupied the entire cross-section of the microchannels except TS2 resulting in periodic flow regime as stated before. However, the sizes of the

bubbles became smaller and dispersed when the mass flux was increased to *600 kg/m^{2}s* and *800 kg/m^{2}s*. The bubbly flow patterns are presented in Fig. 5.5 for two different mass fluxes in the TS4 outlet region at the same heat flux values.

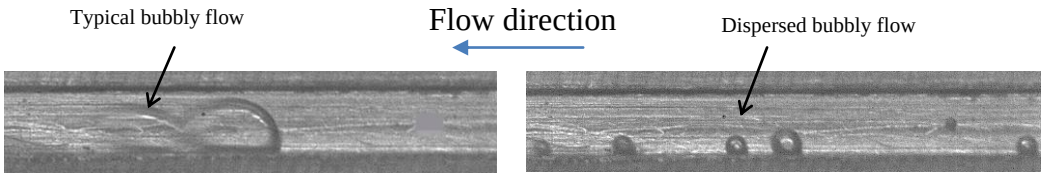

(a) (b)

Figure 5.5 Effect of mass flux on flow boiling patterns in the TS4 outlet region: (a) *q" = 135.7 kW/m^2* and *G = 200 kg/m^{2}s* and (b) *q" = 135.3 kW/m^2* and *G = 800 kg/m^{2}s*.

Periodic flow regime is attributed to periodic fast vapour expansion to the upstream and downstream of the channel in this study as discussed earlier, see figure 5.2. At higher mass flux operations (*G = 600 kg/m^{2}s and 800 kg/m^{2}s*) the periodic flow regime was not encountered since the flow rate is higher. It is because that the backward evaporation momentum force is lower than the forward liquid inertia force at higher mass fluxes, see Lee et al. (2010). These findings match those observed in the earlier studies. Galvis and Culham (2012) observed periodic flow at the mass flux of *365 kg/m^{2}s* in a single copper microchannel test sections. Similarly, Markal et al. (2016) reported periodic flow in parallel silicon microchannels in their tested mass flux range (*G = 151-324 kg/m^{2}s*). Hetsroni et al. (2003, 2005, and 2006) also reported this type of flow especially at low mass flux operations (*G = 32-340 kg/m^{2}s*). They studied flow boiling of a subcooled liquid in parallel multi-microchannels. They stated that as the bubble nucleation begins, the heat flux releases a sudden energy into the vapour bubble, which grows rapidly. This rapid bubble growth pushes the liquid-vapour interface of the vapour slugs towards to upstream and downstream location and leads to a back flow since the length of the microchannels are very small compared to conventional size channels. On the other hand, Mirmanto (2012) did not observe periodic flow regime in his experimental study conducted in *601 – 1106 kg/m^{2}s* mass flux range.

5.2.2 Effect of Aspect Ratio on Flow Patterns

The flow patterns in the three tested microchannels having the same hydraulic diameter and channel length but different channel aspect ratio are presented and discussed in this section in order to reveal the effect of aspect ratio on flow boiling patterns.

Fig. 5.6 depicts the flow patterns for the TS2 at the *400 kg/m^{2}s* mass flux value for several heat fluxes. The bubbles nucleated, detached from the nucleation sites on the surface of the channel as well as channel edge as isolated bubbles and moved along with the fluid in the flow direction. At this condition the bubbles were very small compared to the channel size and did not coalesce with each other. The flow is characterized as bubbly flow, see Fig. 5.6 (a). As the heat flux was increased more, the bubbles started to coalesce with each other and span the lateral dimension of the channel resulting in elongated slugs as shown in Fig. 5.6 (b). Periodic flow regime was not seen in this test section. The regime turned to a churn flow with increasing heat flux to higher values. This regime is shown in Fig. 5.6 (c) for a heat flux of *374.4 kW/m^2*. In this regime, the structure of the large elongated slugs and vapour pockets alternated and resulted in random motion and the interface disappeared. The tail of the slug was no longer distinguishable properly at this condition. At much higher heat flux inputs the annular flow regime appeared in the microchannel where the liquid layer was present on the wall of the channel and the continuous gas flow occurred in the centre, see Fig. 5.6 (d). Moreover, droplet entrainment was also encountered in the vapour core of the annular flow in this test section.

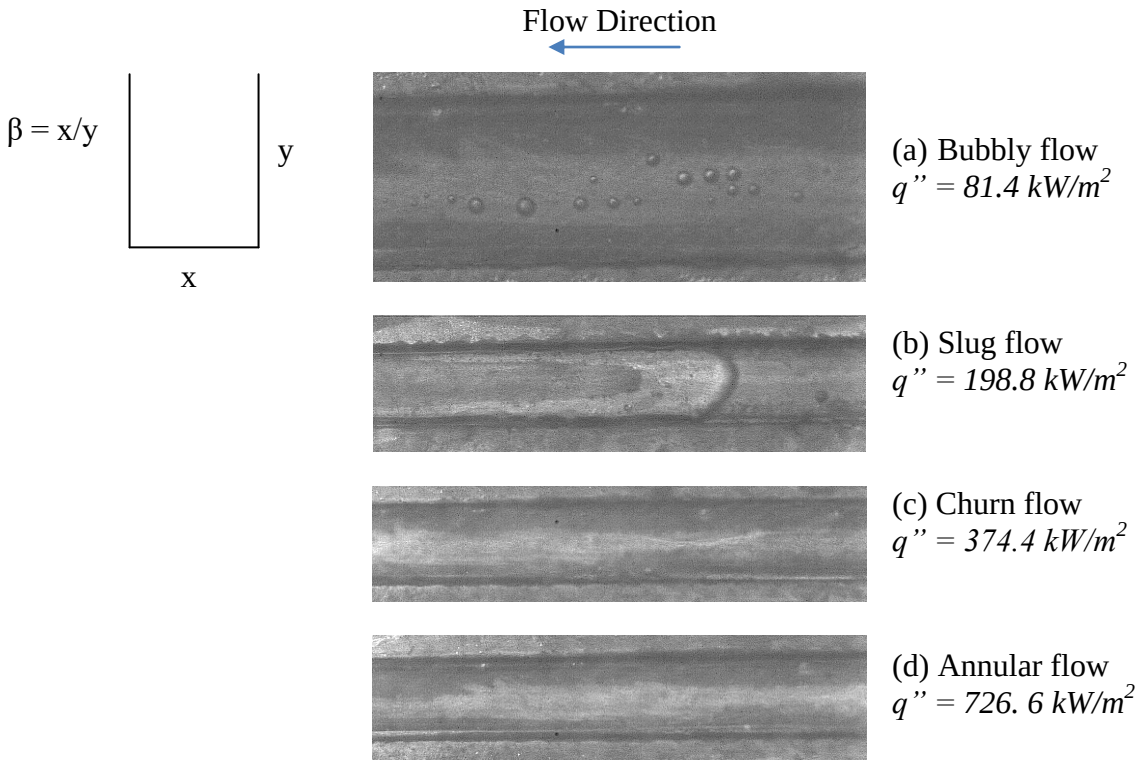

Figure 5.6 Flow patterns in the TS2 at the outlet region, for several heat fluxes at G = *400 kg/m^{2}s*.

The flow patterns near the outlet region are presented in Fig. 5.7 for the TS1 at the mass flux of *400 kg/m^{2}s* for four heat fluxes. The bubbles nucleated, detached from the nucleation sites only at the edge of the channel. This was different to what was observed in the $\beta = 4.94$ channel, i.e. the bubbles nucleated, detached from the nucleation sites on the surface of the channel and the channel edge. The observed bubbles were smaller than the channel size but larger than the bubbles observed in the TS2. The distribution of the bubbles was not dispersed unlike in the TS2. This is likely to be related to channel width since the TS1 is narrower than the TS2. Coalescence of the bubbles with each other was not observed at this flow regime. This flow regime was defined as bubbly flow and shown in Fig. 5.7 (a). As the heat flux was increased to *100.1 kW/m^2* just after the bubbly flow, the bubbles started to coalescence with each other and became as large as the channel size to form elongated slugs, see Fig. 5.7 (b). The formed elongated slugs came also from the middle region of the test section and merged with slugs in the outlet region. In the literature, some researchers reported that slug flow

occurs early after the boiling incipience when the channel size is too small. For example, Harirchian and Garimella (2009a) did not observe bubbly flow in the two smallest tested microchannels (D_h = *0.16* and *0.307mm*) whilst they reported bubbly flow in the larger microchannels (D_h = *0.4-0.749 mm*). In this study, bubbly flow was still observed in the TS1 at small heat flux values. As the heat flux was increased, the flow regime became churn flow and annular flow. The churn flow and annular flow regimes are shown in Figs. 5.7 (c) and 5.7 (d), respectively, for the TS1. The characteristics of the churn flow were similar to those observed in the TS2. However, in the annular flow regime unlike the TS2, no droplets were seen in the vapour core of the annular flow.

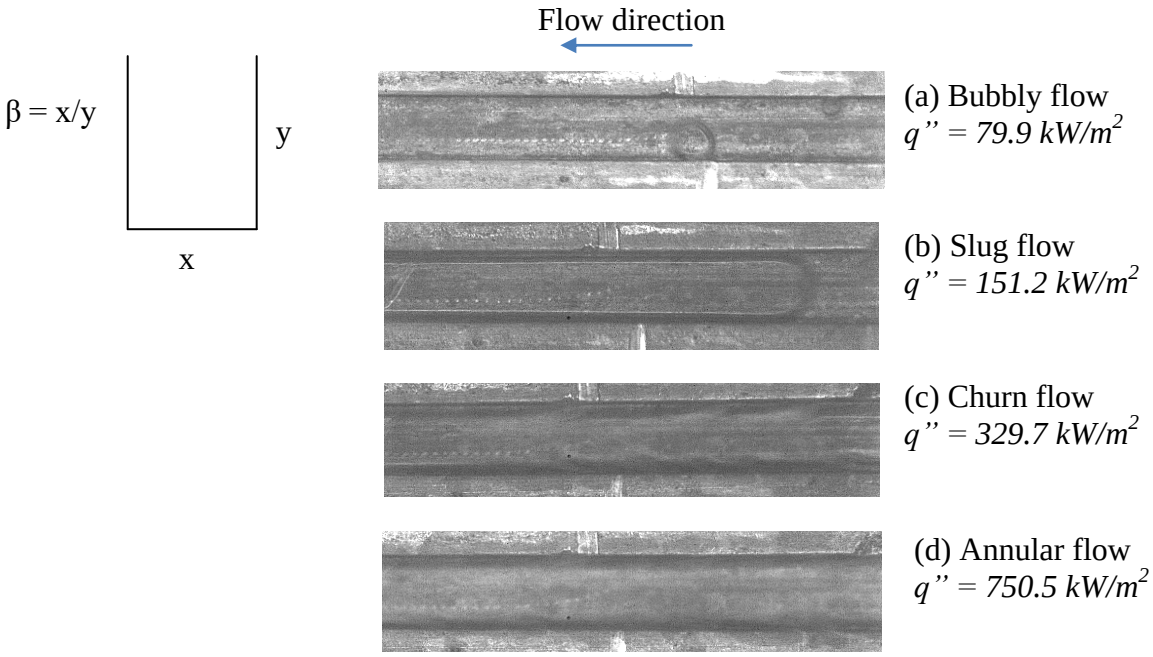

Figure 5.7 Flow patterns in the TS1 at the outlet region, for several heat fluxes at G = *400 kg/m^{2}s*.

The observed flow patterns at the outlet region for the TS3 are depicted in Fig. 5.8 for different heat flux inputs at the *400 kg/m^{2}s* mass flux value. Contrary to TS1 and TS2, bubbly flow was not encountered in the TS3 outlet region. The bubbly flow was visualised at the middle region of the channel after the boiling incipience for a small heat flux input interval. The onset of slug flow appeared at the outlet region at this condition. As mentioned before, Harirchian and Garimella (2009a) did not observe

bubbly flow in the two narrowest channels. Slug flow appeared right after boiling incipience for these microchannels similar with the TS3 in this study. Slug flow is shown in Fig. 5.8 (a) as an example for the TS3. With the increase in heat flux, the flow regime turned to churn flow similar to TS1 and TS2, see Fig. 5.8 (b). Higher heat flux inputs transformed the regime from churn flow to annular flow, which is depicted in Fig. 5.8 (c) for *774.3 kW/m^2* heat flux input. In the annular flow regime for this microchannel, no droplets entrainment was observed in the vapour core of the annular flow, similar to the TS1.

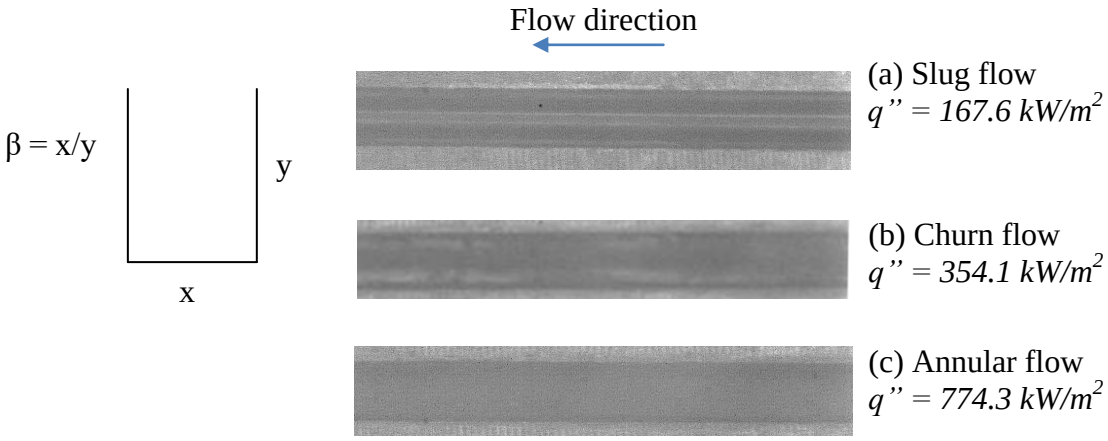

Figure 5.8 Flow patterns in the TS3 at the outlet region, for several heat fluxes at G = *400 kg/m^{2}s*.

These findings confirm the relation between the flow patterns and channel aspect ratio. In this study, the hydraulic diameter of the microchannels was kept constant and only channel aspect ratio was varied. In the literature, many studies reported that the hydraulic diameter affects the flow regimes and shapes. However, it can be seen from the above discussion that the channel aspect ratio has also an influence on the flow regimes. For example, bubbly flow was not encountered in the smallest aspect ratio mirochannel ($\beta = 0.5$) at the outlet region. Slug flow regime appeared just after boiling incipience condition. On the other hand, isolated small bubbles were observed at the outlet region for the microchannel having the largest aspect ratio ($\beta = 4.94$) after boiling incipience. In the TS1 shapes of the bubbles were elongated rather than isolated in the bubbly flow regime. The reason for this might be that the channel aspect ratio of the TS1 is smaller than the TS2. So that bubbles become elongated due to the confined

space. As the aspect ratio decreases more bubbly flow is not seen, the flow regime becomes slug flow as shown above for the TS3. Moreover, droplet entrainment occurred in the vapour core of the annular flow regime in the TS2 whilst this phenomenon was not observed for other microchannel test sections.

5.2.3 Comparison with Flow Pattern Maps

In this section, experimental flow patterns are compared to flow pattern maps existing in the literature including two adiabatic flow pattern maps and several flow boiling flow pattern maps. The selected flow pattern maps were generated for non-circular microchannels (especially rectangular) having *1 mm* or less hydraulic diameter for the appropriate comparison with the current experimental study. As stated previously, the visualization study was performed on three locations along the microchannels. The experimental flow patterns for the comparison are selected outlet region flow patterns. Because boiling started at the outlet for all test sections, see figs. 5.3 (a-d). Also, the flow regime is liquid flow for the inlet and middle regions at the first three-four heat fluxes after boiling incipience since the subcooling is ~ *14 K* during the experiments.

Triplett et al. (1999) conducted experiments in horizontal circular microchannels (D_i = *1.1* and *1.45 mm*) and semi-triangular (triangular with one corner smoothed) microchannels (D_h = *1.09* and *1.49 mm*) using air and water. They recorded flow patterns in the middle of the test sections and proposed flow maps for each test section. It is worth to mention that the flow pattern map proposed for the *1.09 mm* semi-triangular test section is used for comparison in here. Because the cross-section of the semi-triangular channel is similar to the rectangular channel rather than the tube since it has corners. Hassan et al. (2005) created universal flow map for horizontal rectangular channels having hydraulic diameter in a range of *0.1 mm* and *1 mm* for air/water adiabatic two-phase flow. The maps of Triplett et al. (1999) and Hassan et al. (2005) were chosen for comparison in order to see whether the adiabatic flow pattern maps can predict flow boiling patterns or not. Moreover, the map of Hassan et al. (2005) was used because it is a universal flow pattern map and it was proposed for horizontal rectangular microchannels with a hydraulic diameter less than *1 mm*. Figures 5.9 (a-d) and 5.10 (a-d) display the comparisons of the experimental observed flow patterns for four test

sections with the Hassan et al. (2005) and Triplett et al. (1999) flow pattern maps. As can be seen from figures 5.9 (a-d), the map proposed by Triplett et al. (1999) well predicts the flow pattern data of churn flow for all test sections. On the other hand, the map reasonably predicts the annular flow pattern data but gives poor prediction for other flow pattern data for all test sections. The Hassan et al. (2005) flow pattern map reasonably predicts the annular and churn flow pattern data similar to the map of Triplett et al. (1999) for all test sections, see figs. 5.10 (a-d). Moreover, intermittent flow regime is also estimated reasonably by the Hassan et al. (2005) flow pattern map. It is worth mentioning that the Hassan et al. (2005) named the elongated bubbly flow and slug flow regimes as the intermittent flow regime in their study. Therefore, slug flow and bubbly/slug flow regimes in this study can be compared with the intermittent flow regime area in the Hassan et al. (2005) flow map.

The possible explanation of the partial agreement with the flow pattern maps in figures 5.9 (a-d) and 5.10 (a-d) is the fact that different channel material and surface characteristics were used at different experimental operations. The Triplett et al. (1999) flow map is based on adiabatic flow pattern data in stainless tube at the middle of the test section. However, the flow boiling pattern data performed in this study is for copper rectangular microchannels. Moreover, Hassan et al. (2005) universal flow pattern map was constructed using existing experimental data available in the literature. However, these data were collected by adiabatic experiments. It can be seen that, the transition lines between the flow patterns are similar for the flow pattern maps of Triplett et al. (1999) and Hassan et al. (2005).

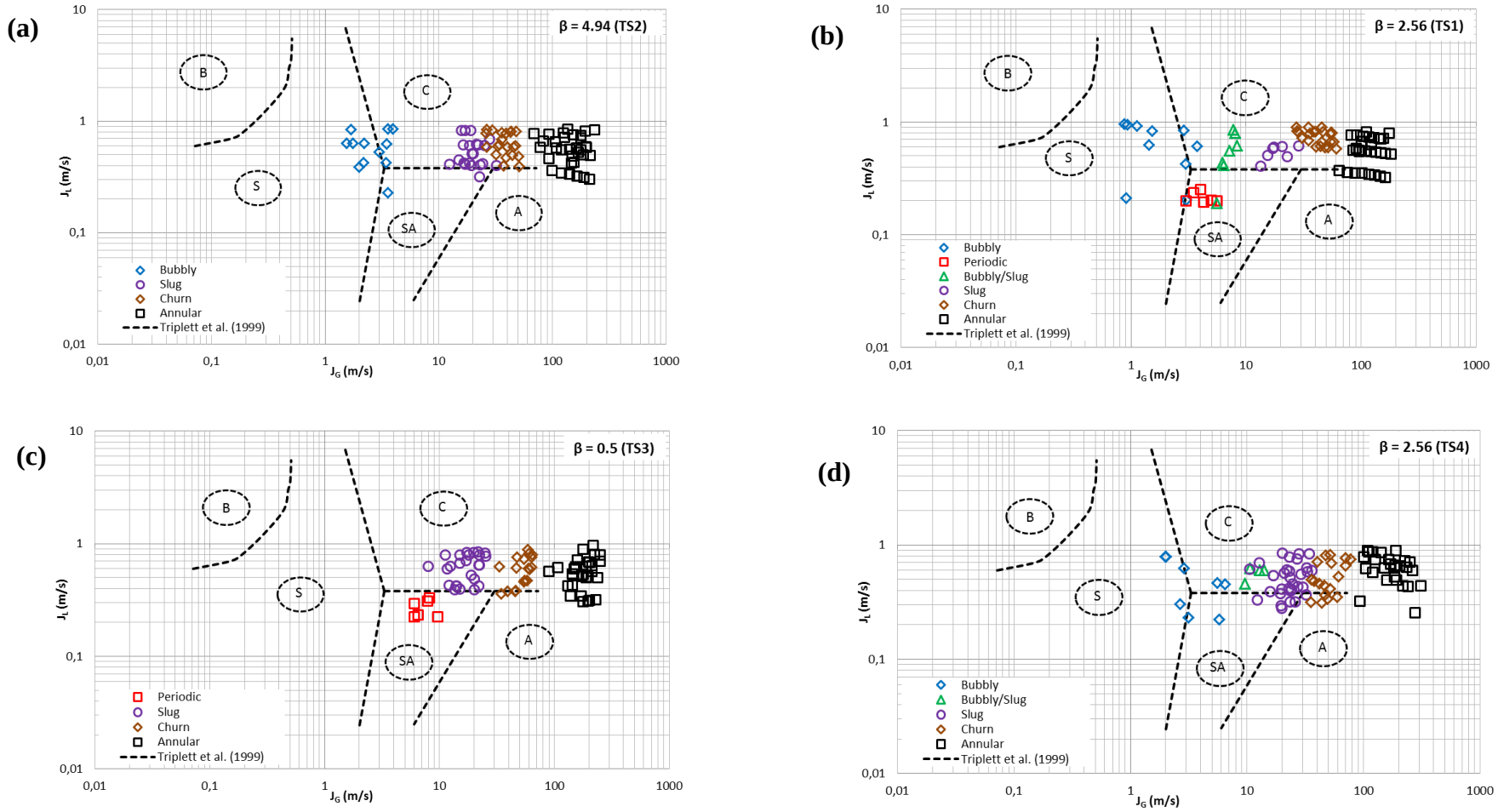

Figure 5.9 Comparison of the experimental flow patterns at the outlet region with flow pattern map of Triplett et al. (1999): (a) TS2, (b) TS1, (c) TS3 and (d) TS4. B: Bubbly flow, S: Slug flow, C: Churn flow, SA: Slug-Annular flow and A: Annular flow.

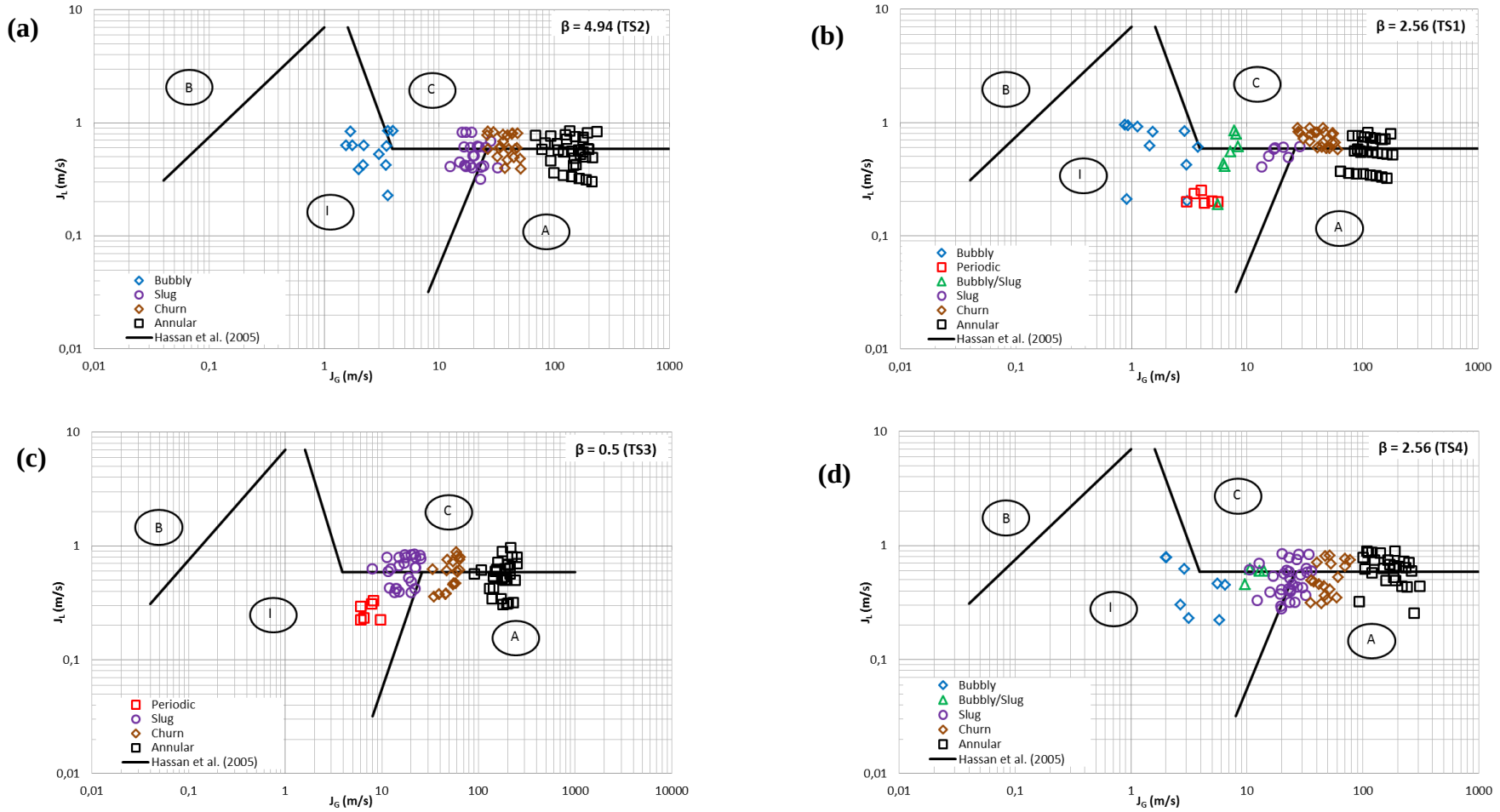

Figure 5.10 Comparison of the experimental flow patterns at the outlet region with flow pattern map of Hassan et al. (2005): (a) TS2, (b) TS1, (c) TS3 and (d) TS4. B: Bubbly flow, C: Churn flow, I: Intermittent flow and A: Annular flow.

Galvis and Culham (2012) proposed a flow map for rectangular microchannels with *0.217 mm* hydraulic diameter based on their flow boiling experimental study using water. The authors did not mention the observation location. They divided the annular flow regime into the slug-annular and the inverted-annular flow regimes. However, the inverted-annular flow regime was not observed in this study. The slug-annular flow regime in the map of Galvis and Culham (2012) corresponds to annular flow regime in this study. In addition to this, the boiling incipience (IB) regime in their study corresponds to the bubbly flow regime in the current study. The experimental flow pattern data are compared with the flow pattern map of Galvis and Culham (2012) in figure 5.11 (a-d) for microchannels. The bubbly flow and annular flow pattern data were successfully estimated by the map for all test sections. The slug flow regime partially predicted by the map for the TS3 and TS4 microchannels whilst the prediction fails for other test sections. Churn flow pattern data fall in the predicted slug flow area in the map. The partial agreement with the flow map of Galvis and Culham (2012) may be explained by the fact that the experimental conditions and surface characteristics of the Galvis and Culham (2012) data are different than the current study. Moreover, the churn flow and periodic flow were not shown in their flow map although they observed these flow regimes during the experiments. Also the predicted slug flow resulted in higher gas superficial velocity than the experimental result. It is because, the hydraulic diameter of the channel ($D_h = 0.217\ mm$) in their study were approximately two times smaller than the current experiment. As the size decreases, the superficial velocity of gas becomes higher at the similar heat flux and mass flux.

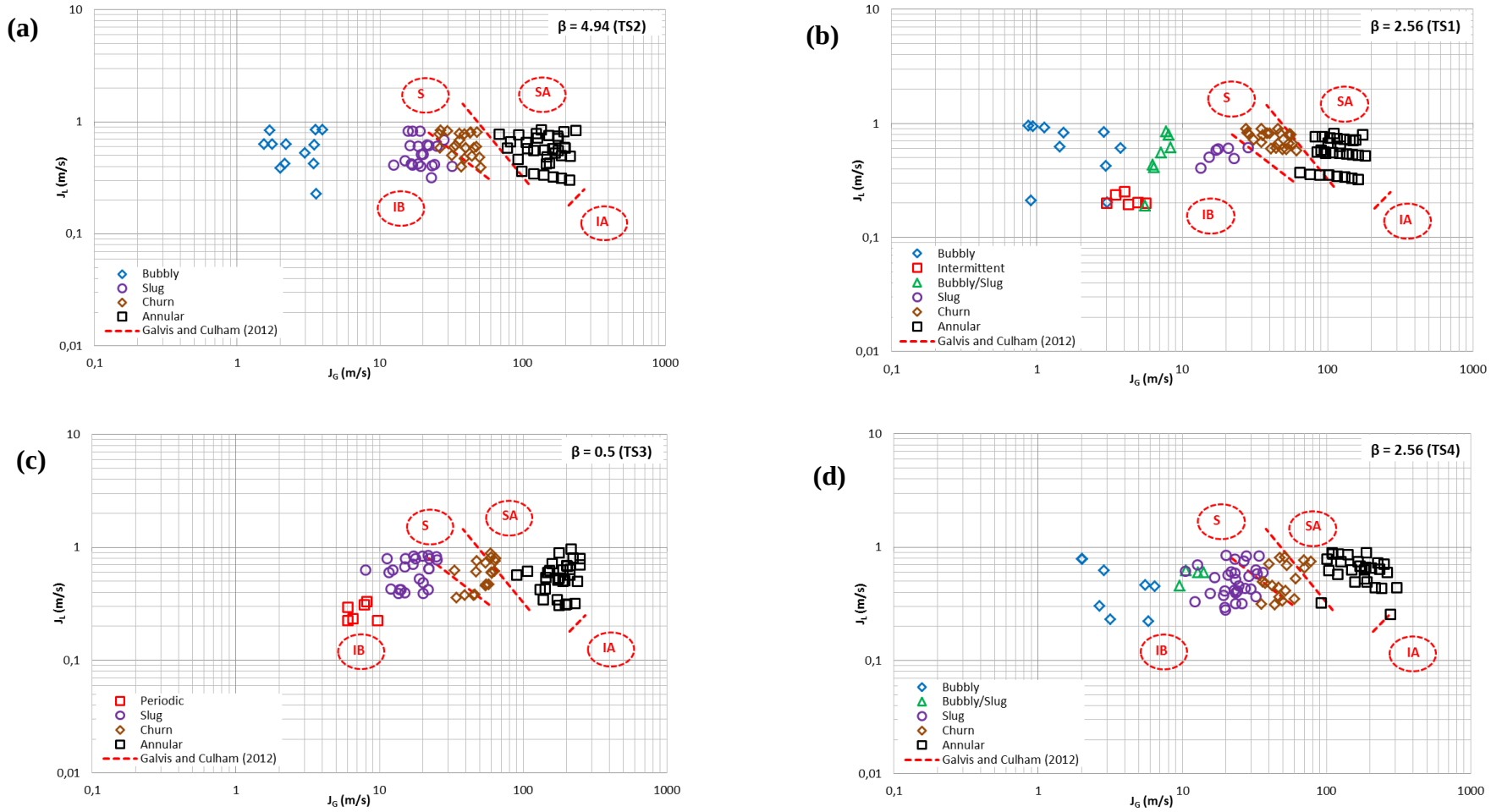

Figure 5.11 Comparison of the experimental flow patterns at the outlet region with flow pattern map of Galvis and Culham (2012): (a) TS2, (b) TS1, (c) TS3 and (d) TS4. IB: Boiling incipience, S: Slug flow, SA: Slug-Annular flow and IA: Inverted-Annular flow.

In addition to the above flow maps, the experimental data are also compared with flow pattern maps generated by Sobierska et al. (2006) and Harirchian and Garimella (2009a). The former was conducted using water in rectangular vertical microchannels with *1.2 mm* hydraulic diameter. Harirchian and Garimella (2009a) proposed flow pattern maps for seven rectangular parallel micorchannels. The ranges of hydraulic diameters are *0.159 mm-0.706 mm*. The working fluid was FC-77 in their experiments. The map proposed by the authors for the *0.54 mm* hydraulic diameter test section was chosen for comparison due to hydraulic diameter similarity with the current study. It is worth mentioning that the bubbly-slug flow area in the map of Harirchian and Garimella (2009a) corresponds to slug flow regime in this study. The churn-wispy annular and churn-annular flow areas in the map correspond to churn and annular flow regimes, respectively, in the current study. The experimental flow regime data for the microchannels in the current study are compared with the Harirchian and Garimella (2009a) flow pattern map in Fig. 5.12 (a-d). The bubbly flow pattern data for the microchannels were predicted well by the map except for the mass flux of *200 kg/m^{2}s*. Also, the annular flow regime for the TS4 was predicted fairly well by the map. However, other experimental flow regimes could not be predicted well by the map. The reason of the poor prediction of the Harirchian and Garimella (2009a) map could be the working fluid. They used FC-77 in their experiments and the de-ionised water was used as working fluid in the current study. The comparisons of the experimental flow pattern data with Sobierska et al. (2006) map are presented in Fig. 5.13 (a-d) for microchannels. The bubbly flow regime data for the microchannels fall in predicted slug flow region in the map whilst some of slug pattern data were predicted by the map. On the other hand, the churn flow pattern data fall in the predicted annular flow region in the map of Sobierska et al. (2006). The annular flow pattern data were predicted successfully and accurately by the map. The possible explanations for the flow pattern map of Sobierska et al. (2006) being inaccurate for some flow patterns is the map was generated for subcooled boiling and the churn flow pattern data were not identified in the map. Moreover, Sobierska et al. (2006) carried out experiments in vertical channels and the observation point location was only at middle of the test sections. However, in the present experiments the orientation of the microchannels was horizontal and the visualisation at the outlet region was selected for comparison.

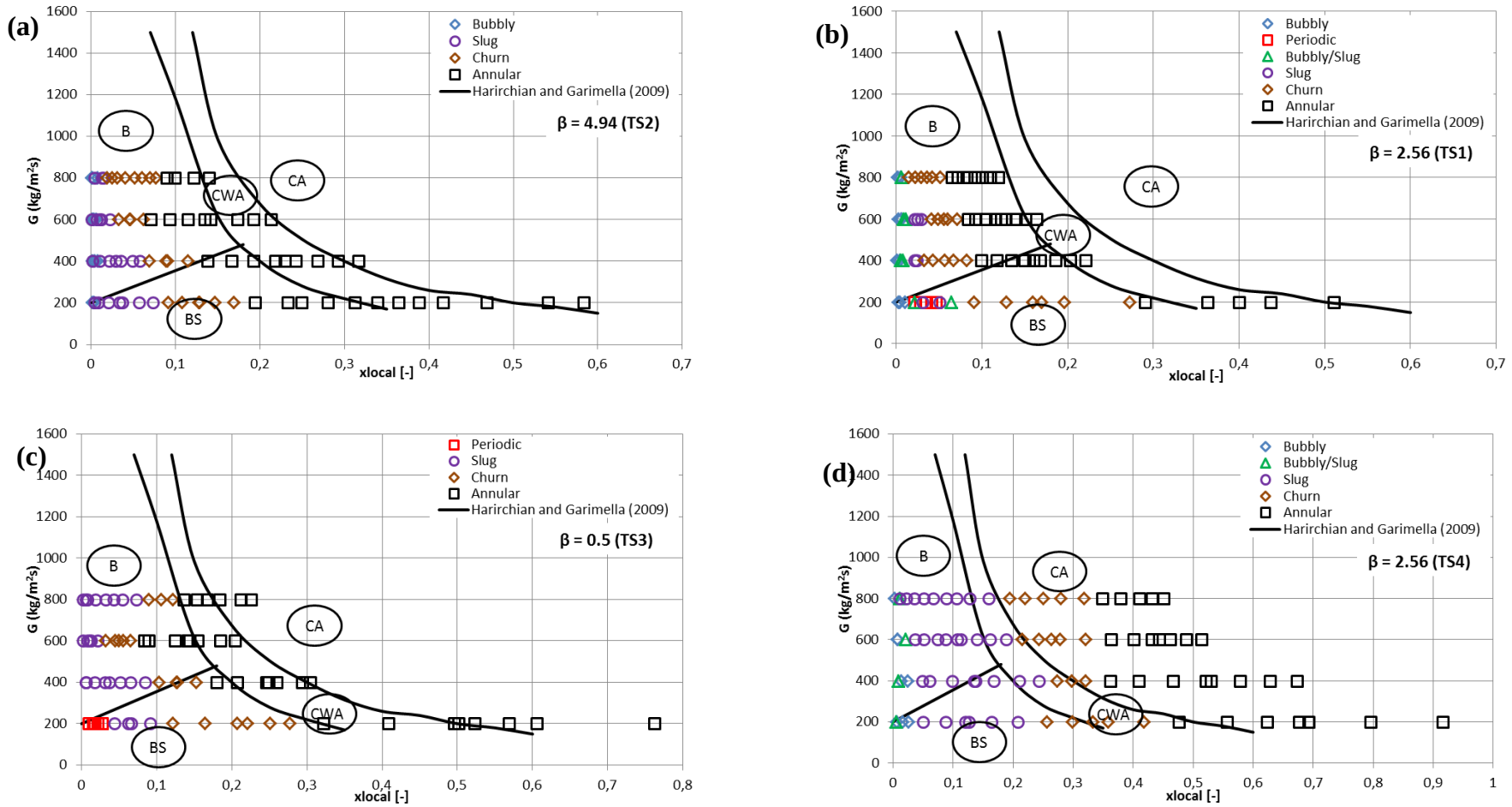

Figure 5.12 Comparison of the experimental flow patterns at the outlet region with flow pattern map of Harirchian and Garimella (2009a): (a) TS2, (b) TS1, (c) TS3 and (d) TS4. B: Bubbly incipience, BS: Bubbly-Slug flow, CWA: Churn-Wispy annular flow and CA: Churn-Annular flow.

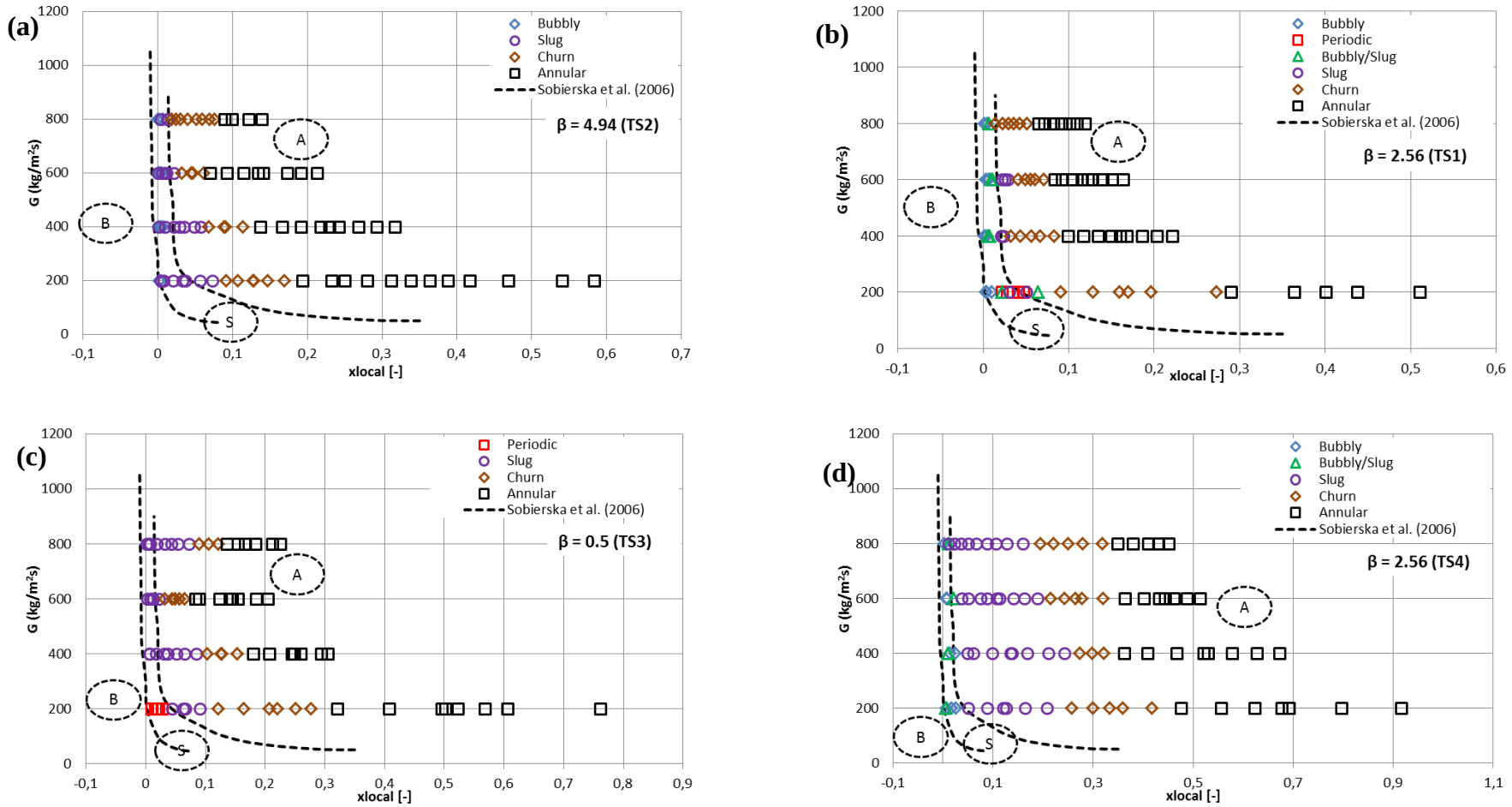

Figure 5.13 Comparison of the experimental flow patterns at the outlet region with flow pattern map of Sobierska et al. (2006): (a) TS2, (b) TS1, (c) TS3 and (d) TS4. B: Bubbly flow, S: Slug flow and A: Annular flow.

5.3 Flow Boiling Heat Transfer

This section examines the flow boiling heat transfer results obtained from the microchannel test sections. The boiling incipience condition and the boiling curve of each test section are assessed. The effects of mass flux, heat flux and channel aspect ratio on the local flow boiling heat transfer coefficient are presented and discussed. The reproducibility of the experimental data is also shown. The experimental data were recorded at steady state condition. The steady state condition refers to data obtained when the temperature, pressure and flow rate readings do not change over the time at values greater than the uncertainty values. Once steady state condition reached at the desired test conditions, the mass flux was kept constant and the heat flux was increased in a stepwise manner. The mass flux ranged from *200* to *800 kg/m^{2}s* and the heat flux was from *0* to *1350 kW/m^2* during the tests.

5.3.1 Boiling Incipience

Boiling incipience is of interest because this parameter needs to be highlighted in micro-scale flows for several reasons. Firstly, abrupt bubble formation might cause safety problems in some applications such as electronic devices or nuclear reactors, see Piasecka et al. (2004). Secondly, knowing the boiling incipience condition is necessary in order to obtain maximum design limit for single-phase flow applications. On the other hand, it provides knowledge of the lower design limit intended for flow boiling applications.

Boiling incipience can be detected on the *ΔP-q"* curve, *q"-ΔT_{sub}* curve or *h-q"* curve by increasing heat flux at a fixed mass flux condition. A number of researchers have considered that onset of nucleate boiling point is the point when the calculated single-phase pressure drop line deviates from the experimental pressure drop data line on the above curves in the flow transition from single phase flow to flow boiling, see Kennedy et al. (2000), Ghiaasiaan and Chedester (2002) and Wang et al. (2014). On the other hand, some other researchers such as Qu and Mudawar (2002b) and Liu et al. (2005) identified the boiling incipience using a high speed camera and a microscope. These researchers characterized the boiling incipience condition when the first bubble started to nucleate in the channel.

In the literature, it has been reported that the pressure, flow rate, fluid temperatures and wall temperatures fluctuations with flow reversal and whist-like sound accompany bubble nucleation at the boiling incipience condition which is called onset of flow boiling instability, see Kennedy et al. (2000), Qu and Mudawar (2004) and Mosyak et al. (2012). To assess the boiling incipience condition, the fluctuations in the fluid inlet temperature, fluid outlet temperature, wall temperature and pressure drop are plotted in Fig. 5.14 for the *2.56* aspect ratio microchannel (TS1) at $G = 200\ kg/m^2s$ over a *50 s* period. Figure 5.14 (a, b) displays the signals at zero heat flux (before applying heat to the test section) and indicates very stable signals with insignificant fluctuations. The amplitude of fluctuations were *0.1 K*, *0.06 K*, *0.1 K* and *0.31 kPa* for the fluid inlet, outlet and wall temperature and pressure drop, respectively. When the heat flux was increased to $64.9\ kW/m^2$, boiling commenced and small bubbles were observed inside the channel. At this condition, the signal demonstrated large periodic fluctuations as seen in Fig. 5.14 (c, d) accompanied by whist-like sound and reverse flow. The fluctuations amplitude for the inlet, outlet and wall temperatures and pressure drop signal were *5 K*, *4.5 K*, *0.1 K* and *3.9 kPa*, respectively. It is interesting to note that the fluctuation in wall temperature at boiling incipience is found to be insignificant compared to fluctuations in inlet, outlet fluid temperatures and pressure drop.

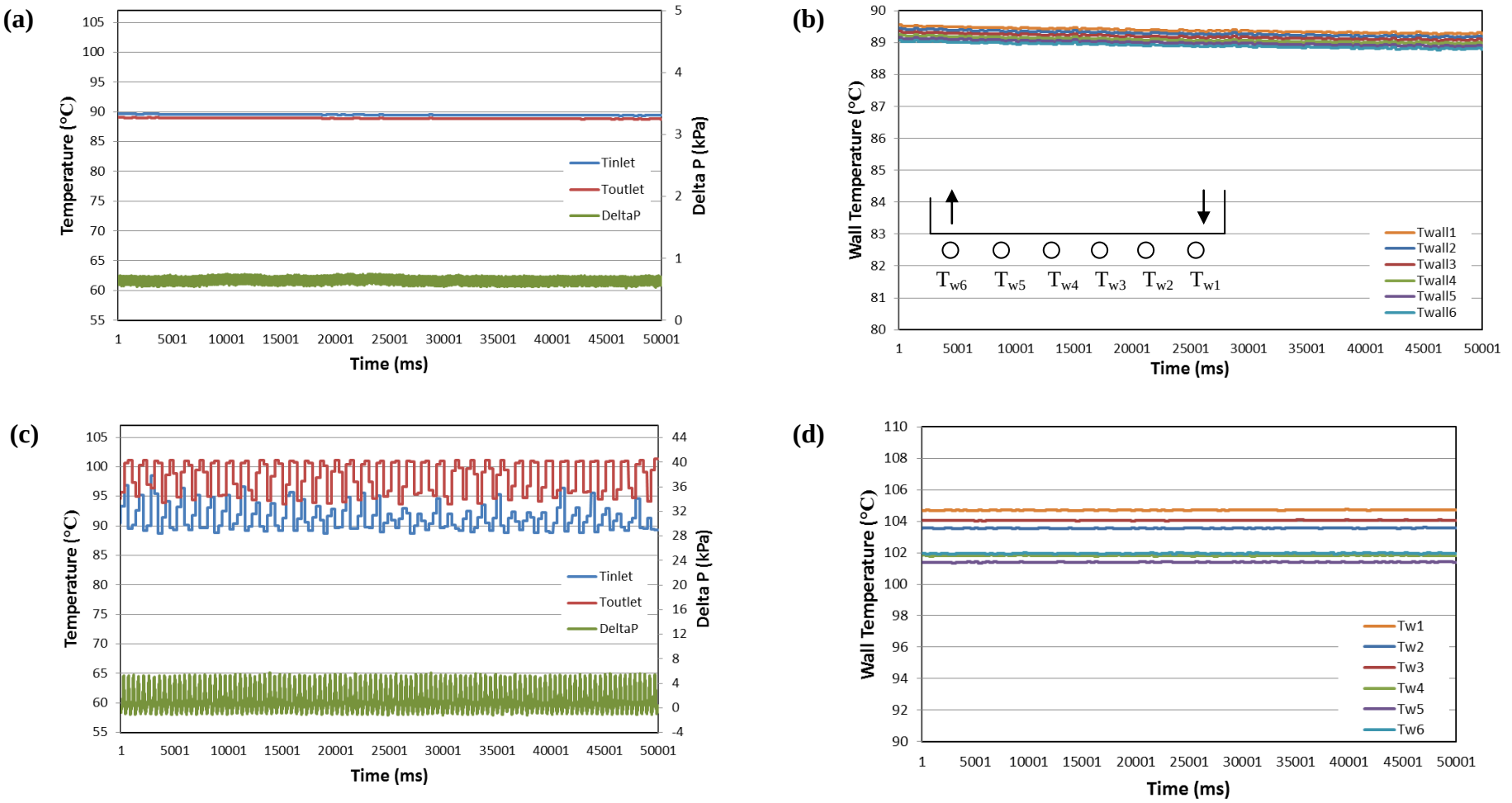

Figure 5.14 Fluctuations in fluid inlet, outlet and wall temperature and pressure drop at $G = 200\ kg/m^2s$ for the TS1; (a) $q'' = 0\ kW/m^2$, (b) $q'' = 0\ kW/m^2$, (c) $q'' = 64.9\ kW/m^2$ and (d) $q'' = 64.9\ kW/m^2$.

The fluctuations in the above mentioned parameters were also observed at boiling incipience at higher mass flux. Figure 5.15 depicts the fluctuations recorded at boiling incipience for $G = 400\ kg/m^2s$. When boiling started at $q'' = 99\ kW/m^2$, significant fluctuations in the temperatures and pressure drop were recorded with a whist-like sound and reverse flow. The fluctuations amplitude at this condition was *2 K*, *5 K*, *0.1 K* and *5 kPa* respectively for the inlet, outlet and wall temperature and pressure drop.

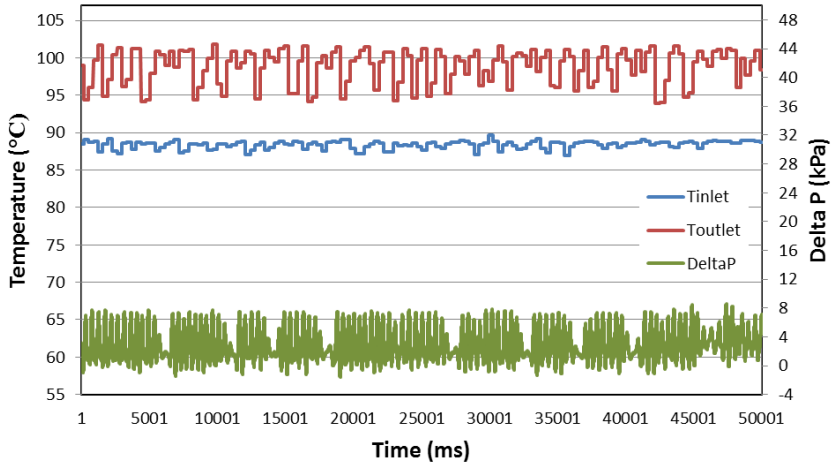

(a)

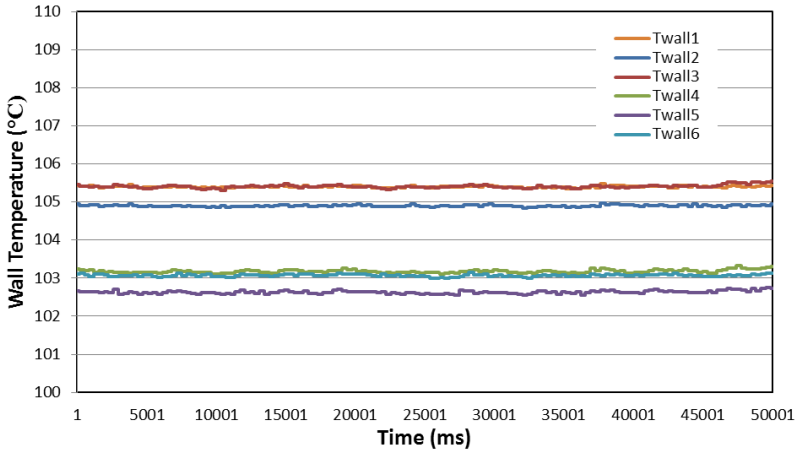

(b)

Figure 5.15 Fluctuations in fluid inlet, outlet and wall temperature and pressure drop at $q'' = 99\ kW/m^2$ and $G = 400\ kg/m^2s$ for the TS1; (a) Fluctuations in T_{inlet}, T_{outlet} and ΔP, (b) Fluctuations in T_{wall}.

Flow reversal can also be detected from the pressure drop signal in Figs. 5.14 and 5.15 where the signal shows negative values. The small bubbles nucleated at the channel corners as stated in section 5.2 and the boiling process was initiated. Similar findings were also visualized by Qu and Mudawar (2002b), Liu et al. (2005) and Soupremanien et al. (2011) who reported that the bubbles were started to nucleate near the channel corners at boiling incipience as shown in Fig. 5.16.

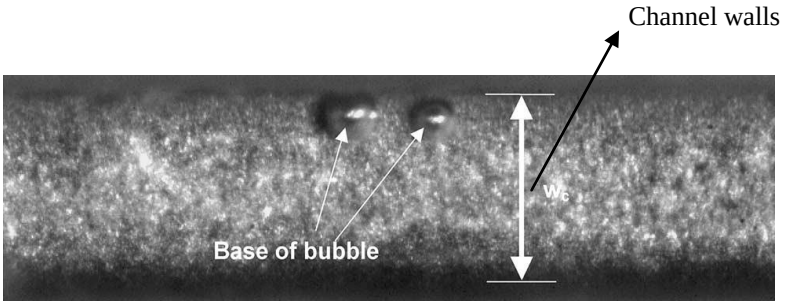

Figure 5.16 Visualisation of bubbles at onset of nucleate boiling, Liu et al. (2005).

Figures 5.14 and 5.15 are provided for the purpose of an example obtained from the TS1 at $G = 200\ kg/m^2s$ and $G = 400\ kg/m^2s$. Similar behaviours are also observed for other experimental conditions and test sections at boiling incipience.

Accordingly, classical boiling curves are depicted in Fig. 5.17 (a-d) on the basis of data at $z/L = 0.6$ location with increasing heat flux gradually for each test section at different mass fluxes. From the graphs below we can see that when the wall superheat is between 3 and 5 K there is a steep change in slope of the plots indicating the Onset of Nucleate Boiling (ONB) which implies the transition from single-phase region to flow boiling region. At boiling incipience the wall superheat dropped slightly in all test sections and increased again with heat flux, see Fig. 5.17 (a-d). When the heat flux was increased more, the dry-out can also clearly be detected in the Fig. 5.17 (d). This is due to an abrupt increase in the wall temperature at this location caused by dry-out condition. From figure 5.17 (a-d), we can also infer that the ONB point shows little dependence on the mass flux where higher heat flux values were recorded at the ONB as the mass flux increased, see Fig 5.17 (a-d) ONB point. However, beyond the ONB point the mass flux has no significant effect on the boiling curves. These findings are in accord with recent studies indicating that the mass flux effect is insignificant on the boiling curve, see

Mahmoud (2011), Soupremanien et al. (2011), Mirmanto (2012) and Galvis and Culham (2012). Mahmoud (2011) analysed the boiling curves of the seamless and welded tubes having *1.1 mm* inner diameter at two locations over the mass flux range of *280 kg/m^{2}s* and *490 kg/m^{2}s*. The mass flux had no effect on the boiling curve even near the exit of the tube where the convective boiling is believed to be dominant by the author.

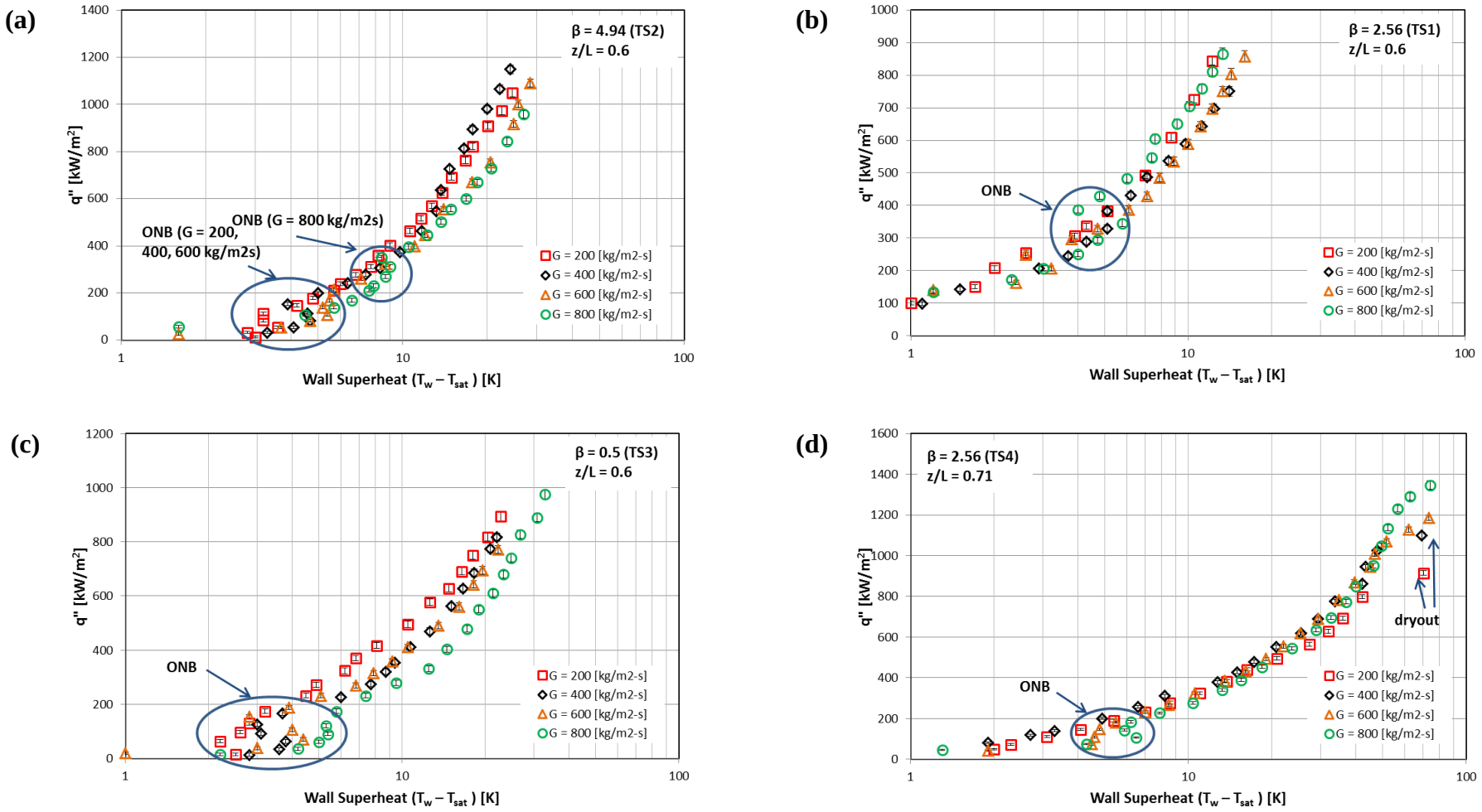

Figure 5.17 Classical boiling curve; (a) TS2 at *z/L = 0.6*, (b) TS1 at *z/L = 0.6*, (c) TS3 at *z/L = 0.6* and (d) TS4 at *z/L = 0.71*.

5.3.2 Effect of Heat flux, Mass flux and Channel Aspect Ratio on Heat Transfer Coefficient

The effect of heat flux, mass flux and channel aspect ratio on the average and local flow boiling heat transfer coefficient for each test section are presented and discussed in this part. The local flow boiling heat transfer coefficients are plotted versus local thermodynamic vapour quality and axial distance over the microchannels in order to investigate the dominant heat transfer mechanism(s) and the channel aspect ratio effect on the local heat transfer coefficient.

5.3.2.1 Effect of heat flux

The effect of heat flux plays an important role in addressing the issue of defining dominant heat transfer mechanism(s) in conventional scale and micro-scale. As stated previously, when the heat transfer coefficient increases with increasing heat flux and does not change with mass flux and vapour quality, nucleate boiling mechanism is expected to be dominant. In addition, when the heat transfer coefficient increase with increasing mass flux and vapour quality and does not depend on heat flux convective boiling is thought to be prevailing heat transfer mechanism. The heat flux effect is presented and discussed for each test section. The graphs are segregated into the form of low and moderate heat flux input and high heat flux input in order to determine the heat flux effect on the local heat transfer coefficient clearly.

Figure 5.18 (a-c) display the experimentally determined local heat transfer coefficient plotted against the local vapour quality with the low and moderate heat flux input at constant mass flux ($G = 200\ kg/m^2s$) for the TS2, TS1 and TS3, respectively. The subcooled condition ($\sim 14\ K$) de-ionized water was supplied to the channel and it was progressively heated with the channel axial length. So that, the left hand side of the zero vapour quality is referred as a subcooled region whereas the right hand side of the zero vapour quality is named as the saturated region. As seen in the figures, boiling commenced near the outlet of the channels (see the sudden increase in the heat transfer coefficient at the first heat flux input) with a clear heat flux effect. Analysing the figures 5.18 (a-c) the heat transfer coefficient rapidly increased to peak value with vapour quality from the subcooled region to the boiling incipience point ($x_{local} = 0\text{-}0.02$). The

corresponding flow patterns were bubbly flow and elongated slugs (slug flow) in this region. Beyond this point, the heat transfer coefficient had a slightly decreasing trend or remained almost constant for vapour quality of $0.02 < x_{local} < 0.2$. The flow regimes were changed to churn and annular flow regimes at this condition. The possible explanation of the constant trend of the heat transfer coefficient after the onset of nucleate boiling point might be due to the presence of nucleating bubbles inside the thin liquid film even during the churn and annular flow, see Kandlikar and Balasubramanian (2005). Kandlikar and Balasubramanian (2005) investigated flow boiling of water in parallel copper rectangular microchannels ($D_h = 0.33$ *mm* and $L = 63.5$ *mm*). They reported that the flow boiling heat transfer coefficient slightly decreased or remained constant with vapour quality. They observed nucleating bubbles at the walls during liquid flow and in the thin liquid film during churn and annular flow. They attributed the trend of flow boiling heat transfer coefficient versus vapour quality to these nucleating bubbles.

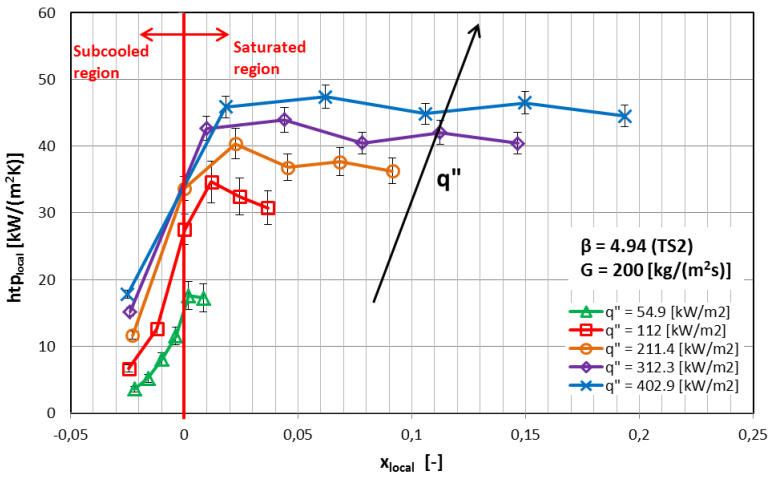

(a)

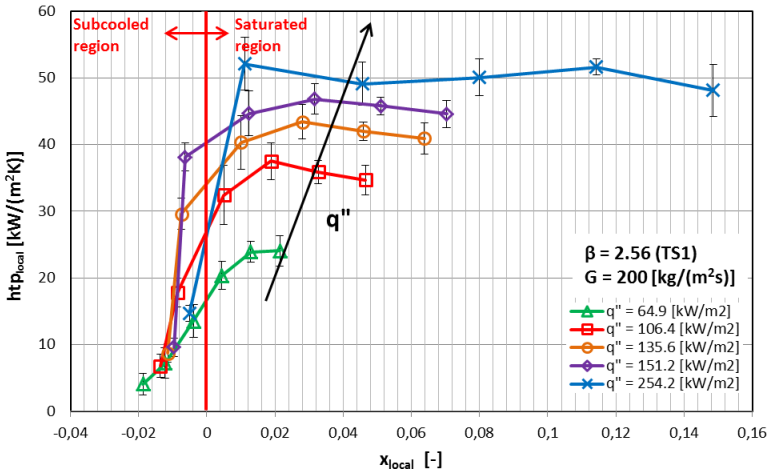

(b)

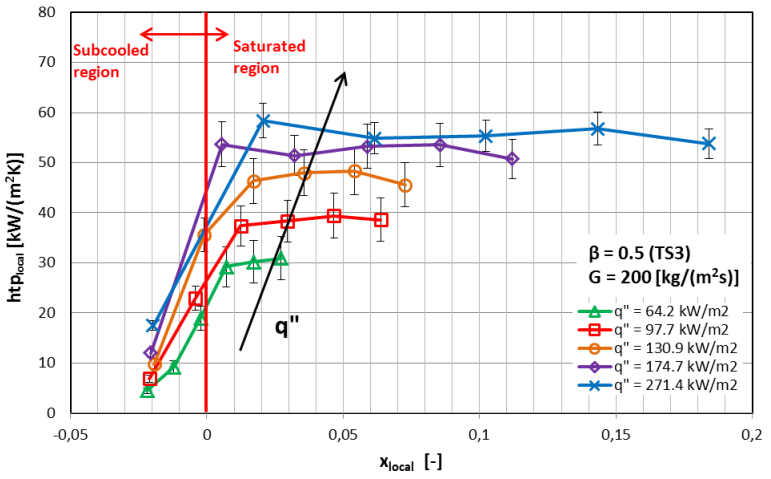

(c)

Figure 5.18 Effect of low and moderate heat flux input and local thermodynamic quality on the local heat transfer coefficient at *200 kg/m^{2}s* for; (a) TS2, (b) TS1 and (c) TS3.

These results reveal that the heat transfer coefficient increased with heat flux and are independent of the vapour quality at low and medium heat flux inputs or vapour quality of $0.02 < x_{local} < 0.2$. For example, the heat transfer coefficient at *402.9 kW/m^2* and *0.09* quality is *27 %* higher than the heat transfer coefficient at *211.4 kW/m^2* and *0.09* quality for the TS2. This could be interpreted as nucleate boiling dominant mechanism for these microchannels. These findings are in agreement with Steinke and Kandlikar (2004b), Lee and Garimella (2008) and Lim et al. (2015) results, which showed that the heat transfer coefficient increased with heat flux for low and moderate heat flux input or low vapour quality region ($x_{local} < 0.2$) and slightly decreased or remained constant with

vapour quality in the saturated region. On the other hand, some other researchers reported that the heat transfer coefficient sharply declined with vapour quality in the saturated region, see Steinke and Kandlikar (2004a), Sobierska et al. (2006) and Galvis and Culham (2012). These researchers attributed this trend of heat transfer coefficient to partial dry-out due to rapid bubble growth of the bubbles or high pressure drop existence in micro-scale channels. In this study, the heat transfer coefficient also decreased sharply with local vapour quality at high mass flux conditions that are discussed in the following sections.

Accordingly, the local heat transfer coefficient is depicted as a function of vapour local quality and high heat flux input in Figs. 5.19-5.21 at constant mass flux ($G = 200\ kg/m^2s$) for the microchannels TS2, TS1 and TS3, respectively. Additionally, the heat transfer coefficient is plotted against to dimensionless axial channel distance to determine the heat transfer variation clearly. For high heat flux input, the effect of heat flux on the heat transfer coefficient is insignificant. The dimensionless axial channel distance plots show that there is a small clear heat flux effect in the region near the channel inlet ($z/L < 0.2$). After that, the heat transfer coefficient becomes independent of the heat flux indicated by the heat transfer coefficient curves merge together for all heat flux values. The corresponding flow regimes were annular or churn flow at this condition.

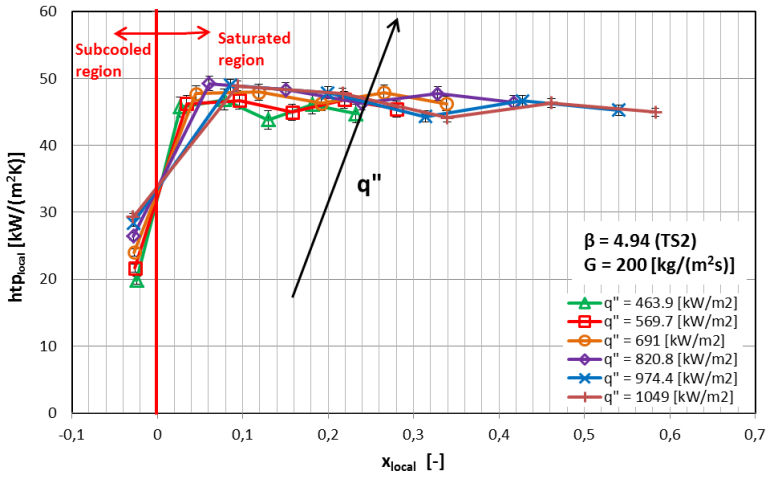

(a)

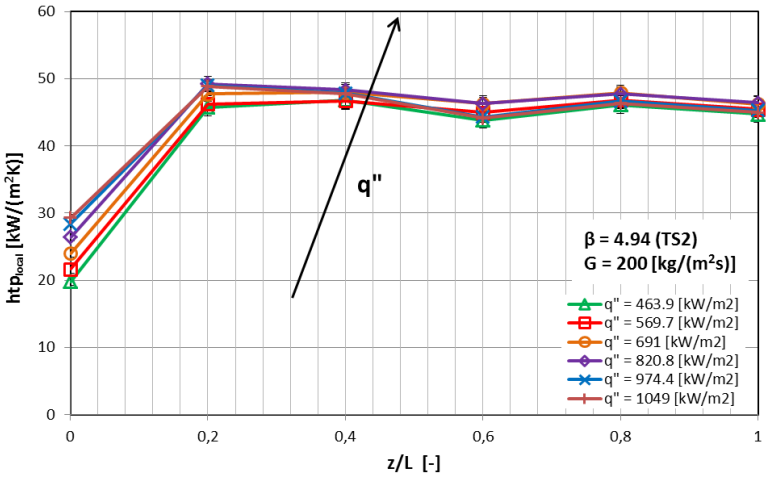

(b)

Figure 5.19 Effect of high heat flux input on the local heat transfer coefficient for the TS2 at 200 kg/m^{2}s; (a) versus local thermodynamic quality and (b) versus axial distance.

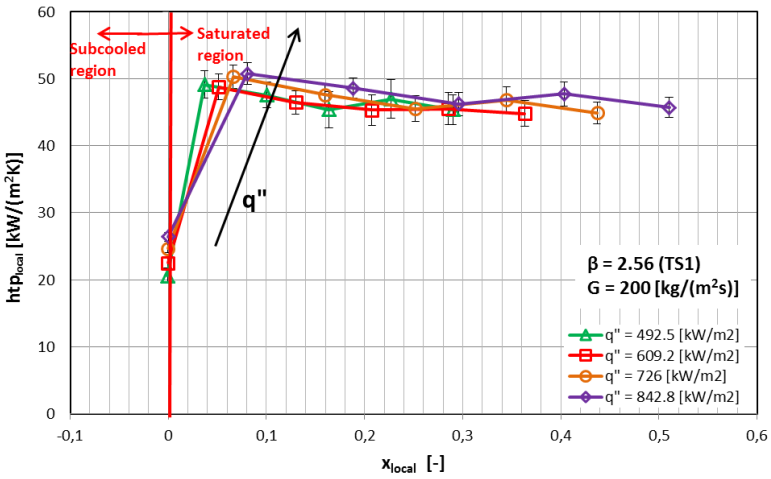

(a)

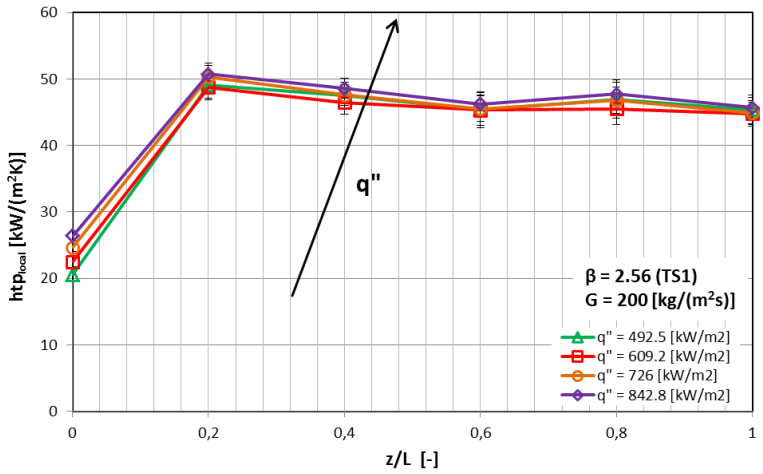

(b)

Figure 5.20 Effect of high heat flux input on the local heat transfer coefficient for the TS1 at 200 kg/m^{2}s; (a) versus local thermodynamic quality and (b) versus axial distance.

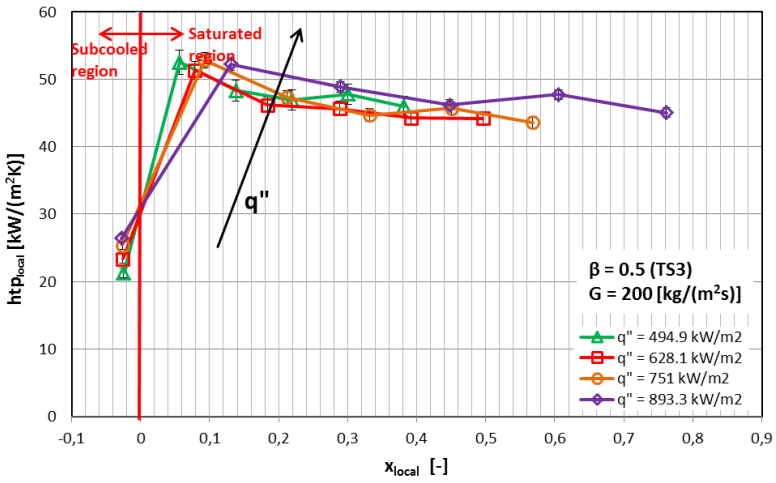

(a)

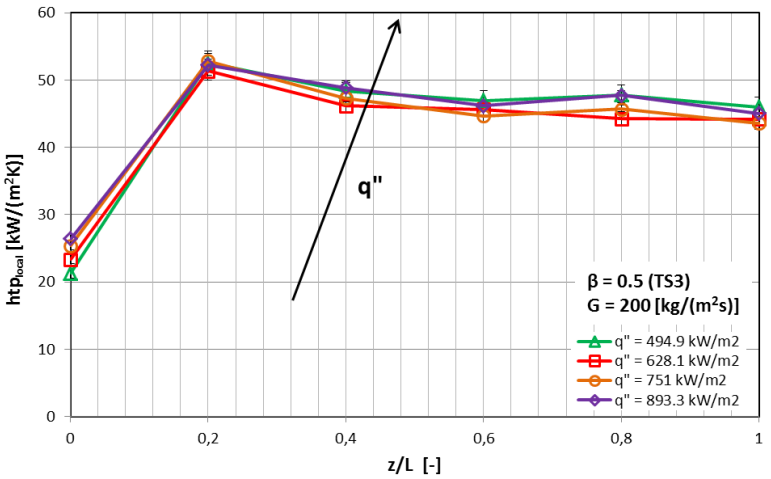

(b)

Figure 5.21 Effect of high heat flux input on the local heat transfer coefficient for the TS3 at 200 kg/m^{2}s; (a) versus local thermodynamic quality and (b) versus axial distance.

The observed elongated slugs seemed stagnant for a while before the fresh liquid pushes it to the downstream side of the channels. Thus, at low and medium heat flux input, it is probable that the elongated slugs leave the channel before the liquid film dries out. The clear heat flux effect observed at the low and medium heat flux input could be attributed to this process during the nucleation cycle. At high heat flux input partial dry-out might the reason of the insignificant heat flux effect on the heat transfer coefficient. Partial dry-out was captured in the channels using high-speed camera where a vapour blanket was observed near the middle and outlet of the channels during the tests. However, no significant increase in the wall temperature was observed at this condition. Moreover, the heat transfer coefficient slightly decreased with the vapour quality for all test sections at high heat flux input as can be seen clearly in Figs. 5.19-5.21. At higher mass fluxes, the heat transfer coefficient declined sharper than at the lower mass flux conditions. The local heat transfer coefficient is plotted as a function of local quality for the TS2 at 600 kg/m^{2}s of mass flux low and moderate and high heat flux input in Fig. 5.22 (a-c).

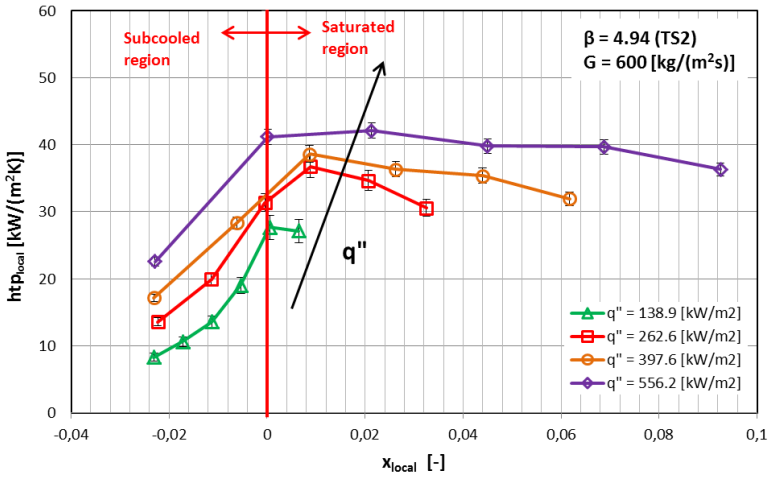

(a)

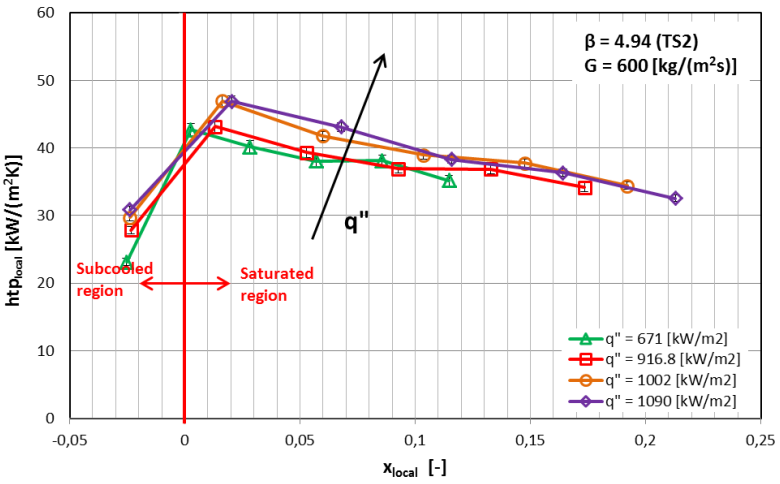

(b)

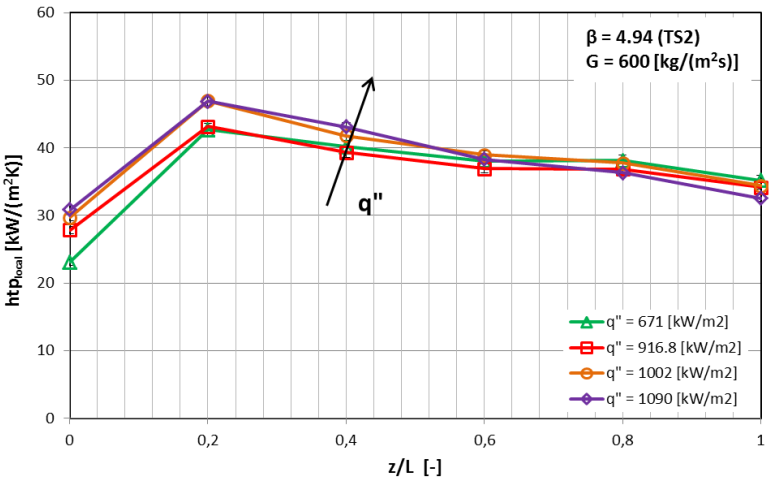

(c)

Figure 5.22 Effect of heat flux for the TS2 at 600 kg/m^{2}s; (a) Low and moderate heat flux input, (b) High heat flux input and (c) High heat flux input over axial distance.

As can be seen from the Fig. 5.22, the heat transfer coefficient increased with heat flux and slightly decreased or became constant with local vapour quality at low and medium heat flux input similar to lower mass flux tests. However, at higher heat flux input, the heat transfer coefficient decreased significantly with the local vapour quality in difference to the lower mass flux tests. In order to determine the reason of the decreasing trend of the local heat transfer coefficient with local vapour quality, the variation in saturation temperature with dimensionless axial channel distance is plotted in Fig. 5.23 for the last three applied heat fluxes and for the TS2 at *600 kg/m^{2}s*. The local saturation temperature values were calculated based on the local pressures. The local pressure values were determined using an assumption that the flow boiling pressure drop decreases linearly along the microchannels as mentioned in Chapter 3. As can be seen from the Figure 5.23, the saturation temperature varies more than the wall temperature from the entry towards the outlet of the channel. The difference between the wall temperature and saturation temperature increase towards to the outlet at the fixed value of mass flux and heat flux. This means that the high pressure drop is responsible for the diminish in the heat transfer coefficient with vapour quality, rather than partial dry-out in the microchannels.

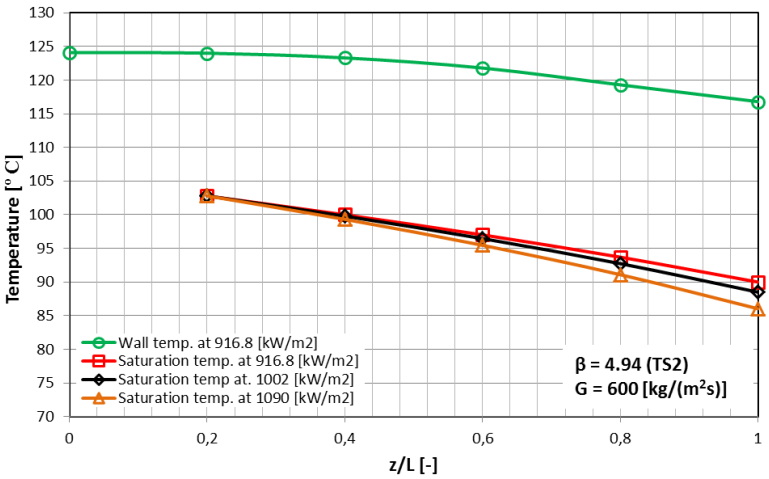

Figure 5.23 Saturation temperature variations along the channel axial distance for the TS2 at 600 kg/m^{2}s mass flux and range of heat fluxes.

In order to know the behaviour of the heat transfer coefficient in the whole saturated boiling region ($0 \leq x_{local} < 1$), the longer microchannel test section (TS4) having *0.56*

mm hydraulic diameter, *2.56* aspect ratio and *86.8 mm* length was tested. Figure 5.24 (a-d) depicts the local boiling heat transfer coefficients versus local vapour quality and axial dimensionless channel distance as a function of low and moderate and high heat flux input at constant mass flux ($G = 200\ kg/m^2s$).

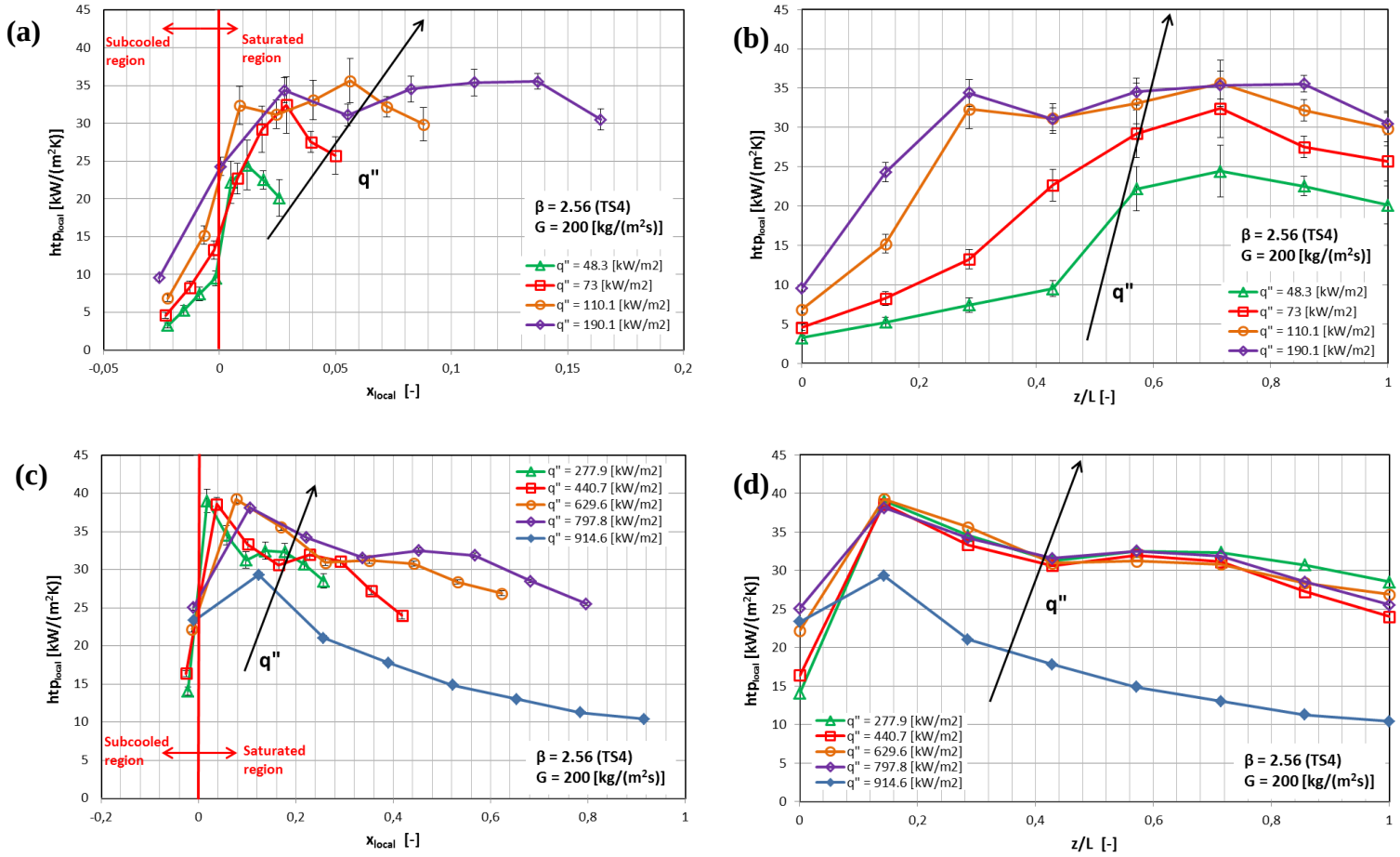

Figure 5.24 Effect heat flux input on the local heat transfer coefficient for the TS4 at 200 kg/m^{2}s; (a) Effect of low and moderate heat flux input and local quality, (b) Effect of low and moderate heat flux input over axial distance, (c) Effect of high heat flux input and local quality and (d) Effect of high heat flux input over axial distance.

Similar to other channels, the local heat transfer coefficient has a steep increase to ONB point from the subcooled region between the local vapour quality *0* and *0.02*. After that, the heat transfer coefficient exhibited slightly decreasing trend or remained constant at low and medium heat flux input. The nucleate boiling mechanism controls the boiling process at this condition similar to other channels. However, at high heat flux input, the heat transfer coefficient has a slightly different trend than the other test sections. The heat transfer coefficient declined sharper with local vapour quality than the other channels at the same mass flux condition. The reason for this that the pressure drop is obviously higher in this channel due to its longer length compared to other channels. Moreover, it can be seen in Figs. 5.24 (c-d) that the heat transfer coefficient drops suddenly, which can be attributed to the dry-out occurrence at the *914.6 kW/m^2* heat flux input. The dry-out can also be seen in the boiling curve of the test section (Fig. 5.17 (d)), which was presented on page 176.

5.3.2.2 Effect of mass flux

The local vapour quality and mass flux effects on the local heat transfer coefficient at almost the same heat flux input and constant inlet temperature and inlet pressure (T_i = *89°C* and P_i = *115 kPa*) is illustrated in Fig. 5.25 for all test sections. The graphs show that there has been a steady fall in the heat transfer coefficient with increasing mass flux for all test sections at a similar heat flux input. Additionally, the local heat transfer coefficient exhibits slightly decreasing trend as the local vapour quality increases at the mass flux of *200 kg/m^{2}s* for all test sections except the longer test section. However, the decreasing trend of the heat transfer coefficient with the local vapour quality is sharper at higher mass flux operations as explained above. As stated previously, the heat transfer coefficient exhibits increasing trend as the local vapour quality and mass flux increased in the convective boiling controlled region. Also, the dominant flow pattern is expected to be annular flow during this mechanism. However, different trend of the local heat transfer was reported by other researchers in microchannels but they reported that the convective boiling is the prevailing heat transfer process (see Chapter 2 literature review part, section 2.4.3.2). For example, Qu and Mudawar (2003c) and Balasubramanian et al. (2013) reported that the heat transfer coefficient increased with increasing mass flux but decreased in increase in vapour quality. But, they concluded that the convective boiling is the dominant heat transfer mechanism. The former

explained the decline in the local heat transfer coefficient with quality due to the fluid re-deposition and droplet entrainment in the annular flow regime. On the other hand, Lee and Garimella (2008) found that the heat transfer coefficient increased with heat flux at low and moderate heat flux inputs whereas it decreased with heat flux at higher heat flux input. The authors stated that nucleate boiling controlled the boiling process at low and medium heat flux input whereas convective boiling became the dominant heat transfer mechanism at higher heat flux input. However, they did not present any mass flux effect on the heat transfer coefficient as evidence.

In conclusion, the strong heat flux effect was detected at low and medium heat flux input for all microchannel test sections. The heat transfer coefficient increased with heat flux and that did not change much with local vapour quality especially at the low mass flux condition ($G = 200\ kg/m^2s$). At higher mass fluxes the heat transfer coefficient again enhanced as the heat flux increased but decreased with local vapour quality at low and medium heat flux input. This behaviour is attributed to high pressure drop gradient as explained above. The effect of heat flux on the heat transfer coefficient was found to be insignificant at high heat flux input. It was found there is a small, but clear, heat flux effect in the region near the channel inlet ($z/L < 0.2$). After that, the heat transfer coefficient curves merged together for all heat flux values. On the other hand, the heat transfer coefficient declined as the mass flux increased at same heat flux input for all test sections. The reason of this behaviour might be attributed to the pressure drop gradient becoming larger and the elongated bubbles grow and move faster at high mass flux input that suppresses the nucleate boiling process. Taken together, these findings show that the nucleate boiling mechanism was the dominant heat transfer mechanism at low and medium heat flux input for all test sections in this work. On the other hand, the dominant heat transfer mechanism was unclear at high heat flux input for all microchannel test sections.

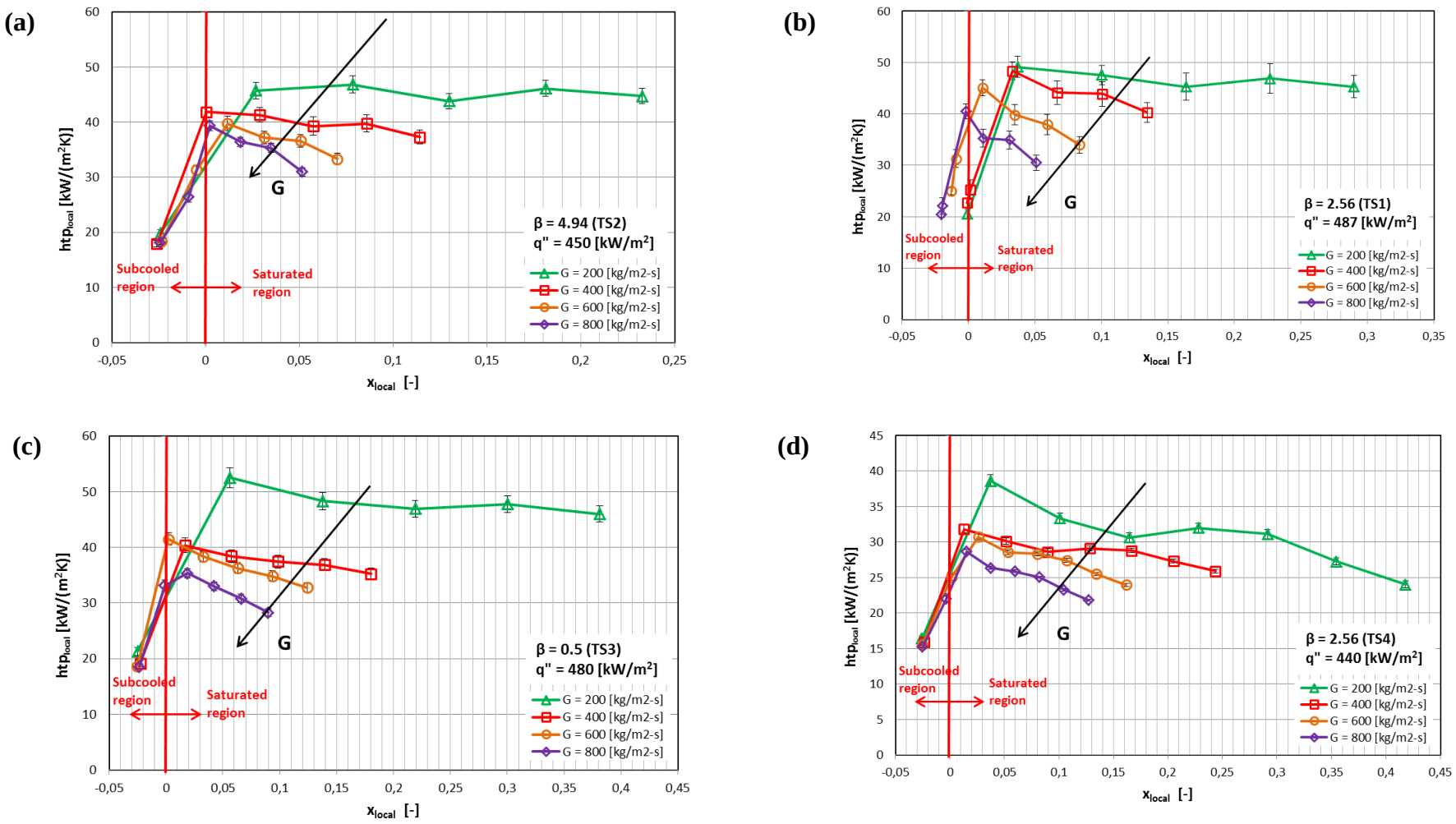

Figure 5.25 Effect of mass flux and local vapour quality on the local heat transfer coefficient at the constant heat flux; (a) TS2, (b) TS1, (c) TS3, (d) TS4.

5.3.2.3 Effect of channel aspect ratio

The hydraulic diameter effect on the heat transfer coefficient was investigated by many studies in the literature as discussed in Chapter 2. However, very little is known about the effect of channel aspect ratio on the heat transfer coefficient. Previous studies about the channel aspect ratio effect on the heat transfer coefficient did not keep constant other geometrical parameters such as hydraulic diameter and length of the microchannel. Therefore, it is difficult to draw a conclusion about the influence of aspect ratio on the heat transfer coefficient in microchannels. In this study, hydraulic diameter and channel length were kept constant (D_h = *0.56 mm, L = 62 mm*) for three microchannel test sections where the aspect ratio was changed (β = *0.5, 2.56* and *4.94*). Fig. 5.26 (a-b) are produced to determine the effect of aspect ratio and local vapour quality and on the local heat transfer coefficient at constant mass flux ($G = 200\ kg/m^2s$) for two different heat flux inputs. Moreover, the variation in the local heat transfer coefficient over the dimensionless axial channel distance is depicted for three test sections in Fig. 5.26 (c-d). It can be seen from the trends in Fig. 5.26 that the channels having smaller aspect ratio exhibited better heat transfer performance for low/medium heat flux input up to local quality *0.2*. However, at high heat flux input, the channel aspect ratio has little effect on the local heat transfer coefficient. A very small effect at high heat flux input can be seen in Fig. 5.26 (d) until the middle region of the channel ($z/L \leq 0.6$). However, after that, the heat transfer coefficient curves appeared to merge together for the microchannels. These results were also obtained for other mass flux conditions (*G = 400, 600* and *800* kg/m^2s). In order to see this trend clearly, the average heat transfer coefficient versus heat flux for the microchannels is plotted at the *200* kg/m^2s and *600* kg/m^2s mass fluxes in Fig. 5.27 (a-b).

Figure 5.27 (a-b) confirm that the channels having smaller aspect ratio has a better heat transfer performance up to ~ *480 – 500* kW/m^2 heat flux input. The channel aspect ratio has no effect on the heat transfer coefficient beyond this heat flux operations. These findings are in agreement with those presented in the above subsections where the heat transfer coefficient increased with heat flux at low and medium heat flux input but became constant at high heat flux input. Since the controlling heat transfer mechanism was found to be nucleate boiling at low and medium heat flux input, a possible explanation for the better heat transfer performance of the smaller aspect ratio channel

might be that the density of the nucleating bubbles is higher in the deeper channels. As presented before, the nucleation starts near the channel corners before approaching at the surfaces of the channels. Therefore deeper channels exhibited better heat transfer performance in nucleate boiling region. At higher heat flux input, the nucleate boiling is supressed. Hence, the heat transfer coefficient became less sensitive to channel aspect ratio.

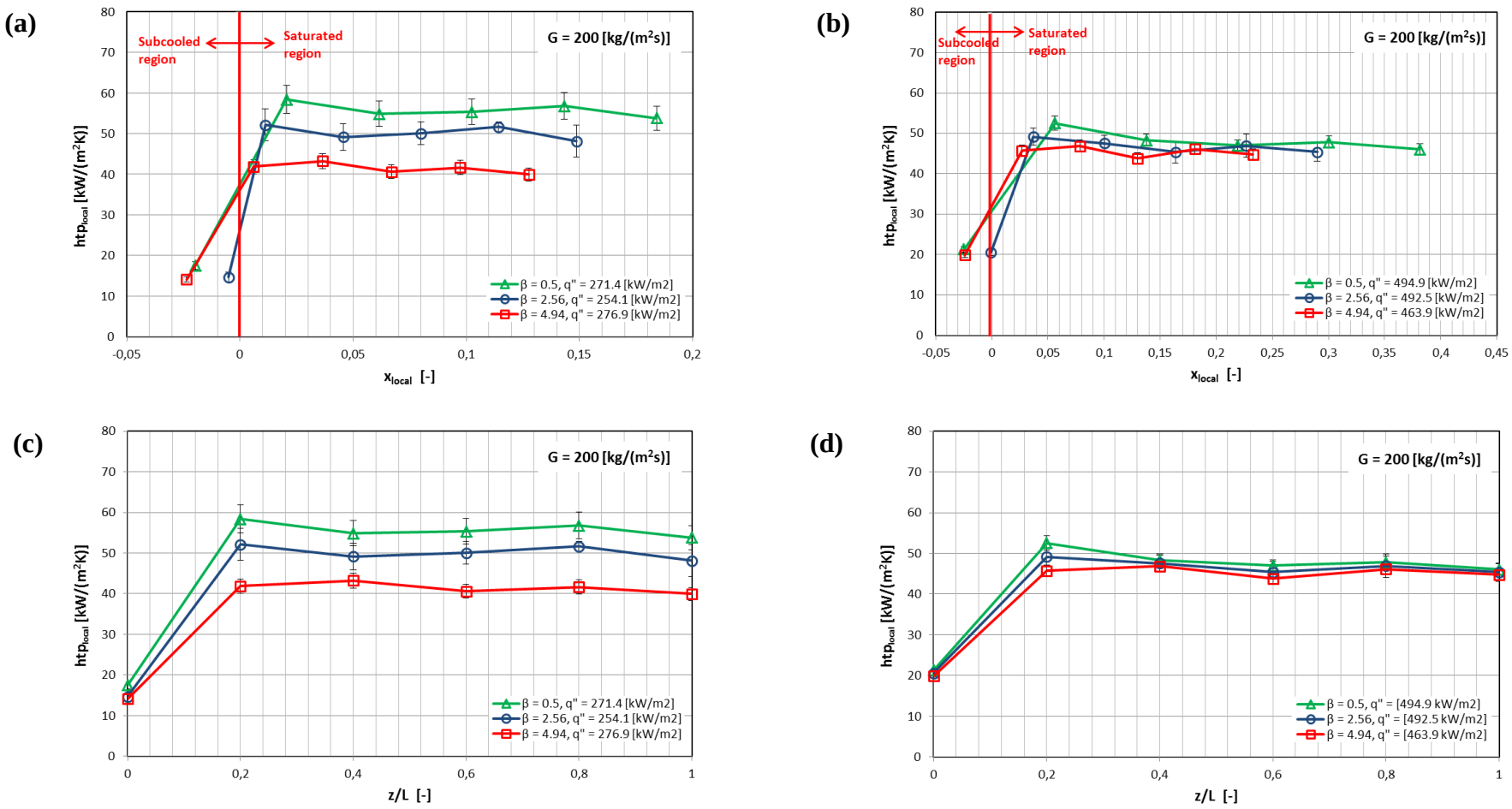

Figure 5.26 Effect of channel aspect ratio on the local heat transfer coefficient; (a) versus local vapour quality at G = 200 kg/m^{2}s and low heat flux input, (b) versus local vapour quality at G = 200 kg/m^{2}s and high heat flux input, (c) versus dimensionless distance at G = 200 kg/m^{2}s and low heat flux input, (d) versus dimensionless distance at G = 200 kg/m^{2}s and high heat flux input.

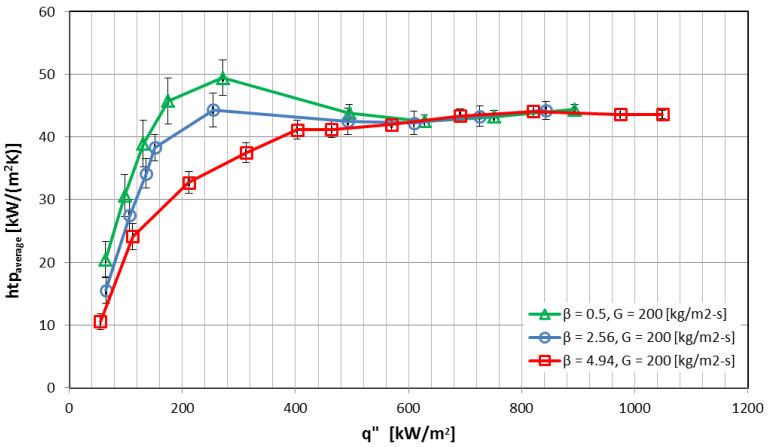

(a)

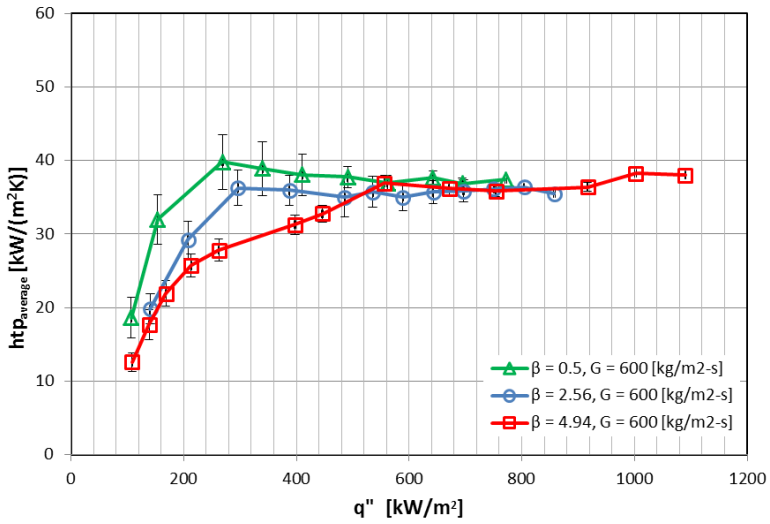

(b)

Figure 5.27 Effect of aspect ratio and heat flux on the average heat transfer coefficient for the three test sections; (a) at G = 200 kg/m^{2}s and (b) at G = 600 kg/m^{2}s.

5.3.2.4 Effect of heated length

Flow boiling characteristics in micro-scale are still not completely understood with published results reporting contradicting results as presented in Chapter 2. Therefore, there is a discrepancy about the prevailing heat transfer mechanism in micro-scale. Possible reasons might be that the heated lengths, surface characteristics and experimental conditions vary from one study to another. Only a few studies were conducted about the effect of heated length on the flow boiling heat transfer characteristics in microchannels, see Karayiannis et al. (2012). In this section, heat

transfer characteristics of two microchannels having the same hydraulic diameter (D_h = *0.56 mm*) and channel aspect ratio (β = *2.56*) but different heated length (L = *62* and *86.8 mm*) were compared to investigate the heated length effect on the flow boiling heat transfer coefficient. As presented in figures 5.18 (b), 5.20 (a-b) and 5.24 (a-d), the flow boiling heat transfer coefficient increased up to the onset of nucleate boiling point in a local vapour quality range of *0-0.02*. Then, the heat transfer coefficient slightly decreased or remained constant for both microchannels. However, the heat transfer coefficient for the longer microchannel decreased sharper than the shorter channel with local vapour quality due to its high pressure drop compared to the shorter channel. The effect of heated length on the flow boiling heat transfer coefficient as a function of local vapour quality and dimensionless axial distance for the investigated microchannels at constant exit quality and heat flux and the mass flux of *200 kg/m^{2}s* are presented in Figs. 5.28 (a-d). As can be seen from figs. 5.28 (a-d), the values of the heat transfer coefficient for the shorter microchannel are higher than the longer microchannel for both conditions. Figures 5.28 (a, c) show that, the required heat flux is higher for the shorter channel to obtain same exit quality. A possible explanation could be that more nucleation sites were activated in the shorter channel over the heated length at high heat fluxes. Since the nucleation sites are strongly related with the surface roughness, the surface of the shorter channel may be rougher than the longer one. Another reason could be that as the heated length was increased the boiling initiates at low heat flux input. This is because the fluid outlet temperature increases with the increase in heated length at the same heat flux and mass flux input. So that, in a longer channel the superheated de-ionised water occurs at low heat flux values compared to a shorter channel. Thus, higher heat fluxes are needed in the shorter channel to obtain same exit quality with the longer channel.

The values of the heat transfer coefficient were again higher in the shorter channel at the same heat flux as can be seen from figs. 5.28 (b, d). This is due to the fact that the pressure drop increased with the channel length which affected the local saturation temperature. The linear assumption technique was used to calculate the local saturation temperature in the current study as stated before. Consequently, the local saturation temperature is lower for the longer channel which results in smaller heat transfer coefficient at the mass flux and heat flux condition.

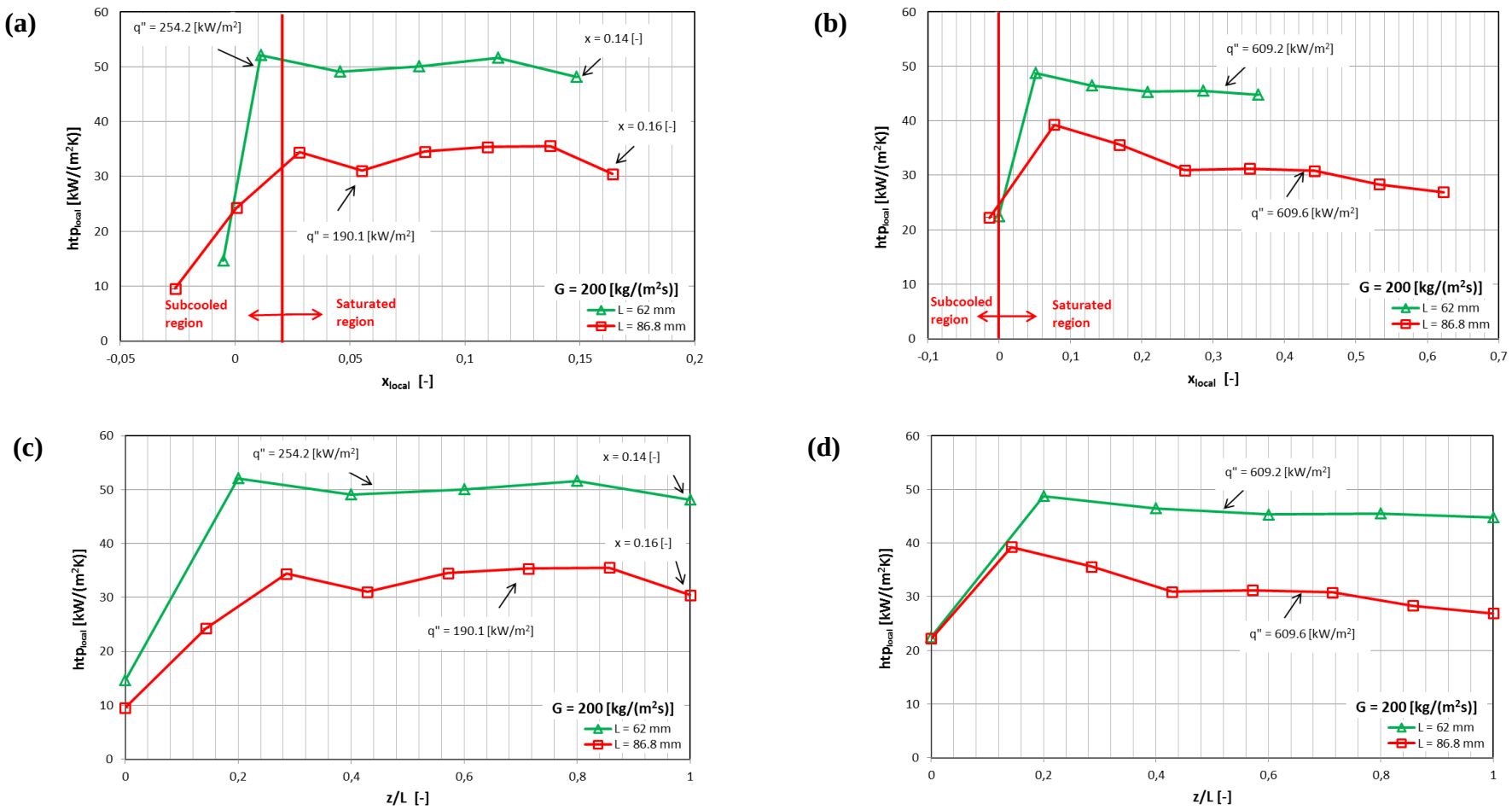

Figure 5.28 Effect of heated length on the local heat transfer coefficient; (a) versus local vapour quality at G = 200 kg/m^{2}s and constant exit quality, (b) versus local vapour quality at G = 200 kg/m^{2}s constant heat flux, (c) versus dimensionless distance at G = 200 kg/m^{2}s and constant exit quality, (d) versus dimensionless distance at G = 200 kg/m^{2}s and constant heat flux.

5.3.2.5 Repeatability of the data

The repeatability of the data is important in experimental studies in order to verify the reliability of the data. Reliable measurements should give identical results using the same measurement procedure and instrument under the same conditions after a time period. This issue becomes particularly important in micro-scale because repeatability and accurate measurement become harder to obtain with the decrease in the size. Also, the heat transfer process is greatly affected by the surface conditions. Hence, the heat transfer characteristics affected by the surface conditions vary more in the materials such as copper and aluminium. Two weeks after the first experiment, the single experimental condition was selected for each microchannels to repeat the experiments. Figure 5.29 (a-d) displays the repeated data of the experiments at the *400 kg/m^{2}s* mass flux, *89ºC* inlet temperature and *115 kPa* inlet pressure. The figures reveal that the experimental data is reasonably repeatable particularly at high heat flux values. The repeatability of the data deviates at boiling incipience since onset of nucleate boiling condition has large flow instabilities and unique characteristics. The corresponding *MAE* values are *7.94 %, 10.58 %, 6.69 %, 4.72 %* for TS1, TS2, TS3 and TS4, respectively.

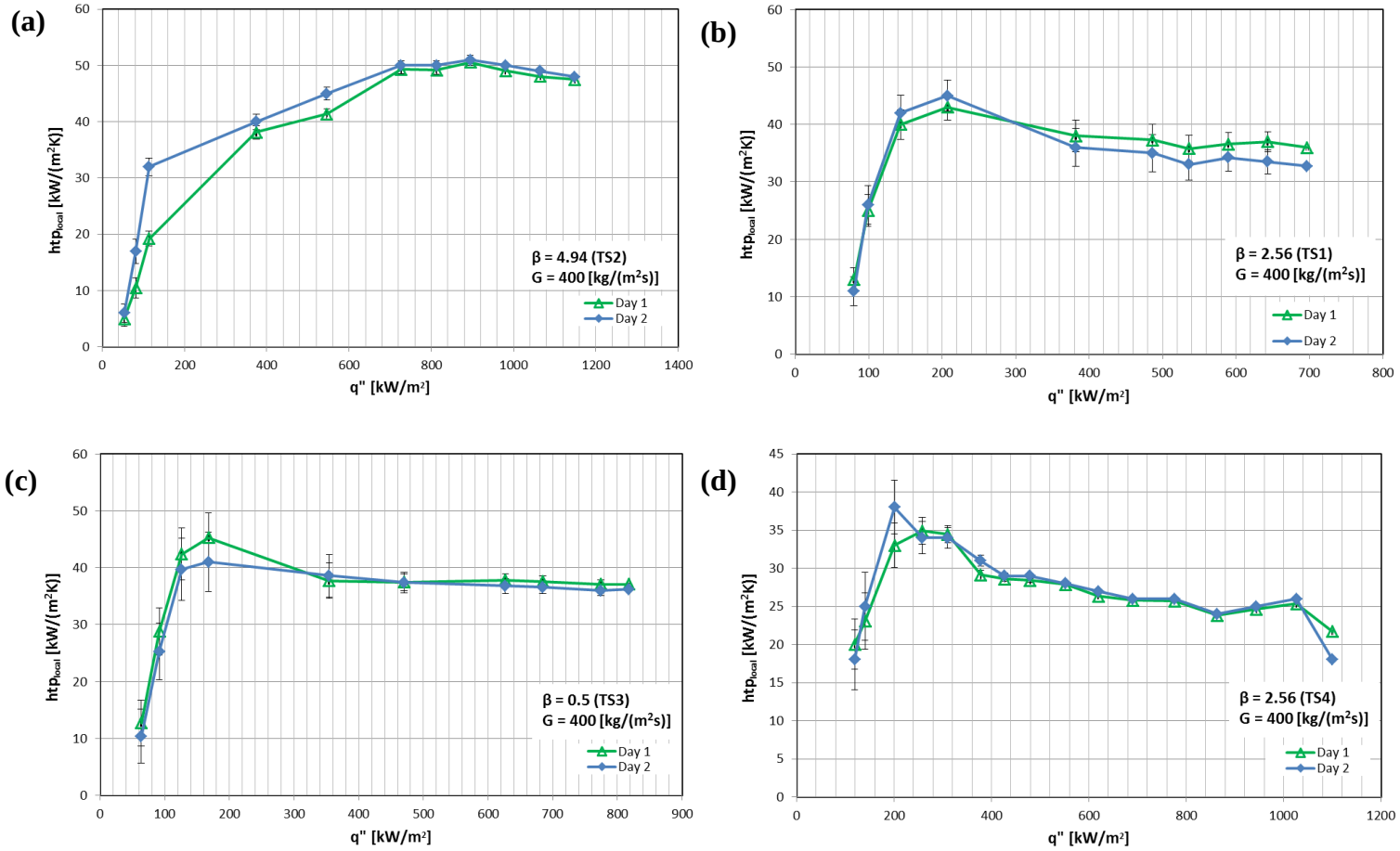

Figure 5.29 Repeatability of the local heat transfer data at a mass flux of G = 400 kg/m^{2}s at z/L = 0.6: (a) TS2, (b) TS1, (c) TS3 and (d) TS4 at z/L = 0.71.

5.4 Comparison of the data with Flow Boiling Heat Transfer Correlations

The flow boiling heat transfer coefficient data obtained in this study were compared to four widely used conventional scale and nine widely used micro-scale flow boiling heat transfer correlations from the literature. In this section, conventional scale and micro-scale correlations used in this study are described and discussed. Moreover, the data is compared with selected correlations for a selected value of mass flux and globally using the percentage of the data (α) within $\pm$ *30 %* error bars and the *MAE* method for each test section.

5.4.1 Conventional Scale Flow Boiling Heat Transfer Correlations and Comparison with the data

In the literature, many researchers such as Bao et al. (2000), Kosar et al. (2005), Lee and Garimella (2008) and Basu et al. (2001) presented comparison of their flow boiling heat transfer data obtained in micro-scale with conventional scale correlations. However, these correlations generally under-predicted or over-predicted the heat transfer coefficient at micro-scale level. This might be attributed to the fact that the conventional scale correlations do not consider the microscale effects such as surface tension and confinement. Since the surface tension force becomes dominant as the diameter decreases, this effect needs to be considered in micro-scale systems. In this study, the experimental heat transfer coefficient data were compared with Shah (1982), Gungor and Winterton (1986), Kandlikar (1990) and Liu and Winterton (1991) conventional scale correlations. The equations for these correlations are given in appendix A.

Figure 5.30 shows the comparison of the experimental data at the exit thermocouple reading with conventional scale correlations at the mass flux of *200 kg/m^{2}s* for each microchannel test section to show the trend. The first reason for choosing the exit heat transfer coefficient for the comparison is the working fluid entering the channel in a subcooled state (*~14 K*). Therefore, saturated boiling conditions do not exist at the inlet and middle of the channel especially when the heat flux is low. The second reason is that the empirical correlations were generally developed using the exit experimental

data. Therefore, data at the exit were used for the appropriate comparison. The last applied heat flux data for the longer test section is not included due to dry-out occurrence. The ± *30 %* error bands are also illustrated in Fig. 5.30. From the data in Fig. 5.30, it is apparent that all correlations except the Kandlikar (1990) correlation failed to capture the trend of the experimental data for all test sections. The correlation of Shah (1982), Gungor and Winterton (1990) and Liu and Winterton (1991) could reasonably predict the data at low heat fluxes. However, at high heat fluxes they highly over-predicted the experimental data. The dominant heat transfer mechanism was found to be nucleate boiling in all test sections at low and medium heat fluxes as presented in section 5.3. Also, the dominant heat transfer mechanism is generally nucleate boiling in conventional scale systems, see Chapter 2 literature review part. As can be seen in Fig. 5.30, the prediction of the correlations of Shah (1982), Gungor and Winterton (1990) and Liu and Winterton (1991) increase linearly with heat flux since they were developed for the conventional scale systems. Therefore, it is not surprising that these correlations could predict the data reasonably at low and medium heat fluxes. Whilst the Kandlikar (1990) correlation predicted well the experimental heat transfer coefficient for the test sections TS2 and TS4, it under-predicted the data for the TS1 and TS3. To draw a conclusion the experimental heat transfer data for all thermocouple locations are compared with correlations for all tested mass flux using MAE method (global comparison) in the following sections.

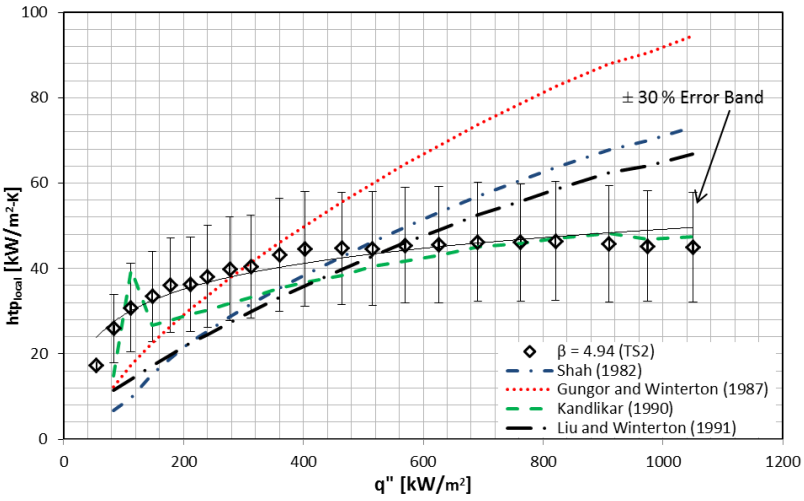

(a)

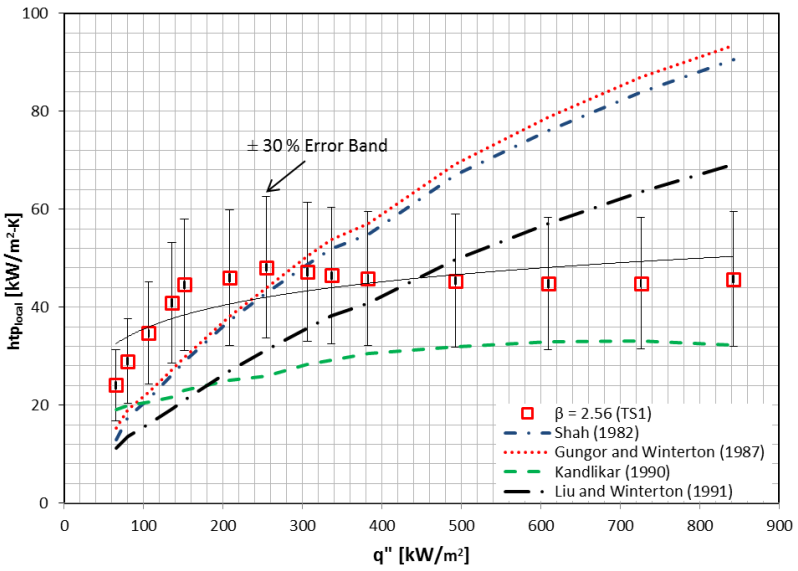
± 30 % Error Band
β = 2.56 (TS1)
Shah (1982)
Gungor and Winterton (1987)
Kandlikar (1990)
Liu and Winterton (1991)
htp_local [kW/m²-K]
q" [kW/m²]
0
20
40
60
80
100
0
100
200
300
400
500
600
700
800
900

(b)

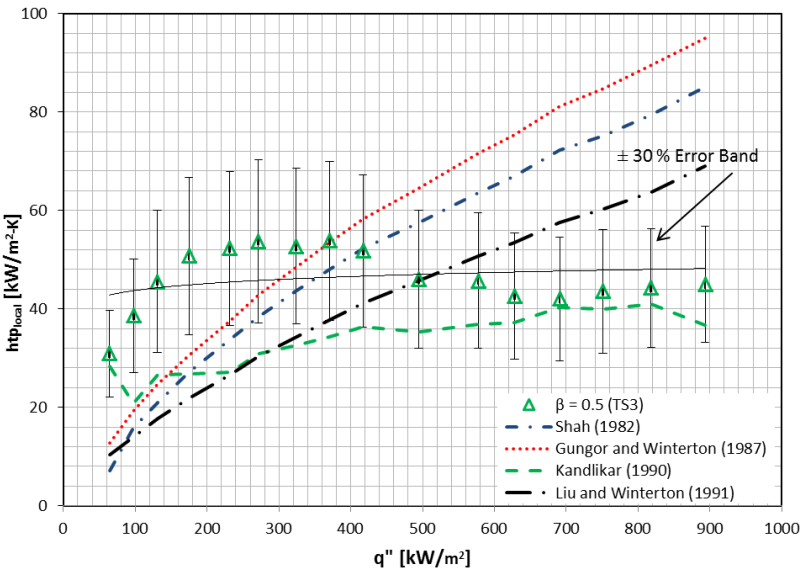
± 30 % Error Band
β = 0.5 (TS3)
Shah (1982)
Gungor and Winterton (1987)
Kandlikar (1990)
Liu and Winterton (1991)
htp_local [kW/m²-K]
q" [kW/m²]
0
20
40
60
80
100
0
100
200
300
400
500
600
700
800
900
1000

(c)

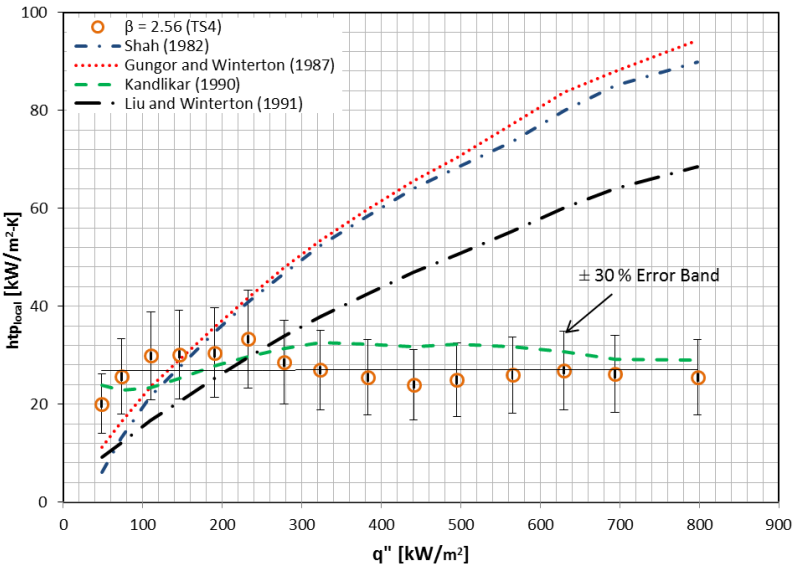

(d)

Figure 5.30 Comparison of the experimental local heat transfer data at the exit with macroscale correlations at the mass flux of G = 200 kg/m^{2}s: (a) TS2, (b) TS1, (c) TS3 and (d) TS4.

5.4.1.1 The correlation of Shah (1982)

Shah (1982) compared the convective and nucleate boiling components in the total flow boiling heat transfer coefficient. He selected the larger one as a flow boiling heat transfer coefficient. The nucleate boiling component was defined as a function of boiling number *Bo* whereas the convective boiling component was described as a function of convection number *NCO*. The correlation is valid over a reduced pressure range of *0.004-0.8*. The comparison of the experimental heat transfer data with the Shah (1982) correlation for each microchannel test section is provided in Fig. 5.31. As can be seen from the Fig. 5.31 the correlation cannot predict the experimental data accurately. The corresponding MAE values *45.9 %, 41.9 %, 49.8 %* and *55.1 %* for the channels TS1, TS2, TS3 and TS4, respectively. The percentage of the data within the ± *30 %* error bars are *36 %, 37.9 %, 34.8 %* and *36.3 %* for the channels TS1, TS2, TS3 and TS4 respectively, see Table 5.1.

5.4.1.2 The correlation of Gungor and Winterton (1987)

The correlation was developed for water, R-11, R-12, R-22, R-113 and R-114 using an experimental data bank (4300 data points). The authors developed the correlation in the form of Chen type correlation by adding the micro-convective mechanism and conventional macro-convective mechanism. The convective boiling multipliers *S* and *F* were defined as a function of the Boiling number *Bo* and Martinelli parameter (*X*) in the correlation. Fig. 5.32 compares the experimental data with the correlation of Gungor and Winterton (1987). The experimental data was predicted by the correlation even less well than for the Shah (1982) correlation with a MAE of *46.6 %, 50.5 %, 56.4 %* and *72.8 %* for the channels TS1, TS2, TS3 and TS4, respectively. Also the percentage of the data within the ± *30 %* error bars is poor as *38.8 %, 38.1 %, 31.8 %* and *29.1 %* for the channels TS1, TS2, TS3 and TS4, respectively, see Table 5.1.

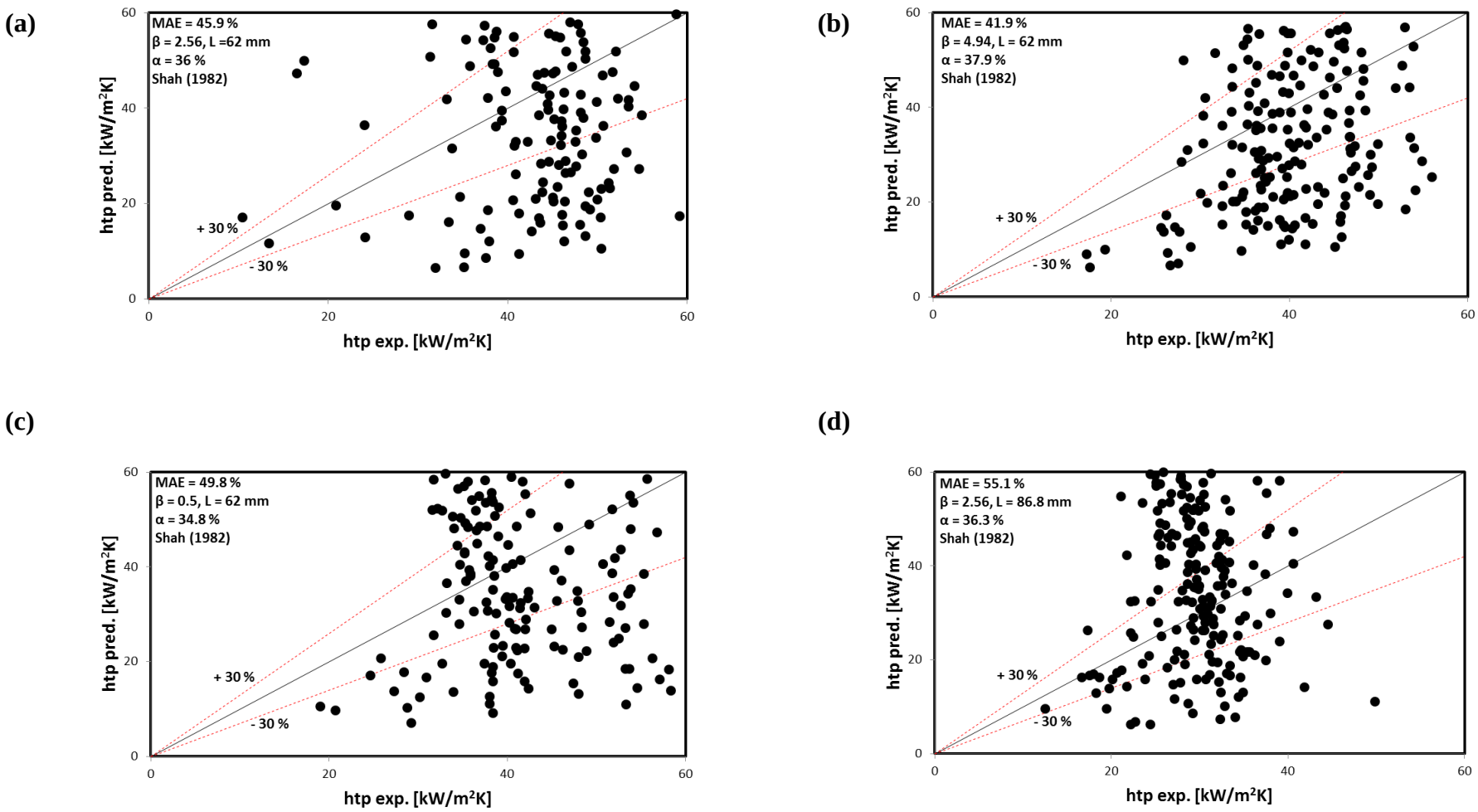

Figure 5.31 Comparison of the experimental heat transfer data with the Shah (1982) correlation: (a) TS1, (b) TS2, (c) TS3 and (d) TS4 microchannels.

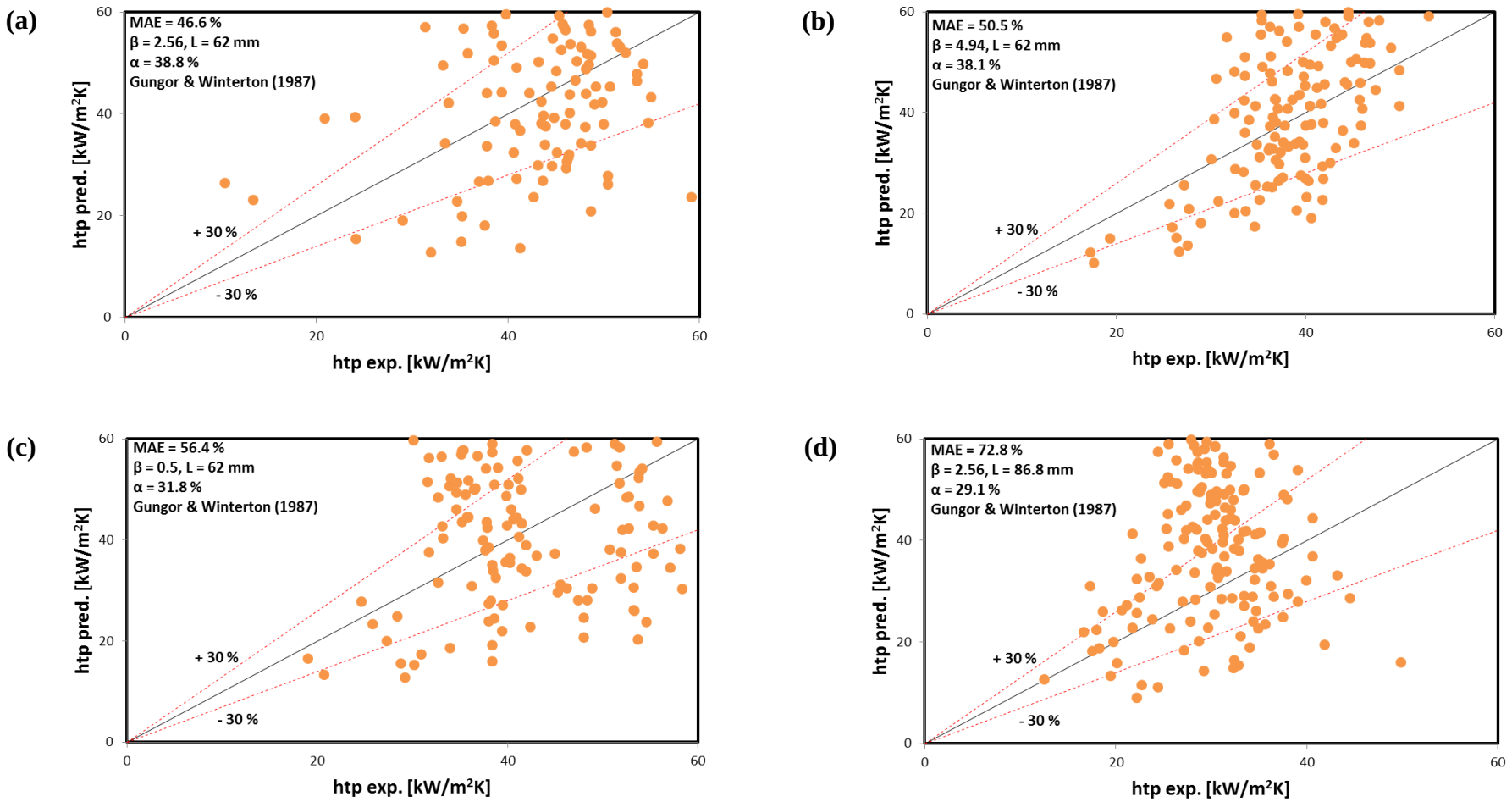

Figure 5.32 Comparison of the experimental heat transfer data with the Gungor and Winterton (1987) correlation: (a) TS1, (b) TS2, (c) TS3 and (d) TS4 microchannels.

5.4.1.3 The correlation of Kandlikar (1990)

Kandlikar (1990) developed a flow boiling heat transfer correlation for water and refrigerants based on 5264 data points. He used the convection number *NCO* to determine the dominant mechanism, i.e. whether convection or nucleation similar to Shah (1982). Additionally the fluid properties were considered with a fluid dependent parameter F_{fl} in the nucleate boiling component. The comparison of the experimental data with the Kandlikar (1990) correlation is displayed in Fig. 5.33. The experimental data was over predicted by the correlation. The corresponding MAE values are *58.2 %*, *65 %*, *66.8 %* and *70.6%* for the channels TS1, TS2, TS3 and TS4, respectively. The percentage of the data within the ± *30 %* error bands are *36.2 %*, *46.4 %*, *24.8 %* and *38. 6%* for the channels TS1, TS2, TS3 and TS4, respectively, see Table 5.1. As stated previously, the correlation followed the trend with data at the mass flux of *200 kg/ m^2s* and exit thermocouple location readings for all test sections. However, it can be seen that the correlation performs poor to predict the experimental data in a global comparison. It can be deduced from here that the Kandlikar (1990) correlation gives better prediction at the low mass flux inputs rather than high mass flux inputs.

5.4.1.4 The correlation of Liu and Winterton (1991)

Contrary to other researchers, Liu and Winterton (1991) did not correlate the nucleate boiling component with the boiling number *Bo*. They used the pool boiling correlation of Cooper to correlate nucleate boiling component. Similar to Gungor and Winterton (1987) they multiplied convection and nucleate boiling components with enhancement and suppression factors. The experimental data is compared with the Liu and Winterton (1991) correlation in Fig. 5.34. The experimental data were predicted better by this correlation compared to other conventional-scale correlations used in this study. The corresponding MAE values are *33.9 %*, *28.6 %*, *35.3 %* and *42.1 %* for the TS1, TS2, TS3 and TS4, respectively. The correlation resulted in the best prediction for the TS2 with *57 % α* value. For other channels the percentage of the data within ± *30 %* error bands (α) are *46.6 %*, *44.7 %* and *43.1 %* for the TS1, TS3 and TS4, respectively, see Table 5.1.

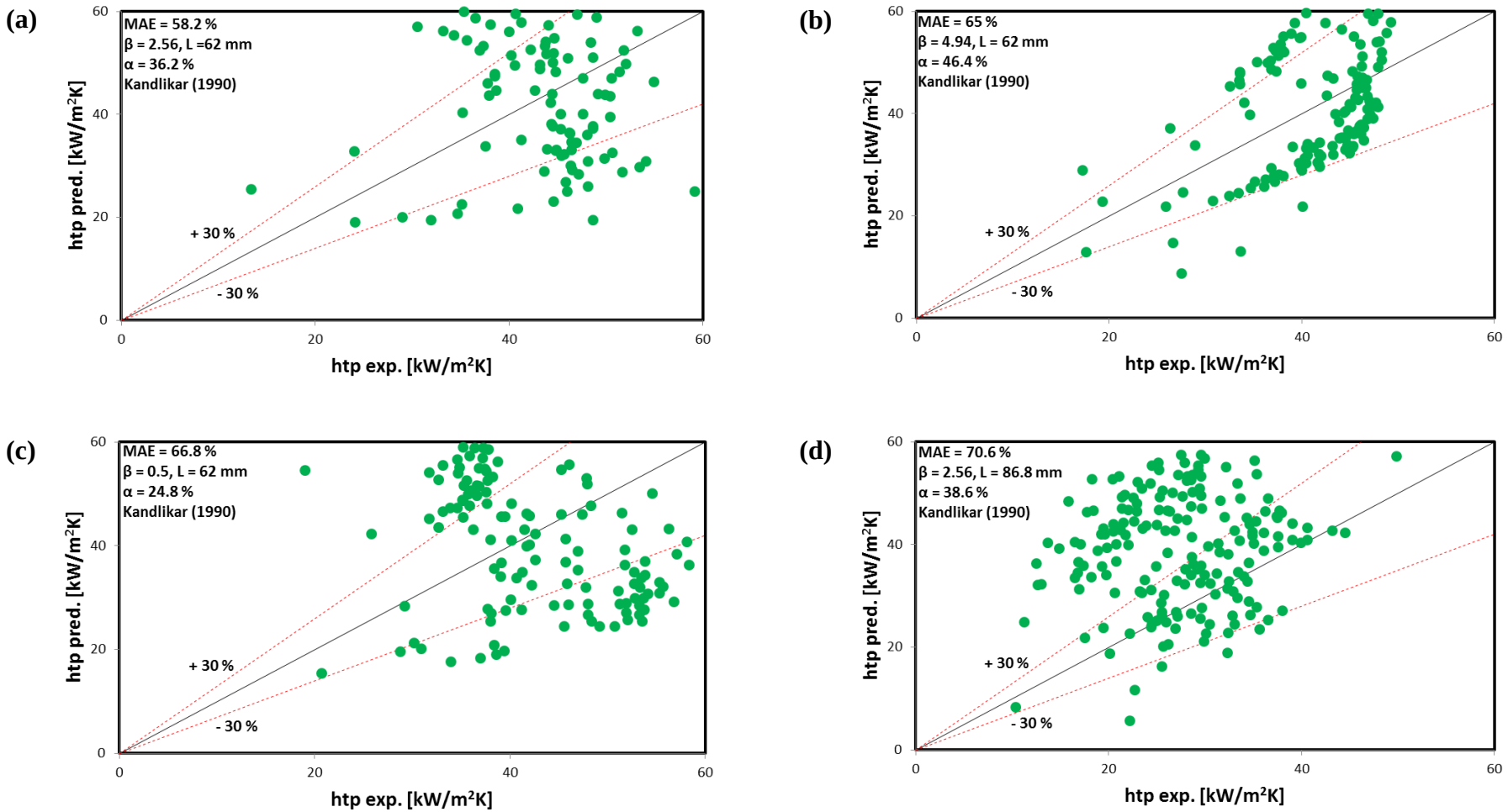

Figure 5.33 Comparison of the experimental heat transfer data with the Kandlikar (1990) correlation: (a) TS1, (b) TS2, (c) TS3 and (d) TS4 microchannels.

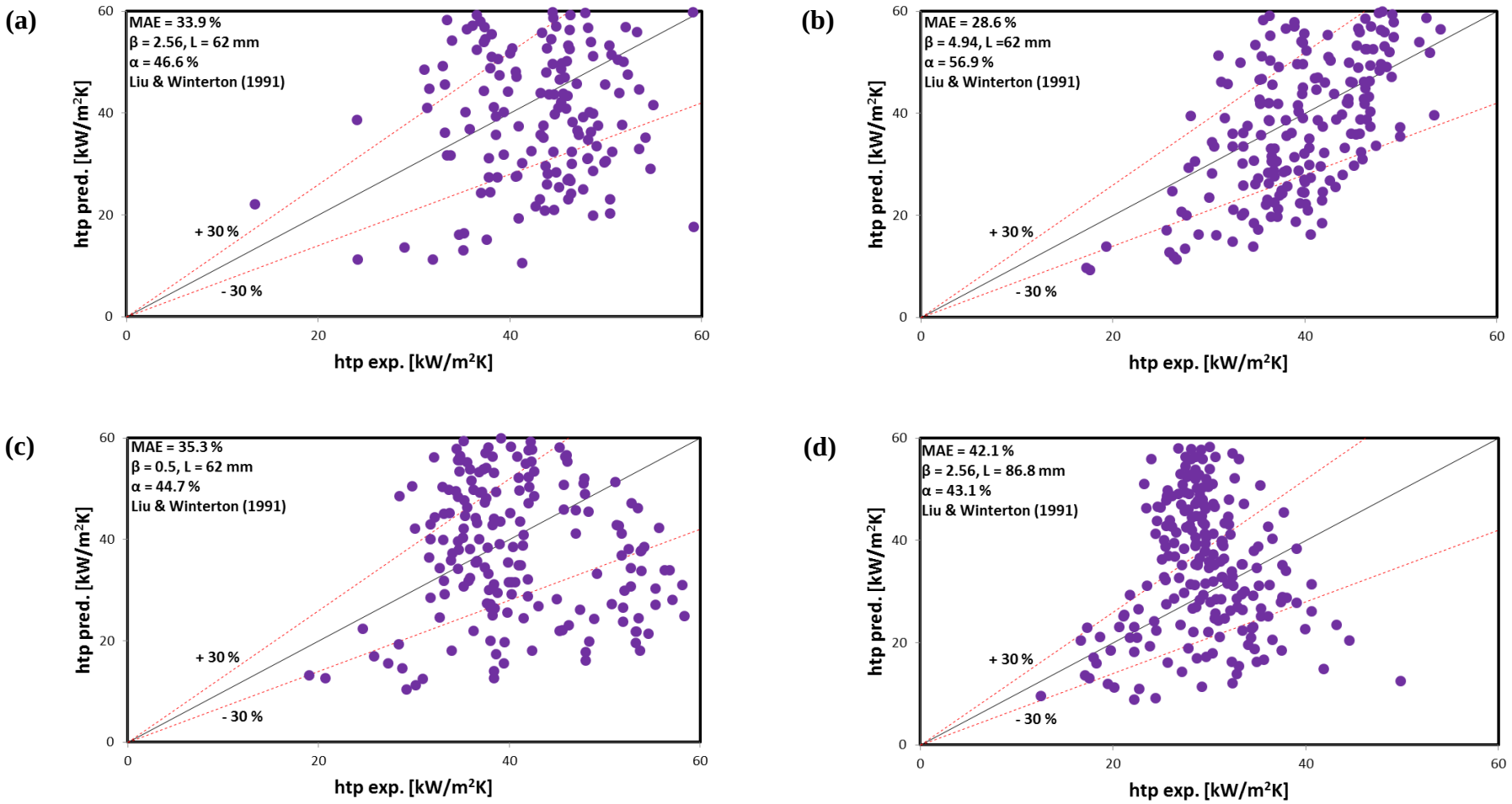

Figure 5.34 Comparison of the experimental heat transfer data with the Liu and Winterton (1991) correlation: (a) TS1, (b) TS2, (c) TS3 and (d) TS4 microchannels.

Table 5.1 MAE and the percentage of data within ± 30 % error bands for conventional-scale correlations.

Correlation	β = 2.56 (TS1)		β = 4.94 (TS2)		β = 0.5 (TS3)		β = 2.56 (TS4)	
	MAE %	α %	MAE %	α %	MAE %	α %	MAE %	α %
Shah (1982)	45.9	36	41.9	37.9	49.8	34.8	55.1	36.3
Gungor & Winterton (1987)	46.6	38.8	50.5	38.1	56.4	31.8	72.8	29.1
Kandlikar (1990)	58.2	36.2	65	46.4	66.8	24.8	70.6	38.6
Liu& Winterton (1991)	33.9	46.6	28.6	56.9	35.3	44.7	42.1	43.1

In this section, the comparisons of the experimental flow boiling heat transfer data with the conventional-scale correlations of Shah (1982), Gungor and Winterton (1987), Kandlikar (1990) and Liu and Winterton (1991) were presented. As can be seen from figures 5.31-5.34 and table 5.1, the conventional-scale correlations could not predict well the experimental heat transfer coefficients for all test sections. The reason of the poor prediction of the Shah (1982) correlation could be the correlation parameters. The nucleate boiling component was defined by the Boiling number (*Bo*) function. Other parameters such as fluid properties and surface roughness, which affect nucleate boiling significantly, were not considered in the correlation. A possible explanation for the poor predictions of the Gungor and Winterton (1987) and Liu and Winterton (1991) correlations could be attributed to the heat flux term which was included in the nucleate boiling term as well as the convective boiling term. Consequently, the predicted heat transfer coefficients increased more than the experimental heat transfer coefficients as the heat flux was increased.

5.4.2 Micro-Scale Flow Boiling Heat Transfer Correlations and Comparison with the data

In this section, the flow boiling heat transfer coefficient data were compared with the nine micro-scale correlations. The conventional-scale correlations could not predict the data as discussed in section 5.4.1. Therefore, nine micro-scale correlations were selected to compare with the experimental data namely Yu et al. (2002), Kandlikar and Balasubramanian (2004), Lee and Mudawar (2005a), Sun and Mishima (2009), Li and Wu (2010a) and Lim et al. (2015). These correlations were developed for water. However, Lazarek and Black (1982) and Mahmoud and Karayiannis (2011) 1 and 2 correlations are also included which were developed based on refrigerants. The equations for these correlations are given in appendix A.

Figure 5.35 displays the comparison of the local flow boiling heat transfer data at the exit for all heat flux inputs with the micro-scale correlations. At low heat flux inputs none of the correlations except the correlation of Kandlikar and Balasubramanian (2004) correlation captured the trend and predicted the experimental data. The Lazarek and Black (1982), Yu et al. (2002), Sun and Mishima (2009), Li and Wu (2010a) and

Mahmoud and Karayiannis (2011) correlations captured the trend but under-predicted the experimental data at low heat flux inputs. However, at medium and high heat flux inputs, Lee and Mudawar (2005a), Li and Wu (2010a) and Mahmoud and Karayiannis (2011) correlations followed the trend of the experimental data and resulted in fair predictions for all test sections. The Lee and Mudawar (2005a) correlation over-predicted the experimental data for the TS2, TS4 microchannels at medium and high heat flux inputs. On the other hand, Li and Wu (2010a) and Mahmoud and Karayiannis (2011) correlations predicted the data well, especially at high heat flux inputs. The Lim et al. (2015) correlation highly under predicted the experimental data for all heat flux inputs. The detailed comparisons (global comparison) of the experimental data with each correlation are presented in the following sections.

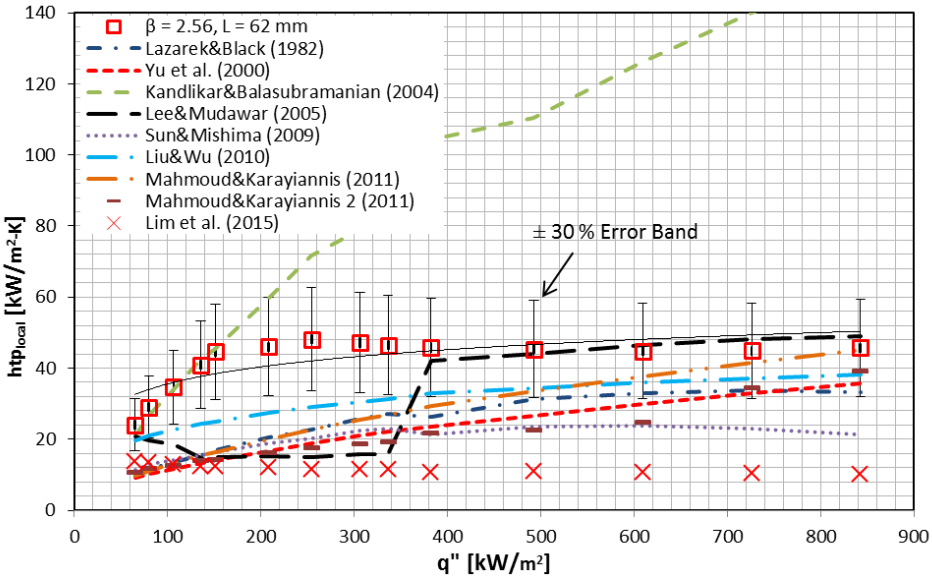

(a)

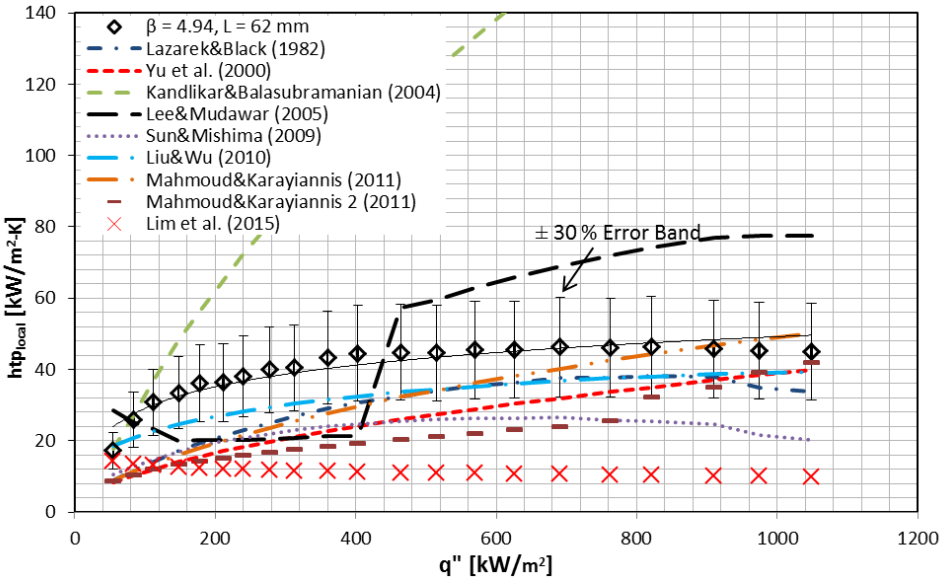
β = 4.94, L = 62 mm
Lazarek&Black (1982)
Yu et al. (2000)
Kandlikar&Balasubramanian (2004)
Lee&Mudawar (2005)
Sun&Mishima (2009)
Liu&Wu (2010)
Mahmoud&Karayiannis (2011)
Mahmoud&Karayiannis 2 (2011)
Lim et al. (2015)
± 30 % Error Band
htp_local [kW/m²-K]
q" [kW/m²]
0
20
40
60
80
100
120
140
0
200
400
600
800
1000
1200

(b)

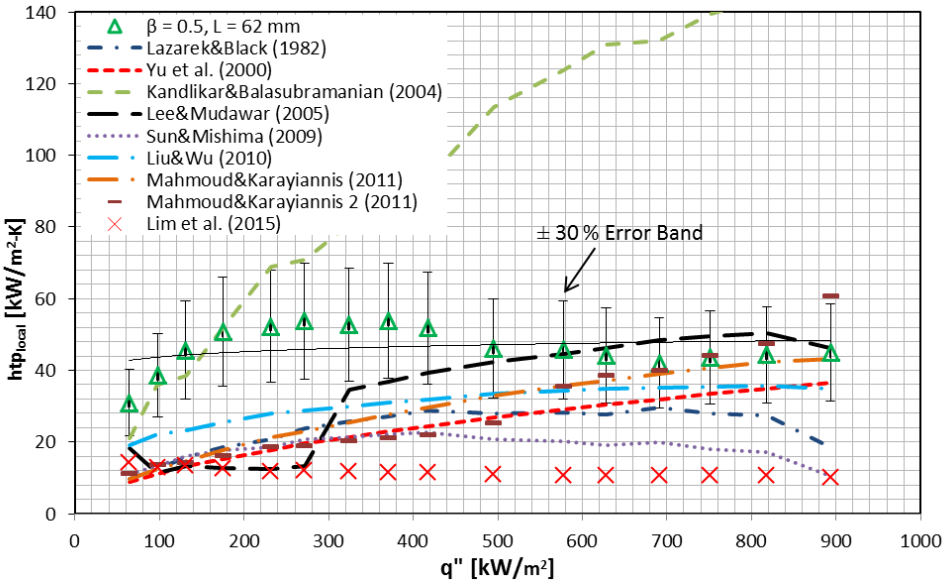
β = 0.5, L = 62 mm
Lazarek&Black (1982)
Yu et al. (2000)
Kandlikar&Balasubramanian (2004)
Lee&Mudawar (2005)
Sun&Mishima (2009)
Liu&Wu (2010)
Mahmoud&Karayiannis (2011)
Mahmoud&Karayiannis 2 (2011)
Lim et al. (2015)
± 30 % Error Band
htp_local [kW/m²-K]
q" [kW/m²]
0
20
40
60
80
100
120
140
0
100
200
300
400
500
600
700
800
900
1000

(c)

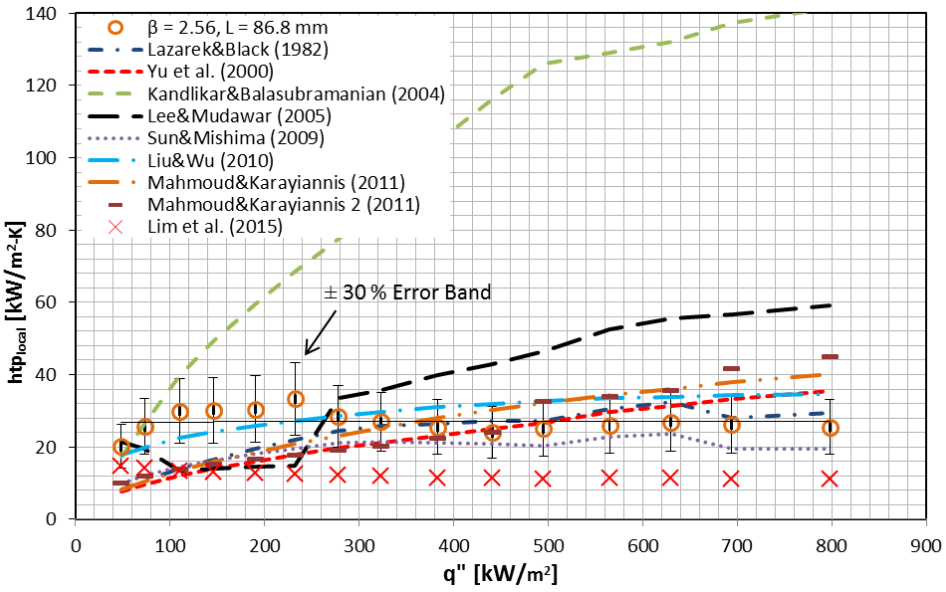

(d)

Figure 5.35 Comparison of the experimental local heat transfer coefficient at the exit with microscale correlations at the mass flux of 200 kg/m^{2}s: (a) TS1, (b) TS2, (c) TS3 and (d) TS4.

5.4.2.1 The correlation of Lazarek and Black (1982)

Lazarek and Black (1982) carried out sets of experiments to investigate flow boiling heat transfer in a vertical circular stainless steel tube having *3.1 mm* diameter and *126 mm* heated length using R-113 as the working fluid as stated in Chapter 2 in the literature review part. They found that nucleate boiling is the dominant heat transfer mechanism in their tests. They proposed a flow boiling heat transfer correlation based on their data (728 data points) where the heat transfer coefficient was correlated as a function of the Boiling number (*Bo*), Reynolds number (*Re*), fluid thermal conductivity (k_L) and channel diameter (*D*) as shown in equations 5.1 and 5.2, see appendix A for details. This means that the correlation was developed based on the dominance of nucleate boiling but also considers the effects of fluid properties and channel diameter. Although the Lazarek and Black (1982) correlation developed based on refrigerant R-113, the correlation was selected because the dominant heat transfer mechanism was found to be nucleate boiling at low and medium heat flux inputs in this study. The experimental data for all test sections were compared with the correlation of Lazarek and Black (1982) globally in Fig. 5.36. As can be seen from Fig. 5.36, although half of the experimental data is within the percentage of the ± *30 %* error bands for all test sections, the correlation gives poor prediction for the experimental heat transfer data. The corresponding MAE values are *32.5 %*, *26.6 %*, *30.6 %* and *30.2 %* for the TS1, TS2, TS3 and TS4, respectively. The percentage of the data within the ± *30 %* error bands are *48.7 %*, *61.1 %*, *51.2 %* and *51.8 %* for the TS1, TS2, TS3 and TS4, respectively, see Table 5.2.

$$h_{tp} = \frac{k_L}{D} 30 \,\mathrm{Re}_L^{0.857}\, Bo^{0.714} \tag{5.1}$$

$$= k_L 30 G^{0.143} D^{-0.143} q^{0.714} h_{\mathrm{lg}}^{-0.714} \mu_L^{-0.857} \tag{5.2}$$

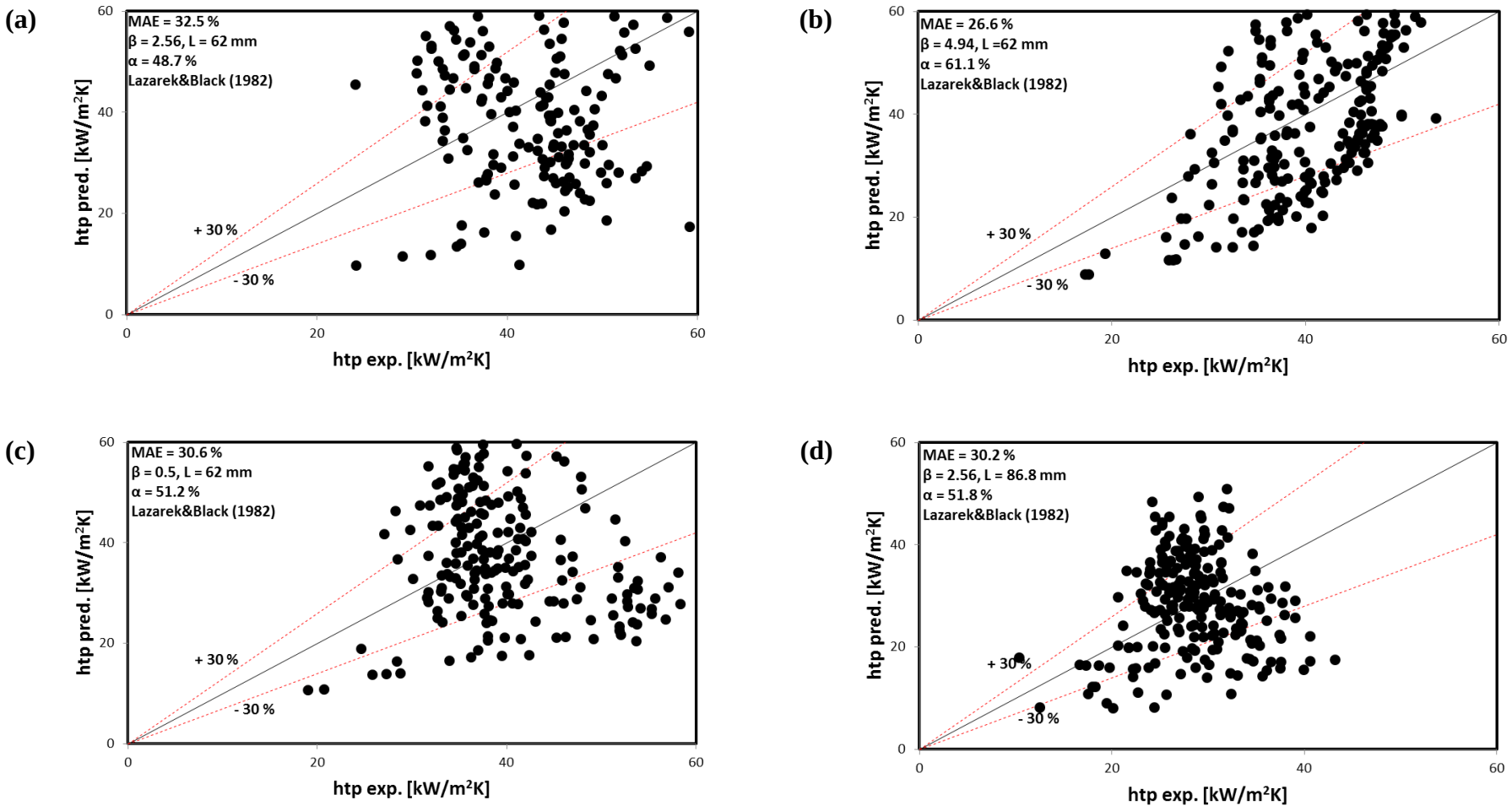

Figure 5.36 Comparison of experimental heat transfer data with Lazarek and Black (1982) correlation: (a) TS1, (b) TS2, (c) TS3 and (d) TS4.

5.4.2.2 The correlation of Yu et al. (2002)

Yu et al. (2002) investigated subcooled flow boiling of water in horizontal tube with a diameter of *2.98 mm*. The flow boiling heat transfer coefficient was correlated as a function of liquid Weber number (We_L) and Boiling number (Bo) as shown in equations 5.3 and 5.4, see appendix A for details. The correlation considered the nucleate boiling and convective boiling components equally as shown in equations 5.3 and 5.4. Therefore the prediction was better than the correlation of Lazarek and Black (1982) as can be seen from Fig. 5.37. The correlation predicted well the experimental data of the TS4 with a *20.2 %* MAE value and *75.5 %* α value. On the other hand, the experimental data for the microchannel TS3 was predicted reasonably with a MAE value of *26.5 %*. However, the correlation under-predicted the experimental data for the TS1 and TS2 microchannels resulted in *37.5 %* and *30.5 %* MAE, respectively, see Table 5.2.

$$h_{tp} = 6.4\times10^{6}(Bo^{2}We_{L})^{0.27}\left(\frac{\vartheta_g}{\vartheta_L}\right)^{0.2} \tag{5.3}$$

$$= 6.4\times10^{6}\left(\frac{Bo^{2}\vartheta_L G^{2} D}{\mu_L}\right)^{0.27}\left(\frac{\vartheta_g}{\vartheta_L}\right)^{0.2} \tag{5.4}$$

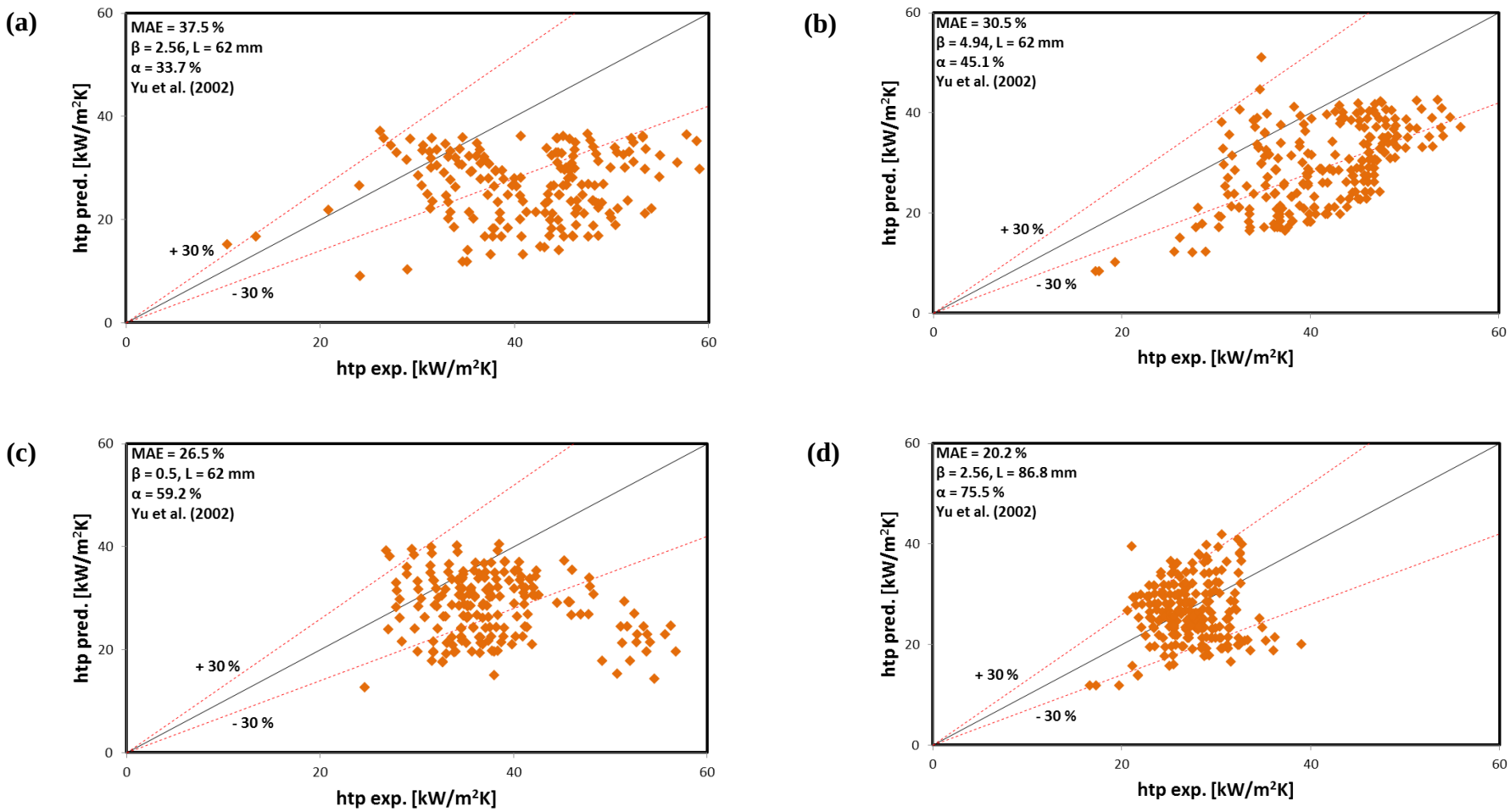

Figure 5.37 Comparison of experimental heat transfer data with Yu et al. (2002) correlation: (a) TS1, (b) TS2, (c) TS3 and (d) TS4.

5.4.2.3 The correlation of Kandlikar and Balasubramanian (2004)

Kandlikar and Balasubramanian (2004) modified the correlation of Kandlikar (1990) which was developed for conventional-scale tubes. The new correlation was extended by the authors to be applied in especially low Reynolds number conditions ($Re < 1600$). The correlation was developed for a wide range of refrigerants and water in vertical and horizontal tubes with *0.19 mm* and *32 mm* diameter range. Figure 5.38 compares the experimental data with the Kandlikar and Balasubramanian (2004) correlation for all test sections. The correlation predicted better the experimental data compared to old version. The MAE values were between *58.2 %* and *70.6 %* for the old correlation. However, the error values for the test sections ranged from *35.2 %* to *55.7 %* in the new version of the correlation, see table 5.2.

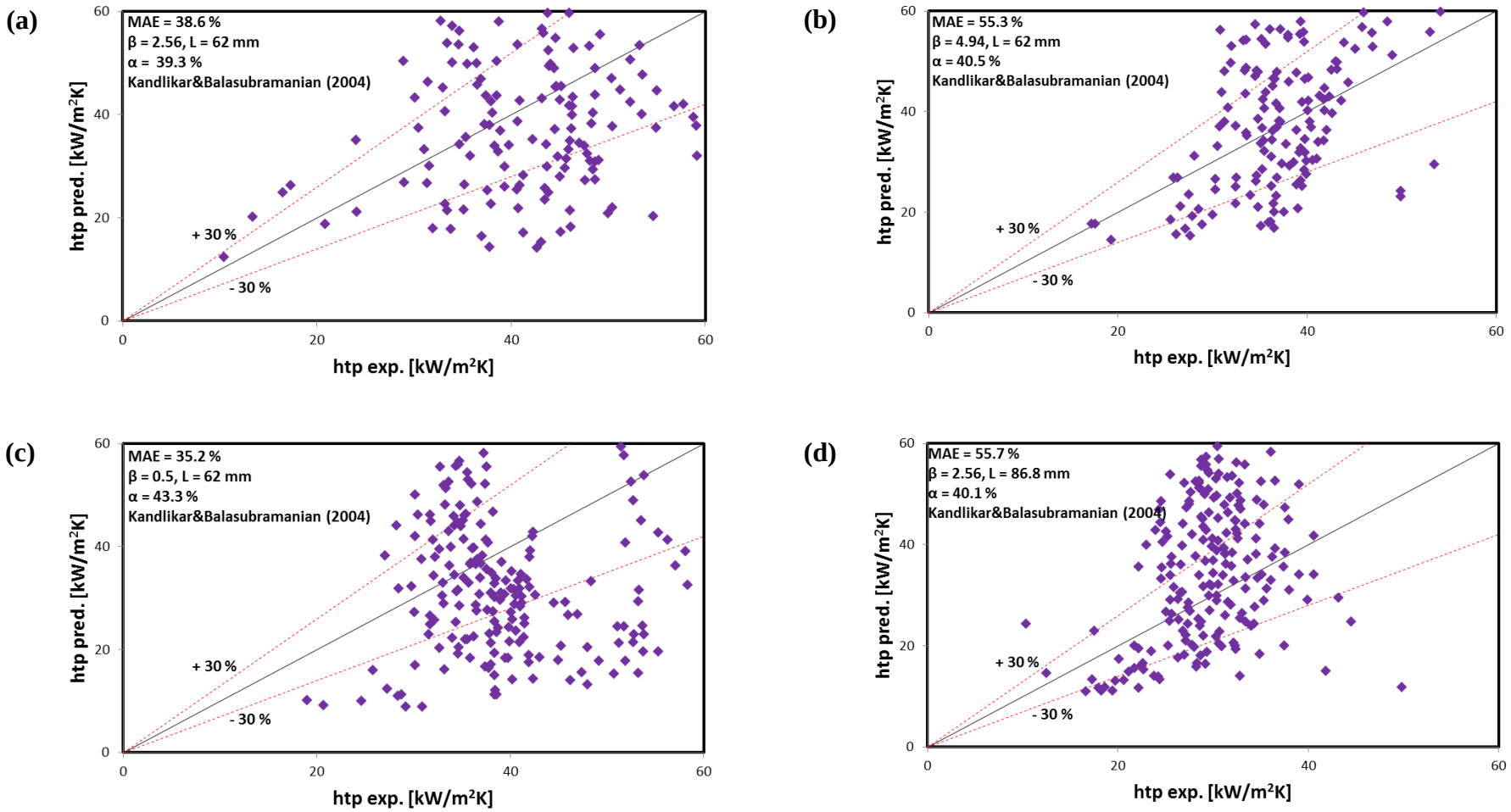

Figure 5.38 Comparison of experimental heat transfer data with Kandlikar and Balasubramanian (2004) correlation: (a) TS1, (b) TS2, (c) TS3 and (d) TS4.

5.4.2.4 The correlation of Lee and Mudawar (2005a)

Lee and Mudawar (2005a) proposed a correlation for flow boiling heat transfer in a rectangular microchannel with a *0.35 mm* hydraulic diameter. The correlation was based on the *318* heat transfer data points of refrigerant R134a and water. They proposed three correlations for a three vapour quality range of $x < 0.05$, $0.05 < x < 0.55$ and $x > 0.55$. The heat transfer coefficient was correlated as a function of Boiling number (*Bo*), liquid Weber number (We_L), Martinelli parameter (X) and single-phase heat transfer coefficient. The experimental data are compared to correlation of Lee and Mudawar (2005a) in Fig. 5.39. As can be seen from Fig. 5.39, the correlation under predicted the experimental data for the TS1, TS2 and TS3 with a mean absolute error values of *50.6 %*, *38.7 %* and *41.8 %*, respectively. However, the data within the percentage of the ± *30 %* error bands increase as the aspect ratio of the channel increase. Moreover, the experimental data for the TS4 was predicted better than the other channels by the correlation with a MAE of *28.5 %* and α of *48.6 %*, see Table 5.2. A possible reason for the failure of this correlation could be attributed to the fact that the heat transfer coefficient was correlated using Martinelli parameter (X) only in low quality region ($x < 0.05$) where the heat flux effect is strong in this region. The Martinelli parameter (X) is flow parameter which does not have any term including heat flux effect. Another possible explanation could be the experimental methodology. Lee and Mudawar (2005a) varied the mass flux whilst they kept constant the heat flux. However, the heat flux was increased at constant mass flux during experiments in this study.

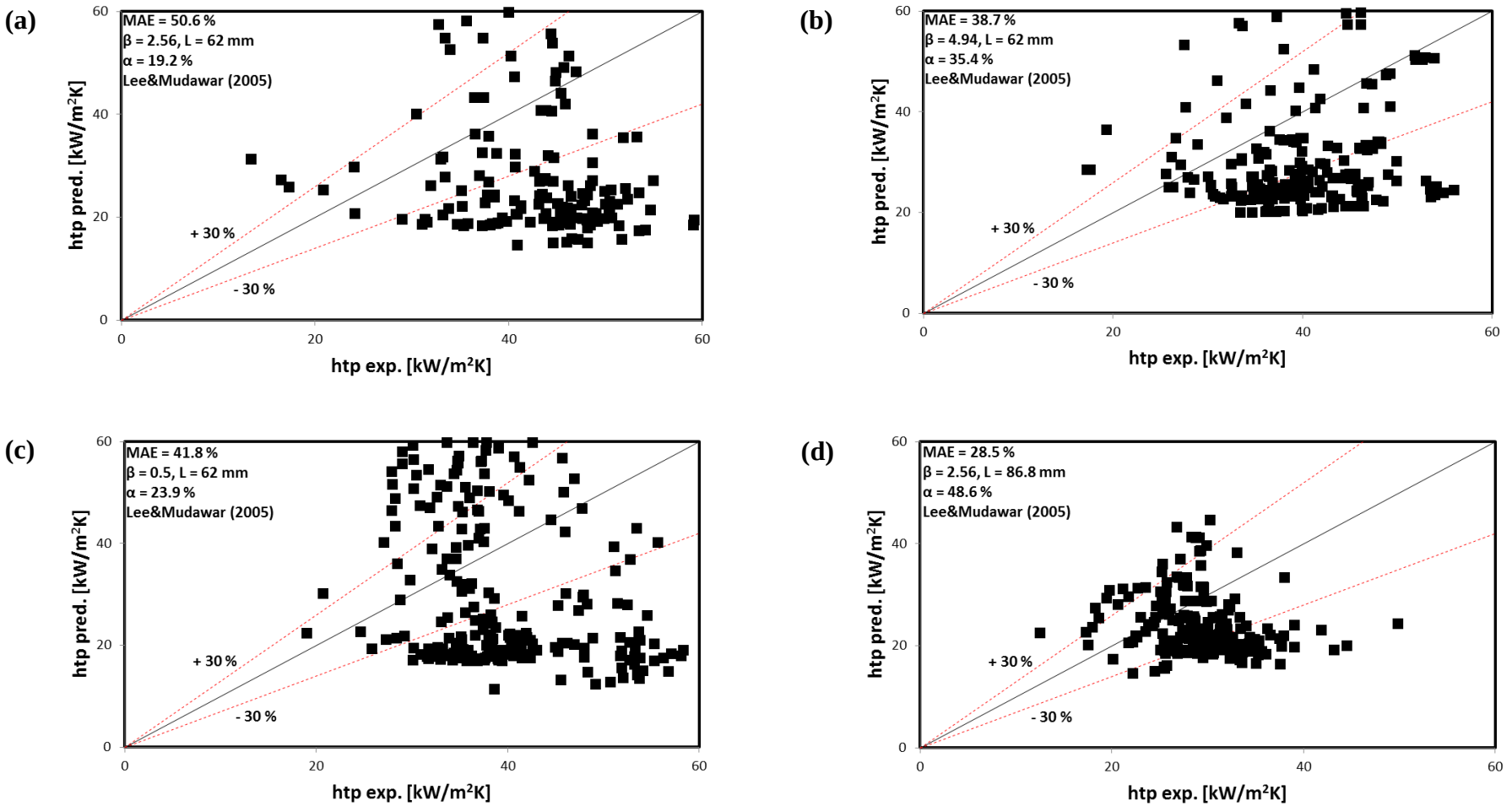

Figure 5.39 Comparison of experimental heat transfer data with Lee and Mudawar (2005a) correlation: (a) TS1, (b) TS2, (c) TS3 and (d) TS4.

5.4.2.5 The correlation of Sun and Mishima (2009)

Sun and Mishima (2009) compared the *2505* flow boiling heat transfer data points obtained from *11* liquids including water and *0.21-6.05 mm* diameter range microchannels with *13* correlations. They concluded that the Lazarek and Black (1982) type correlations give better predictions than the Chen type correlations. Accordingly, they modified the Lazarek and Black (1982) correlation by introducing the liquid Weber number (We_L) which is the convective boiling term. Since the Lazarek and Black (1982) correlation based on the dominance of nucleate boiling, the correlation of Sun and Mishima (2009) considered the convective boiling component by introducing the liquid Weber number (We_L). Consequently, the correlation performed better than the Lazarek and Black (1982) correlation. Figure 5.40 compares the experimental data with the Sun and Mishima (2009) correlation. The correlation predicted the experimental data reasonably with less than *30 %* mean absolute error values for all test sections. Moreover, the percentage of the data within the ± *30 %* error bars are more than *60 %* for the TS2, TS3 and TS4 and *50.3 %* for the TS1 microchannel as shown in Fig. 5.40, see Table 5.2.

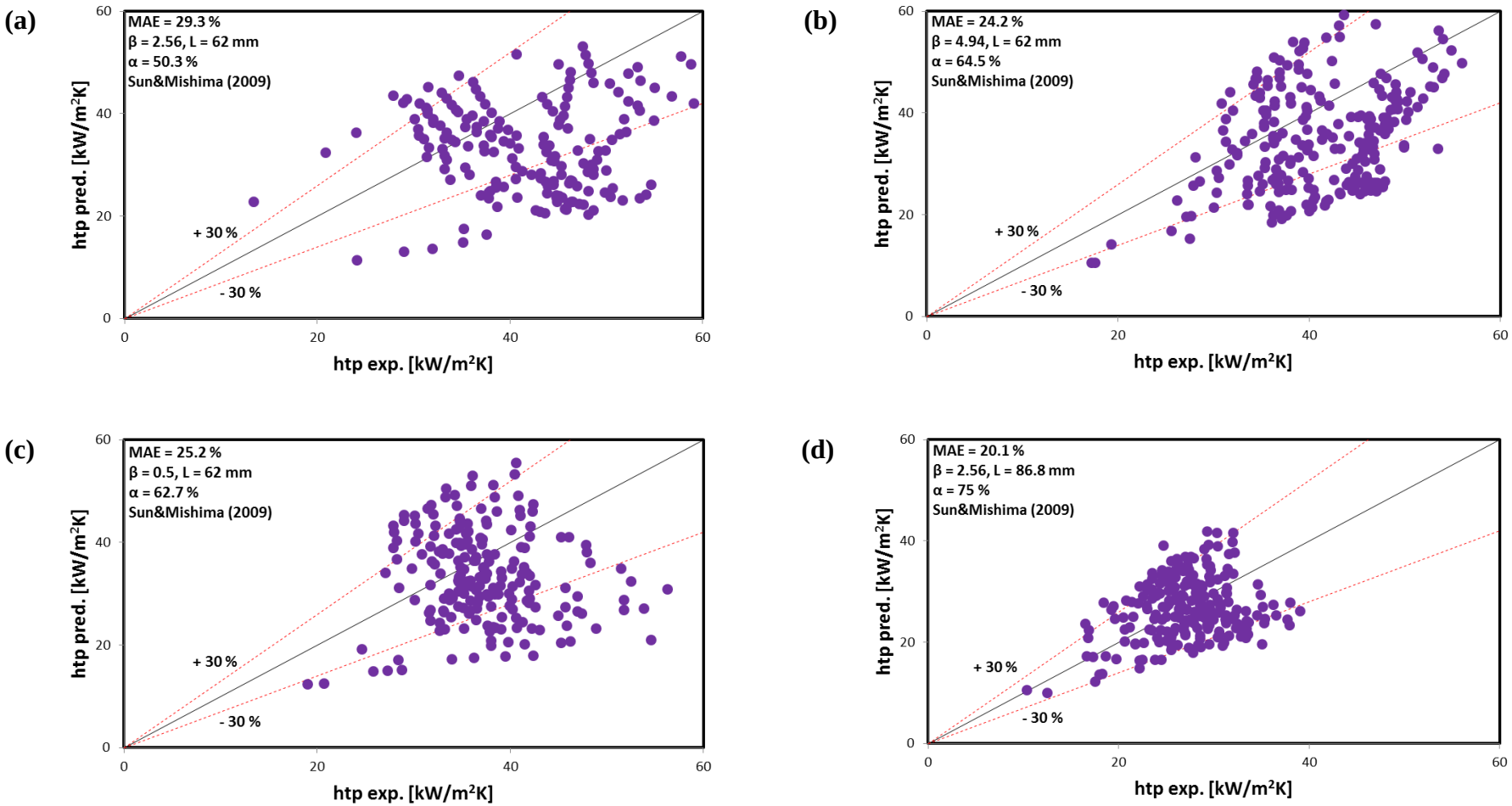

Figure 5.40 Comparison of experimental heat transfer data with Sun and Mishima (2009) correlation: (a) TS1, (b) TS2, (c) TS3 and (d) TS4 microchannels.

5.4.2.6 The correlation of Li and Wu (2010a)

Li and Wu (2010a) proposed a flow boiling heat transfer coefficient correlation based on the twelve fluids including water and tubes having *0.148-3.25 mm* diameter range. They correlated the heat transfer coefficient as a function of Boiling number (*Bo*), Bond number (*Bd*) and liquid Reynolds number (Re_L) as shown in equations 5.5 and 5.6, see appendix A for details. The authors used the Bond number (*Bd*) in the correlation in order to consider the surface tension effect.

$$h_{tp} = 334 Bo^{0.3} (Bd\, \mathrm{Re}_L^{0.36})^{0.4} \frac{k_L}{D_h} \tag{5.5}$$

$$= 334 Bo^{0.3} (\frac{g \Delta \rho D_h^2\, \mathrm{Re}_L^{0.36}}{\sigma})^{0.4} \frac{k_L}{D_h} \tag{5.6}$$

The experimental data were compared with the Li and Wu (2010a) correlation in Fig. 5.41. The correlation predicted well the experimental data for the TS2, TS3 and TS4 with a MAE value of *19.3 %*, *15.8 %* and *13.7 %*, respectively. The percentage of the data within ± *30 %* error bands are also quite good, having *97.4 %*, *89.5 %* and *99.1 %* for the TS2, TS3 and TS4, respectively. However, the correlation performed less well compared to the other microchannels for the TS1 with a *27.1 %* MAE value. The percentage of the data within ± 30 % error bands is also lower (*60.8 %*) compared to other microchannels, see Table 5.2. A possible explanation for the success of this correlation compared to other correlations could be the inclusion of the surface tension effect in the correlation. Since the surface tension and confinement effects have strong influence in microchannels, inclusion of the surface tension parameter into the correlation could be the reason of the good performance of the Li and Wu (2010a) correlation.

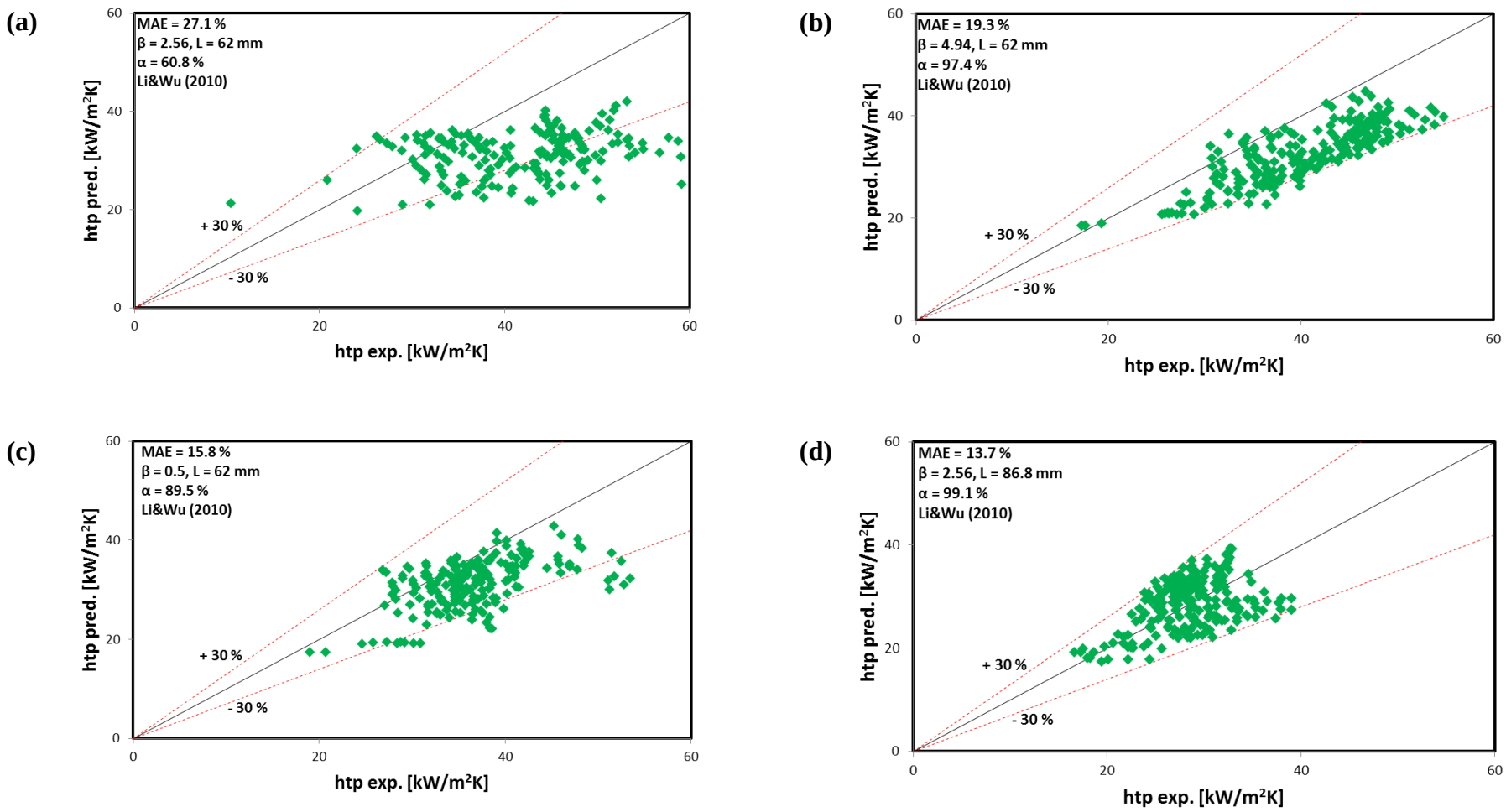

Figure 5.41 Comparison of experimental heat transfer data with Li and Wu (2010a) correlation: (a) TS1, (b) TS2, (c) TS3 and (d) TS4 microchannels.

5.4.2.7 Correlations of Mahmoud and Karayiannis (2011)

Mahmoud and Karayiannis (2011) developed two heat transfer coefficient correlations based on 8561 data points for R134a covering a diameter range from 0.52 mm to 4.26 mm. In the first correlation the heat transfer coefficient was correlated as a function of Boiling number (*Bo*), liquid Weber number (We_L), liquid Reynolds number (Re_L) and confinement number (*Co*). In the second correlation, the experimental data was correlated using the superposition method of Chen (1966). The authors used the Cooper pool boiling correlation instead of the Forster and Zuber (1955) correlation in the original Chen correlation (1966). The details of the correlations proposed by Mahmoud and Karayiannis (2011) are given in appendix A. The experimental heat transfer data were compared to Mahmoud and Karayiannis (2011) correlations in Figs. 5.42 and 5.43. The first correlation (Lazarek and Black type correlation) predicted well the experimental data for the TS2, TS3 and TS4 with a MAE value less than 25 % and α value more than 65 %. The experimental data for the TS1 were predicted worse by the correlation compared to other microchannels. The corresponding MAE value for this microchannel is 31 % and the percentage of the data within ± 30 % error bands is 56.9 %, see Table 5.2. On the other hand the second correlation (Chen type correlation) of authors predicted the experimental data less well than the first type correlation for all test sections as can be seen in Fig. 5.41. A possible explanation for the success of the first correlation could be the inclusion of the confinement effect in the correlation. It is worth mentioning that the Lazarek and Black type correlation performed better than the Chen type correlation.

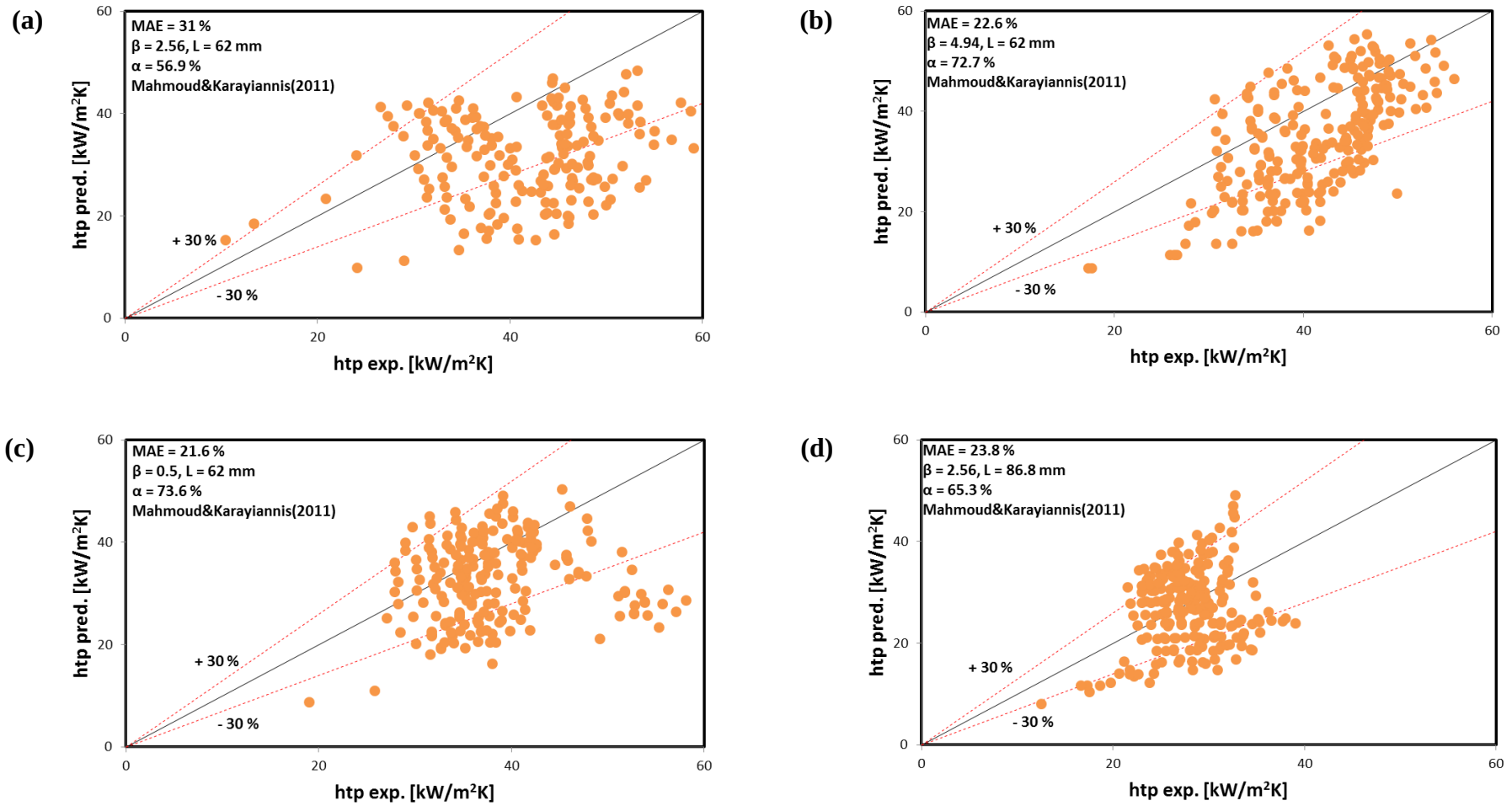

Figure 5.42 Comparison of experimental heat transfer data with Mahmoud and Karayiannis 1 (2011) correlation: (a) TS1, (b) TS2, (c) TS3 and (d) TS4 microchannels.

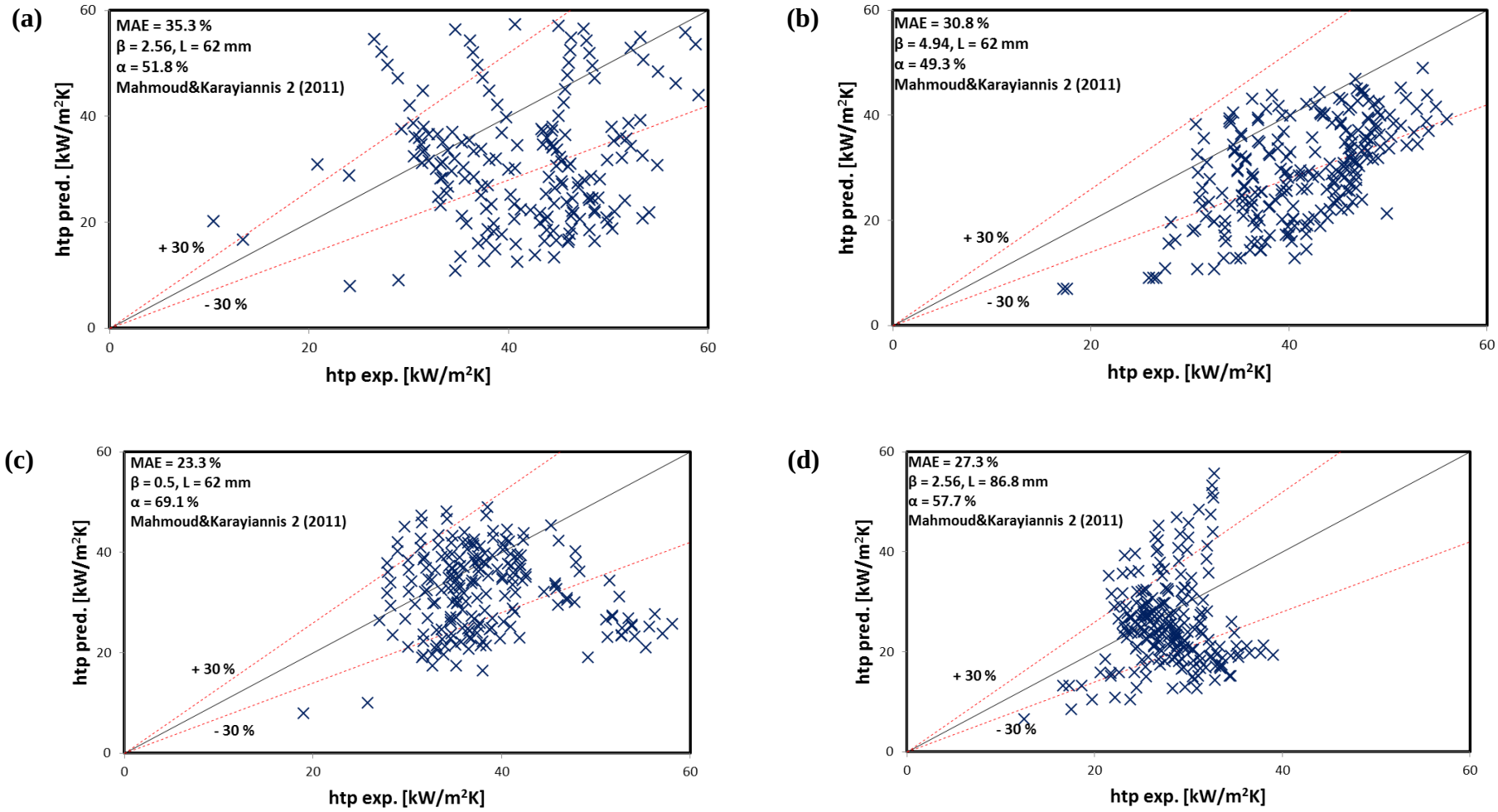

Figure 5.43 Comparison of experimental heat transfer data with Mahmoud and Karayiannis 2 (2011) correlation: (a) TS1, (b) TS2, (c) TS3 and (d) TS4 microchannels.

5.4.2.8 The correlation of Lim et al. (2015)

Lim et al. (2015) investigated the flow boiling heat transfer characteristics of water in a rectangular copper microchannel with *0.5 mm* hydraulic diameter. The authors compared their data with several correlations. They found that the available correlations over-predicted their experimental data. Moreover, the authors stated that the heat transfer process in microchannels is dominated by nucleate boiling rather than convective boiling. Consequently, they proposed a new correlation modifying the liquid Froude number (Fr_L) to become a criteria for flow pattern transition to annular flow. They correlated the heat transfer coefficient as a function of modified liquid Froude number (Fr_L), Reynolds number (*Re*) and Boiling number (*Bo*). Figure 5.44 depicts the comparison of the experimental data with the Lim et al. (2015) correlation. The correlation highly under-predicted the experimental data for all test sections with a MAE value of *65.8 %, 64.1 %, 58.9 %, 36.1 %* for the test sections TS1, TS2, TS3 and TS4, respectively, see Table 5.2. A possible reason for the poor prediction of this correlation could be attributed to the exclusion of the convective boiling component during the boiling process. Convective boiling was also found to be the prevailing heat transfer mechanism in microchannels by some researchers as presented in Chapter 2.

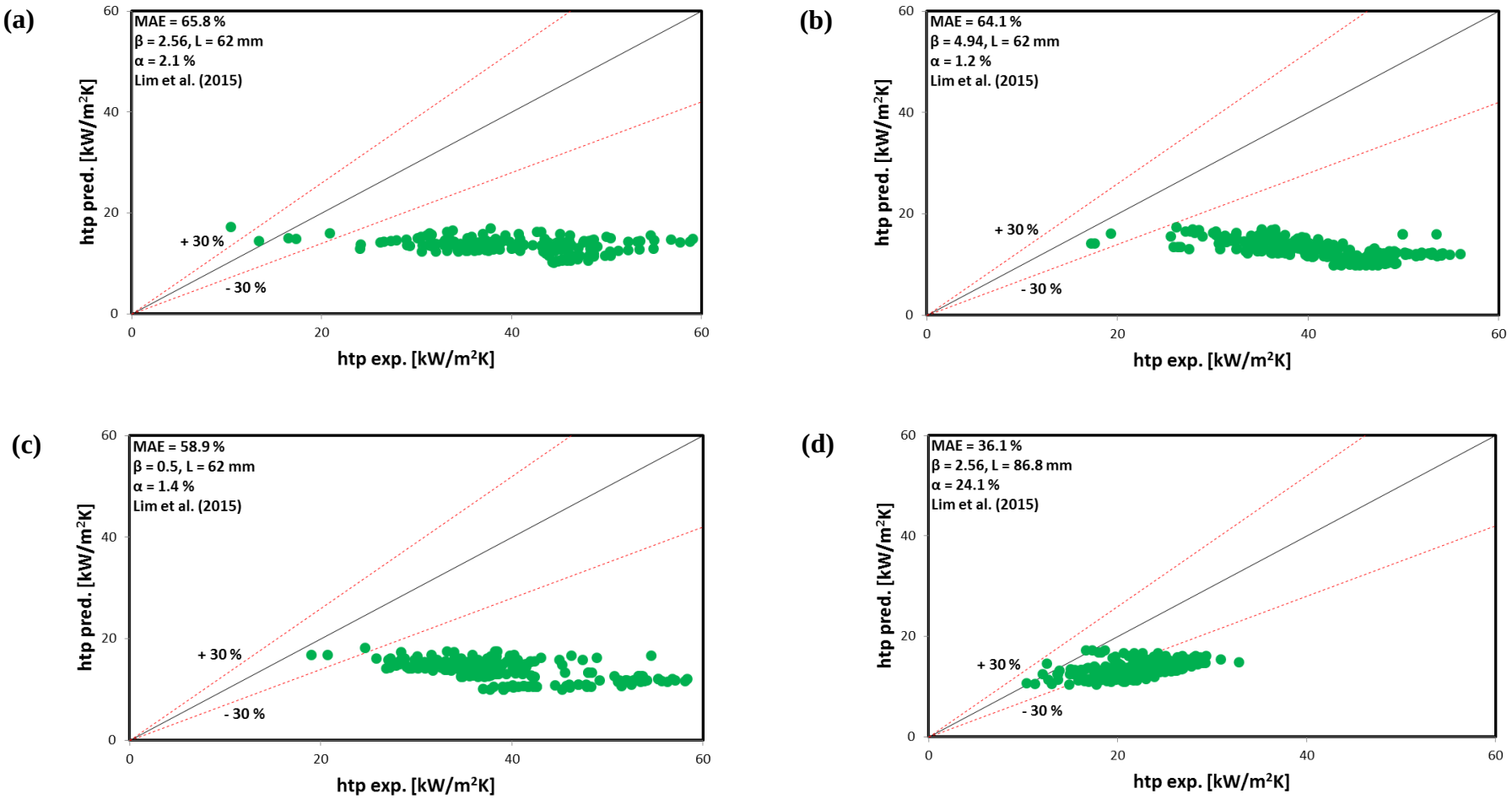

Figure 5.44 Comparison of experimental heat transfer data with Lim et al. (2015) correlation: (a) TS1, (b) TS2, (c) TS3 and (d) TS4 microchannels.

Table 5.2 MAE and the percentage of data within ± 30 % error bands for micro-scale correlations.

Correlation	β = 2.56 (TS1)		β = 4.94 (TS2)		β = 0.5 (TS3)		β = 2.56 (TS4)	
	MAE %	α %	MAE %	α %	MAE %	α %	MAE %	α %
Lazarek&Black (1982)	32.5	48.7	26.6	61.1	30.6	51.2	30.2	51.8
Yu et al. (2002)	37.5	33.7	30.5	45.1	26.5	59.2	20.2	75.5
Kandlikar&Balasubramanian (2004)	38.6	39.3	55.3	40.5	35.2	43.3	55.7	40.1
Lee&Mudawar (2005a)	50.6	19.2	38.7	35.4	41.8	23.9	28.5	48.6
Sun& Mishima (2009)	29.3	50.3	24.2	64.5	25.2	62.7	20.1	75
Li&Wu (2010a)	27.1	60.8	19.3	97.4	15.8	89.5	13.7	99.1
Mahmoud&Karayiannis 1 (2011)	31	56.9	22.6	72.7	21.6	73.6	23.8	65.3
Mahmoud&Karayiannis 2 (2011)	35.3	51.8	30.8	49.3	23.3	69.1	27.3	57.7
Lim et al. (2015)	65.8	2.1	64.1	1.2	58.9	1.4	36.1	24.1

In this section, the comparisons of the flow boiling heat transfer data obtained from experiments with the micro-scale correlations were presented. As can be seen from figures 5.36-5.44 and table 5.2, the micro-scale correlations performed better than the conventional-scale correlations. The correlations of Sun and Mishima (2009), Li and Wu (2010a), Mahmoud and Karayiannis 1 (2011) and Mahmoud and Karayiannis 2 (2011) predicted fairly well the experimental data for the tested microchannels and experimental range.

5.5 Summary

The flow boiling heat transfer and flow pattern results are presented and discussed for investigated four microchannels. The conclusions from the obtained results can be summarized as follows:

5.5.1 Flow Patterns and Flow Pattern Maps

The bubbly flow, slug flow, churn flow and annular flow were visualised in the tested microchannels. Moreover, an additional flow regime (periodic flow) was visualised in the microchannels except the TS2. The flow patterns changed from single-phase flow to bubbly flow, bubbly flow to slug flow, slug flow to churn flow and churn flow to annular flow with increasing heat flux for all test sections. The flow patterns changed as the fluid moves from the inlet region to the outlet region. Therefore, the observation location was found to be one of the sources of the discrepancies for flow patterns in the microchannels.

The variation in the mass flux also affected the observed flow patterns. The flow patterns transformed from annular flow pattern to single-phase flow with the increase in mass flux. The periodic flow regime was only observed at lower mass flux conditions ($G = 200\ kg/m^2s$ and $G = 400\ kg/m^2s$) and it was attributed to periodic fast vapour expansion to the upstream and downstream of the channel in this study. At higher mass flux operations ($G = 600\ kg/m^2s$ *and* $800\ kg/m^2s$) the periodic flow regime was not encountered since the flow rate is higher. It might be attributed to the fact that the backward evaporation momentum force is lower than the forward liquid inertia force at

higher mass fluxes. The channel aspect ratio has little effect on the observed flow patterns. Bubbly flow was not encountered at the smallest aspect ratio microchannel ($\beta = 0.5$). On the other hand, bubbles were dispersed and small in the largest aspect ratio microchannel ($\beta = 4.94$) compared to $\beta = 2.56$ (TS1) microchannel in the bubbly flow regime. The reason for this might be that the channel aspect ratio of the TS1 ($\beta = 2.56$) is smaller than the TS2 ($\beta = 4.94$). So that bubbles become elongated due to the confined space. As the aspect ratio was decreased more, bubbly flow was not seen, the flow regime becomes slug flow as shown for the $\beta = 0.5$ channel. Moreover, droplet entrainment was observed in the annular flow regime for the $\beta = 4.94$ microchannel (TS2) whereas this phenomena was not observed for other microchannels.

The flow pattern maps of Hassan et al. (2005) and Triplett et al. (1999) could not estimate well the experimental data. The map proposed by Galvis and Culham (2012) gave good prediction for the experimental data except the transition from bubbly flow to slug flow regime. The flow pattern maps of Sobierska et al. (2006) and Harirchian and Garimella (2009) reasonably predicted the experimental flow pattern data. The possible reasons of these differences between the experimental flow pattern data and published flow pattern maps might be the different microchannel dimensions and working fluid, observation location, surface characteristics of the microchannels and lack of standardization of flow patterns definition.

5.5.2 Flow Boiling Heat Transfer Characteristics

The heat flux effect was found to be clear on boiling curves. The wall superheats dropped slightly and increased again with heat flux in the tested microchannels. However, the mass flux effect on the boiling curves was insignificant. The heat transfer coefficients increased with heat flux and were independent of the vapour quality at low and medium heat flux inputs. On the other hand, the heat flux effect was insignificant at high heat flux inputs. The heat transfer coefficient decreased as the mass flux increased. The reason of this trend was attributed to the high pressure drop gradient and elongated slugs grow and move faster at higher mass fluxes that suppress nucleate boiling mechanism. In conclusion, the nucleate boiling mechanism was dominant heat transfer mechanism at low and medium heat flux input for all test sections in this work. On the

other hand, the dominant heat transfer mechanism was unclear at high heat flux input for all microchannels.

The channel aspect ratio effect on the heat transfer coefficient was also investigated. It was found that the channels having smaller aspect ratio exhibited better heat transfer performance up to certain heat flux values (~ *480 – 500 kW/m*^{2}). The channel aspect ratio did not have influence on the heat transfer coefficient for higher heat flux conditions. These results might be attributed to the fact that the nucleate boiling is the dominant heat transfer mechanism at low and medium heat flux input. Therefore, the better heat transfer performance of the smaller aspect ratio channel might be that the density of the nucleating bubbles is higher in the deeper channels since the nucleation starts near the channel corners before approaching to the surfaces of the channels. So that deeper channels presented better heat transfer performance in the nucleate boiling region. At higher heat flux input, the nucleate boiling was supressed. Hence, the channel aspect ratio effect became insignificant on the heat transfer coefficient.

The heat transfer coefficient for the shorter microchannel was found to be higher than the longer microchannel. It might be attributed to the fact that the high values of heat fluxes in the shorter channel may activate more nucleation sites over the heated length of the channel. Another possible explanation might be that as the heated length increased the boiling incipience was shifted to the lower heat flux values. This is because the fluid outlet temperature increases with the increase in heated length at the same mass and heat flux input. So that, the fluid becomes superheated at lower heat flux input in the longer channel compared to a shorter channel. Thus, higher heat fluxes are needed in the shorter channel to obtain same exit quality as in the longer channel. Another possible reason could be the increase in the pressure drop with the increase of channel length which affects the local saturation temperature. So that, the local saturation temperature becomes lower for the longer channel which results in a smaller heat transfer coefficient at the same mass flux and heat flux condition.

5.5.3 Comparisons of the Experimental Results with Existing Heat Transfer Correlations

The heat transfer coefficient data obtained from the experiments were compared to macro-scale and micro-scale correlations available in the literature. The macro-scale correlations were poor to predict experimental results. The micro-scale correlations proposed by Sun and Mishima (2009), Li and Wu (2010a) and Mahmoud and Karayiannis (2011) reasonably predicted the experimental results. From the comparisons Li and Wu (2010) and Mahmoud and Karayiannis (2011) correlations can be recommended for predicting experimental results of the tested microchannels in the current study.

Chapter 6

Flow Boiling Pressure Drop Results and Discussions

6.1 Introduction

The pressure drop characteristics are another vital design parameter that should be considered in addition to heat transfer characteristics to design efficient microchannel heat exchangers. Although microchannels have superior heat transfer performance compared to large-scaled channels, the associated channel pressure-drop penalty, expected to be higher because of their small size leading to high power consumption. Single-phase pressure drop and friction factor characteristics of the microchannels in this study were found to obey the conventional-scale theory as presented in Chapter 4. The flow boiling pressure drop characteristics in the tested microchannels are presented and discussed in this chapter. The effect of heat flux, mass flux and channel aspect ratio on flow boiling pressure drop will be assessed. Furthermore, the comparisons of the experimental data with existing macro-scale and micro-scale two-phase pressure drop correlations will be evaluated.

This chapter begins with a brief introduction that is given in Section 6.1. It is followed by presenting the flow boiling pressure drop characteristics, which are included in Section 6.2. Section 6.3 gives the comparisons of the experimental data with two-phase pressure drop correlations and the summary is presented in Section 6.4.

6.2 Flow Boiling Pressure Drop Characteristics

The total pressure drop in the microchannels was measured with a differential pressure transducer located at the inlet and exit of the channels. The accuracy and reliability of the differential pressure transducer was validated by performing single-phase experiments as presented in Chapter 4. Henceforth, the net pressure drop can be determined by subtracting the pressure loss components due to sudden contraction and enlargement and *90°* turns from the measured pressure drop using Eq. (3.5) and Eq. (3.8) presented in Chapter 3. Since the de-ionised water was delivered to the microchannels in a subcooled state (T_i = *89 ºC* and P_i = *115 kPa*), the channel pressure drop consist of two components namely flow boiling pressure drop component and single-phase pressure drop component during flow boiling. The subcooled and saturated lengths of the TS2 microchannel at several heat fluxes and *400 kg/m^{2}s* mass flux are presented in Fig. 6.1 as an example. It can be seen from the data in Fig. 6.1 that the saturated area increases as the heat flux increases. For example, for the *81.5 kW/m^2* heat flux the saturated region was *0.85 mm* (*1.37 %* of the channel length). As the heat flux increases to *152.6 kW/m^2* the saturated region became *27.63 mm* (*44.56 %* of the channel length). Moreover, the saturated length was *56.5 mm* (*91.13 %* of the channel length) at the maximum heat flux input (*1149 kW/m^2*). It is worth mentioning that the saturated region does not occupy the entire channel even at the highest heat flux input since the de-ionised water was delivered to microchannels in a subcooled state (T_i = *89 ºC*).

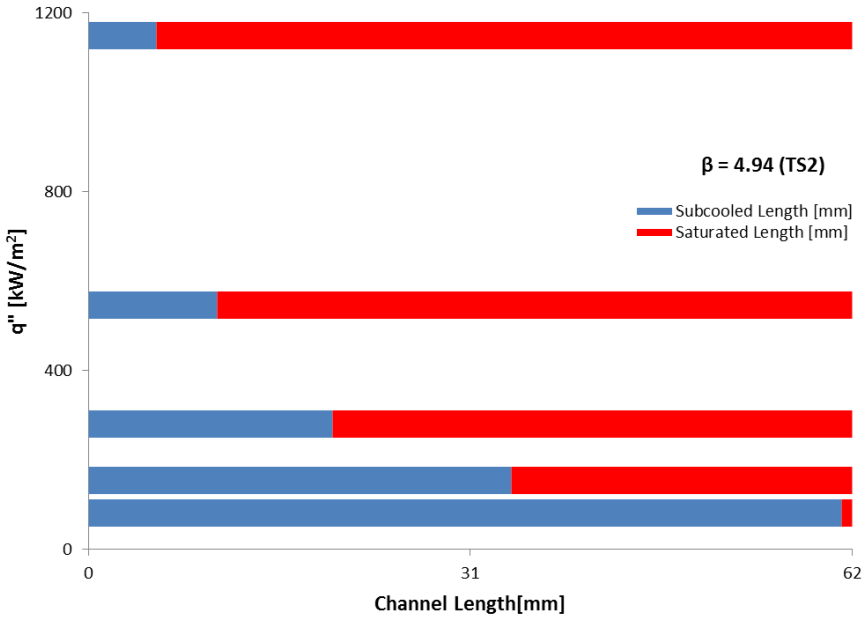

Figure 6.1 Saturated and subcooled lengths at several heat fluxes and 400 kg/m^{2}s mass flux for the TS2.

Thus, the flow boiling pressure drop is calculated by subtracting the single-phase pressure drop from the net channel pressure drop using equations (3.17)-(3.24) in Chapter 3. The obtained flow boiling pressure drop includes frictional and accelerational pressure drop components in horizontal channels as discussed in Chapter 2. The components of accelerational and frictional pressure drop can be calculated using either the SFM or the HFM. The equations of frictional and accelerational flow boiling pressure drop components are given below in equations 6.1-6.4 for both models.

Frictional Pressure Drop

$$\Delta P_f = \frac{2 f_L L G^2 \nu_L}{D_h}\left[1+\frac{x_e}{2}\left(\frac{\nu_{Lg}}{\nu_L}\right)\right] \qquad \text{(HFM)} \qquad (6.1)$$

$$\Delta P_f = \frac{L_{tp}}{x_e}\int_0^{x_e}\frac{2 f_l G^2 (1-x_e)^2 \nu_l}{D_h}\phi_l^2 dx \qquad \text{(SFM)} \qquad (6.2)$$

Accelerational Pressure Drop

$$\Delta P_a = G^2 \nu_{\mathrm{lg}} x_e \qquad \text{(HFM)} \qquad (6.3)$$

$$\Delta P_a = G^2 \nu_l \left[\frac{x_e^2}{\alpha_e} \left(\frac{\nu_g}{\nu_l} \right) + \frac{(1-x_e)^2}{1-\alpha_e} - 1 \right] \qquad \text{(SFM)} \qquad (6.4)$$

Both models and their comparisons with experimental data are presented and discussed in the following subsections in detail. This section examines the effect of heat flux, mass flux and channel aspect ratio on the total flow boiling pressure drop as well as the frictional and accelerational flow boiling pressure drop components.

6.2.1 Effect of Heat Flux and Mass Flux on Flow Boiling Pressure Drop

In single-phase flow, the channel pressure drop increases with mass flux at fixed heat flux input and inlet fluid temperature. On the other hand, for a given mass flux the channel pressure drop decreases as the heat flux or inlet fluid temperature increases. This is because the thermophysical properties of water such as density and viscosity change with the variation in the temperature. However, the effect of heat flux on the pressure drop in flow boiling is different than single-phase flow. The flow boiling pressure drop increases with heat flux after boiling commences at constant mass flux operations, see Warrier et al. (2002) Singh et al. (2008) and Markal et al. (2016). The effects of heat flux and mass flux on flow boiling pressure drop are depicted in Fig. 6.2 for all test sections.

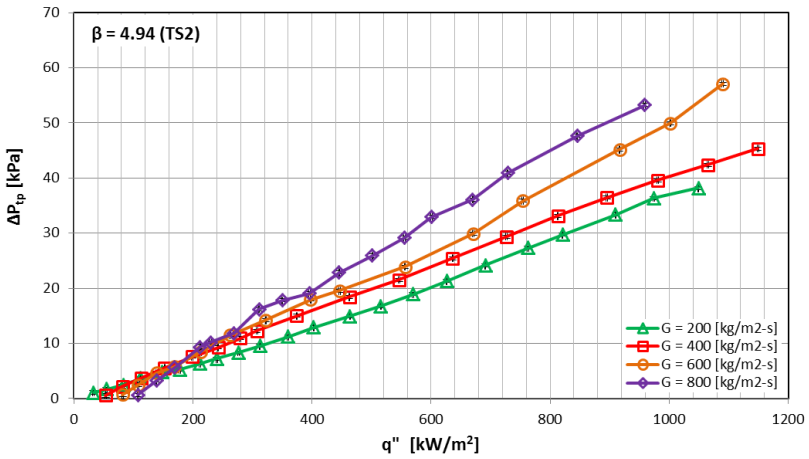
β = 4.94 (TS2)
ΔP_tp [kPa]
q" [kW/m²]
G = 200 [kg/m2-s]
G = 400 [kg/m2-s]
G = 600 [kg/m2-s]
G = 800 [kg/m2-s]

(a)

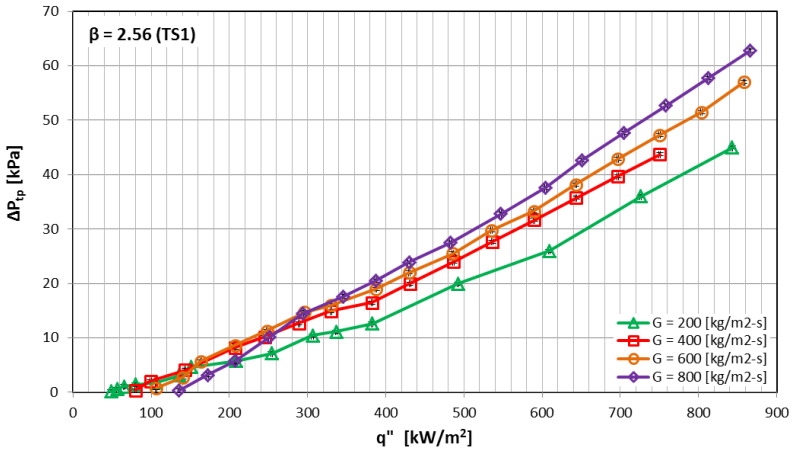
β = 2.56 (TS1)
ΔP_tp [kPa]
q" [kW/m²]
G = 200 [kg/m2-s]
G = 400 [kg/m2-s]
G = 600 [kg/m2-s]
G = 800 [kg/m2-s]

(b)

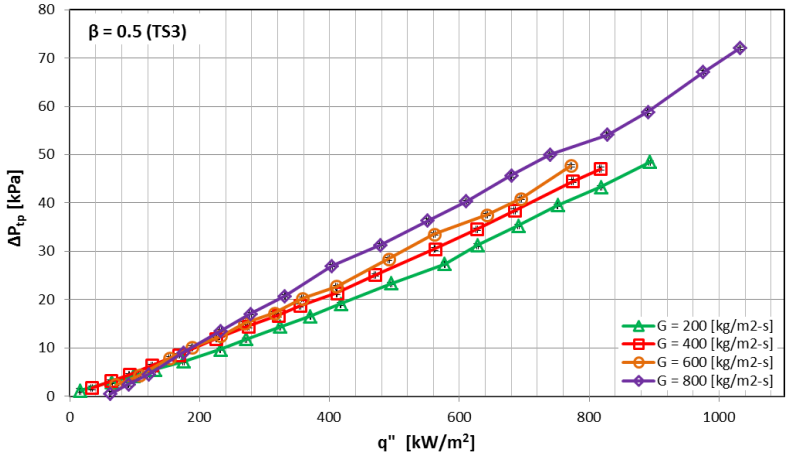
β = 0.5 (TS3)
ΔP_tp [kPa]
q" [kW/m²]
G = 200 [kg/m2-s]
G = 400 [kg/m2-s]
G = 600 [kg/m2-s]
G = 800 [kg/m2-s]

(c)

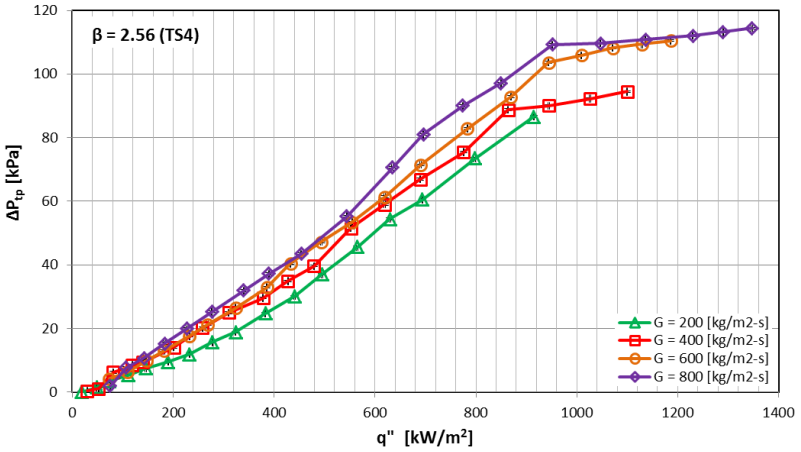

(d)

Figure 6.2 Effect of mass flux and heat flux on the flow boiling pressure drop for the: (a) TS2, (b) TS1, (c) TS3 and (d) TS4.

As can be seen from Fig. 6.2 the flow boiling pressure drop enhances almost linearly as the heat flux and mass flux increases for microchannels. A possible explanation for this could be that the increase in heat flux enhances the bubble population and reduces the subcooled length during flow boiling that increases the flow resistance in the microchannels. Also, applied heat flux to the microchannels is a function of exit vapour quality. Therefore, as exit vapour quality increases both frictional and accelerational pressure drop components increase as can be seen through equations 6.1-6.4. The flow boiling pressure drop is depicted versus exit vapour quality in Fig. 6.3 for all test sections. As seen in the figure, the flow boiling pressure drop increases with the increase in exit vapour quality as expected since the increase in vapour quality enhances the bubble generation in the microchannels as stated above.

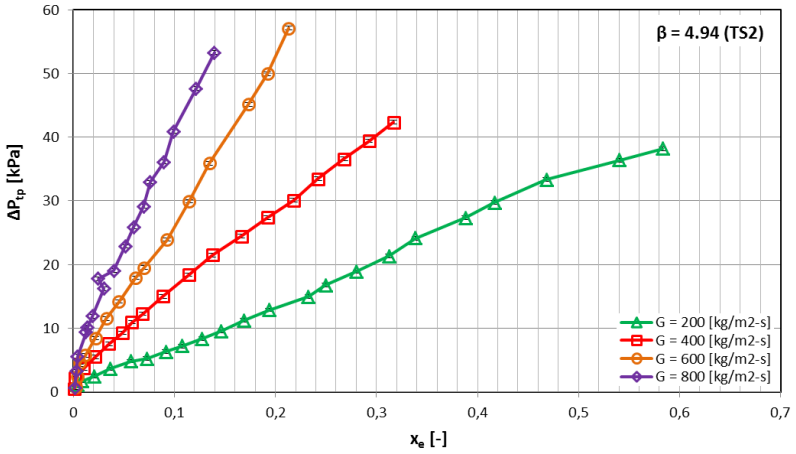
β = 4.94 (TS2)
ΔP_tp [kPa]
x_e [-]
G = 200 [kg/m2-s]
G = 400 [kg/m2-s]
G = 600 [kg/m2-s]
G = 800 [kg/m2-s]

(a)

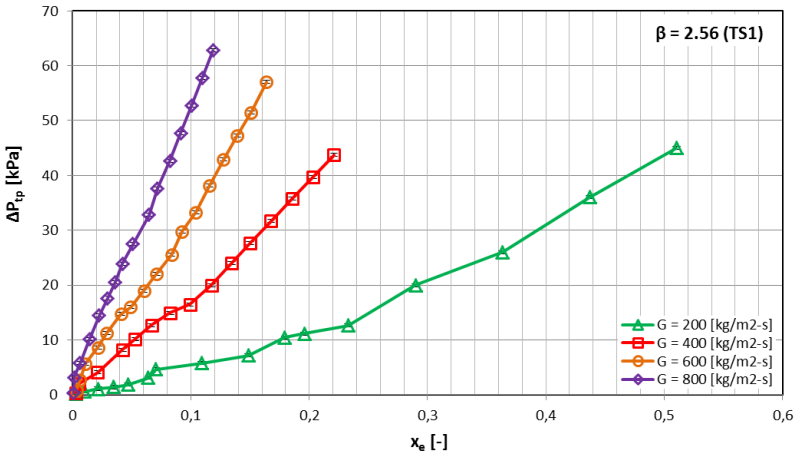
β = 2.56 (TS1)
ΔP_tp [kPa]
x_e [-]
G = 200 [kg/m2-s]
G = 400 [kg/m2-s]
G = 600 [kg/m2-s]
G = 800 [kg/m2-s]

(b)

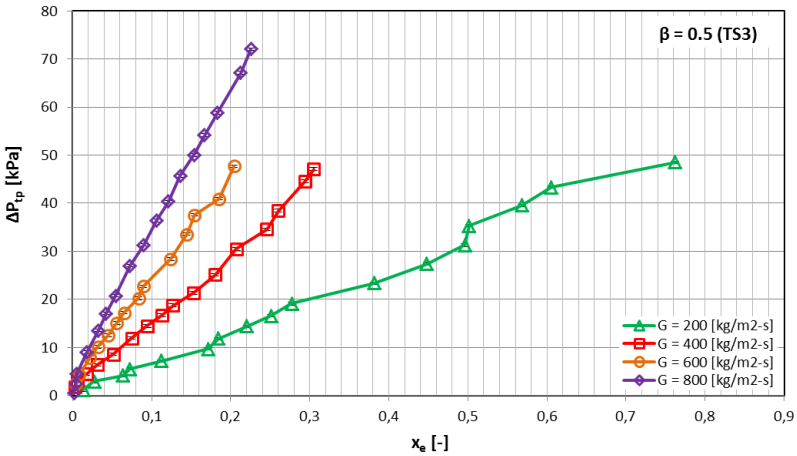
β = 0.5 (TS3)
ΔP_tp [kPa]
x_e [-]
G = 200 [kg/m2-s]
G = 400 [kg/m2-s]
G = 600 [kg/m2-s]
G = 800 [kg/m2-s]

(c)

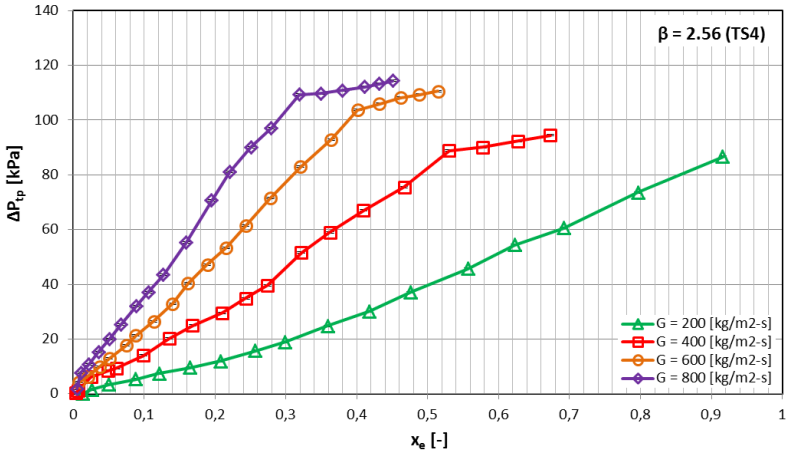

(d)

Figure 6.3 Effect of exit quality and mass flux on the flow boiling pressure drop for the: (a) TS2, (b) TS1, (c) TS3 and (d) TS4.

On the other hand, Figs. 6.2 and 6.3 reveal that the flow boiling pressure drop is a strong function of the mass flux. This is due to the fact that as the mass flux increases the difference between the inertia force and the evaporation momentum force becomes larger which increases the accelerational pressure drop component. The frictional pressure drop component also becomes higher at high mass fluxes. The mass flux effect can also be seen in equations 6.1-6.4, where the accelerational and frictional pressure drop components increase with G^2. These results are consistent with data obtained in the literature; Sobierska et al. (2006), Yun et al. (2006), Mahmoud (2011), Mirmanto (2012) and Markal et al. (2016).

6.2.2 Effect of Aspect Ratio on Flow Boiling Pressure Drop

The effect of channel diameter on single-phase and flow boiling pressure drop was investigated by many researchers in the literature. They found that the pressure drop increases as the channel diameter decreases in both single-phase and flow boiling regions, see Tong et al. (1997), Karayiannis et al. (2008), Lee and Garimella (2008), Mahmoud (2011) and Mirmanto (2012). This trend is apparent because the pressure drop and the channel diameter changes inversely proportional both, in single-phase and flow boiling region. However, only few studies examined the effect of aspect ratio on flow boiling pressure drop in microchannels. The flow boiling pressure drop versus heat

flux at two different mass fluxes are plotted in Fig. 6.4 for the three microchannel test sections having different aspect ratios. It can be deduced that the flow boiling pressure drop increases as the channel aspect ratio decreases. For example, at the mass flux $G = 200\ kg/m^2s$ and heat flux $600\ kW/m^2$, when the channel aspect ratio was decreased from *4.94* to *2.56*, the flow boiling pressure drop increased approximately by *35.2* %. Further reduction in the aspect ratio from *2.56* to *0.5* resulted in a smaller increase, i.e. approximately *11.1 %* at $G = 200\ kg/m^2s$ and $q'' = 600\ kW/m^2$. The total change of the flow boiling pressure drop from $\beta = 4.94$ to $\beta = 0.5$ was *50.8 %* at the similar values of heat flux and mass flux.

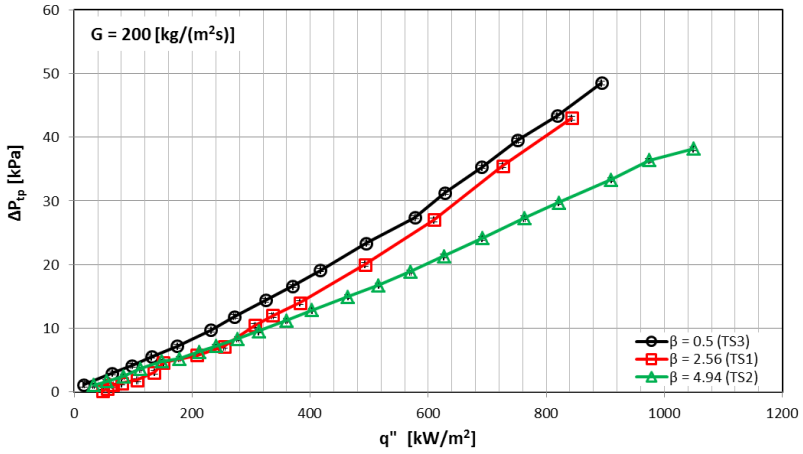

(a)

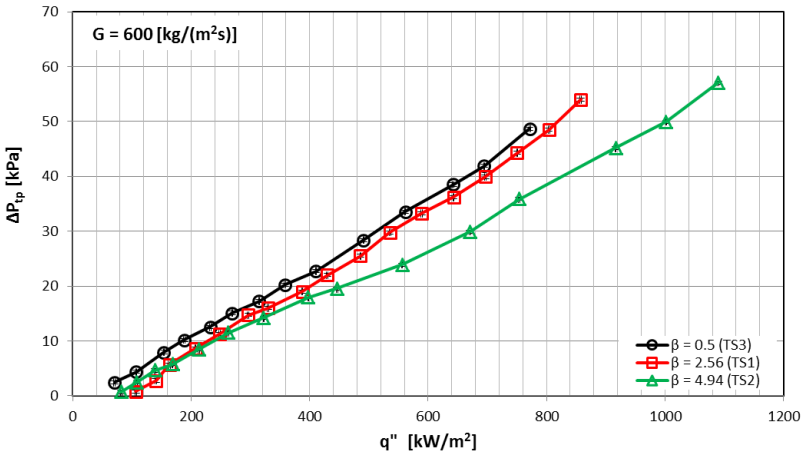

(b)

Figure 6.4 The effect of aspect ratio on the flow boiling pressure drop at: (a) G = 200 kg/m^{2}s and (b) G = 600 kg/m^{2}s.

Singh et al. (2008) investigated pressure drop in a single silicon microchannels with *142 μm* hydraulic diameter, *20 mm* channel length and varying aspect ratios (*β = 1.23-3.75*). They found that the flow boiling pressure drop attained to its maximum value for the *β = 1.23* microchannel and decreased to its minimum value for the *β = 1.56* microchannel. Then the flow boiling pressure drop was found to increase as the aspect ratio increased to *1.73*, *2.56*, *3.60* and *3.75*, respectively. However, the authors only presented pressure drop versus aspect ratio figures at fixed heat flux and mass flux input. Since the variation in the flow boiling pressure drop with heat flux and mass flux were not shown by the authors, it is difficult to relate their results with the current study. In a recent study, Markal et al. (2016) reported that the relationship between the total pressure drop (single-phase region + flow boiling region) and the channel aspect ratio was not regular. The authors carried out sets of flow boiling experiments in silicon parallel multi-microchannels having the same hydraulic diameter and length (D_h *= 100 μm* and *L = 48 mm*) but different aspect ratio (*β = 0.37-5*). They stated that the irregular relationship between the total pressure drop and channel aspect ratio is due to the complex physical nature of the flow boiling phenomenon. In another study, Soupremanien et al. (2011) found that the flow boiling pressure drop varies inversely proportional with the channel aspect ratio. They tested two stainless steel microchannels having *1.4 mm* hydraulic diameter and *83 mm* channel length but different aspect ratio (*β = 2.3* and *β = 7*). Similar to the current study, the flow boiling pressure drop increased as the channel aspect ratio was decreased in their findings.

In order to gain a better understanding for the channel aspect ratio effect on the flow boiling pressure drop, the two components of the flow boiling pressure drop as a function of the heat flux (accelerational pressure drop component and frictional pressure drop component) are depicted in Fig. 6.5 at the *600 kg/m^{2}s* mass flux for the three microchannel test sections. The frictional flow boiling pressure drop is due to the wall shear stress between the working fluid and channel walls whilst the source of the accelerational flow boiling pressure drop is the expansion and motion of the bubbles during flow boiling. The Mishima and Hibiki (1996) accelerational pressure drop equation (see appendix B) was used to construct Fig. 6.5. The frictional pressure drop was plotted after subtracting the calculated accelerational pressure drop from total measured flow boiling pressure drop. This approach was used by some researchers in

the literature, see Mahmoud (2011) and Mirmanto (2012). From figure 6.5 we can infer that the accelerational pressure drop component increased as the heat flux increased for all microchannels. However, the frictional pressure drop component trend is different as can be seen from Fig 6.5. The frictional pressure drop component firstly increased with heat flux, then it decreased approximately after a heat flux value of *400 kW/m^2* for the channel TS3. On the other hand, the frictional pressure drop increased for the channel TS2 with heat flux up to *400 kW/m^2*. Beyond this heat flux value, the frictional pressure drop maintained constant until *760 kW/m^2* heat flux and then started to decrease with heat flux.

A possible explanation for the trends of the accelerational and frictional pressure drop components might be that the smaller channel aspect ratio channel had higher vapour quality at the similar heat and mass flux input. The flow pattern was found to be annular flow at higher vapour qualities as presented in Chapter 5. Since the accelerational pressure drop is due to formation of the bubbles and motion, it is not surprising that the accelerational pressure drop increased with heat flux as the flow pattern changes from bubbly flow to annular flow with the increase in heat flux. On the other hand, the frictional pressure drop decreased at higher vapour qualities. Because the liquid film becomes thinner during annular flow and the viscosity of de-ionised water decreases at higher vapour qualities resulting in a decreasing frictional pressure drop. Furthermore, the trend of frictional pressure drop component of TS1 needs a comment. The different frictional pressure drop trend of TS1 may be attributed to the surface roughness. Since the average surface roughness of TS1 is slightly higher than the other test sections, it is expected that the frictional pressure drop component of TS1 reaches the maximum value at higher heat fluxes than the other test sections, see Chapter 3 page 104. As can be seen from Fig. 6.5 (b), the value of the frictional pressure drop component of TS1 became lower than the accelerational pressure drop component value at high heat fluxes. However, the maximum point of frictional pressure drop component could not be seen on the observed heat flux range in Fig. 6.5 (b).

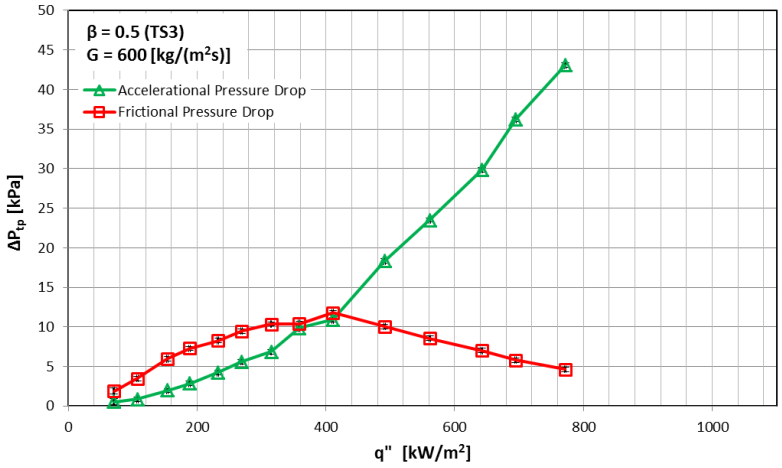

(a)

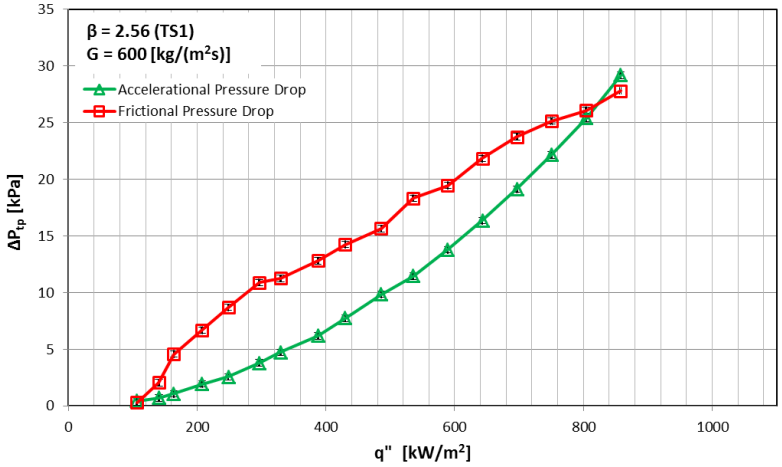

(b)

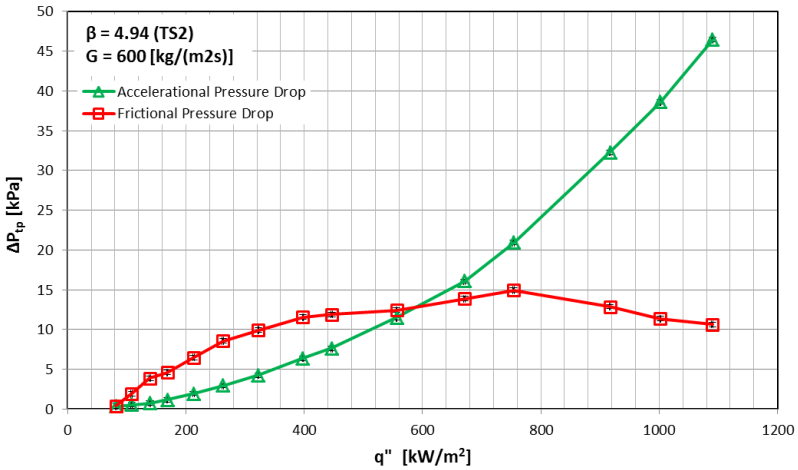

(c)

Figure 6.5 Frictional and accelerational pressure drop components at the mass flux of 600 kg/m^{2}s for the (a) TS3, (b) TS1 and (c) TS2.

6.3 Comparison of the data with Pressure Drop Correlations

In the current study, the experimental flow boiling pressure drop data for the tested microchannels were compared to two conventional scale and eight micro-scale two-phase pressure drop correlations available in the literature. The equations and details of the correlations are given in appendix B. These conventional scale and micro-scale two-phase pressure drop correlations are described and discussed in this section. Furthermore, the comparison of the experimental flow boiling pressure drop data with the correlations are presented for all thermocouple locations for all tested mass flux using MAE method (global comparison) and for a selected value of mass flux for each microchannel test section.

6.3.1 Conventional Scale Two-phase Pressure Drop Correlations and Comparison with the Data

Two-phase pressure drop were generally predicted using two common approaches in the literature. The first method is the HFM where the liquid and vapour phases are treated as one homogenous phase flow. Moreover, both phases are assumed to have same velocity in the HFM method. On the other hand, the flow is separated into only liquid and only vapour forms in the SFM. The SFM assumes that the vapour and liquid phases have constant but possibly different velocities. As stated in previous subsections, the total two-phase pressure drop contains accelerational and frictional pressure drop components in horizontal flows. Both pressure drop components can be calculated in a straightforward way using Eq. (6.1) and Eq. (6.3) in the HFM, see Collier and Thome (1994). However, the void fraction (α_e) is needed to be evaluated carefully and accurately in the accelerational component of the SFM. Moreover, an accurate approach is needed in order to predict the two-phase multiplier (ϕ_L^2) in the frictional pressure drop component of the SFM. Accordingly, many researchers developed equations and models to predict the void fraction and two-phase multiplier to calculate the two-phase pressure drop in the SFM approach.

In this section, the experimental flow boiling pressure drop data were compared with the correlation of Lockhart and Martinelli (1949) and the homogenous flow model (1994) for the tested microchannels. Figure 6.6 depicts the comparison of the flow

boiling pressure drop data with conventional scale correlations at the mass flux of *200 kg/m^{2}s* for each microchannel test section. From the figure, it can be seen that both models captured the trend of the experimental data very well for all test sections. The homogenous flow model could reasonably predict the experimental data at the heat flux values lower than 150 *kW/m^2*. However, at higher heat fluxes (*q" > 150 kW/m^2*) the model over predicted the data for all test sections. On the other hand, the Lockhart-Martinelli (1949) model gives good prediction until *450-500 kW/m^2* heat flux values. But it is over estimating the experimental data at higher heat flux values beyond this point, similar to the HFM. Moreover, the abrupt increase of the prediction value in Figs. 6.6 (a-d) for the Lockhart-Martinelli (1949) model can be attributed to the variation in the Chisholm constant (*C*). As presented in Chapter 2 on pages 72-73 and appendix B, the two-phase frictional multiplier and the void fraction are the function of the *C* in Lockhart-Martinelli (1949) model. The constant takes higher value when the liquid and gas flows change from laminar flow to turbulent flow at higher vapour qualities. Consequently, the total pressure drop prediction value increases as the *C* takes higher values. Furthermore, it is worth mentioning that Fig. 6.6 was generated to see the trend of the macro-scale models with the experimental flow boiling pressure drop data of the tested microchannels. The flow boiling pressure drop data are compared with the models globally in the following subsections in order to draw a conclusion.

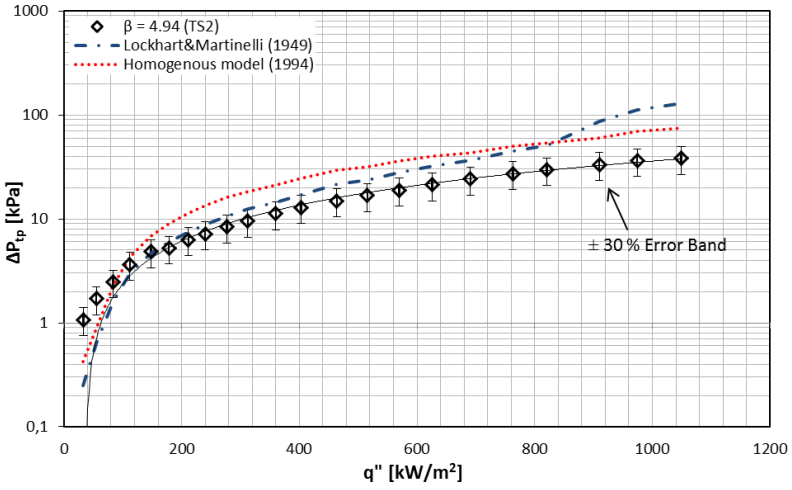

(a)

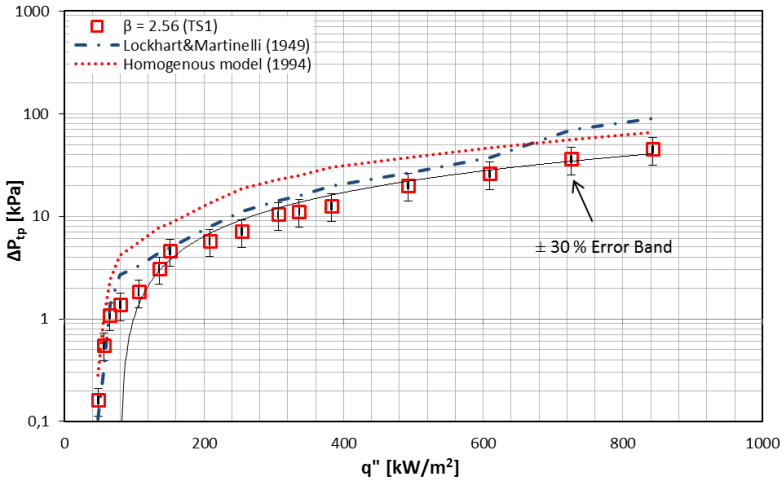
β = 2.56 (TS1)
Lockhart&Martinelli (1949)
Homogenous model (1994)
± 30 % Error Band
ΔP_tp [kPa]
q" [kW/m²]
1000
100
10
1
0,1
0
200
400
600
800
1000

(b)

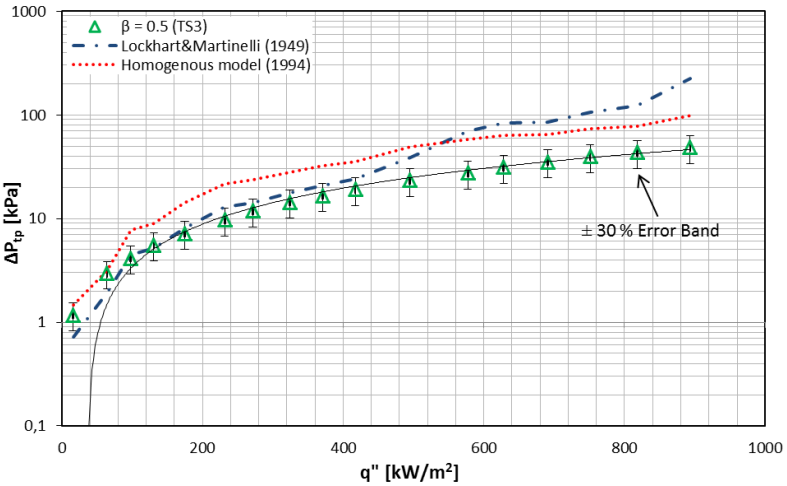
β = 0.5 (TS3)
Lockhart&Martinelli (1949)
Homogenous model (1994)
± 30 % Error Band
ΔP_tp [kPa]
q" [kW/m²]
1000
100
10
1
0,1
0
200
400
600
800
1000

(c)

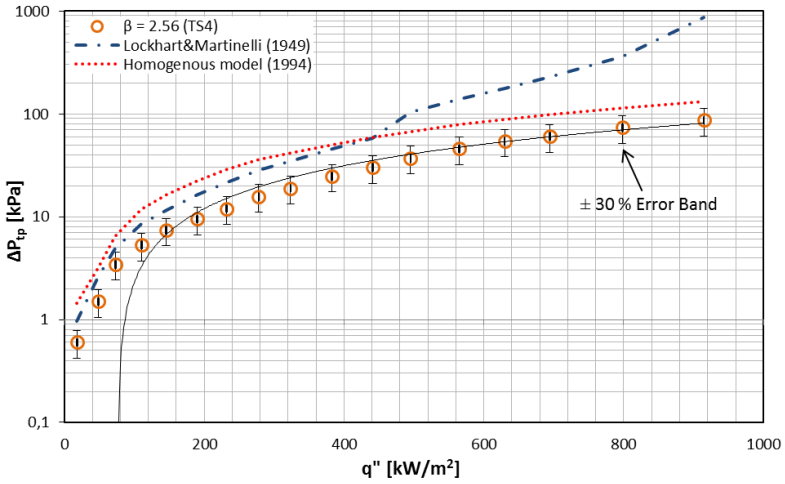

(d)

Figure 6.6 Comparison of the experimental flow boiling pressure drop data with conventional scale correlations at the mass flux of 200 kg/m^{2}s: (a) TS2, (b) TS1, (c) TS3 and (d) TS4.

6.3.1.1 The Lockhart-Martinelli (1949) model

Lockhart and Martinelli (1949) developed a method to predict the frictional pressure drop component using a two-phase multiplier based on data of air, water, benzene, kerosene and various oil flow in tubes having *1.5-25.8 mm* inner diameter. The two-phase multiplier was calculated depending on whether the flow regime of the liquid and vapour phases are laminar or turbulent, see appendix B. The correlation reasonably predicted the experimental data for the TS1 with a *MAE* of *30.6 %* as shown in Fig. 6.7. Half of the data for this channel was in the ± *30 %* error bands (α). However, the correlation becomes worse for the channels TS2 and TS3. The mean absolute error found to be *39.4 %* and *44 %*, respectively, for these channels. On the other hand, the data of the TS4 channel was predicted poorer by the Lockhart-Martinelli model with a MAE of *109.2 %*, see Table 6.1. The possible explanation could be the transition to turbulent flow occurs earlier in longer microchannel where the Chisholm constant takes higher value and consequently the Lockhart-Martinelli model over estimates the experimental data, see equations 6.5-6.10. As can be seen figures 6.6 (a-d) the Lockhart-Martinelli prediction deviates from the experimental trend line earlier in the longer microchannel compared to the other channels. In turbulent flow, the liquid film may be

disrupted at high heat flux values causing the decrease in the the wall shear stress which decreases the frictional pressure drop component.

$$\Delta P_a = \frac{G^2}{\rho_L}\left[\frac{x_e{}^2}{\alpha_e}\frac{\rho_L}{\rho_g} + \frac{(1-x_e)^2}{(1-\alpha_e)} - 1\right] \tag{6.5}$$

$$\alpha_e = \frac{1}{1+0.28X_M} \tag{6.6}$$

$$X_M = \left(\frac{1-x_e}{x_e}\right)^{0.64}\left(\frac{\rho_g}{\rho_L}\right)^{0.36}\left(\frac{\mu_L}{\mu_g}\right)^{0.07} \tag{6.7}$$

$$\Delta P_f = \frac{L_{tp}}{x_e}\int_0^{x_e}\frac{2f_L G^2}{D_h\rho_L}\phi_L^2 dx \tag{6.8}$$

$$\phi_L^2 = 1 + \frac{C}{X} + \frac{1}{X^2} \tag{6.9}$$

$$X = \left(\frac{f_L}{f_g}\right)^{0.5}\left(\frac{\rho_g}{\rho_L}\right)^{0.5}\left(\frac{1-x_e}{x_e}\right) \tag{6.10}$$

C = 5 for laminar liquid-laminar gas flow

C = 12 for laminar liquid-turbulent gas flow

C = 10 for turbulent liquid-laminar gas flow

C = 20 for turbulent liquid-turbulent gas flow.

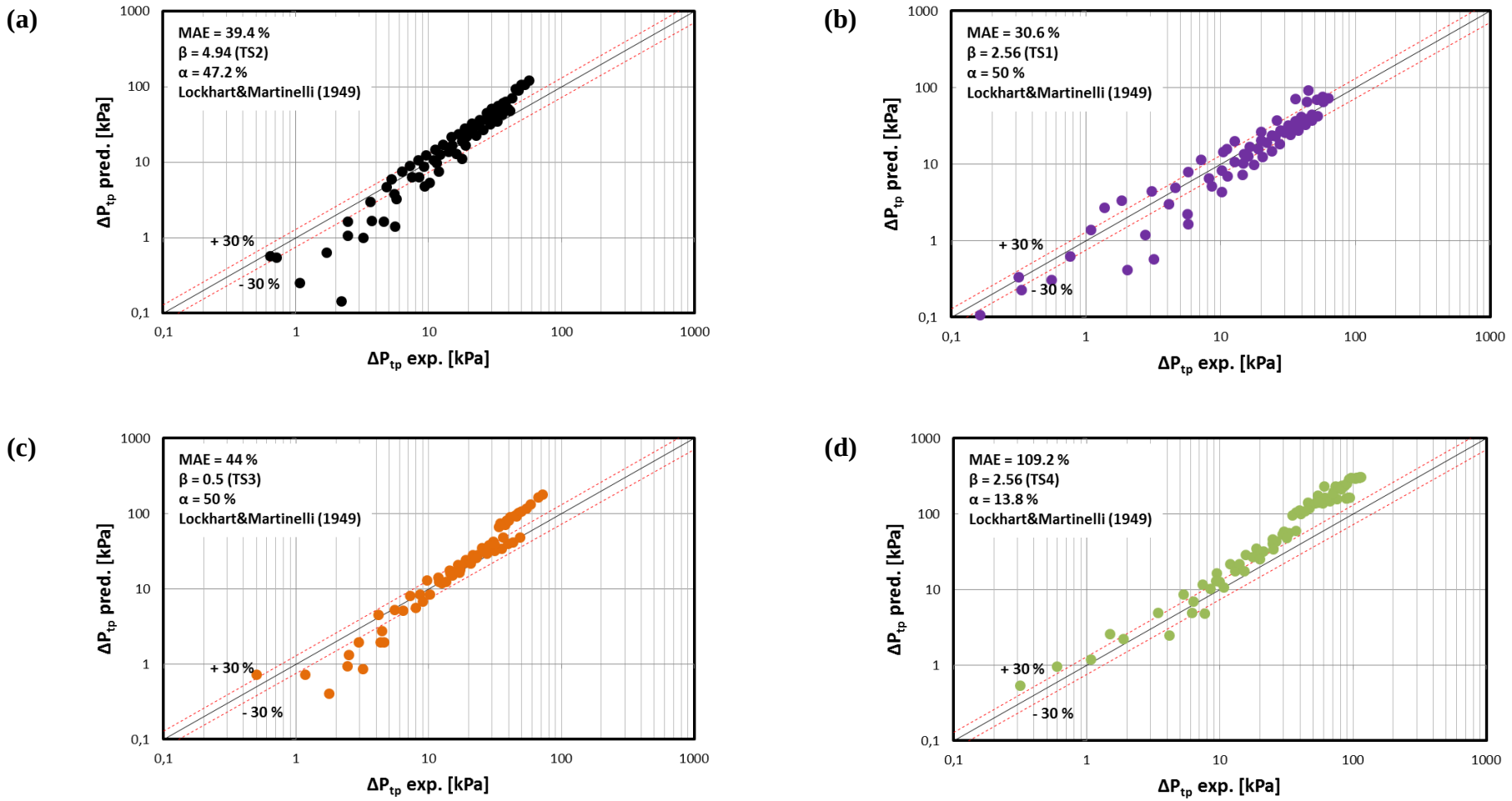

Figure 6.7 Comparison of experimental flow boiling pressure drop data with the Lockhart-Martinelli (1949) model: (a) TS2, (b) TS1, (c) TS3 and (d) TS4.

6.3.1.2 The Homogenous flow (1994) model

The homogenous flow model was developed based on laminar and turbulent steam-water mixture flow in horizontal circular tubes for a vapour quality from *0.01* to *1*. In the HFM both phases are mixed and modelled as one continuous phase as discussed before, see Collier and Thome (1994). Moreover the slip velocity between the phases is assumed to be negligible. The liquid frictional factor was taken *0.003* in this study for the HFM which was recommended by Qu and Mudawar (2003b), see appendix B. Figure 6.8 displays the comparison of the experimental data with the homogenous flow model. The model could not predict the experimental data accurately for all test sections. The mean absolute error (*MAE*) resulted in *176.6 %*, *170 %*, *242.7 %* and *187.2 %* for the TS2, TS1, TS3 and TS1, respectively. Also the percentage of the data within the ± *30 %* error bands (α) is poor as *6.4 %*, *1.9 %*, *7.45 %* and *0 %* for the channels TS2, TS1, TS3 and TS1, respectively, see Table 6.1. The Lockhart-Martinelli (1949) separated flow model predicted the experimental data better than the homogeneous flow model (1994) as shown in figures 6.7 (a-d) and 6.8 (a-d). The possible reason could be the void fraction correlations in both models are different. Lockhart and Martinelli developed the void fraction correlation mainly based on the annular flow regime which suggests that the dominant flow regimes in the current study (annular and elongated bubbly flow).

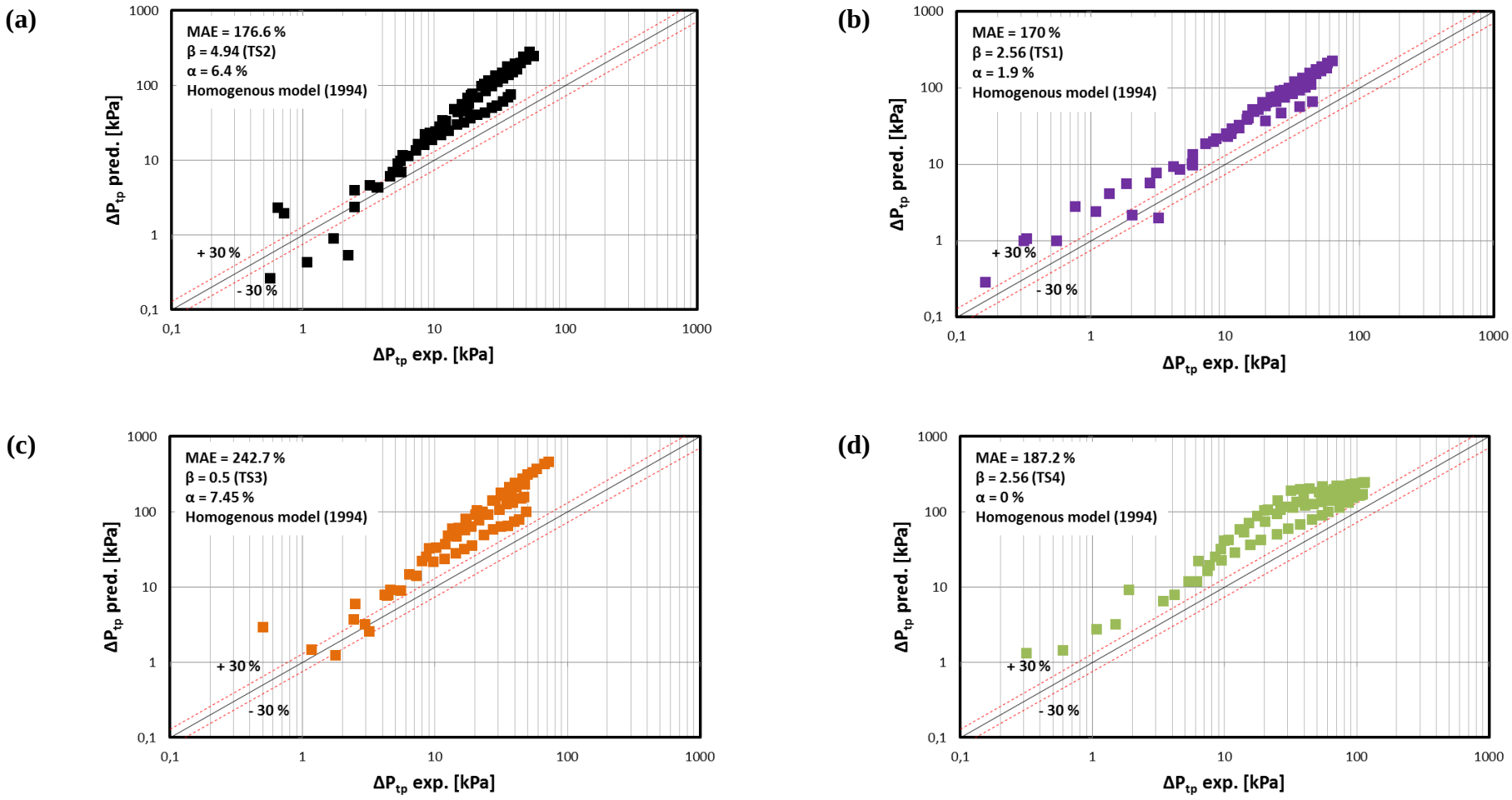

Figure 6.8 Comparison of experimental flow boiling pressure drop data with the homogeneous flow model (1994): (a) TS2, (b) TS1, (c) TS3 and (d) TS4.

6.3.2 Micro-Scale Two-Phase Pressure Drop Correlations and Comparison with the Data

In this section, the experimental flow boiling pressure drop data are compared with eight micro-scale correlations. The selected correlations for the comparison are Mishima and Hibiki (1996), Warrier et al. (2002), Yu et al. (2002), Qu and Mudawar (2003b), Lee and Garimella (2008), Zhang et al. (2010), Li and Wu (2010b) and Lee et al. (2010) correlations. The selected correlations were generally recommended for water as working fluid. However, the Warrier et al. (2002) correlation, which was developed for refrigerant FC-84, is also included due to the channel geometry similarity with the current study (rectangular channel). Most researchers modified the Chisholm constant (C) or developed a different method to calculate the void fraction in Lockhart-Martinelli model, see appendix B. The details of the each correlation are given in the following subsections.

Figure 6.9 presents the comparison of the experimental flow boiling pressure drop data with selected micro-scale correlations at a mass flux of $200\ kg/m^2s$ for each microchannel test section. Figure 6.9 shows that the trend of the experimental data can be captured by the correlations for all test sections. The Warrier et al. (2002), Lee and Garimella (2008) and Li and Wu (2010b) correlations over predicted the experimental data for all test sections at all heat flux inputs. At low heat flux inputs, the Mishima and Hibiki (1996) and Yu et al. (2002) correlations slightly under-predicted the experimental data whilst the correlations of Qu and Mudawar (2003b), Zhang et al. (2010) and Lee et al. (2010) gave a good prediction. However, the experimental data were predicted very well by the correlations of Mishima and Hibiki (1994), Yu et al. (2002), Qu and Mudawar (2003b) and Zhang et al. (2010) for the medium and high heat flux inputs. The global comparison of the experimental data with each correlation is presented in the following subsections.

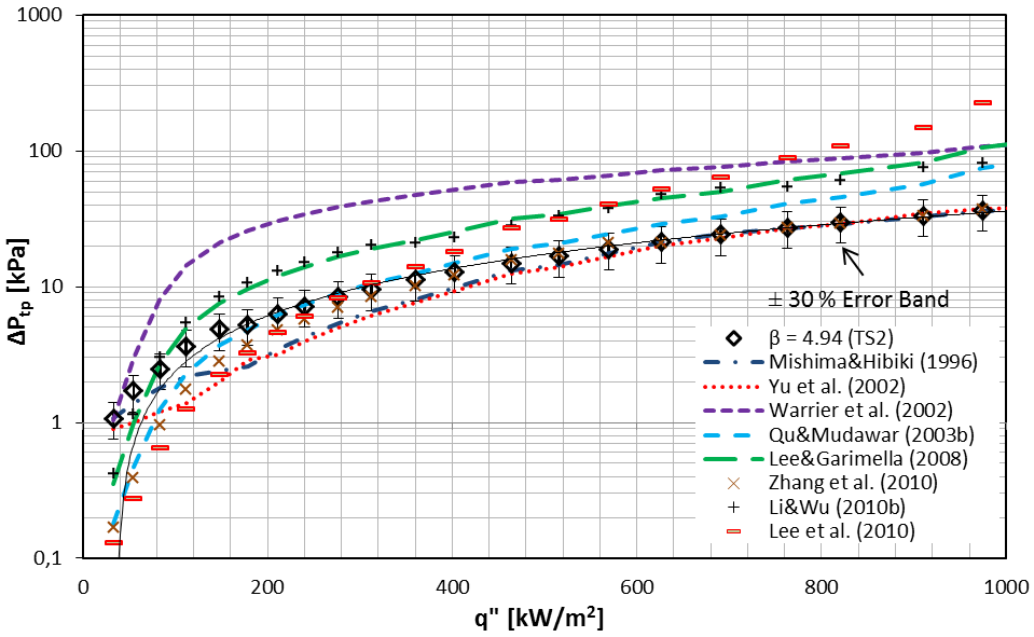
1000
100
10
1
0,1
ΔP_tp [kPa]
0
200
400
600
800
1000
q" [kW/m²]
± 30 % Error Band
β = 4.94 (TS2)
Mishima&Hibiki (1996)
Yu et al. (2002)
Warrier et al. (2002)
Qu&Mudawar (2003b)
Lee&Garimella (2008)
Zhang et al. (2010)
Li&Wu (2010b)
Lee et al. (2010)

(a)

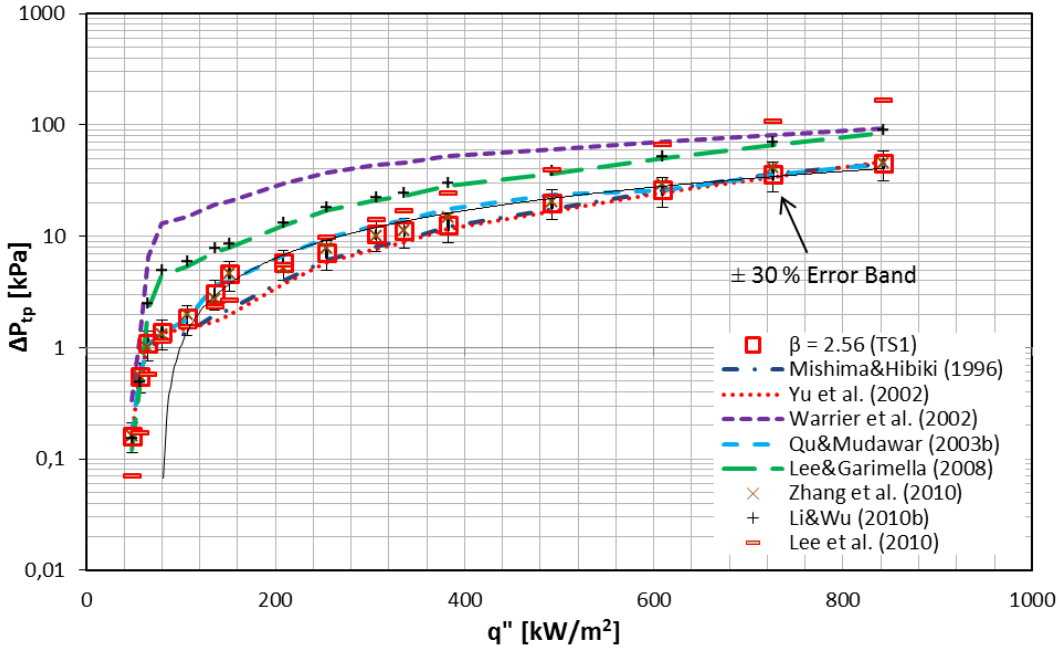
1000
100
10
1
0,1
0,01
ΔP_tp [kPa]
0
200
400
600
800
1000
q" [kW/m²]
± 30 % Error Band
β = 2.56 (TS1)
Mishima&Hibiki (1996)
Yu et al. (2002)
Warrier et al. (2002)
Qu&Mudawar (2003b)
Lee&Garimella (2008)
Zhang et al. (2010)
Li&Wu (2010b)
Lee et al. (2010)

(b)

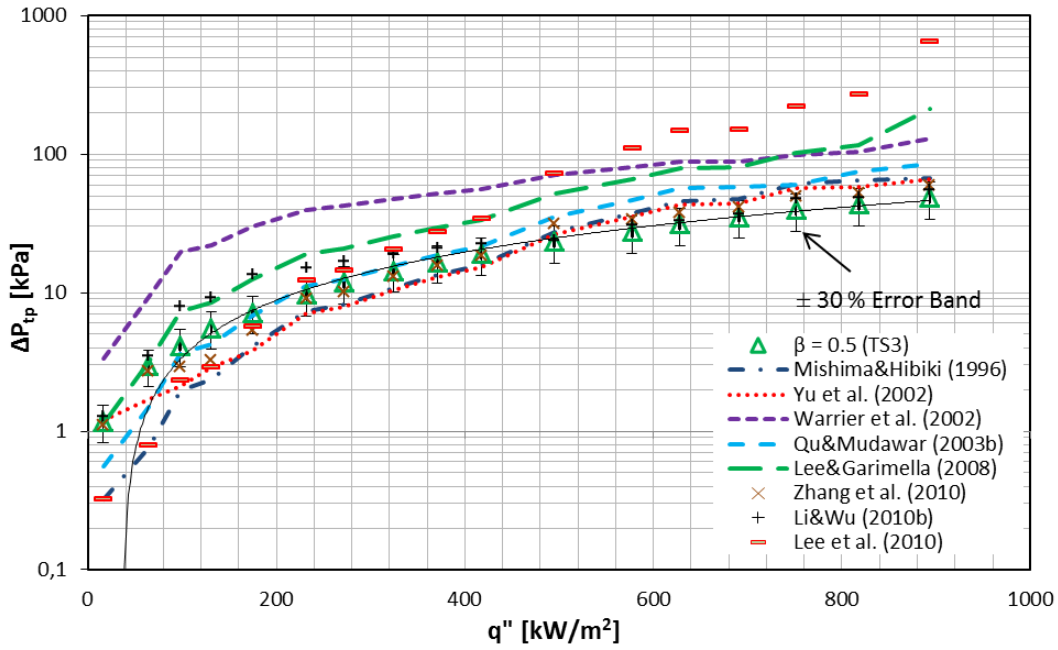

(c)

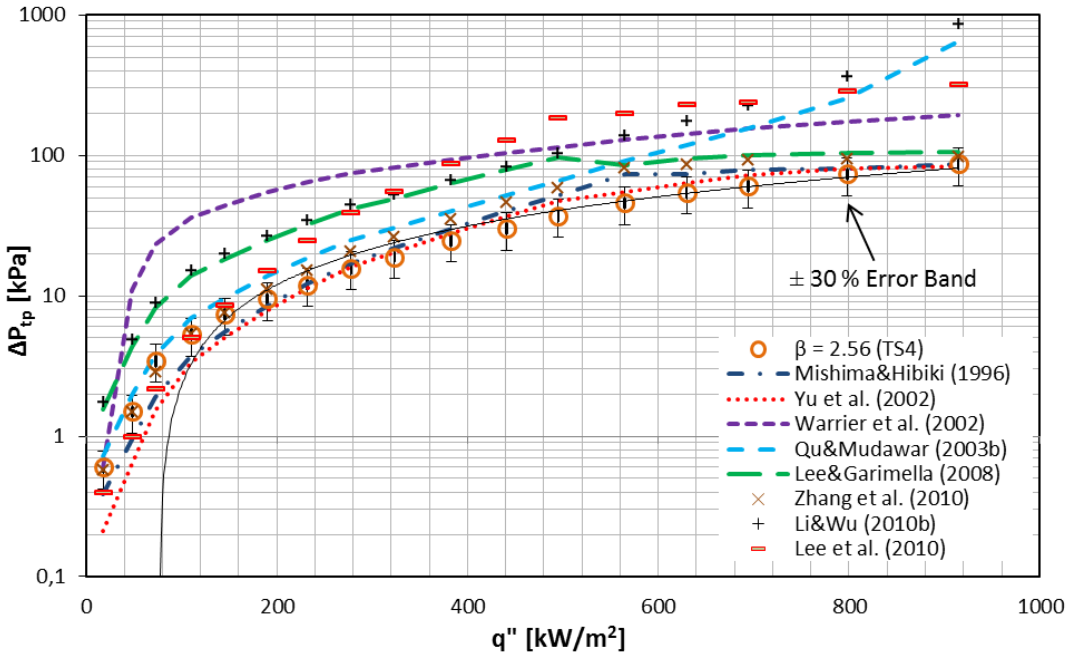

(d)

Figure 6.9 Comparison of the experimental flow boiling pressure drop data with micro-scale correlations at a mass flux of 200 kg/m^{2}s: (a) TS2, (b) TS1, (c) TS3 and (d) TS4.

6.3.2.1 Mishima and Hibiki (1996) correlation

Mishima and Hibiki (1996) carried out an experimental study in glass and aluminium tubes in an inner diameter range of *1.05* and *4 mm* using air and de-ionized water. They modified the *C* in order to correlate the two-phase frictional pressure drop component. They found that the *C* decreased as the tube inner diameter decreased, see equation 6.11. The details of the correlation are given in appendix B.

The comparisons of the experimental data with the correlation of Mishima and Hibiki (1996) are depicted in Fig. 6.10 for all test sections. As can be seen from Figures 6.9 (a-d) and 6.10 (a-d), the correlation underestimated the experimental data, see also Table 6.1. The reason of this may be due to the fact that Mishima and Hibiki used *1 mm* tube as the smallest diameter in their study. However, the hydraulic diameters of the microchannels are *0.56 mm* in the current study. Equation 6.11 shows that the smaller diameter results in smaller Chisholm constant and consequently the two-phase frictional multiplier (ϕ_L^2) decreases. It can also be seen from figures 6.10 (a-d) the correlation fairly predicted the experimental data for the microchannels except the TS4. The reason of this might be attributed to the channel length. The exit vapour quality becomes higher for the longer microchannel at the similar mass and heat flux input. Therefore, the correlation over predicted the experimental data for the longer channel compared to other channels.

$$C = 21[1 - e^{-319D}] \tag{6.11}$$

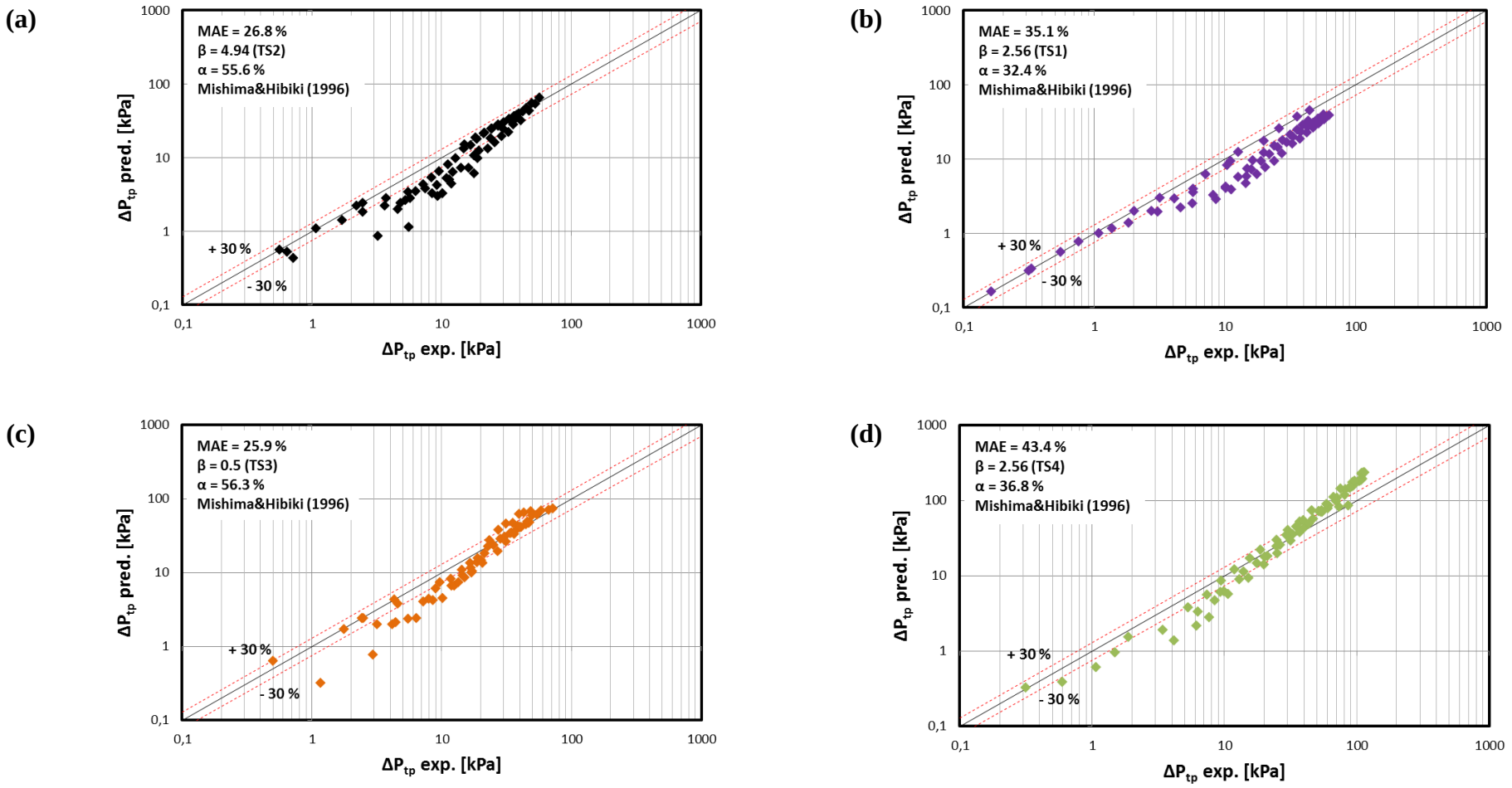

Figure 6.10 Comparison of experimental flow boiling pressure drop data with the Mishima-Hibiki (1996) correlation: (a) TS2, (b) TS1, (c) TS3 and (d) TS4.

6.3.2.2 Yu et al. (2002) correlation

Yu et al. (2002) investigated two-phase pressure drop, flow boiling heat transfer and critical heat flux of water in a horizontal circular tube of *2.98 mm* diameter and *910 mm* heated length over a mass flux range of *50-200 kg/m^{2}s*. They reported that the Lockhart-Martinelli (1949) model over-estimated their experimental data. Accordingly, the authors modified the two-phase frictional multiplier (ϕ_L^2) in Lockhart-Martinelli model, see equation 6.12.

$$\phi_L^2 = \frac{1}{X^{1.9}} \tag{6.12}$$

Figure 6.11 compares the experimental data with the Yu et al. (2002) correlation for all test sections. As can be seen from figures 6.9 (a-d) and 6.11 (a-d), the correlation under-predicts the experimental data at low heat flux input (low vapour quality region). However, at medium and high heat flux input, the correlation performs better, see Table 6.1. This behaviour can be attributed to the fact that the flow boiling pressure drop was predicted using the Lockhart-Martinelli (1949) model at low vapour quality since both vapour and liquid are laminar. As the vapour quality increases, equation 6.12 was used to calculate the pressure drop. As a result, the modification of the two-phase frictional multiplier in Yu et al. (2002) correlation resulted in better prediction for flow boiling pressure drop in the current study as can be seen from the *MAE* values in both correlations.

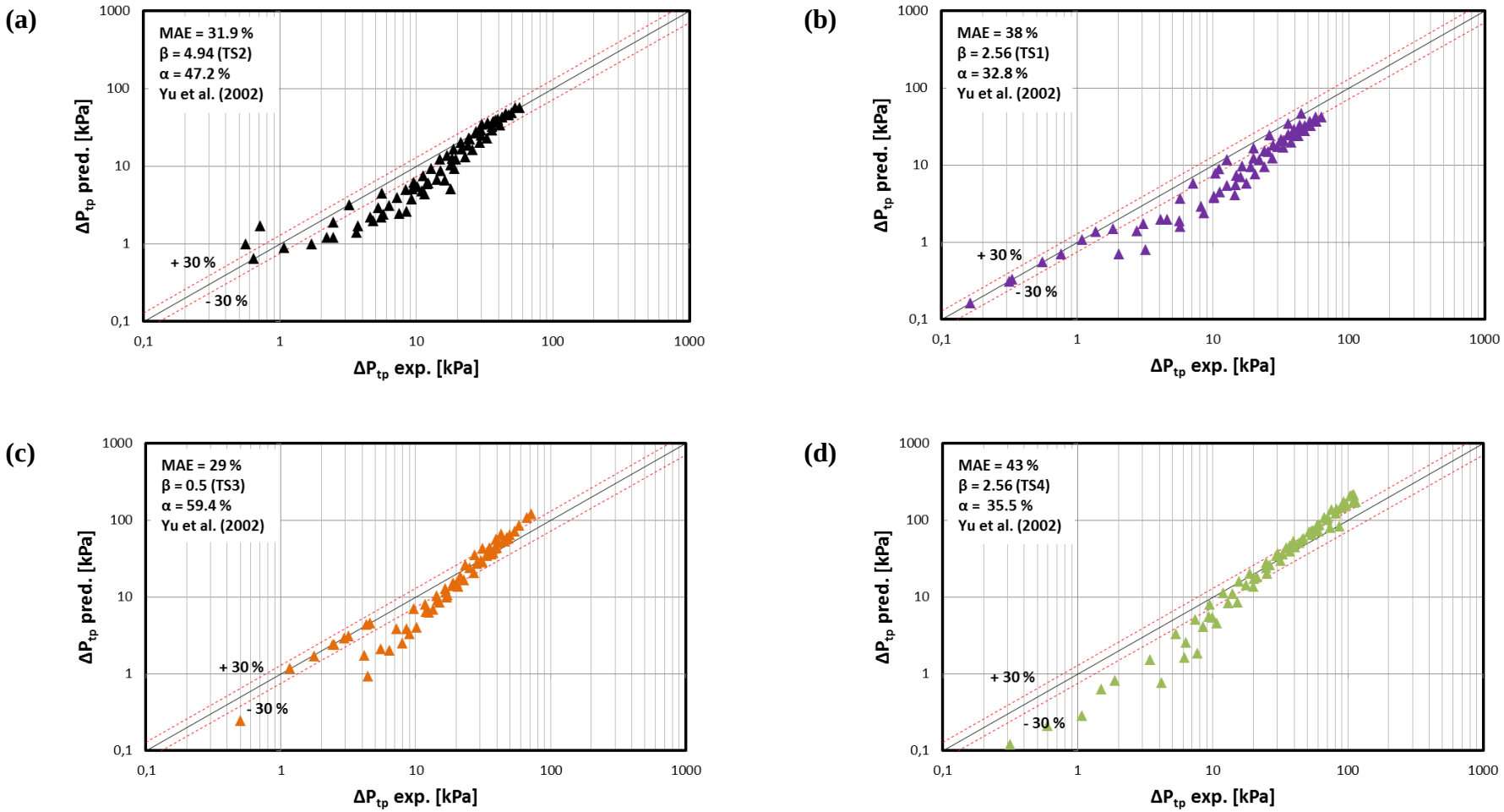

Figure 6.11 Comparison of experimental flow boiling pressure drop data with the Yu et al. (2002) correlation: (a) TS2, (b) TS1, (c) TS3 and (d) TS4.

6.3.2.3 Warrier et al. (2002) correlation

Warrier et al. (2002) performed single-phase and flow boiling experiments in parallel aluminium rectangular microchannel having *0.75 mm* hydraulic diameter using FC-84 as working fluid. The authors attained a constant value (*38*) for the Chisholm's constant (*C*) in order to calculate two-phase frictional multiplier (ϕ_L^2). It is worth mentioning that, the authors calculated the density of the FC-84 vapour using the ideal gas law and they assumed that the viscosity of the fluid equals to the viscosity of R-113. The experimental data were compared with the Warrier et al. (2002) correlation in Fig. 6.12. As can be seen from fig. 6.12, the correlation highly over predicted the experimental data for all test sections with a MAE values ranging from *183.2 %* to *276.4 %*, see Table 6.1. The reason of the poor performance of the correlation might be attributed to constant value of the Chisholm's constant which should be normally variable due to the interaction of the phases with each other. As presented in the above correlations, the Chisholm constant is important parameter since it considers the frictional contributions resulting from the interaction between phases. Therefore, the value of Chisholm constant should be variable with respect to the interaction between phases. Furthermore, they reported that the dominant flow regime is laminar liquid and laminar vapour in their study. Therefore, Chisholm constant should be smaller than *38*.

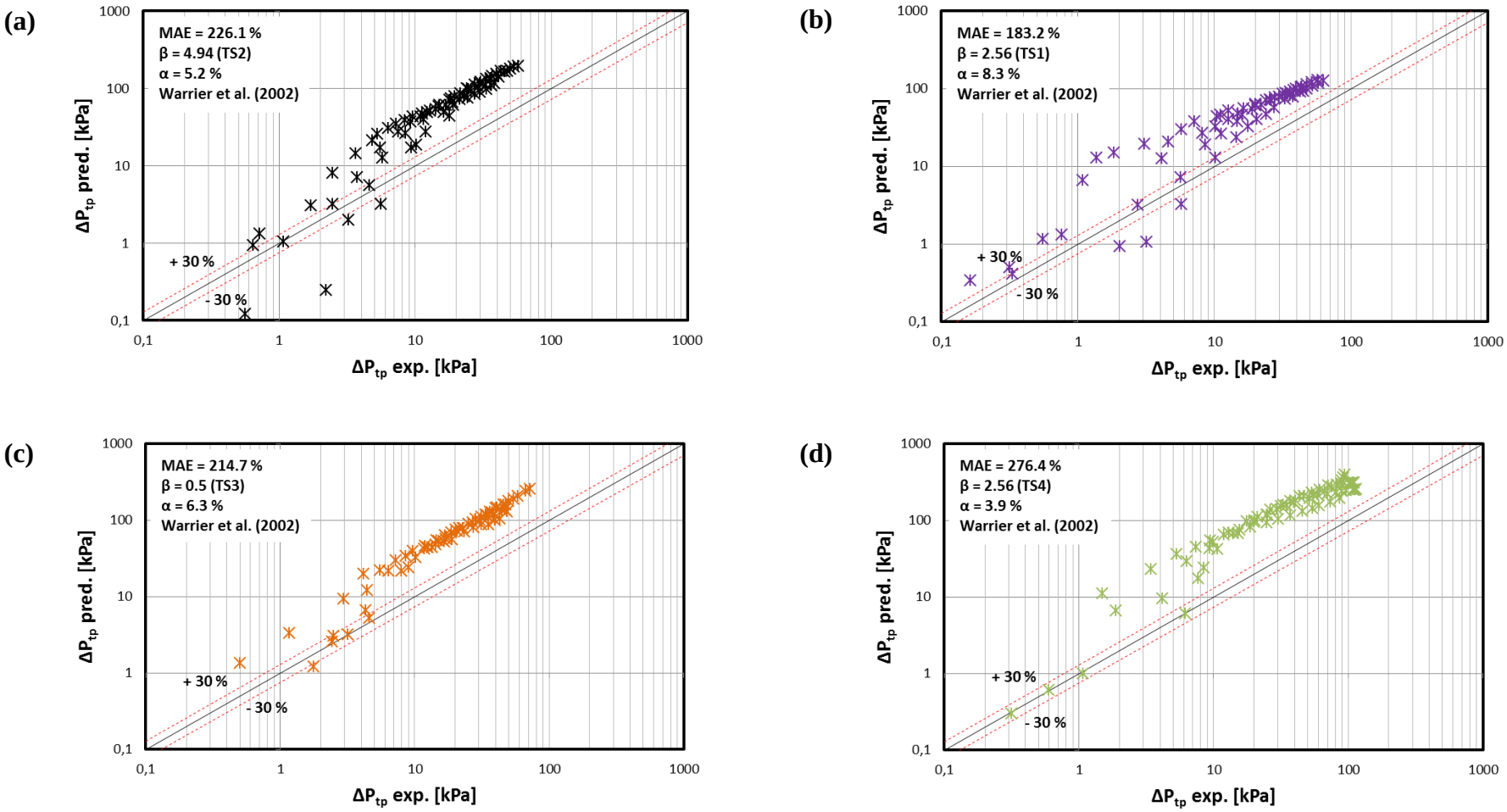

Figure 6.12 Comparison of experimental flow boiling pressure drop data with the Warrier et al. (2002) correlation: (a) TS2, (b) TS1, (c) TS3 and (d) TS4.

6.3.2.4 Qu and Mudawar (2003b) correlation

Qu and Mudawar (2003b) examined the flow boiling pressure drop and pressure drop instability in parallel oxygen-free copper microchannel heat sink. The channels had *0.35 mm* hydraulic diameter and the working fluid was water. They proposed a new two-phase pressure drop correlation modifying the correlation of Mishima and Hibiki (1996). The authors considered the effect of channel size and mass flux in their correlation, see equation 6.13.

$$C = 21(1 - e^{-3190 D_h})(0.00418G + 0.0613) \tag{6.13}$$

The experimental data were compared with the correlation of Qu and Mudawar (2003b) in Fig. 6.13. The experimental data were predicted very well by the correlation (*MAE = 12.4 %*) for the TS1 as can be seen from the figure. However, for the TS2 and TS3 the performance of the prediction became poor (*MAE = 50.1 %* and *49.2 %*). On the other hand, the correlation over predicted the experimental data of the TS4 channel (*MAE = 143.1 %*). The correlation predicts only *9.9 %* of the data within the error bands for the channel TS4, see also Table 6.1. It can be concluded from figures 6.10 (a-d) and 6.13 (a-d) that the Qu and Mudawar (2003b) correlation performed less well than the Mishima and Hibiki (1996) correlation. So we can infer from that the mass flux effect in the Chisholm constant reduced the performance of the correlation.

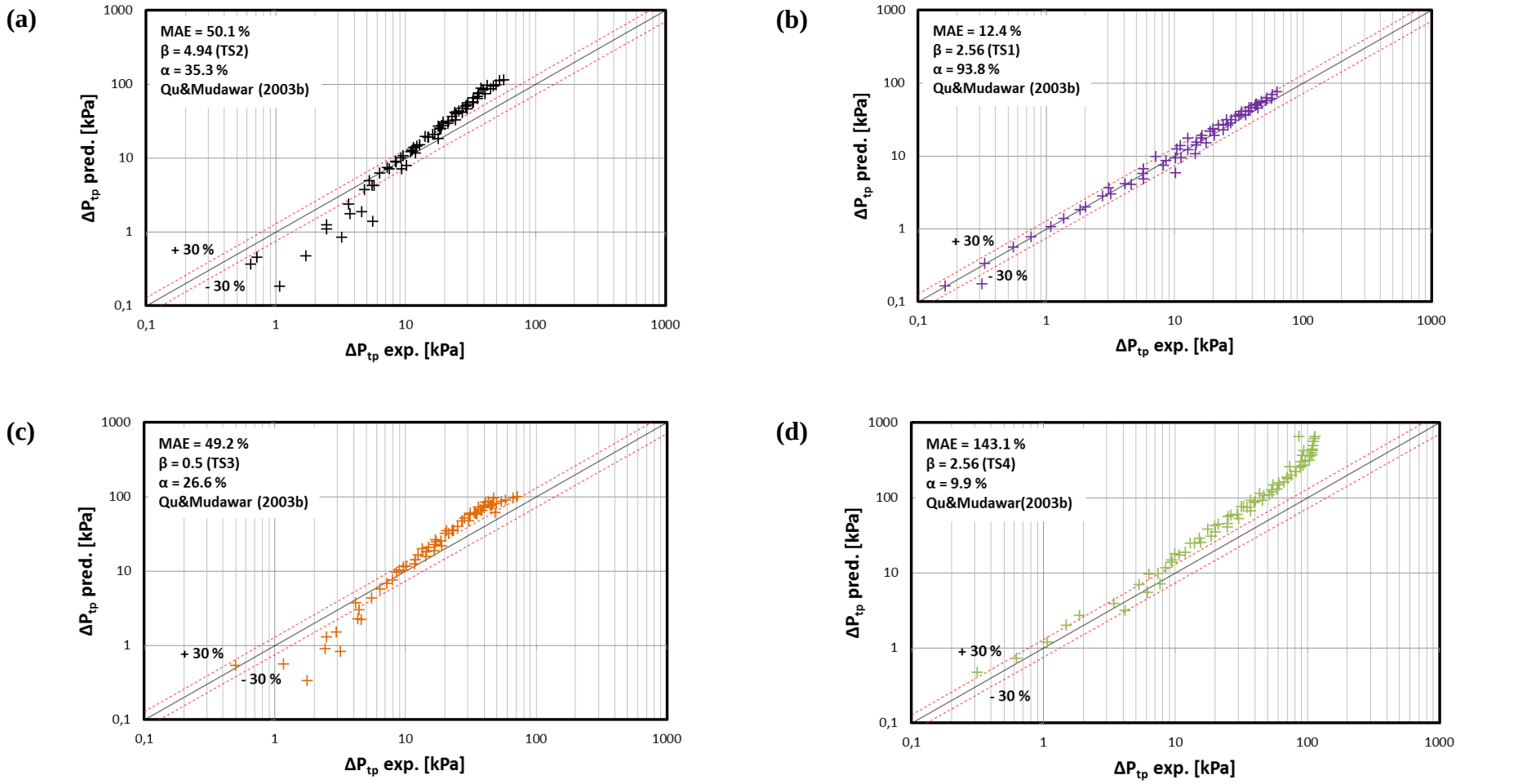

Figure 6.13 Comparison of experimental flow boiling pressure drop data with the Qu and Mudawar (2003b) correlation: (a) TS2, (b) TS1, (c) TS3 and (d) TS4.

6.3.2.5 Lee and Garimella (2008) correlation

Lee and Garimella (2008) investigated saturated flow boiling heat transfer and pressure drop of de-ionised water in parallel silicon microchannels with a hydraulic diameter range of *0.16-0.57 mm*. They modified the Chisholm's constant similar to Qu and Mudawar (2003b) correlation which takes into account the effect of hydraulic diameter and mass flux, see equation 6.14. The experimental data were compared with the Lee and Garimella (2008) correlation in Fig. 6.14. Although the correlation captured the experimental trend (Figures 6.9 (a-d)), it highly overestimated the experimental data for all test sections similar to Qu and Mudawar (2003b) as can be seen from the figure with a *MAE* range of *70.6-155 %*, see Table 6.1.

$$C = 2566 G^{0.5466} D_h^{0.8819} (1 - e^{-319 D_h}) \tag{6.14}$$

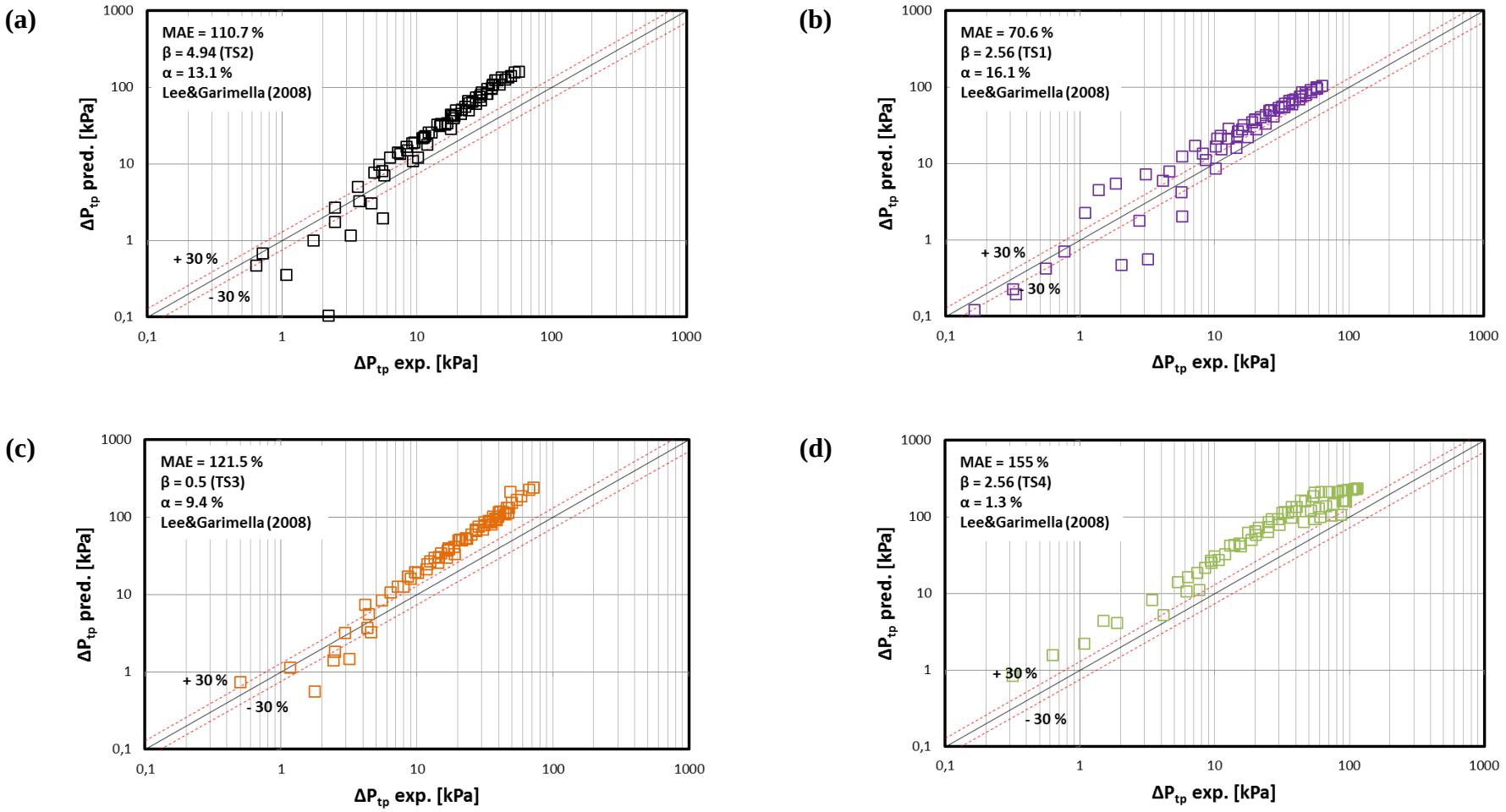

Figure 6.14 Comparison of experimental flow boiling pressure drop data with the Lee and Garimella (2008) correlation: (a) TS2, (b) TS1, (c) TS3 and (d) TS4.

6.3.2.6 Zhang et al. (2010) correlation

Zhang et al. (2010) analysed two-phase frictional pressure drop component and void fraction based on thirteen two-phase pressure drop correlations from the literature. They investigated the dominant parameters to correlate the two-phase frictional multiplier and void fraction using artificial neural network. They concluded that vapour quality, mass flux and system pressure have no considerable effects. On the other hand, the channel hydraulic diameter and the Laplace constant (*La*) have strong effects on the two-phase frictional multiplier and void fraction. Accordingly, they modified the Chisholm constant (*C*) using *La* as presented in equation 6.15.

$$C = 21\left(1 - \exp\left(-\frac{0.358}{La}\right)\right) \tag{6.15}$$

Figure 6.15 shows the global comparison between the experimental data and the correlation of Zhang et al. (2010). The correlation over predicted the data for the β = *2.56* (TS4) channel and predicted only *39.5 %* of the data within the ± 30 % error bands as shown in Fig. 6.15 (d). On the other hand, the correlation predicted well the experimental data for other channels as can be seen from Figs. 6.15 (a-c). Here *68.1-70.3 %* of the data were predicted within the ± *30 %* error bands at MAE values ranging from *19.5-23.4 %*, see also Table 6.1.

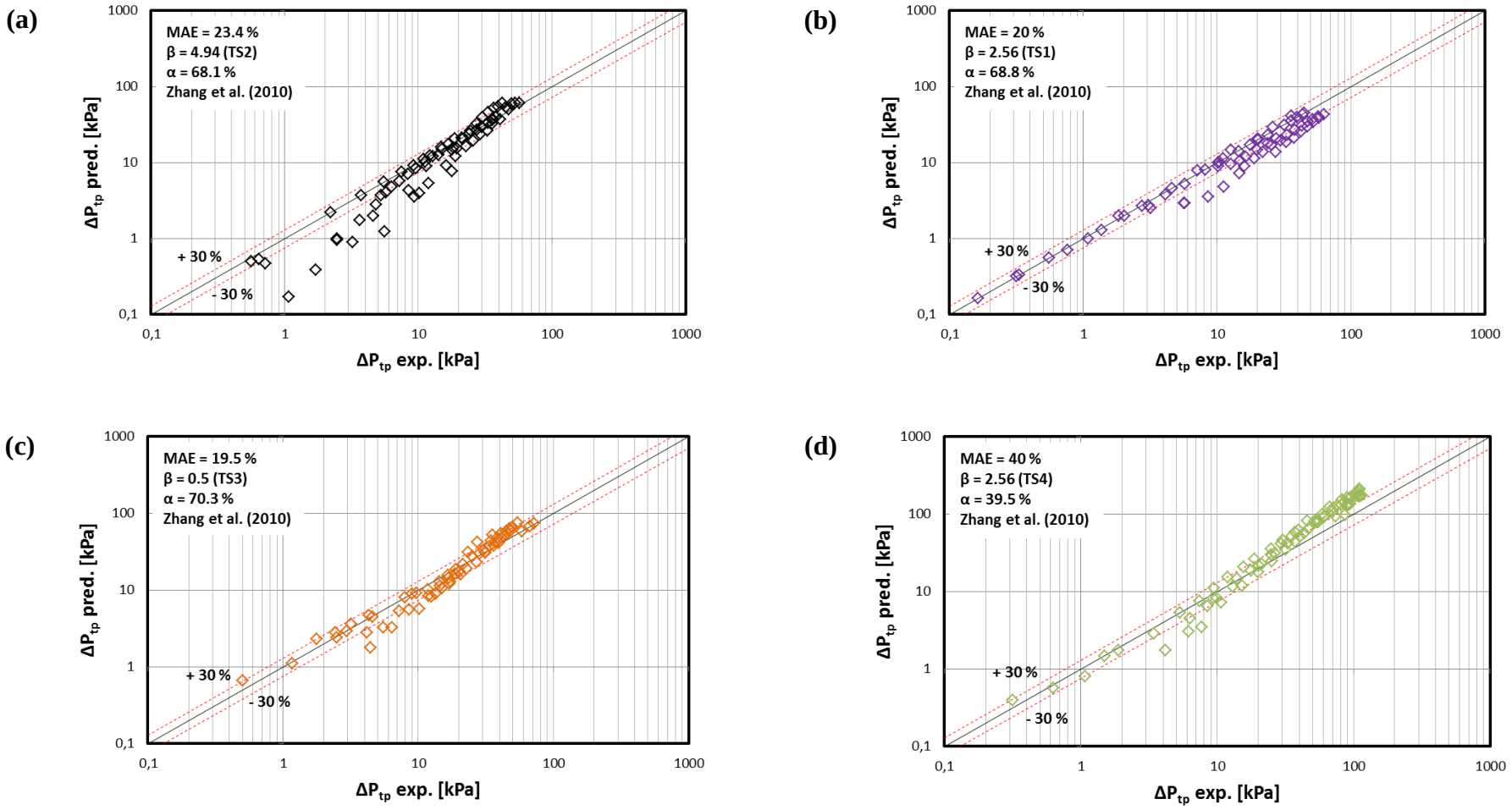

Figure 6.15 Comparison of experimental flow boiling pressure drop data with the Zhang et al. (2010) correlation: (a) TS2, (b) TS1, (c) TS3 and (d) TS4.

6.3.2.7 Li and Wu (2010b) correlation

Li and Wu (2010) collected experimental results of adiabatic two-phase pressure drop in microchannels from the literature which contains *769* data points, *12* different fluids and a hydraulic diameter range of *0.15-3.25 mm*. The authors modified the Chilshom's parameter (*C*) of two-phase multiplier using Bond number (*Bd*) and Reynolds number (*Re*), see equation 6.16.

$$C = \begin{cases} 11.9 Bd^{0.45} & Bd \le 1.5 \\ 109.4(Bd\,\mathrm{Re}^{0.5})^{-0.56} & 1.5 < Bd \le 11 \end{cases} \tag{6.16}$$

Figure 6.16 presents the comparison of the experimental data with the correlation of Li and Wu (2010b). The correlation could not predict the data accurately for all test sections with a *MAE* range of *48.6-179.8 %*, see Table 6.1. It is clear from Figs. 6.16 b-d, the performance of the correlation decreased significantly as the heated length increased. This is because the slope of the experimental pressure drop curve is less than the curve of the prediction as can be clearly seen in Fig. 6.9 (d). Consequently, the percentage of the deviation increased as the vapour quality increased.

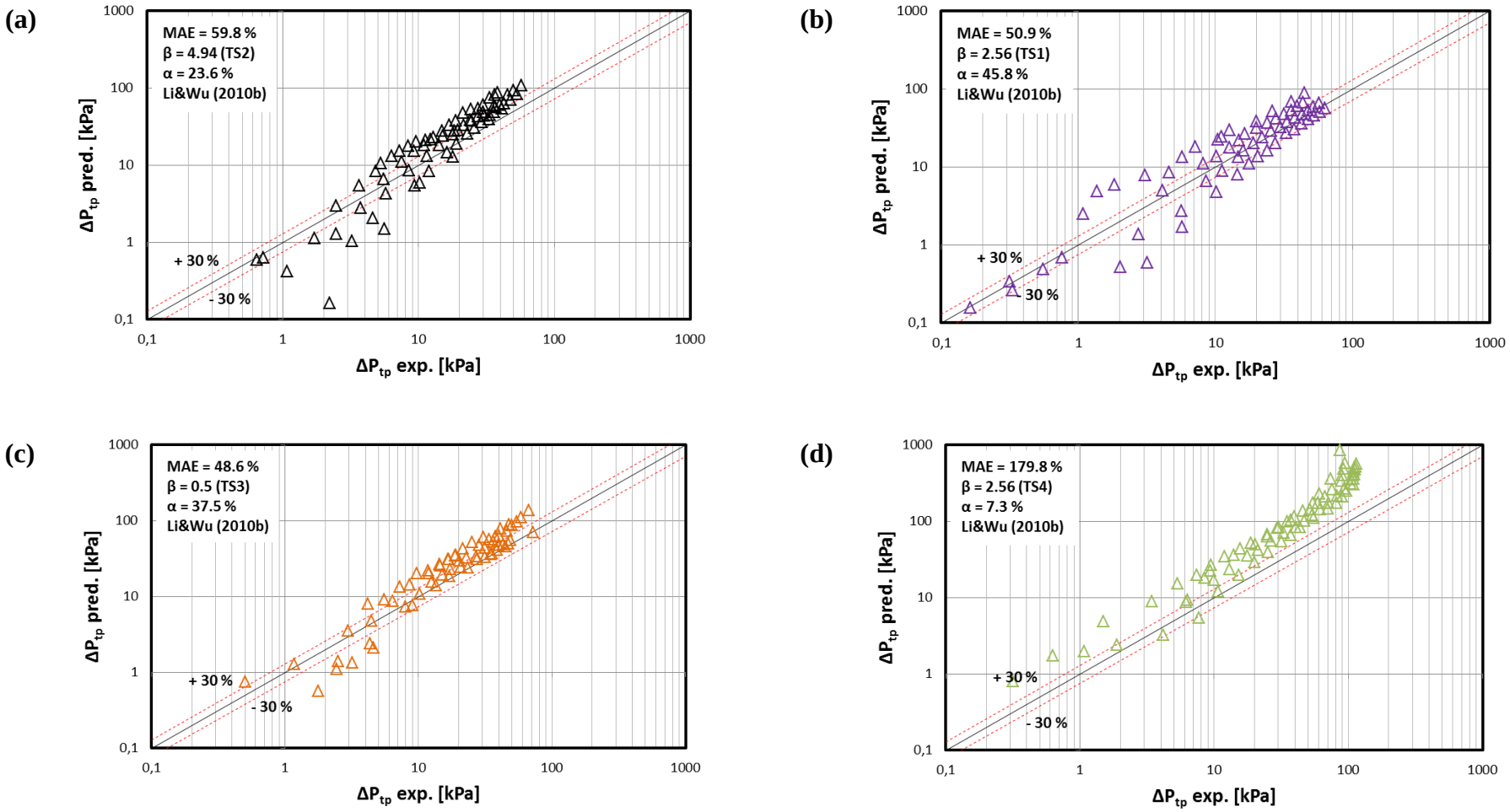

Figure 6.16 Comparison of experimental flow boiling pressure drop data with the Li and Wu (2010b) correlation: (a) TS2, (b) TS1, (c) TS3 and (d) TS4.

6.3.2.8 Lee et al. (2010) correlation

Lee et al. (2010) reviewed the pressure drop and heat transfer data of microchannels from the existing literature. The existing database covered seven working fluids including water and the hydraulic diameter less than *3 mm*. They concluded that the Chisholm constant is a function of the Bond number (*Bd*) and exit vapour quality. Accordingly they correlated the Chilshom's constant (*C*) using Bond number (*Bd*) and exit vapour quality as presented in equation 6.17.

$$C = 121.6(1 - e^{-22.7\,Bd})x_e^{1.85} \tag{6.17}$$

The experimental data were compared with the Lee et al. (2010) correlation in Fig. 6.17. As can be seen from the figure, the correlation cannot give accurate estimation for the flow boiling pressure drop data in all test sections. The *MAE* values are found to be *79 %*, *47.6 %*, *98.5 %* and *82.1 %* for the test sections TS2, TS1, TS3 and TS4, respectively, see Table 6.1. The correlation predicts the low and medium pressure drop values better than the high pressure drop values which corresponds to low exit qualities. The reason of this may be attributed to the exponent of vapour quality in equation 6.17. As the exit vapour quality increases the Chisholm constant increases due to the *1.85* exponent of the vapour quality which gives much higher prediction than the original Lockhart-Martinelli model.

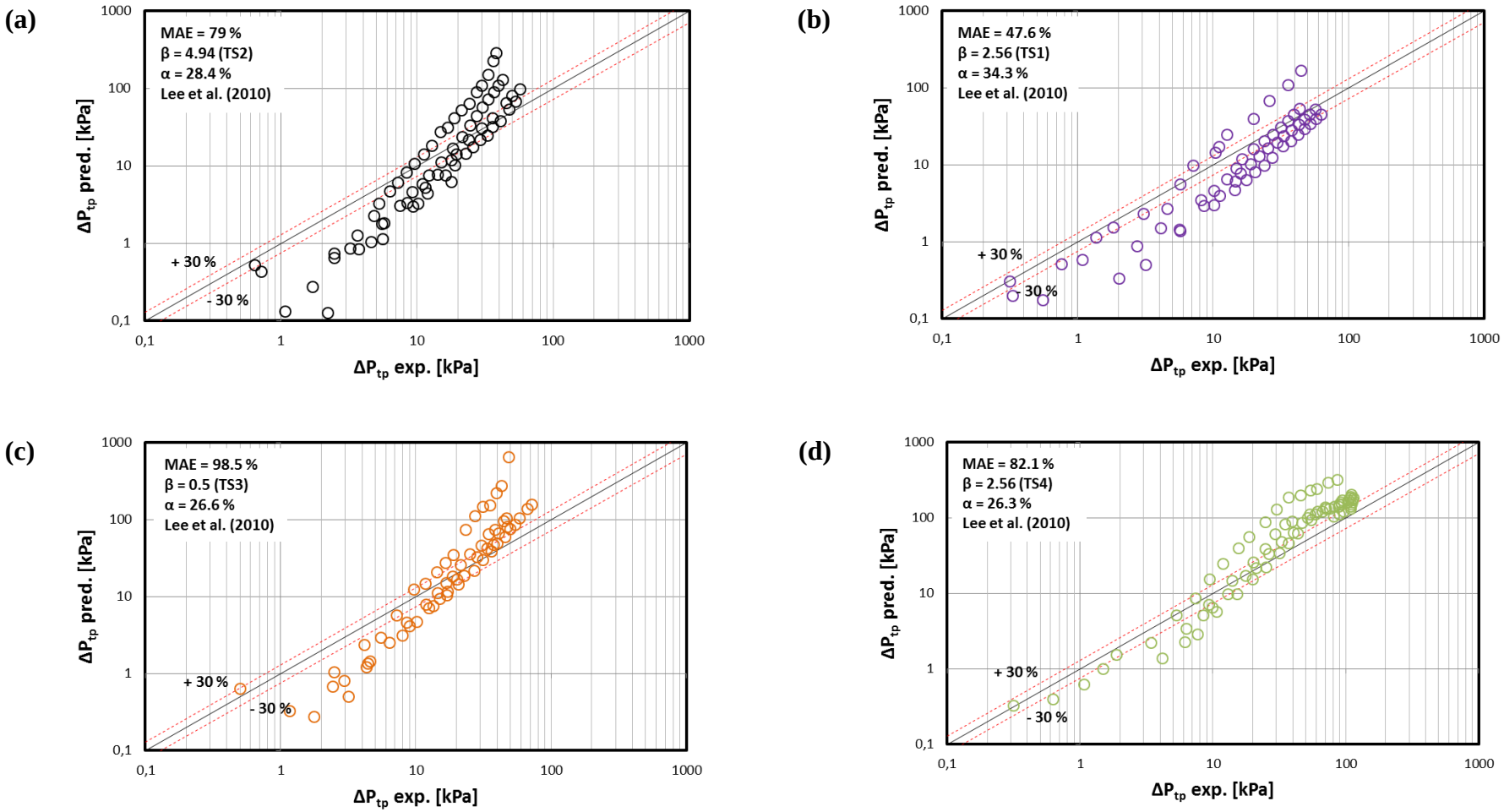

Figure 6.17 Comparison of experimental flow boiling pressure drop data with the Lee et al. correlation (2010): (a) TS2, (b) TS1, (c) TS3 and (d) TS4.

Table 6.1 MAE and the percentage of data within ± 30 % error bands for flow boiling pressure drop correlations.

Correlation	β = 2.56 (TS1)		β = 4.94 (TS2)		β = 0.5 (TS3)		β = 2.56 (TS4)	
	MAE %	α %	MAE %	α %	MAE %	α %	MAE %	α %
Lockhart&Martinelli (1949)	30.6	50	39.4	47.2	44	50	109.2	13.8
Homogenous model (1994)	170	1.9	176.6	6.4	242.7	7.45	187.2	0
Mishima&Hibiki (1996)	35.1	32.4	26.8	55.6	25.9	56.3	43.4	36.8
Yu et al. (2002)	38	32.8	31.9	47.2	29	59.4	43	35.5
Warrier et al. (2002)	183.2	8.3	226.1	5.2	214.7	6.3	276.4	3.9
Qu&Mudawar (2003b)	12.4	93.8	50.1	35.3	49.2	26.6	143.1	9.9
Lee&Garimella (2008)	70.6	16.1	110.7	13.1	121.5	9.4	155	1.3
Zhang et al. (2010)	20	68.8	23.4	68.1	19.5	70.3	40	39.5
Li&Wu (2010b)	50.9	45.8	59.8	23.6	48.6	37.5	179.8	7.3
Lee et al. (2010)	47.6	34.3	79	28.4	98.5	26.6	82.1	26.3

6.4 Summary

In this chapter, the flow boiling pressure drop results were presented and discussed for the tested four microchannels at constant inlet temperature (*89 ºC*) and inlet pressure (*115 kPa*) over a mass flux range of *200-800 kg/m^{2}s*. The results showed that the flow boiling pressure drop increased almost linearly with heat flux and mass flux for all test sections. Increasing heat flux enhances the bubble generation rate during flow boiling that augment the flow resistance in the microchannels. On the other hand, as the mass flux increases the accelerational pressure drop component increases due to increase in the difference between the inertia force and the evaporation momentum force. The frictional pressure drop component also becomes higher at high mass fluxes. The channel aspect ratio effect on the flow boiling pressure drop was also examined. It was found that the flow boiling pressure drop increases as the channel aspect ratio decreases.

Furthermore, the experimental flow boiling pressure drop data were compared with two macro-scale correlations and eight micro-scale correlations available in the literature. The Lockhart-Martinelli (1949) correlation predicted the experimental data better than the homogeneous flow model (1994). The micro-scale correlations proposed by Mishima and Hibiki (1996), Yu et al. (2002) and Zhang et al. (2010) reasonably predicted the experimental flow boiling pressure drop results. Among these, the correlation of Zhang et al. (2010) performed better than the other selected correlations to predict the experimental flow boiling pressure drop data of the microchannels in the current study.

Chapter 7

Conclusions and Recommendations

7.1 Conclusions

In this experimental study, single-phase and flow boiling heat transfer and pressure drop were investigated in microchannel test sections. Four oxygen free copper test sections were tested in the experiments. Three microchannel test sections having same length ($L = 62\ mm$) and hydraulic diameter ($D_h = 0.561\ mm$) but different aspect ratio ($\beta = 0.5,\ 2.56$ and 4.94) were examined in order to determine the effect of channel aspect ratio on single-phase flow and flow boiling. In addition to this, a longer test section ($D_h = 0.561\ mm$, $L = 86.8\ mm$ and $\beta = 2.56$) was tested in order to reveal the effect of channel heated length. In single-phase flow tests, temperature and pressure readings were obtained to identify the discrepancy between the results and theory. Moreover, effect of channel aspect ratio on the single-phase friction factor and heat transfer was investigated. In flow boiling tests, mass flux, heat flux, vapour quality, heated length and channel aspect ratio effects on the observed flow patterns, heat transfer coefficient and two-phase pressure drop results were examined. A high-speed, high-resolution camera was used to record flow patterns near the upstream, near the middle and near the downstream of the microchannels. Finally, the results were compared to existing heat transfer and pressure drop correlations available in the literature. The key findings that can be reached from this study are presented below.

7.1.1 Single-Phase Heat Transfer and Friction Factor

Single-phase experiments were performed at $35\ ^{o}C$ inlet temperature and atmospheric pressure over a Reynolds number range from 150 to 3800. The main conclusions are:

- Hydrodynamically and thermally developing flow conditions were dominant for all test sections in the experiment.
- Laminar to turbulent flow transition was found to be in a Reynolds number range consistent with published results in the literature.
- The experimental friction factor data were fairly agreed with the conventional scale developing flow and fully developed flow correlations in the turbulent regime.
- The effect of channel aspect ratio on the single-phase friction factor was insignificant.
- The effect of channel aspect ratio on the Nusselt number was insignificant.

7.1.2 Flow Patterns and Flow Pattern Maps

The visualization study was conducted in the current research in a range of mass fluxes of *200-800 kg/m^{2}s* and at inlet pressure and temperature of *115 kPa* and *89 ºC* respectively. The results showed the following points:

- The bubbly flow, slug flow, churn flow and annular flow patterns were visualized in the microchannels. An additional flow pattern (periodic flow) was also observed except the $\beta = 4.94$ test section.
- The flow patterns changed from single-phase flow to bubbly flow, bubbly flow to slug flow, slug flow to churn flow and churn flow to annular flow as the heat flux was increased.
- The flow patterns were found to be different at different locations at the same mass and heat flux input.
- The channel aspect ratio has an effect on the flow patterns. The bubbles were dispersed and small in the largest aspect ratio channel ($\beta = 4.94$). As the aspect ratio was decreased the bubbles became elongated due to confinement.
- The flow pattern map of Galvis and Culham (2012) predicted well the experimental data except the transition from bubbly flow to slug flow regime.

The flow pattern maps of Sobierska et al. (2006) and Harirchian and Garimella (2009) reasonably predicted the experimental flow pattern data.

7.1.3 Flow Boiling Heat Transfer Characteristics

The experimental flow boiling heat transfer coefficient data was obtained for all microchannels at the same experimental range for flow pattern regime visualizations under steady-state conditions. The following findings can be summarized:

- The effect of heat flux was clear on boiling curves whilst the mass flux effect on the boiling curves was insignificant.
- The heat transfer coefficient increased with heat flux and was independent of the local vapour quality at low and medium heat fluxes. However, effect of heat flux was insignificant at high heat fluxes.
- The heat transfer coefficient decreased when the mass flux was increased because of the high pressure drop.
- The heat transfer coefficient increased as the channel aspect ratio decreased up to heat flux values about *480-500 kW/m^2*. For higher heat fluxes, the channel aspect ratio had no effect on the heat transfer coefficient.
- The heat transfer coefficient for the shorter channel was higher than the longer channel.
- The conventional scale correlations could not predict the experimental results.
- The micro-scale correlations proposed by Sun and Mishima (2009), Li and Wu (2010) and Mahmoud and Karayiannis (2011) reasonably predicted the experimental results.

7.1.4 Flow Boiling Pressure Drop Characteristics

The flow boiling pressure drop results were presented for the microchannel test sections at constant inlet temperature (*89 ºC*) over a mass flux range of *200-800 kg/m^{2}s*. The key findings can be drawn:

- The flow boiling pressure drop increased as the heat flux and mass flux increased for all test sections.
- The flow boiling pressure drop increased as the channel aspect ratio was decreased.
- The flow boiling pressure drop correlations of Mishima and Hibiki (1996), Yu et al. (2002) and Zhang et al. (2010) reasonably predicted the experimental flow boiling pressure drop results.

Taken together, the present study makes several noteworthy contributions to the literature on the effect of channel aspect ratio in single-phase and two-phase flows in micro-scale. As summarized above, the channel aspect ratio has no effect on the single-phase pressure drop and heat transfer characteristics. This study also demonstrates, for the first time, that single channel aspect ratio affects the flow boiling characteristics. The current data highlight the considerable influence of the channel aspect ratio as well as channel hydraulic diameter on the flow patterns, heat transfer performance and pressure drop characteristics during flow boiling in microchannels. Such knowledge is valuable in order to provide design recommendations for industrial micro evaporators.

7.2 Recommendations

Based on the experimental work performed in the current study, it can be recommended that further research in this field would be of great help in the following points:

- The effect of heat flux and channel aspect ratio on the flow boiling heat transfer coefficient needs further investigation at high heat fluxes. Different fluids having lower boiling points can be used to avoid burnout of the experimental facility.
- The visualization study should be performed synchronously for different locations of the channel.

- The effect of channel heated length on the flow boiling heat transfer coefficient needs further investigation using one more channel having different heated length.
- The results also showed that the available two-phase pressure drop and heat transfer correlations did not perform very well. Therefore, new flow boiling heat transfer and pressure drop correlations are needed based on a wide range of test sections and experimental conditions.

REFERENCES

Agostini, B., Thome, J.R., Fabri, M. and Michel, B. High heat flux two phase cooling in silicon multi-microchannels. *IEEE Transactions on Components and Packaging Technologies*, 31(3):691-701, 2008a.

Agostini, B., Revellin, R., Thome, J.R., Fabbri, M., Michel, B., Calmi, D. and Kloter, U. High heat flux flow boiling in silicon multi-microchannels - Part III: Saturated critical heat flux of R236fa and two-phase pressure drops. *International Journal of Heat and Mass Transfer*, 51(21-22):5426-5442, 2008b.

Akbar, M.K., Plummer, D.A. and Ghiaasiaan S.M. On gas-liquid two-phase flow in small diameter vetical tubes. *International Journal of Multiphase Flow*, 29:855-865, 2003.

Ali, R. Phase change phenomena during fluid flow in microchannels. PhD thesis, Royal Institute of Technology, Stockholm, Sweden, 2010.

Anwar, Z., Björn, P. and Rahmatollah, K. Flow boiling heat transfer and dryout characteristics of R600a in a vertical minichannel, *Heat Transfer Engineering*, 36(14):1230-1240, 2015.

Baker, O. Simultaneous flow of oil and gas. *Oil gas Journal*, 53:185, 1954.

Balasubramanian, K., Jagirdar, M., Lee, P.S., Teo, C.J. and Chou, S.K. Experimental investigation of flow boiling heat transfer and instabilities in straight microchannels. *International Journal of Heat and Mass Transfer*, 66:655-671, 2013.

Bao, Z.Y., Fletcher, D.F. and Haynes, B.S. Flow boiling heat transfer of Freon R11 and HCFC123 in narrow passages. *International Journal of Heat and Mass Transfer*, 43: 3347-3358, 2000.

Basu, S., Ndao, S., Michna, G.J., Peles, Y. and Jensen, M.K. Flow boiling of R134a in circular microtubes-Part I: Study of Heat Transfer Characateristics. *ASME Journal of Heat Transfer*, 133(5):051502-051511, 2001.

Bergles, A.E. and Rohsenow, W.M. The determination of forced-convection surface boiling heat transfer, *ASME Journal of Heat Transfer*, 86:365-372, 1964.

Bergles, A.E. Review of instability in two-phase systems, *Hemisphere Publishing Corporation,* Washington, 1977.

Bergles, A.E. and Kandlikar, S.G. On the nature of critical heat flux in microchannels, *Journal of Heat Transfer*, 127:101-107, 2005.

Blasius, H. Ähnlichkeitsgesetz bei Reibungsvorgängen in Flüssigkeiten, Forschg. *Arb. Ing.-Wes.*, 131, 1913.

Bogojevic, D., Sefiane, K., Walton, A.J., Lin, H., and Cummins, G. Two-phase flow instabilities in a silicon microchannels heat sink. *International Journal of Heat and Fluid Flow*, 30:854-867, 2009.

Bogojevic, D., Sefiane, K., Walton, A.J., Lin, H., Cummins, G., Kenning, D.B.R. and Karayiannis, T.G. Experimental investigation of non-uniform heating effect on flow boiling instabilities in a microchannel-based heat sink. *International Journal of Thermal Sciences*, 50:309-324, 2011.

Boyd, R.D. Subcooled flow boiling critical heat flux and its application to fusion energy components. Part 1. A review of fundamentals of CHF and related data base. *Fusion Technologies*, 7:7 – 30, 1985.

Boure, J.A., Bergles, A.E. and Tong, L.S. Review of two-phase flow instability. *Nuclear Engineering Design*, 25:165-192, 1973.

Brauner, N. and Moalem-Maron, D. Identification of the range of small diameter conduits regarding two-phase flow pattern transitions. *International Communications Heat Mass Transfer*, 19:29-39, 1992.

Brutin, D., Topin, F. and Tadrist, L. Experimental study of unsteady convective boiling in heated minichannels. *International Journal of Heat and Mass Transfer*, 46: 2957-2965, 2003.

Celata, G.P., Cumo, M., McPhail, S. and Zummo, G. Characterization of fluid dynamic behaviour and channel wall effects in microtube. *International Journal of Heat and Fluid Flow*, 27:135-143, 2006.

Chang, K.H. and Pan, C. Two-phase flow instability for boiling in a microchannel heat sink. *International Journal of Heat and Mass Transfer*, 50(11-12):2078-2088, 2007.

Chen, L. Flow patterns in upward two-phase flow in small diameter tubes. PhD thesis, Brunel University London, London, UK, 2006.

Chen, L., Tian, Y.S. and Karayiannis, T.G. The effect of tube diameter on vertical two-phase flow regimes in small tubes. *International Journal Heat and Mass Transfer*, 49: 4220-4230, 2006.

Chen, T. and Garimella, S.V. Measurements and high-speed visualizations of flow boiling of a dielectric fluid in a silicon microchannel heat sink. *International Journal Multiphase Flow*, 32:957-971, 2006.

Chisholm, D. A theoretical basis for the Lockhart–Martinelli correlation for two-phase flow. *International Journal of Heat Mass Transfer*, 10:1767–1778, 1967.

Choi, C.W., Yu, D.I. and Kim, M.H. Adiabatic two-phase flow in rectangular microchannels with different aspect ratios: Part I – Flow pattern, pressure drop and void fraction. *International Journal of Heat and Mass Transfer*, 54(1-3):616-624, 2011.

Coleman, J.W. and Garimella, S. Characterization of two-phase flow patterns in small diameter round and rectangular tubes. *International Journal of Heat and Mass Transfer*, 42:2869-2881, 1999.

Coleman, H.W. and Steele, W.G. *Experimentation, Validation, and Uncertainty Analysis for Engineers*. *John Wiley and Sons*, New Jersey, USA, third edition, 2009.

Collier, J.G. and Thome, J.R. *Convective Boiling and Condensation*. *Oxford University Press*, Oxford, UK, third edition, 1994.

Consolini, L. and Thome, J. R. Micro-channel flow boiling heat transfer of R-134a, R-236fa, and R-245fa. *Microfluidics and Nanofluidics*, 6(6):731-746, 2009.

Cornwell, K. and Kew, P.A. Boiling in small parallel channels. *Proceedings of the CEC Conference on energy Efficiency in Process Technology*, Athens, 624-638, 1993.

Davis, E.J. and Anderson, G.H. The incipience of nucleate boiling in forced convection flow. *AIChE Journal*, 12:774-780, 1966.

Dittus, F.W. and Boelter, L.M.K. Heat transfer in automobile radiators of the tubular type. *University of California Publications in Engineering*, 2:443-461, 1930.

Galvis, E. and Culham, R. Measurements and flow pattern visualization of two phase flow boiling in single channel microevaporator. *International Journal of Multiphase Flow*, 42:52-61, 2012.

Gamrat, G., Favre-Marinet, M. and Asendrych, D. Conduction and entrance effects on laminar liquid flow and heat transfer in rectangular microchannels. *International Journal of Heat and Mass Transfer*, 48:2943–2954, 2005.

Gamrat, G., Favre-Marinet, M., Le Person, S., Baviere, R. and Ayela, F. An experimental study and modelling of roughness effects on laminar flow in microchannels. *Journal of Fluid Mechanics*, 594:399–423, 2008.

Gao, P., Le Person, S. and Favre-Marinet, M. Scale effect on hydrodynamics and heat transfer in two-dimensional mini and microchannels. *International Journal of Thermal Sciences*, 45:1017–1027, 2002.

Gedupudi, S., Karayiannis, T.G. and Kenning, D.B.R. Modelling pressure fluctuations during flow boiling in microchannels with inlet compressibility and resistance. *Proceedings of the 7th World Conference on Experimental Heat Transfer, Fluid Mechanics and Thermodynamics*, 2009a.

Gedupudi, S., Kenning, D.B.R. and Karayiannis, T.G. 1-D modelling of pressure fluctuations due to confined bubble growth during flow boiling in a microchannel. *Proceedings of the 2nd Micro and Nano Flows Conference*, 2009b.

Gedupudi, S., Karayiannis, T.G. and Kenning, D.B.R. Approaches to 1-D modelling of flow reversal during flow boiling in a microchannel. *Proceedings of the 11th UK National Heat Transfer Conference*, 2009c.

Ghiaasiaan, S. M. and Chedester, R.C. Boiling incipience in microchannels. *International Journal of Heat and Mass Transfer*, 45:4599-4606, 2002.

Gnielinski, V. New equations for heat and mass transfer in turbulent pipe and channel flow. *International Chemical Engineering*, 16:359 – 368, 1976.

Gungor, K.E. and Winterton, R.H.S. Simplified general correlation for saturated and comparisons of correlations with data. *The Canadian Journal of Chemical Engineering*, 65(1):148 – 156, 1987.

Guo, Z-Y. and Li, Z-X. Size effect on single-phase channel flow and heat transfer at microscale. *International Journal of Heat and Fluid Flow*, 24(3):284-298, 2003.

Harirchian, T. and Garimella, S.V. Effects of channel dimension, heat flux, and mass flux on flow boiling regimes in microchannels. *International Journal of Multiphase Flow*, 35(4):349-362, 2009a.

Harirchian, T. and Garimella, S.V. The critical role of channel cross-sectional area in microchannel flow boiling heat transfer. *International Journal of Multiphase Flow*, 35:904-913, 2009b.

Harirchian, T. and Garimella, S.V. A comprehensive flow regime map for microchannel flow boiling with quantitative transition criteria. *International Journal of Heat and Mass Transfer*, 53:2694-2702, 2010.

Harms, T.M., Kazmierczak, M.J. and Gerner, F.M. Developing convective heat transfer in deep rectangular microchannels. *International Journal of Heat and Fluid Flow*, 20:149–157, 1999.

Hassan, I., Vailancourt, M. and Pehlivan, K. Two – phase flow regime transitions in microchannels: A comparative experimental study. *Microscale Thermophysical Engineering*, 9:165 – 182, 2005.

Hetsroni, G., Mosyak, A., Segal, Z. and Pogrebnyak, E. Two-phase flow pattern in parallel micro-channels. *International Journal of Multiphase Flow*, 29:341-360, 2003.

Hetsroni, G., Mosyak, A., Pogrebnyak, E. and Segal, Z. Explosive boiling of water in parallel microchannels. *International Journal of Multiphase Flow*, 31:371-392, 2005.

Hetsroni, G., Mosyak, A., Pogrebnyak, E. and Segal, Z. Periodic boiling in parallel microchannels at low vapour quality. *International Journal of Multiphase Flow*, 32:1141-1159, 2006.

Hewitt, G.F. and Roberts, D.N. Study of two-phase flow patterns by simultaneous x-ray and flash photography. *Atomic energy research establishment Harwell AERE-M*. 2159, 1969.

Hsieh, S-S., Lin, C-Y., Huang, C-F. and Tsai, H-H. Liquid flow in a micro-channel. *Journal of Micomechanical and Microengineering*, 14:436 – 445, 2004.

Huh, C. and Kim, M.H. Two-phase pressure drop and boiling heat transfer in a single horizontal microchannel. *Proceedings of the 4th International Conference on Nanochannels, Microchannels and Minichannels*, 1097-1104, 2006.

Huh, C. and Kim, M.H. Pressure drop, boiling heat transfer and flow patterns during flow boiling in a single microchannel. *Heat Transfer Engineering*, 28(8-9):730 – 737, 2007.

Huo, X., Tian, Y.S. and Karayiannis, T.G. Flow boiling heat transfer in small diameter tubes. *Advances in compact heat exchangers*, R. T. Edwards, Inc., 5:95-111, 2007.

Inasaka, F., Nariai, H. And Shimura, T. Pressure drops in subcooled flow boiling in narrow tubes. *Heat Transfer-Japanese Research*, 18:70-82, 1989.

Kadam, S.T. and Kumar R. Twenty first century cooling solution: Microchannel heat sinks. *International Journal of Thermal Sciences*, 85:73 – 92, 2014.

Kandlikar, S.G. A general correlation for saturated two-phase flow boiling heat transfer inside horizontal and vertical tubes, *Journal of Heat Transfer, Transactions of the ASME*, 112:219-228, 1990.

Kandlikar S. G. Two-phase flow patterns, pressure drop, and hear transfer during boiling in minichannel flow passages of compact evaporators. *Heat Transfer Engineering*, 23(1):5-23, 2002.

Kandlikar, S.G. and Grande, W.J. Evolution of microchannel flow passages—thermo hydraulic performance and fabrication technology. *Heat Transfer Engineering*, 25(1):3-17, 2003.

Kandlikar S. G. and Balasubramanian, P. An extension of the flow boiling correlation totransition, laminar, and deep laminar flows in minichannels and microchannels. *Heat Transfer Engineering*, 25: 86-93, 2004.

Kandlikar S. G. and Balasubramanian, P. An experimental study on the effect of gravitational orientation on flow boiling of water in 1054 x 197 μm parallel minichannels. *Transactions of ASME*, 127: 820-829, 2005.

Kandlikar, S.G. High flux heat removal with microchannels-A roadmap of challenges and opportunities. *Heat Transfer Engineering*, 26:5-14, 2005.

Kandlikar, S.G. Nucleation characteristics and stability considerations during flow boiling in microchannels. *Experimental Thermal Fluid Sciences*, 30: 441-447, 2006.

Kandlikar, S.G., Kuan, W.K., Willistein, D.A. and Borrelli, J. Stabilization of flow boiling in microchannels using pressure drop elements and fabricated nucleation sites. *Journal of Heat Transfer*, 128(4):389-396, 2006.

Kandlikar, S.G. History, Advances, and Challenges in Liquid Flow and Flow Boiling Heat Transfer in Microchannels: A Critical Review. *ASME Journal of Heat Transfer*, 134:034001-1-15, 2012.

Karayiannis, T.G., Shiferaw, D. and Kenning, D.B.R. Flow boiling in small-to-micro-diameter tubes: experimental results and modelling. *ECI International Conference on Heat Transfer and Fluid Flow in Microscale*, 21-26, 2008.

Karayiannis, T.G., Shiferaw D., Kenning, D.B.R. and Wadekar, V.V. Flow pattern and heat transfer for flow boiling in small to micro diameter tubes, *Heat Transfer Engineering*, 31(4):257 – 275, 2010.

Karayiannis, T.G., Mahmoud, M.M. and Kenning, D.B.R. A study of discrepancies in flow boiling results in small to microdiameter metallic tubes, *Experimental Thermal and Fluid Science*, 36:126-142, 2012.

Kawahara, A., Chung, P.M-Y. and Kawaji, M. Investigation of two-phase flow patterns, void fraction and pressure drop in a micro-channel. *International Journal Multiphase Flow*, 28(9):1411–1435, 2002.

Kays, W.M. and London, A.L. *Compact Heat Exchangers*. reprint *3rd edition Krieger Publishing*, Malabara, FL, USA, 1998.

Kennedy, J.E., Roach Jr., G.M., Dowling, M.E., Dowling, Abdel- Khalik, S.I., Ghiaasiaan, S.M., Jeter, S.M. and Qureshi, Z.H. The onset of flow instability in uniformly heated horizontal microchannels, *ASME Journal of Heat Transfer*, 122:118–125, 2000.

Kew, P.A. and Cornwell, K. Correlations for the prediction of boiling heat transfer in small diameter channels. *Applied Thermal Engineering*, 17(8-10):705-715, 1997.

Keyes, R.W. Physical limits and digital electronics. *Proceedings of the IEEE*, 63:740–767, 1975.

Kosar, A., Kuo, C.J. and Peles, Y. Boiling heat transfer in rectangular microchannels with reentrant cavities. *International Journal of Heat and Mass Transfer*, 48:4867-4886, 2005.

Kosar, A., Kuo, C.J. and Peles, Y. Suppression of boiling flow oscillations in parallel microchannels by inlet restrictors. *Journal of Heat Transfer*, 128(3):251-260, 2006.

Kuan, W.K. and Kandlikar, S.G. Experimental study on the effect of stabilization on flow boiling heat transfer in microchannels. *Heat Transfer Engineering*, 28(8-9):746-752, 2007.

Kuo, C.-J. and Peles, Y. Flow boiling instabilities in microchannels and means or mitigation by reentrant cavities. *Journal of Heat Transfer*, 130, 2008.

Kuo, C.-J. and Peles, Y. Presssure effects on flow boiling instabilities in parallel microchannels. *International Journal of Heat and Mass Transfer*, 52:271-280, 2009.

Lazarek, G.M. and Black, S.H. Evaporative heat transfer, pressure drop and critical heat flux in a small vertical tube with R-113, *International Journal of Heat and Mass Transfer*, 25(7):945-960, 1982.

Lee, P-S., Garimella, S.V. and Liu, D. Investigation of heat transfer in rectangular microchannels. *International Journal of Heat and Mass Transfer*, 48:1688 – 1704, 2005.

Lee, J. and Mudawar, I. Two-phase flow in high heat flux microchannel heat sink for refrigeration cooling applications: Part II-heat transfer characteristics. *International Journal of Heat and Mass Transfer*, 48:941-955, 2005a.

Lee, J. and Mudawar, I. Two-phase flow in high-heat-flux micro-channel heat sink for refrigeration cooling applications: Part I - Pressure drop characteristics. *International Journal of Heat and Mass Transfer*, 48(5):928-940, 2005b.

Lee, P.-S. and Garimella, S.V. Saturated flow boiling heat transfer and pressure drop in silicon microchannel arrays. *International Journal of Heat and Mass Transfer*, 51(3-4):789-806, 2008.

Lee, J. and Mudawar, I. Fluid flow and heat transfer characteristics of low temperature two – phase micro – channel heat sink – part1: experimental methods and flow visualization results. *International Journal of Heat and Mass Transfer*, 51:4315 – 4326, 2008.

Lee, J. and Mudawar, I. Low-temperature two phase microchannel cooling for high heat flux thermal management of defence electronics. *IEEE Transactions on Components and Packaging Technologies*, 32(2):453-465, 2009.

Lee, H.J., Liu, D.Y. and Alyousef Y. and Yao, S – C. Generalized two – phase pressure drop and heat transfer correlations in evaporative micro/mini – channels. *Journal of Heat Transfer*, 132:041004-1 – 041004 – 9, 2010.

Li, W. and Wu, Z. A general correlation for evaporative heat transfer in micro/mini-channels. *International Journal of Heat and Mass Transfer*, 53:1778 – 1787, 2010a.

Li, W. and Wu, Z. A general correlation for adiabatic two – phase pressure drop in micro/mini – channels. *International Journal of Heat and Mass Transfer*, 53:2732 – 2739, 2010b.

Lim, T-W., You, W-S., Choi, J-H. and Kim H-S. Experimental investigation of heat transfer in two phase flow boiling, *Experimental Heat Transfer*, 28:23-36, 2015.

Lin, S., Kew, P.A. and Cornwell, K. Flow boiling of refrigerant R141b in small tubes. *Chemical Engineering Research and Design*, 79(4):417-424, 2001.

Liu, Z. and Winterton, R.H.S. A general correlation for saturated and subcooled flow boiling in tubes and annuli, based on a nucleate pool boiling equation. *International Journal of Heat Mass Transfer*, 34:2759-2766, 1991.

Liu, D., Lee, P-S. and Garimella, S.V. Prediction of the onset of nucleate boiling in microchannel flow. *International Journal Heat Mass Transfer,* 48:5134- 5149, 2005.

Liu, G., Xu., J., Yang, Y. and Zhang, W. Active control of flow and heat transfer in silicon microchannels. *Journal of Micromechanical Microengineering*, 20:1-16, 2010.

Liu, D., Weng, X. and Xu, X. Experimental study on the heat transfer coefficient of water flow boiling in mini/microchannels. *Experimental Thermal and Fluid Science,* 35(7):1392-1397, 2011.

Lockhart, R.W. and Martinelli, R.C. Proposed correlation of data for isothermal two-phase two-component flow in pipes. *Chemical Engineering Progress*, 45-39, 1949.

Mahmoud, M.M. Flow boiling of R134a in vertical mini-diameter tubes. PhD thesis, Brunel University London, London, UK, 2011.

Mandhane, J.M., Gregory, G.A. and Aziz, K. A flow pattern map for gas-liquid flow in horizontal pipes. *Chemical Enginerring Progress*, 56:39-48, 1974.

Maranzana, G., Perry, I. and Maillet, D. Mini and microchannels: influence of axial conduction in the walls. *International Journal of Heat and Mass Transfer*, 47:3993–4004, 2004.

Markal, B., Aydin, O. and Avci, M. Effect of aspect ratio on saturated flow boiling in microchannels. *International Journal of Heat and Mass Transfer*, 93:130 – 143, 2016.

Martín-Callizo, C., Ali, R. and Palm, B. New experimental results on flow boiling of R-134a in a vertical microchannel. *UK Heat Transfer Conference Proceedings*, Edinburgh 10-11 September, 2007a.

Martín-Callizo, C., Palm, B., and Owhaib, W. Subcooled flow boiling of R134a in vertical channels of small diameters. *International Journal of Multiphase Flow*, 33:822 – 832, 2007b.

McNeil, D.A., Raeisi, A.H. and Kew, P.A. Flow boiling heat-transfer in micro to macro transition flows. *International Journal of Heat and Mass Transfer*, 65:289-307, 2013.

Megahed, A. and Hassan, I. Two-phase pressure drop and flow visualization of FC-72 in a silicon microchannel heat sink. *International Journal Heat and Fluid Flow*, 30:1171-1182, 2009.

Mehendale, S.S., Jacobi, A. M. and Shah, R. K. Fluid flow and heat transfer at micro- and meso-scales with application to heat exchanger design. *Applied Mechanics Reviews*, 53(7):175–193, 2000.

Mirmanto, M. Single-phase flow and flow boiling of water in horizontal rectangular microchannels. PhD thesis, Brunel University London, London, UK, 2012.

Mishima, K. and Hibiki, T. Some characteristics of air-water two-phase flow in small diameter vertical tubes. *International Journal of Multiphase Flow*, 22(4):703-712, 1996.

Missaggia, L.J., Walpole, J.N., Liau, Z.L. and Phillips, R.J. Microchannel heat sinks for two-dimensional high-power-density diode laser arrays. *IEEE Journal of Quantum Electronics*, 25 (9):1988-1992, 1989.

Moriyama, K., Inoue, A. and Ohira, H. The thermohydraulic characteristics of two-phase flow in extremely narrow channels: The frictional pressure drop and heat transfer of boiling two-phase flow, analytical model. *Transactions of the Japan Society of Mechanical Engineers Series B*, 58(546):393–400, 1992.

Mortada, S., Zoughaib, A., Arzano-Daurelle, C. and Clodic, D. Boiling heat transfer and pressure drop of R-134a and R-134yf in minichannels for low mass fluxes, *International Journal of Refrigeration*, 35(4):962-973, 2012.

Mosyak, A., Rodes, L. and Hetsroni, G. Boiling incipience in parallel micro-channels with low mass flux subcooled water flow. *International Journal of Multiphase Flow*, 47:150-159, 2012.

Natrajan, V.K. and Christensen, K.T. The impact of surface roughness on flow through a rectangular microchannel from the laminar to turbulent regimes. *Microfludics and Nanofluidics*, 9(1):95-121, 2010.

Ong, C.L. and Thome, J.R. Flow boiling heat transfer of R134a, R236fa and R245fa in a horizontal 1.030 mm circular channel. *Experimental Thermal and Fluid Science*, 33(4):651-663, 2009.

Özdemir, M.R., Mahmoud, M.M. and Karayiannis, T.G. Flow boiling heat transfer in a rectangular copper microchannel. *International Conference on Advances in Mechanical Engineering*, Istanbul, 2015.

Peng, X.F. Peterson, G.P. Convective heat transfer and flow friction for water flow in microchannel structures. *International Journal of Heat and Mass Transfer*, 39:2599–2608, 1996.

Peng, X.F. and Wang, B.X. Forced convection and boiling characteristics in microchannel. *Proceedings of 11th IHTC*, 1:371 – 390, 1998.

Petty, M.C. *Molecular electronics from principles to practice*. *John Wiley & Sons*, London, UK, 2007.

Petukhov, B.S. and Popov, V.N. Theoretical calculation of heat exchange in turbulent flow in tubes of an incompressible flow with variable physical properties. *High Temp.*, 1(1):69-83, 1963.

Pfund, D., Rector, D., Shekarriz, A., Popescu, A. and Welty, J. Pressure drop measurements in a microchannel, *AIChE Journal*, 46(8):1496–1507, 2000.

Phillips, R.J. Forced convection, Liquid Cooled, Microchannel Heat sinks. MSc thesis, Massachusetts Institute of Technology, Cambridge, USA, 1987.

Phillips, R.J. Microchannel heat sinks, *Advances in Thermal Modelling of Electronic Components and Systems*, 2:109 – 184, 1990.

Piasecka M., Hoejowska, S. and Poniewski, M.E. Experimental evaluation of flow boiling incipience of subcooled fluid in a narrow channel. *International Journal of Heat and Fluid Flow*, 25:159-172, 2004.

Piasecka M. and Poniewski, M.E. Influence of selected parameters on boiling heat transfer in Minichannels. *Proceedings of the 2nd International Conference on Microchannels and Minichannels*, 515-522, 2004.

Pop, E. and Goodson, K.E. Thermal phenomena in nanoscale transistors. *Journal of Electronic Packaging*, 128:102 – 108, 2006.

Qi, S.L., Zhang, P., Wang, R.Z. and Xu, L.X. Flow boiling of liquid nitrogen in micro-tubes: Part I - The onset of nucleate boiling, two-phase flow instability and two-phase flow pressure drop. *International Journal of Heat and Mass Transfer*, 50(25-26):4999-5016, 2007.

Qu, W. and Mudawar, I. Experimental and numerical study of pressure drop and heat transfer in a single-phase micro-channel heat sink. *International Journal of Heat and Mass Transfer*, 45(12):2549-2565, 2002a.

Qu, W. and Mudawar, I. Prediction and measurement of incipient boiling heat flux in microchannel heat sinks. *International Journal Heat and Mass Transfer*, 45:3933-3945, 2002b.

Qu, W. and Mudawar, I. Flow boiling heat transfer in two-phase microchannel heat sinks-I. Experimental investigation and assessment of correlation methods. *International Journal of Heat and Mass Transfer*, 46:2755 – 2771, 2003a.

Qu, W. and Mudawar, I. Measurement and prediction of pressure drop in two-phase micro-channel heat sinks. *International Journal of Heat and Mass Transfer*, 46(15):2737-2753, 2003b.

Qu, W. and Mudawar, I. Flow boiling heat transfer in two phase microchannel heat sinks – II. Annular two phase flow model. *International Journal Heat and Mass Transfer*, 46:2773-2784, 2003c.

Qu, W., Yoon, S-M. and Mudawar, I. Two-phase flow and heat transfer in rectangular microchannels. *Journal of Electronic Packaging*, 126(3):288-300, 2004.

Qu, W. and Mudawar, I. Transport phenomena in two-phase micro-channel heat sinks. *Journal of Electronic Packaging*, 126:213–224, 2004.

Revellin, R. and Thome, J.R. Experimental investigation of R134a and R245fa two-phase flow in microchannels for different flow conditions. *International Journal of Heat and Fluid Flow*, 28(1):63-71, 2007.

Ribatski, G., Wojtan, L. and Thome, J. R. An analysis of experimental data and prediction methods for two-phase frictional pressure drop and flow boiling heat transfer in micro-scale channels. *Experimental Thermal and Fluid Science*, 31:1-19, 2006.

Ribatski, G. A critical overview on the recent literature concerning flow boiling and two-phase flows inside micro-scale channels. *Experimental Heat Transfer*, 26:198-246, 2013.

Rosa, P., Karayiannis, T.G. and Collins, M.W. Single-phase heat transfer in microchannels: the importance of scaling effects. *Applied Thermal Engineering*, 29(17-18):3447-3468, 2009.

Ruspini, L.C., Marcel, C.P. and Clausse, A. Two-phase flow instabilities: A review. *International Journal of Heat and Mass Transfer*, 71:521-548, 2014.

Sahar, A.M., Mahmoud, M.M., Wissink, J. and Karayiannis, T.G. Effect of hydraulic diameter and aspect ratio on single phase flow and heat transfer in a rectangular microchannel. *15th UK Heat Transfer Conference*, 7-8 September 2015, Edinburgh, UK.

Saitoh, S., Daiguji, H. Hihara, E. Effect of tube diameter on boiling heat transfer of R134a in horizontal small-diameter tubes. *International Journal of Heat Mass Transfer*, 48:4973-4984, 2005.

Sato, T. and Matsumura, H. On the conditions of incipient subcooled boiling and forced convection, *Bulletin of Japan Society of Mechanical Engineers*, 7:392-398, 1963.

Shah, R.K. A correlation for laminar hydrodynamics entry length solution for circular and non circular ducts. *Journal of Fluids Engineering*, 100:177-179, 1978.

Shah, R.K. and London, A.R. *Laminar flow forced convection in ducts*. *Oxford Academic Press*, New York, USA, Supplement 1 to Advances Heat Transfer, 1978.

Shah, M.M. Chart correlation for saturated boiling heat transfer: equations and further study. *ASHRAE transactions*, 88(1):185-196, 1982.

Shah, R.K. and Bhatti, M.S. Laminar convective heat transfer in ducts, in *Handbook of Single – Phase Convective Heat Transfer*, Kakaç, S., Shah, R.K.and Aung, W., eds., Wiley, New York, Chapter 3.

Sharp, K.V. and Adrian, R.J. Transition from laminar to turbulent flow in liquid filled microtubes. *Experiments in Fluids*, 36(5):741-747, 2004.

Shen, S., Xu, J.L., Zhou, J.J. and Chen, Y. Flow and heat transfer in microchannels with rough wall surface. *Energy Conversion and Management*, 47:1311–1325, 2006.

Shuai, J., Kulenovic, R. and Groll, M. Heat transfer and pressure drop for flow boiling of water in narrow vertical rectangular channels. *International Conference on Microchannels and Minichannels*, 1: 667 – 673, 2003.

Singh, S.G., Kulkarni, A., Duttagupta, S.P., Puranik, B.P. and Agrawal, A. Impact of aspect ratio on flow boiling of water in rectangular microchannels. *Experimental Thermal and Fluid Science*, 33:153 – 160, 2008.

Sobierska, E., Kulenovic, R., Mertz, R. And Groll, M. Experimental results of flow boiling of water in a vertical microchannel. *Experimental Thermal and Fluid Science*, 31(2):111-119, 2006.

Soupremanien, U., Le Person, S., Favre-Marinet, M. Bultel, Y. Influence of the aspect ratio on boiling flows in rectangular mini-channels. *Experimental Thermal and Fluid Science*, 35:797-809, 2011.

Steinke, M.E. and Kandlikar, S.G. An experimental investigation of flow boiling characteristics of water in parallel microchannels. *ASME Journal of Heat Transfer*, 126:518-526, 2004a.

Steinke, M.E. and Kandlikar, S.G. Control and effect of dissolved air in water during flow boiling in microchannels. *International Journal of Heat and Mass Transfer*, 47:1925-1935, 2004b.

Steinke, M.E. and Kandlikar, S.G. Single-phase liquid friction factors in microchannels. *International Journal of Thermal Sciences*, 45(11):1073-1083, 2006.

Sun, L. and Mishima, K. Evaluation analysis of prediction methods for two-phase flow pressure drop in mini-channels. *International Journal of Multiphase Flow*, 35(1):47-54, 2009.

Suo, M. and Griffith, T. Two-phase flow in capillary tubes. *Journal Basic Engineering*, 86:576-582, 1964.

Taitel, Y. and Dukler, A.E. A model for predicting flow regime transitions in horiozontal and near horizontal gas-liquid flow. *AIChE Journal*, 22:47-55, 1976.

Taitel, Y., Barnea, D. and Dukler, A.E. Modelling flow pattern transition for gas-liquid transitions for steady upward gas-liquid flow in vertical tubes. *AIChE Journal*, 26(3):345-354, 1980.

Thome J.R. Boiling in microchannels: a review of experiment and theory. *International Journal of Heat and Fluid Flow*, 25(2):128-139, 2004.

Thome, J.R. and Dupont, V. Heat transfer assembly. *European Patent EP 1779052B1*, 2007.

Tong, W., Bergles, A.E.and Jensen, M.K. Pressure drop with highly subcooled flow boiling in small-diameter tubes. *Experimental Thermal and Fluid Science*, 15:202–212, 1997.

Tran, T.N., Wambsganss, M.W. and France, D.M. Small circular- and rectangular-channel boiling with two refrigerants. *International Journal of Multiphase Flow*, 22(3):485-498, 1996.

Tran, T.N., Chyu, M.C.Wambsganss, M.W. and France, D.M. Two phase pressure drop of refrigerant during flow boiling in small channels: an experimental investigation and correlation development. *International Journal of Multiphase Flow*, 26:1739-1754, 2000.

Triplett, A.K., Ghiaasiaan, S.M., Abdel-Khalik, S.I. and Sadowski, D.L.. Gas-liquid two-phase flow in microchannels Part I: Two-phase flow patterns. *International Journal of Multiphase Flow*, 25:377-394, 1999.

Tuckerman, D.B. and Pease, R.F.W. High performance heat sink for VLSI. *IEEE Electronic Device Letters*, 2:126-129, 1981.

Tuo, H. and Hrnjak, P. New approach to improve performance by venting periodic reverse flow in microchannel evaporator. *International Journal of Refrigeration*, 36:2187-2195, 2013.

Wang, G., Cheng, P. and Wu, H. Unstable and stable flow boiling in parallel microchannels and in a single microchannel. *International Journal of Heat and Mass Transfer*, 50(21-22):4297-4310, 2007.

Wang, G., Cheng, P. and Bergles, A.E. Effects of inlet/outlet configurations of flow boiling instability in parallel microchannels. *International Journal of Heat and Mass Transfer*, 51:2267-2281, 2008.

Wang, Y. and Sefiane, K. Effects of heat flux, vapour quality, channel hydraulic diameter on flow boiling heat transfer in variable aspect ratio micro-channels using transparent heating. *International Journal of Heat and Mass Transfer*, 55:2235-2243, 2012.

Wang, C., Wang. H., Wang, S. and Gao, P. Experimental study of boiling incipience in vertical narrow rectangular channel. *Annals of Nuclear Energy*, 66:152-160, 2014.

Warrier, G. R., Dhir, V.K. and Momoda, L.A. Heat transfer and pressure drop in narrow rectangular channels, *Experimental Thermal and Fluid Science*, 26:53-64, 2002.

Watel, B. Review of saturated flow boiling in small passages of compact heat exchangers. *International Journal of Thermal Sciences*, 42:107 – 140, 2003.

Wen, D.S., Yan, Y. and Kenning, D.B.R. Saturated flow boiling of water in a narrow channel: time-averaged heat transfer coefficients and correlations. *Applied Thermal Engineering*, 24:1207-1223, 2004.

Wibel, W. and Ehrhard, P. Experiments on the Laminar/Turbulent transition of liquid flows in rectangular microchannels. *Heat Transfer Engineering*, 30(1-2):70-77, 2009.

Wu, H.Y. and Cheng, P. Visualization and measurement of periodic boiling in silicon microchannels. *International Journal of Heat and Mass Transfer*, 46:2603-2614, 2003.

Wu, H.Y. and Cheng, P. Boiling instability in parallel silicon microchannels at different heat flux. *International Journal of Heat and Mass Transfer*, 47:3631-3641, 2004.

Xu, J.L., Cheng, P., and Zhao, T.S. Gas-liquid two phase flow regimes in rectangular channels with mini/micro gaps. *International Journal of Multiphase flow*, 25(3):411 – 432, 1999.

Xu, B., Ooti, K.T., Wong, N.T. and Choi, W.K. Experimental investigation of flow friction for liquid flow in microchannels. *International Communications in Heat and Mass Transfer*, 27(8):1165–1176, 2000.

Xu, J.L., Zhou, J.J. and Gan, Y.H. Static and dynamic flow instability of a parallel microchannel heat sink at high heat flux. *Energy Conversion and Management*, 46:313-334, 2005.

Xu, J., Liu, G., Zhang, W., Li, Q. and Wang, B. Seed bubbles stabilize flow and heat transfer in parallel microchannels. *International Journal of Multiphase Flow*, 35:773-790, 2009.

Xu, S., Guo, Z., Hu, G., Chen, W., Lewis, R. and Wong, C-N. Thermal and flow fields in single board computer cabin systems using CFD analysis. *Engineering Applications of Computational Fluid Mechanics*, 8(4):574 – 585, 2014.

Yen, T-H., Shoji, M., Takemura, F., Suzuki, Y. and Kasagi, N. Visualization of convective boiling heat transfer in single microchannels with different shaped cross-sections. *International Journal of Heat and Mass Transfer*, 49:3384-3394, 2006.

Yu, W., France, D. M , Wambsganss, M.W. and Hull, J.R. Two-phase pressure drop, boiling heat transfer, and critical heat flux to water in a small-diameter horizontal tube. *International Journal of Multiphase Flow*, 28:927 – 941, 2002.

Yun, R., Heo, J.Y. and Kim, Y. Evaporative heat transfer and pressure drop of R410A in microchannels. *International Journal of Refrigeration*, 29:92 – 100, 2006.

Zhang, M. and Webb, R.L. Correlation of two-phase friction for refrigerants in small-diameter tubes. *Experimental Thermal Fluid Science*, 25:131-139, 2001.

Zhang, T., Tong, T., Chang, J.Y., Peles, Y., Prasher, R., Jensen, M.K., Wen, J.T. and Phelan, P. Ledinegg instability in microchannels. *International Journal of Heat and Mass Transfer*, 52:5661-5674, 2009.

Zhang, W., Hibiki, T. and Mishima, K. Correlations of two – phase pressure drop and void fraction in mini – channel. *International Journal of Heat and Mass Transfer*, 53: 453 – 465, 2010.

Zhang, J., Diao, Y., Zhao, Y. and Zhang, Y. An experimental study of the characteristics of fluid flow and heat transfer in the multiport microchannel flat tube. *Applied Thermal Engineering*, 65:209-218, 2014.

Zhao, T.S. and Bi, Q.C. Co-current air-water two-phase flow patterns in vertical triangular microchannels. *International Journal of Multiphase Flow*, 27:765-782, 2001.

Zhou P., Hom J., Upadhya G., Goodson K. and Munch M. Electro-kinetic microchannel cooling system for desktop computers. *20th IEEE SEMI-THERM Symposium*, 2004.

Appendix A

Flow Boiling Heat Transfer Correlations

Reference	Correlation	Applicability range
Shah (1982)	$h_L = 0.023 Re_L^{0.8} Pr_L^{0.4} \frac{k_L}{D}$ $N_{CO} = \left(\frac{1-x}{x}\right)^{0.8} \left(\frac{\rho_g}{\rho_L}\right)^{0.5}$ $Bo = \frac{q}{G h_{fg}}, h_{cb} = \frac{1.8}{N_{CO}^{0.8}} h_L$ For $N_{CO} > 1$: $h_{nb} = \begin{Bmatrix} 230 Bo^{0.5} & Bo > 0.0003 \\ 1 + 46 Bo^{0.5} & Bo < 0.0003 \end{Bmatrix}$ For $0.1 < N_{CO} < 1$: $h_{nb} = h_L F Bo^{0.5} \exp(2.74 N_{CO} - 0.1)$ $F = \begin{Bmatrix} 14.7 & Bo > 0.0011 \\ 15.43 & Bo < 0.0011 \end{Bmatrix}$ For $N_{CO} < 0.1$: $h_{nb} = h_L F Bo^{0.5} \exp(2.74 N_{CO} - 0.15)$ $h_{tp} = MAX(h_{cb}, h_{nb})$	Based on 780 data points.
Lazarek and Black (1982)	$h_{tp} = \frac{k_L}{D} 30 Re_L^{0.857} Bo^{0.714}$ $Re_L = \frac{G(1-x)D}{\mu_L}$	Based on 728 data points. D = 3.1 mm, R-113

<table>
<tr><td></td><td></td><td>G = 125-750 kg/m^{2}s

Re = 860-5500

P = 130-410 kPa

q” = 14-380 kW/m^2</td></tr>
<tr><td>Gungor and Winterton (1987)</td><td>$$h_{tp} = (SS_2 + FF_2)h_{sp}$$
$$S = 1 + 3000Bo^{0.86}$$
$$F = 1.12\left(\frac{x}{1-x}\right)^{0.75}\left(\frac{\rho_L}{\rho_g}\right)^{0.41}$$
$$S_2 = \begin{cases} Fr_L^{0.1-2Fr_L} \; if \; horizontal \; and \; Fr_L < 0.05 \\ 1 \qquad\qquad\qquad otherwise \end{cases}$$
$$F_2 = \begin{cases} Fr_L^{0.1-2Fr_L} \; if \; horizontal \; and \; Fr_L < 0.05 \\ 1 \qquad\qquad\qquad otherwise \end{cases}$$
$$Fr_L = \frac{G^2}{\rho_L^2 g D_h}$$</td><td>Based on 3600 data points.

Water, R-11, R-12, R-22, R-113 and R-114.

D = 2.95-32 mm

P = 8-20260 kPa</td></tr>
<tr><td>Kandlikar (1990)</td><td>$$h_L = 0.023Re_L^{0.8}Pr_L^{0.4}\frac{k_L}{D}$$
$$h_{tp} = h_L C_1 N_{CO}^{C_2}(25Fr_L)^{C_5} + C_3 Bo^{C_4} F_{fl}$$
$$N_{CO} = \left(\frac{1-x}{x}\right)^{0.8}\left(\frac{\rho_g}{\rho_L}\right)^{0.5}, F_{fl} = 1 \; for \; water$$
<table><tr><td></td><td>$N_{CO} < 0.65$</td><td>$N_{CO} > 0.65$</td></tr><tr><td>C_1</td><td>1.136</td><td>0.6683</td></tr><tr><td>C_2</td><td>-0.9</td><td>-0.2</td></tr><tr><td>C_3</td><td>667.2</td><td>1058</td></tr><tr><td>C_4</td><td>0.7</td><td>0.7</td></tr><tr><td>C_5</td><td>0.3</td><td>0.3</td></tr></table></td><td>Water, R-11, R-12, R-22, R-113, R-134a, R-152a

G = 13 to 8179 kg/m^{2}s, D = 4-32 mm.

q” = 0.3-228 kW/m^2,

Pressure: 40-6420 kPa</td></tr>
</table>

Liu and Winterton (1991)	$$h_{tp} = \sqrt{(Eh_L)^2 + \left(Sh_{coop}\right)^2}$$ $$h_L = 0.023 Re_L^{0.8} Pr_L^{0.4} \frac{k_L}{D}$$ $$h_{coop} = 55 P_r^{0.12-0.434 ln R_p} (-log P_r)^{-0.55} M^{-0.5} q^{0.67}$$ $$E = \left[1 + x Pr_L \left(\frac{\rho_L}{\rho_g} - 1\right)\right]^{0.35}$$ $$S = \frac{1}{1 + 0.055 F^{0.1} Re_L^{0.16}}$$	G = 12.4 to 8179.3 kg/m^{2}s, D = 2.95-32 mm. q" = 0.35-2620 kW/m^2, x = 0-0.948
Yu et al. (2002)	$$h_{tp} = 6.4 \times 10^6 (Bo^2 We_L)^{0.27} \left(\frac{\vartheta_g}{\vartheta_L}\right)^{-0.2}$$ $$We_L = \frac{\vartheta_L G^2 D}{\mu_L}$$	Water, G = 50 to 200 kg/m^{2}s, D = 2.98 mm. P = 200 kPa, x = 0.15-1
Kandlikar and Balasubramanian (2004)	The Kandlikar (1990) correlation was extended. For $Re < 1600$: $$h_{tp,NBD} = 0.6683 N_{CO}^{-0.2} (1-x)^{0.8} h_L + 1058 Bo^{0.7} (1-x)^{0.8} F_{fl} h_L$$ $$h_{tp,CBD} = 1.136 N_{CO}^{-0.9} (1-x)^{0.8} h_L + 667.2 Bo^{0.7} (1-x)^{0.8} F_{fl} h_L$$ $$h_{tp} = MAX\left(h_{tp,NBD}, h_{tp,CBD}\right)$$ $$h_L = \frac{Nuk_L}{D_h}$$	Range of the data in the Kandlikar (1990) correlation above.

	For $Re < 100$: $h_{tp} = h_{tp,NBD}$	
Lee and Mudawar (2005)	For $0 < x < 0.05$: $h_{tp} = 3.856X^{0.267}h_{sp}$ $h_{sp} = Nu_3 \frac{k_L}{D_h}$ for 3 sided heating $h_{sp} = Nu_4 \frac{k_L}{D_h}$ for 4 sided heating $Nu_3 = 8.235\begin{pmatrix}1 - 1.883\beta + 3.767\beta^2 - 5.814\beta^3 \\ +5.361\beta^4 - 2\beta^5\end{pmatrix}$ $X_{vv} = \left(\frac{\mu_L}{\mu_g}\right)^{0.5}\left(\frac{1-x}{x}\right)^{0.5}\left(\frac{\vartheta_L}{\vartheta_g}\right)^{0.5}$ $X_{vt} = \left(\frac{f_L Re_g^{0.25}}{0.079}\right)^{0.5}\left(\frac{1-x}{x}\right)^{0.5}\left(\frac{\vartheta_L}{\vartheta_g}\right)^{0.5}$ $Re_g = \frac{GxD_h}{\mu_g}$ For $0.05 < x < 0.55$: $h_{tp} = 436.48X^{0.665}h_{sp}Bo^{0.522}We_L^{0.351}$ For $0.55 < x$: $h_{tp} = MAX\left(108.6X^{1.665}h_{sp}, h_{sp}\right)$	Water, R-134a D_h = 0.35 mm
Sun and Mishima (2009)	$h_{tp} = \frac{6Re_L^{1.05}Bo^{0.54}k_L}{We_L^{0.191}\left(\rho_L/\rho_g\right)^{0.142}D_h}$	Based on 2505 data points. 11 fluids including water.

		D_h = 0.21-6.05 mm.
Li and Wu (2010)	$$h_{tp} = 334Bo^{0.3}(BdRe_L^{0.36})^{0.4}\frac{k_L}{D_h}$$ $$Bd = \frac{g\Delta\rho D_h^2}{\sigma}$$	Based on 3744 data points. 12 different fluids including water. D_h = 0.148-3.25 mm.
Mahmoud and Karayiannis 1 (2011)	For $x \leq 0.3$: $$h_{tp} = 3414\frac{Bo^{0.625}We_L^{0.2}Re_L^{0.1}}{Co^{0.6}}\frac{k_L}{D}$$ For $0.3 < x$: $$h_{tp} = 5324\left[\frac{Bo^{0.3}We_L^{0.25}}{N_{CO}^{0.25}}\right]^{1.79}\frac{k_L}{D}$$	Based on 8561 data points. R-134a. G = 100 to 500 kg/m^{2}s, D =0.52-4.26 mm. P = 600-1400 kPa
Mahmoud and Karayiannis 2 (2011)	$$h_{tp} = S_{new}h_{cooper} + F_{new}h_{sp}$$ $$h_{cooper} = 55\,\mathrm{Pr}^{(0.12-0.4343\ln e)}(-\log \mathrm{Pr})^{-0.55}MW^{-0.5}q''^{0.67}$$ $$h_{sp} = \begin{cases} 4.36\frac{k_L}{D_h}\, when\, \mathrm{Re}_L < 2000 \\ 0.023\,\mathrm{Re}_L^{0.8}\frac{k_L}{D_h}\, when\, \mathrm{Re}_L > 3000 \end{cases}$$ $$\mathrm{Re}_L = \frac{(1-x)GD_h}{\mu_L}$$	Range of the data in the Mahmoud and Karayiannis 1 (2011) correlation above.

	$F_{new} = (1 + \frac{2.812 Co^{-0.408}}{X})^{0.64}$ $S_{new} = \frac{1}{1 + 2.56 \times 10^{-6} (\mathrm{Re}_L F_{new}^{1.25})^{1.17}}$	
Lim et al. (2015)	$h_{tp} = \frac{Re^{0.196} k_L}{Bo^{0.117} C_{FR}^{0.42} D_h}$ $C_{FR} = 0.4905 + Fr_L(1 - x^{3.134})$	Water, G = 200 to 600 kg/m^{2}s, D_h =0.5 mm. P =110-170 kPa q" = 100-400 kW/m^2 x = 0-0.2

Appendix B

Two – Phase Pressure Drop Correlations

Reference	Correlation	Applicability range
Lockhart - Martinelli (1949)	$\Delta P_a = \frac{G^2}{\rho_L}\left[\frac{x_e^{\,2}}{\alpha_e}\frac{\rho_L}{\rho_g}+\frac{(1-x_e)^2}{(1-\alpha_e)}-1\right]$ $\alpha_e = \frac{1}{1+0.28X_M}$ $X_M = \left(\frac{1-x_e}{x_e}\right)^{0.64}\left(\frac{\rho_g}{\rho_L}\right)^{0.36}\left(\frac{\mu_L}{\mu_g}\right)^{0.07}$ $\Delta P_f = \frac{L_{tp}}{x_e}\int_0^{x_e}\frac{2f_L G^2}{D_h\rho_L}\phi_L^2 dx$ $\phi_L^2 = 1+\frac{C}{X}+\frac{1}{X^2}$ $X = \left(\frac{f_L}{f_g}\right)^{0.5}\left(\frac{\rho_g}{\rho_L}\right)^{0.5}\left(\frac{1-x_e}{x_e}\right)$ C = 5 for laminar liquid – laminar gas flow C = 12 for laminar liquid – turbulent gas flow C = 10 for turbulent liquid – laminar gas flow C = 20 for turbulent liquid – turbulent gas flow	D = 1.5-25.8 mm, Water, Benzene, Kerosene and various Oils.
Homogenous flow model, Collier and Thome (1994)	$\Delta P_a = \frac{G^2}{\rho_{LG}}x_e$ $\Delta P_f = \frac{2f_L L_{tp} G^2}{D_h\rho_L}\left[1+\frac{x_e}{2}\left(\frac{\rho_L}{\rho_{Lg}}\right)\right]$ $f_L = 0.003$	Steam-water, laminar and turbulent, circular horizontal channels. x = 0.01-1. $\dot{m} = 1.9\times10^{-3} - 51.1\times10^{-3}$ kg/s.

Mishima and Hibiki (1996)	$\Delta P_a = \frac{G^2}{\rho_L}\left[\frac{x_e^{\,2}}{\alpha_e}\frac{\rho_L}{\rho_g}+\frac{(1-x_e)^2}{(1-\alpha_e)}-1\right]$ $\alpha_e = \frac{1}{1+0.28X_M}$ $X_M = \left(\frac{1-x_e}{x_e}\right)^{0.64}\left(\frac{\rho_g}{\rho_L}\right)^{0.36}\left(\frac{\mu_L}{\mu_g}\right)^{0.07}$ $\Delta P_f = \frac{L_{tp}}{x_e}\int_0^{x_e}\frac{2f_L G^2}{D_h\rho_L}\phi_L^2 dx$ $\phi_L^2 = 1+\frac{C}{X}+\frac{1}{X^2}$ $X = \left(\frac{f_L}{f_g}\right)^{0.5}\left(\frac{\rho_g}{\rho_L}\right)^{0.5}\left(\frac{1-x_e}{x_e}\right)$ $C = 21(1-e^{0.319D_h})$	D = 1.05-4 mm, Air-water, horizontal and vertical rectangular channels and tubes. Re_g = 177-9580. Re_L = 542-3720.
Yu et al. (2002)	$\Delta P_a = \frac{G^2}{\rho_L}\left[\frac{x_e^{\,2}}{\alpha_e}\frac{\rho_L}{\rho_g}+\frac{(1-x_e)^2}{(1-\alpha_e)}-1\right]$ $\alpha_e = \left[1+\left(\frac{1-x_e}{x_e}\right)\left(\frac{\rho_g}{\rho_L}\right)^{0.67}\right]^{-1}$ $\Delta P_f = \frac{L_{tp}}{x_e}\int_0^{x_e}\frac{2f_L G^2}{D_h\rho_L}\phi_L^2 dx$ $\phi_L^2 = \frac{1}{X^{1.9}}$ $X = \left(\frac{f_L}{f_g}\right)^{0.5}\left(\frac{\rho_g}{\rho_L}\right)^{0.5}\left(\frac{1-x_e}{x_e}\right)$ $f_g = \frac{0.046}{\mathrm{Re}_g^{0.2}}, \mathrm{Re}_g = \frac{Gx_eD_h}{\mu_g}$	D = 2.98 mm, Water, horizontal pipe. G = 50-200 kg/m^{2}s, x_e = 0.15-1, P = 198 kPa

Warrier et al. (2002)	$\Delta P_a = \frac{G^2}{\rho_L}\left[\frac{x_e^{\,2}}{\alpha_e}\frac{\rho_L}{\rho_g}+\frac{(1-x_e)^2}{(1-\alpha_e)}-1\right]$ $\alpha_e = \frac{1}{1+0.28X_M}$ $X_M = \left(\frac{1-x_e}{x_e}\right)^{0.64}\left(\frac{\rho_g}{\rho_L}\right)^{0.36}\left(\frac{\mu_L}{\mu_g}\right)^{0.07}$ $\Delta P_f = \frac{L_{tp}}{x_e}\frac{2f_{LO}G^2}{D_h\rho_L}\int_0^{x_e}\phi_{LO}^2 dx$ $\phi_L^2 = 1+\frac{C}{X}+\frac{1}{X^2}$ $C = 38$ $X = \left(\frac{f_L}{f_g}\right)^{0.5}\left(\frac{\rho_g}{\rho_L}\right)^{0.5}\left(\frac{1-x_e}{x_e}\right)$ $\phi_{LO}^2 = \phi_L^2\left(\frac{f_L}{f_{LO}}\right)(1-x_e)^2$ $\mathrm{Re}_{LO} = \frac{GD_h}{\mu_L}$	D_h = 0.75 mm, FC-84, rectangular channel
Qu and Mudawar (2003b)	$\Delta P_a = \frac{G^2}{\rho_L}\left[\frac{x_e^{\,2}}{\alpha_e}\frac{\rho_L}{\rho_g}+\frac{(1-x_e)^2}{(1-\alpha_e)}-1\right]$ $\alpha_e = \left[1+\frac{1-x_e}{x_e}\left(\frac{\rho_g}{\rho_L}\right)^{0.67}\right]^{-1}$ $\Delta P_f = \frac{L_{tp}}{x_e}\int_0^{x_e}\frac{2f_L G^2}{D_h\rho_L}\phi_L^2 dx$ $\phi_L^2 = 1+\frac{C}{X_{vv}}+\frac{1}{X_{vv}^{\,2}}$ $C = 21(1-e^{-319D_h})(0.00418G+0.0613)$ $X_{vv} = \left(\frac{\mu_L}{\mu_g}\right)^{0.5}\left(\frac{\rho_g}{\rho_L}\right)^{0.5}\left(\frac{1-x_e}{x_e}\right)^{0.5}$	D_h = 0.35 mm, Water, rectangular channel G = 135-402 kg/m^{2}s q” = 40-130 W/cm^2

Lee and Garimella (2008)	$\Delta P_a = \frac{G^2}{\rho_L}\left[\frac{x_e^{\,2}}{\alpha_e}\frac{\rho_L}{\rho_g}+\frac{(1-x_e)^2}{(1-\alpha_e)}-1\right]$ $\alpha_e = \left[1+\frac{1-x_e}{x_e}\left(\frac{\rho_g}{\rho_L}\right)^{0.67}\right]^{-1}$ $\Delta P_f = \frac{L_{tp}}{x_e}\int_0^{x_e}\frac{2f_L G^2}{D_h\rho_L}\phi_L^2 dx$ $\phi_L^2 = 1+\frac{C}{X_{vv}}+\frac{1}{X_{vv}^{\,2}}$ $C = 2566 G^{0.5466} D_h^{0.8819}(1-e^{-319 D_h})$ $X_{vv} = \left(\frac{\mu_L}{\mu_g}\right)^{0.5}\left(\frac{\rho_g}{\rho_L}\right)^{0.5}\left(\frac{1-x_e}{x_e}\right)^{0.5}$	D_h = 0.162-0.571 mm, Water, rectangular channel. q" = 10-340 W/cm^2, x_e = 0-0.2 T_i = 90.6-95.1 ºC
Zhang et al. (2010)	$\Delta P_a = \frac{G^2}{\rho_L}\left[\frac{x_e^{\,2}}{\alpha_e}\frac{\rho_L}{\rho_g}+\frac{(1-x_e)^2}{(1-\alpha_e)}-1\right]$ $\alpha_e = \frac{1}{1+0.28X_M}$ $X_M = \left(\frac{1-x_e}{x_e}\right)^{0.64}\left(\frac{\rho_g}{\rho_L}\right)^{0.36}\left(\frac{\mu_L}{\mu_g}\right)^{0.07}$ $\Delta P_f = \frac{L_{tp}}{x_e}\int_0^{x_e}\frac{2f_L G^2}{D_h\rho_L}\phi_L^2 dx$ $\phi_L^2 = 1+\frac{C}{X}+\frac{1}{X^2}$ $X = \left(\frac{f_L}{f_g}\right)^{0.5}\left(\frac{\rho_g}{\rho_L}\right)^{0.5}\left(\frac{1-x_e}{x_e}\right)$ $C = 21(1-e^{(-0.358/La)})$ $La = [\sigma / g\Delta\rho]^{0.5} / D_h$	D_h = 0.146-6.25 mm, Horizontal and vertical, rectangular channel and tubes. $Re_f \le 2000$, $Re_g \le 2000$
Li and Wu (2010)	$\Delta P_a = \frac{G^2}{\rho_L}\left[\frac{x_e^{\,2}}{\alpha_e}\frac{\rho_L}{\rho_g}+\frac{(1-x_e)^2}{(1-\alpha_e)}-1\right]$	D_h = 0.148-3.25 mm, 12 different fluids, 769 data points.

	$\alpha_e = \frac{1}{1+0.28X_M}$ $X_M = \left(\frac{1-x_e}{x_e}\right)^{0.64}\left(\frac{\rho_g}{\rho_L}\right)^{0.36}\left(\frac{\mu_L}{\mu_g}\right)^{0.07}$ $\Delta P_f = \frac{L_{tp}}{x_e}\int_0^{x_e}\frac{2f_L G^2}{D_h\rho_L}\phi_L^2 dx$ $\phi_L^2 = 1+\frac{C}{X}+\frac{1}{X^2}$ $X = \left(\frac{f_L}{f_g}\right)^{0.5}\left(\frac{\rho_g}{\rho_L}\right)^{0.5}\left(\frac{1-x_e}{x_e}\right)$ $C = \begin{cases} 11.9Bd^{0.45} \Rightarrow Bd \le 1.5 \\ 109.4(Bd\,\mathrm{Re}^{0.5})^{-0.56} \Rightarrow 1.5 < Bd \le 11 \end{cases}$ $Bd = g\Delta\rho D_h^2/\sigma$	
Lee et al. (2010)	$\Delta P_a = \frac{G^2}{\rho_L}\left[\frac{x_e^{\,2}}{\alpha_e}\frac{\rho_L}{\rho_g}+\frac{(1-x_e)^2}{(1-\alpha_e)}-1\right]$ $\alpha_e = \frac{1}{1+0.28X_M}$ $X_M = \left(\frac{1-x_e}{x_e}\right)^{0.64}\left(\frac{\rho_g}{\rho_L}\right)^{0.36}\left(\frac{\mu_L}{\mu_g}\right)^{0.07}$ $\Delta P_f = \frac{L_{tp}}{x_e}\int_0^{x_e}\frac{2f_L G^2}{D_h\rho_L}\phi_L^2 dx$ $\phi_L^2 = 1+\frac{C}{X}+\frac{1}{X^2}$ $X = \left(\frac{f_L}{f_g}\right)^{0.5}\left(\frac{\rho_g}{\rho_L}\right)^{0.5}\left(\frac{1-x_e}{x_e}\right)$ $C = 121.6(1-e^{-22.7\,Bd})x_e^{1.85}$ $Bd = g\Delta\rho D_h^2/\sigma$	D_h < 3 mm, Water, n – pentane, ammonia, CO_2, R-410a, R-134a and R-12 .

Appendix C

Sensor Calibration Curves

1-) Thermocouple Calibration Results

The K type thermocouples which were used in the current study were calibrated against a precision thermometer (ASL F250 MKII). The thermocouples were tied to the precision thermometer and submerged in an Omega constant temperature circulating liquid bath filled with antifreeze liquid having *130 °C* boiling point. The calibration curves of the thermocouples are presented below in Fig. C.1.

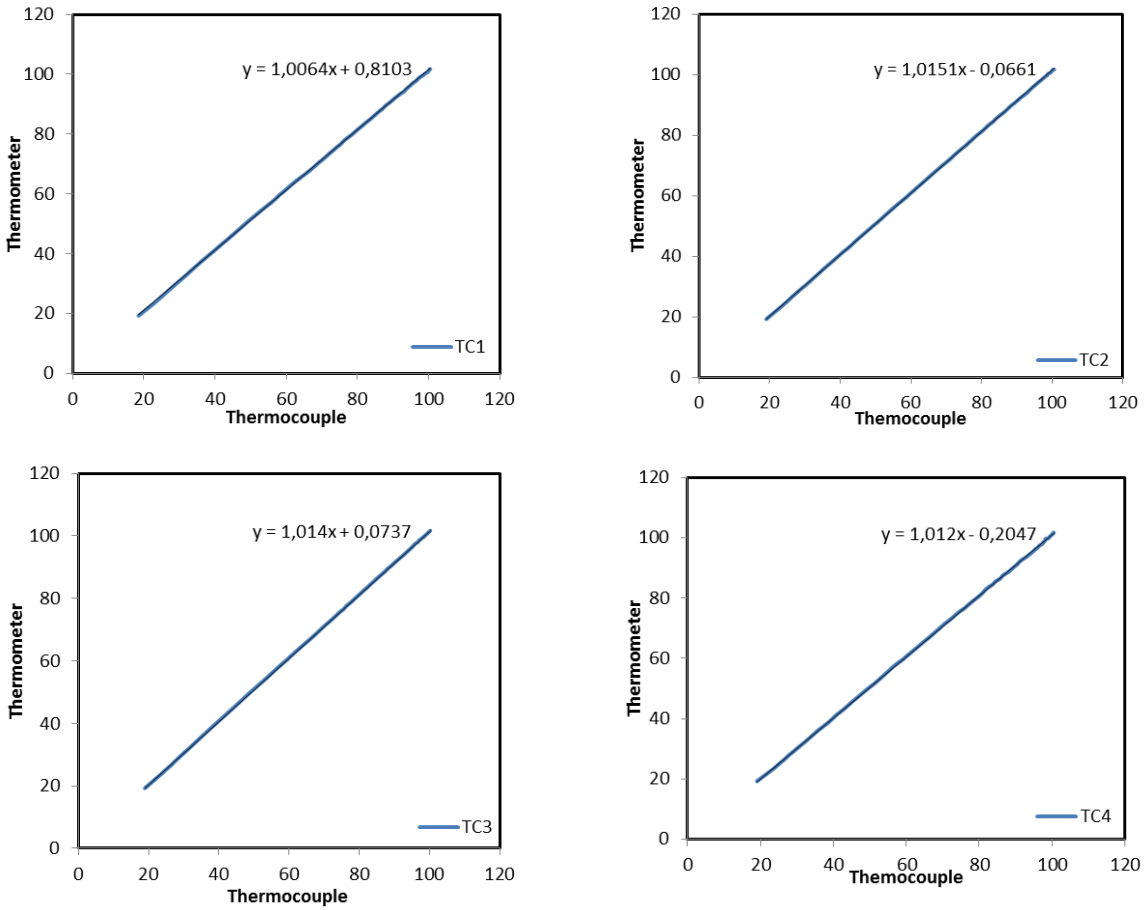

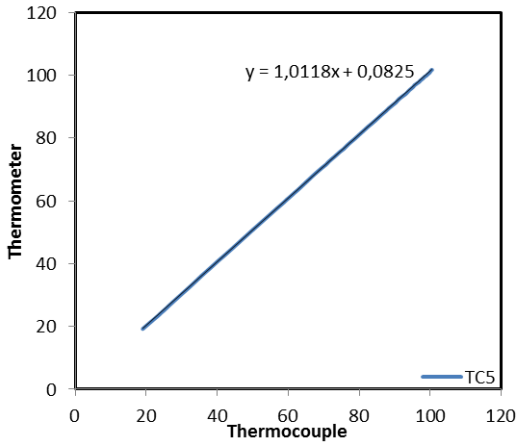
y = 1,0118x + 0,0825
Thermometer
Thermocouple
TC5

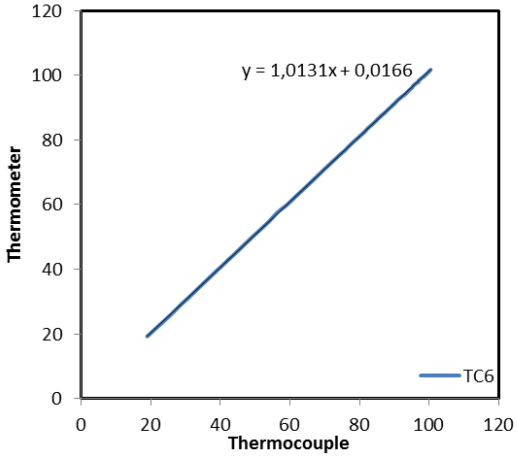
y = 1,0131x + 0,0166
Thermometer
Thermocouple
TC6

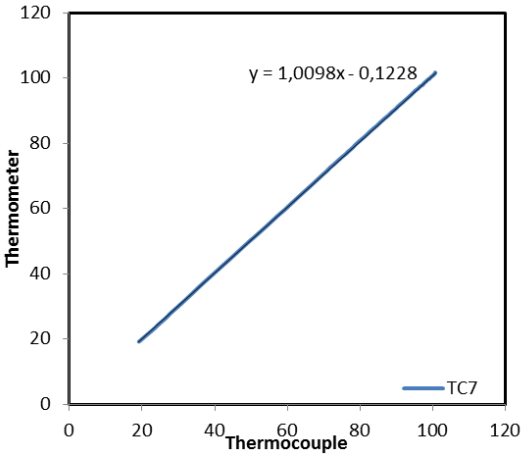
y = 1,0098x - 0,1228
Thermometer
Thermocouple
TC7

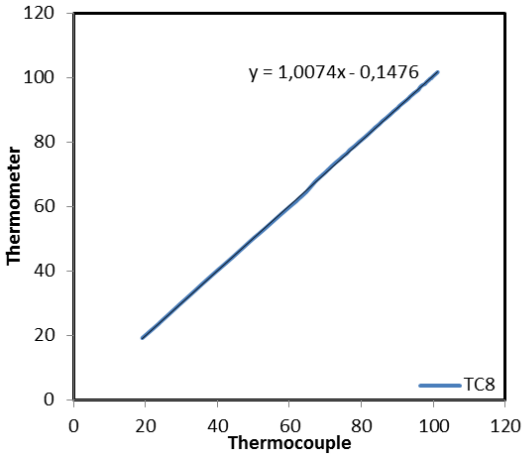
y = 1,0074x - 0,1476
Thermometer
Thermocouple
TC8

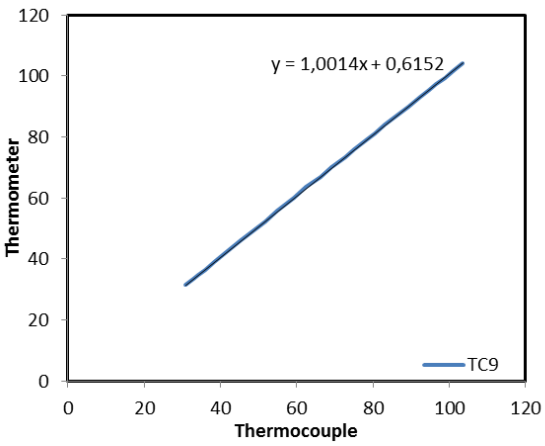
y = 1,0014x + 0,6152
Thermometer
Thermocouple
TC9

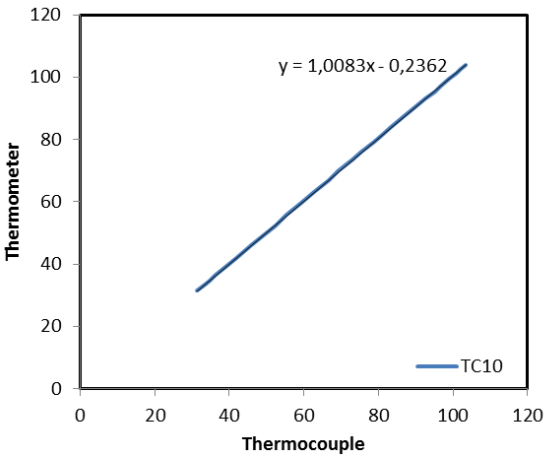
y = 1,0083x - 0,2362
Thermometer
Thermocouple
TC10

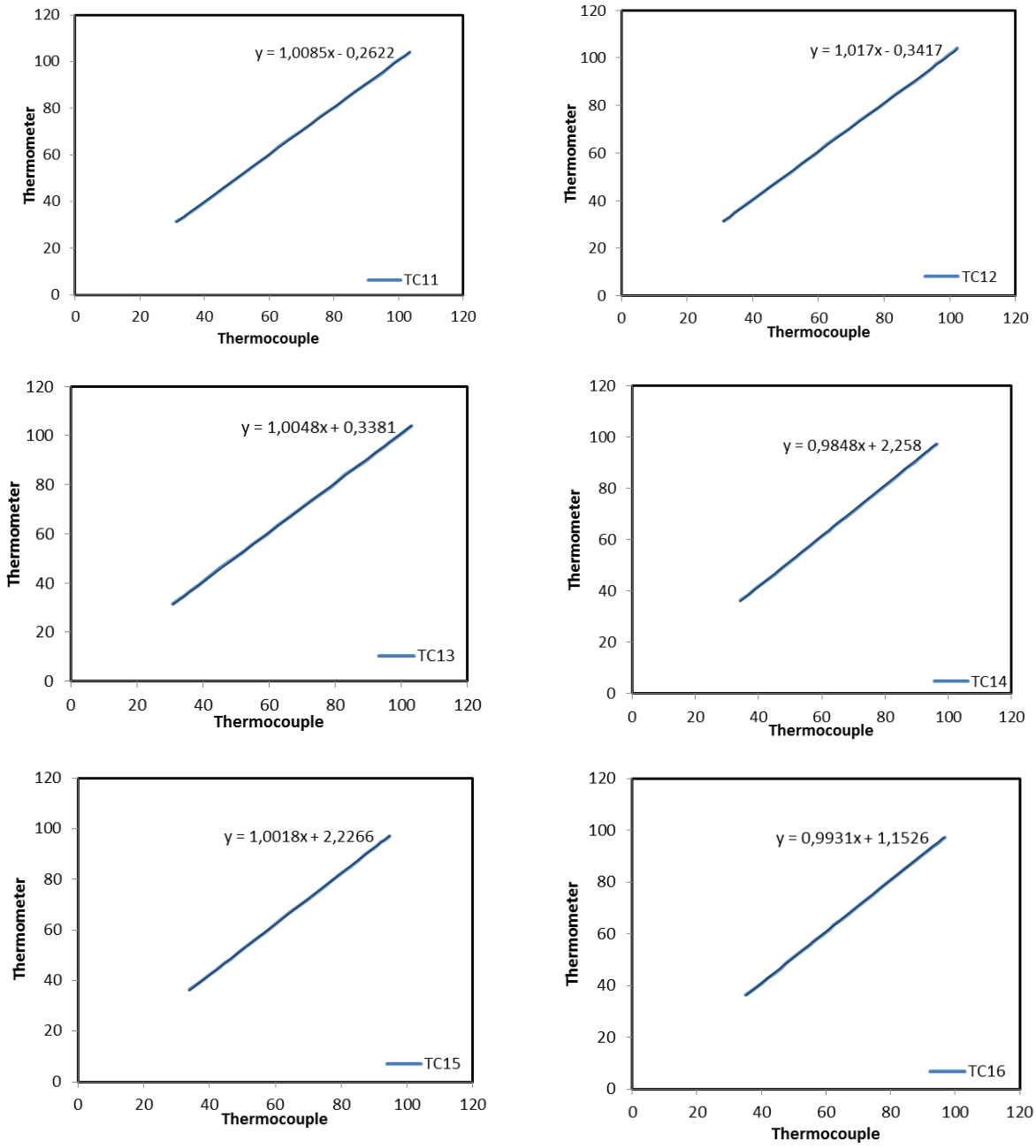

Figure C.1 Thermocouple calibration results

2-) Pressure Transducer Calibration Results

The differential pressure transducer and the inlet local pressure transducer were calibrated against to deadweight tester as stated in Chapter 3. The calibration results of the pressure transducers are provided in Fig. C.2.

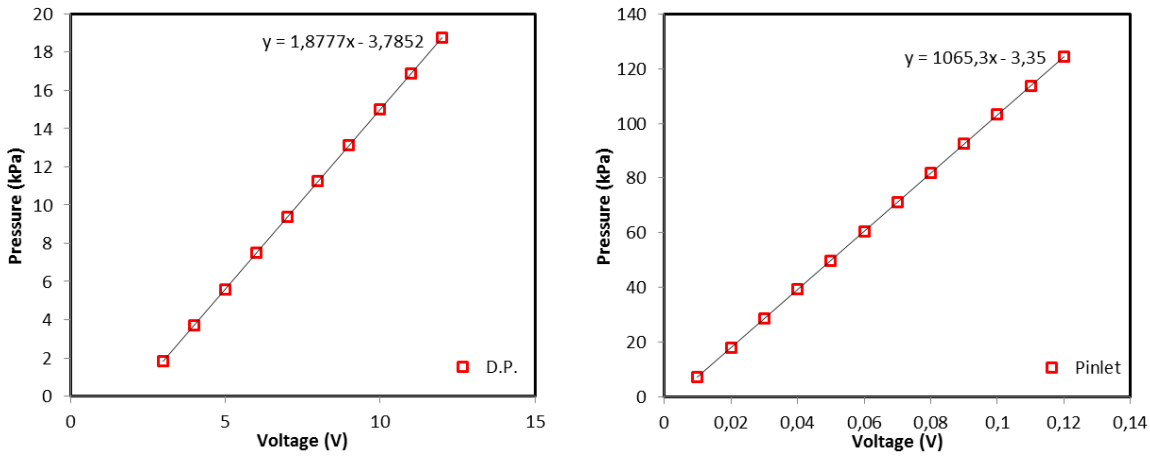

(a) (b)

Figure C.2. Pressure transducers calibration results: (a) Differential pressure transducer calibration curve, (b) Inlet pressure sensor calibration curve.

Publications

A. Conference

1- Sahar, A.M., **Ozdemir, M.R.**, Mahmoud, M. M., Wissink, J. and Karayiannis, T.G. Single-phase flow pressure drop and heat transfer in a rectangular metallic micro channel. *4th Micro and and Nano Flows Conference*, London, 2014.

2- **Ozdemir, M.R.,** Mahmoud, M.M. and Karayiannis, T.G. Flow boiling heat transfer in a rectangular copper microchannel. *International Conference on Advances in Mechanical Engineering*, Istanbul, 2015.

3- **Ozdemir, M.R.,** Mahmoud, M.M. and Karayiannis, T.G. Flow boiling heat transfer in a shallow metallic microchannel. *14th UK Heat Transfer Conference*, Edinburgh, 2015.

B. Journal

1- Sahar, A.M., **Ozdemir, M.R.**, Mahmoud, M. M., Wissink, J. and Karayiannis, T.G. Single-phase flow pressure drop and heat transfer in rectangular metallic microchannels. *Applied Thermal Engineering*, 93:1324-1336, 2016.

2- **Ozdemir, M.R.,** Mahmoud, M.M. and Karayiannis, T.G. Flow boiling heat transfer in a rectangular copper microchannel. *Journal of Thermal Engineering*, 2(2):761-773, 2016.